SOLID STATE CAVITY QUANTUM ELECTRODYNAMICS WITH QUANTUM DOTS COUPLED TO PHOTONIC CRYSTAL CAVITIES

A DISSERTATION
SUBMITTED TO THE DEPARTMENT OF ELECTRICAL ENGINEERING
AND THE COMMITTEE ON GRADUATE STUDIES
OF STANFORD UNIVERSITY
IN PARTIAL FULFILLMENT OF THE REQUIREMENTS
FOR THE DEGREE OF
DOCTOR OF PHILOSOPHY

Arka Majumdar
July 2012

© Copyright by Arka Majumdar 2012
All Rights Reserved

I certify that I have read this dissertation and that, in my opinion, it is fully adequate in scope and quality as a dissertation for the degree of Doctor of Philosophy.

(Dr. Jelena Vuckovic) Principal Adviser

I certify that I have read this dissertation and that, in my opinion, it is fully adequate in scope and quality as a dissertation for the degree of Doctor of Philosophy.

(Dr. David Miller)

I certify that I have read this dissertation and that, in my opinion, it is fully adequate in scope and quality as a dissertation for the degree of Doctor of Philosophy.

(Dr. Hideo Mabuchi)

Approved for the University Committee on Graduate Studies

Acknowledgements

Many people have made my five years as a graduate student fun and productive. First, I would like to thank my advisor, Professor Jelena Vuckovic, for her guidance and support. I also want to thank her for giving me so many opportunities to grow as an academic, sending me to conferences early and often, and giving me responsibilities with equipment purchases, teaching assistantships, mentoring new students etc. When I joined Stanford, I did not have much knowledge on quantum mechanics, and my background was mostly on RF electronics. I will always be thankful to Jelena for giving me an opportunity to work on a very different field than my expertise. I would also like to thank my co-advisor Professor David Miller, who was always available for any question I have. I would like to thank Professor Hideo Mabuchi for agreeing to be on my thesis reading committee. I learnt all the quantum optics from his lectures, as well as discussion with him outside the class-room. Finally I would like to thank Professor Mark Brongersma for agreeing to chair my thesis committee. My first exposure to nanophotonics came from the class I took from him and Professor Shanhui Fan.

I have had great luck to work with some very talented and motivated people on experiments. In my early days of graduate school, I had the opportunity to work with Dr. Dirk Englund, Dr. Andrei Faraon and Dr. Ilya Fushman, three incredibly talented people. I learnt all the experimental techniques from them. I would also like to acknowledge all of my friends and colleagues in the Vuckovic group: Michal Bajcsy, Erik Kim, Armand Rundquist, Gary Shambat, Kelley Rivoire, Sonia Buckley, Jesse Lu, Jan Petykiewicz, Bryan Ellis, Maria Makarova, Mitsuru Toishi, Yiyang Gong, Alexander Papageorge and Ziliang Lin. In particular, I want to thank my close collaborators on the quantum dot project, Michal Bajcsy, Erik Kim and Armand Rundquist its been really great working and hanging out with these guys. I would also like to thank Krishna Balram, Peter McMohan and Kristiaan De Greeve, who helped me whenever I had questions about fabrications or optical setups.

I want to thank the people of the Stanford Nanofabrication Facility. In particular, I want to thank James Conway who trained me on the electron beam lithography system and whose deep knowledge of nanofabrication and maintenance of the equipment are remarkable. I also would like to Thank Tom Carver in Ginzton Microfab (now Stanford nano-characterization center) for helping me with metallization, and figuring out several recipes for electrical control.

I would like to thank my parents for motivating me to pursue graduate school. I would also like to thank my wife Godhuli, for supporting me throughout the graduate school. Finally, I would like to thank the Almighty God.

Abstract

Quantum dots (QDs) coupled to optical cavities constitute a scalable, robust, on-chip, semiconductor platform for probing fundamental cavity quantum electrodynamics. Very strong interaction between light and matter can be achieved in this system as a result of the field localization inside sub-cubic wavelength volumes leading to vacuum Rabi frequencies in the range of 10s of GHz. Such strong light-matter interaction produces an optical nonlinearity that is present even at single-photon level and is tunable at a very fast time-scale. This enables one to go beyond fundamental cavity quantum electrodynamics (CQED) studies and to employ such effects for building practical information processing devices. My PhD work has focused on both fundamental physics of the coupled QD-nanocavity system, as well as on several proof-of-principle devices for low-power optical information processing based on this platform.

We have demonstrated the effects of photon blockade and photon-induced tunneling, which confirm the quantum nature of the coupled dot-cavity system. Using these effects and the photon correlation measurements of light transmitted through the dot-cavity system, we identify the first and second order energy manifolds of the Jaynes-Cummings ladder describing the strong coupling between the quantum dot and the cavity field, and propose a new way to generate multi-Fock states with high purity. In addition, the interaction of the quantum dot with its semiconductor environment gives rise to novel phenomena unique to a solid state cavity QED system, namely phonon-mediated off-resonant dot-cavity coupling. We have employed this effect to perform cavity-assisted resonant quantum dot spectroscopy, which allows us to resolve frequency features far below the limit of a conventional spectrometer. Finally, the applications of such a coupled dot-cavity system in optical information processing including ultrafast, low power all-optical switching and electro-optic modulation are explored. With the light-matter interactions controlled at the most fundamental level, the nano-photonic devices we implemented on this platform operate at extremely low control powers and could achieve switching speeds potentially exceeding 10 GHz.

Contents

1 Introduction 1

1.1 Long distance quantum communication 1

1.2 Optical interconnects 3

1.3 Quantum dots and photonic crystal cavities 4

1.4 Cavity quantum electrodynamics 7

1.5 Outline of the thesis 10

2 Theoretical study of the quantum dot-cavity QED system 12

2.1 Hamiltonian dynamics 12

2.2 Master equation for lossy dynamics 14

2.2.1 Quantum and semiclassical description 15

2.3 Quantum trajectory 16

2.4 Strong coupling 17

2.5 Temporal dynamics of dot-cavity system 18

2.5.1 Semiclassical equation of motion 19

2.5.2 Dependence on the system parameters 22

2.6 All-optical switching with quantum dot-cavity QED system 24

2.6.1 Static response 25

2.6.2 Dynamic response 28

2.7 Theory of electro-optic modulation 33

2.7.1 Frequency response 36

2.7.2 Nonlinear distortion of signal 38

2.7.3 Step response 40

2.7.4 Effect of dephasing on performance of the single QD modulator 44

3 Temporal dynamics and all optical switching with QD-CQED system: Experiment 45

3.1 Temporal Rabi Oscillation 45

3.2 All-optical switch 49

4 Fast electrical control of a single quantum dot-cavity system 57

4.1 Electro-optic modulation: lateral electrical control 57

4.1.1 Switching power 66

4.2 Vertical electrical control 67

5 Photon blockade and photon assisted tunneling 70

5.1 Photon blockade 71

5.1.1 Photon blockade in pulsed operation of the driving field 71

5.1.2 Non-classical state generation via fast control of dipole frequency 77

5.2 Multi-Fock state generation 81

5.2.1 Numerical simulation 83

5.2.2 Experimental result 87

5.2.3 Effect of dephasing on blockade and tunneling 92

5.3 Sub-Poissonian light generation with a bimodal cavity 92

5.3.1 Theory 96

5.3.2 Proposed experiment and preliminary experimental data . . . 104

6 Cavity QED with a Single Quantum Dot in a Photonic Molecule 110

6.1 Introduction 110

6.2 Theory 111

6.3 Characterization of photonic molecule 113

6.4 Strong coupling between a single QD and a photonic molecule 113

6.5 Comparison with bimodal cavity 118

7 Phonon-mediated off-resonant interaction in a quantum dot-cavity system 120
7.1 Theory . . . 121
7.1.1 Theory with pure QD dephasing . . . 122
7.1.2 Theory with cavity enhanced phonon process . . . 123
7.1.3 Simulation results . . . 128
7.1.4 Experimental data . . . 133
7.2 Single photon source . . . 135
7.3 Resonant QD spectroscopy . . . 139
7.3.1 Probing exciton and biexciton . . . 139
7.3.2 Emission saturation and linewidth broadening . . . 142
7.3.3 QD dressing observed via off-resonant cavity . . . 150
7.4 Time resolved study of the off-resonant cavity emission . . . 165
7.5 Phonon assisted inter-dot coupling . . . 168
7.5.1 Theory . . . 168
7.5.2 Coupling between two quantum dots . . . 171

8 Spectral diffusion and its effect on CQED 179
8.1 Theory: QD linewidth broadening . . . 181
8.2 QD charging and modulation . . . 182
8.3 QD linewidth broadening . . . 186

9 Outlook 193
9.1 Coupled cavity array for quantum many body simulation . . . 193
9.2 Coherent control of phonons . . . 195
9.3 Spin-photon interface . . . 196

Bibliography 198

List of Tables

7.1 Details of the QD-cavity systems employed in the first experiment, when the cavity emission is observed by resonantly exciting the QD. Also shown are the fits for two different contributions to the QD linewidth, $\Delta\omega_c$ and $\Delta\omega_0$, and the theoretical estimate for $\Delta\omega_c$ (see Eq. 7.40). 147

7.2 Details of the QD-cavity systems employed in the second experiment, when the QD emission is observed by resonantly exciting the cavity. Also shown are the values of the $\Delta\omega_{c0}$. 147

List of Figures

1.1 (a)Scanning electron microscope image of the fabricated photonic crystal cavity, (b) Atomic Force Microscopy (AFM) image of a $1\mu m^2$ array of self-assembled InAs/GaAs QDs (courtesy of Bingyang Zhang, Stanford University). (c) Scanning electron micro-graph of a hypothetical integrated nano-photonic structure made of photonic crystal cavities and wave-guides. 6
1.2 (a) The QD energy levels. Difference in bandgap between two materials give rise to the barriers for the electrons and the holes; (b) The inhomogeneous broadening of the quantum dots; (c) Single QD lines: delta function like density of states in quantum dot gives rise to very narrow spectral lines in QD photoluminescence. 7

2.1 (a) The transmission spectrum of a strongly coupled QD-cavity system (split resonance) and and empty cavity (single Lorentzian line); (b) The anharmonic dressed state ladder structure. 18

2.2 (a) The schematic of the coupled QD-cavity system. It is driven by a laser pulse, and the cavity output is monitored. (b) The cavity transmission calculated by three different models: the quantum optical (red), semi-classical linear (blue) and non-linear (black) model at low ($\Omega_0/2\pi = 1$ GHz) peak intensity of the driving pulse. All three models match quite well. The input pulse is also shown (green dashed line). The oscillation in the cavity output is due to Rabi oscillation of the photon between the QD and the cavity. Inset shows the cavity transmission spectrum in presence and in absence of the strongly coupled QD. The split resonances are separated approximately by twice the coherent dot-cavity interaction strength g. The spectral shape of laser pulses with pulse-length 5 ps (blue dashed line) and 40 ps (green dashed line) is also shown. Parameters used for the simulations are $g/2\pi = 25$ GHz, $\kappa/2\pi = 29$ GHz and $\gamma/2\pi = 1$ GHz. 20

2.3 (a) Comparison between the temporal cavity transmission obtained via quantum optical (red dashed line) and the semi-classical non-linear (black solid line) models. The cavity transmission is normalized by the maximum cavity transmission and plots are vertically offset for clarity. The two models match quite well at low and high driving power, but at intermediate power, they differ. Inset shows the coherence calculated as $(\langle a^\dagger \sigma\rangle - \langle a^\dagger\rangle\langle\sigma\rangle)/\Omega_0^2$ integrated over time as a function of the driving strength Ω_0. We observe that quantity increases in the intermediate driving power. Parameters used for the simulations: $g/2\pi = 25$ GHz and $\kappa/2\pi = 29$ GHz. 23

2.4 The temporal cavity output obtained from the full quantum optical simulation as a function of (a) the dot-cavity coupling strength g (here $\kappa/2\pi = 20$ GHz; $\delta = 0$ and $\gamma_d = 0$), (b) the cavity field decay rate κ (here $g/2\pi = 20$ GHz; $\delta = 0$ and $\gamma_d = 0$), (c) the dot cavity detuning δ (here $g/2\pi = \kappa/2\pi = 20$ GHz and $\gamma_d = 0$) and (d) the pure QD dephasing rate γ_d (here $g/2\pi = \kappa/2\pi = 20$ GHz and $\delta = 0$). For all the simulations a low excitation power ($\Omega_0/2\pi = 2$) is assumed. . . . 24

2.5 DC transmission characteristics of the all-optical switch made of a strongly coupled QD-cavity system system. The system is on resonance ($\omega_c = \omega_d$), and thus driving laser detunings from both QD and cavity mode are equal $\Delta = \Delta\omega_c = \Delta\omega_d$. (a) The transmission spectra for four different cases. An empty cavity shows a single Lorentzian peak. A strongly coupled QD-cavity system shows two peaks in the transmission, corresponding to the polaritons. The dip reduces both due to the pure QD dephasing, and at high laser power. The change in the dip at different driving laser power $\mathcal{E}$ is due to the QD saturation. The units of $\mathcal{E}/2\pi$ are in GHz. (b) The transmission on resonance with an empty cavity, i.e., at $\Delta\omega_c = 0$ (normalized by the empty cavity transmission) as a function of the driving laser strength. 26

2.6 Comparison between two methods: quantum optical and semi-classical. The integrated cavity transmission is plotted as a function of the delay between two pulses. The two methods match quite well at zero and large time delay. However, they differ at the minimum transmission due to destructive interference between two pulses. 27

2.7 (a) Figure showing the on-off ratio (as defined in the text) under CW driving, as a function of g and κ. (b) On-off ratio as a function of the ratio g/κ for different κ. An increase in on-off ratio is observed with increase in both g and κ. For, this simulation $\mathcal{E}/2\pi = 0.1$ GHz. 29

2.8 The cavity transmission as a function of time (horizontal axis) when two pulses interact with the coupled QD-cavity system, for different delays between two pulses (vertical axis). We present both results obtained by full quantum optical calculation (a) and semi-classically (b). The pulse-length is 40ps and $\mathcal{E}/2\pi = 1$ GHz. For this weak excitation limit, the two approaches yield nearly identical results. At small delay between the two pulses, the pulses overlap, and they behave as a single pulse. At larger delay, two pulses do not meet, and propagate independently of each other. For each input pulse we obtain two output pulses due to Rabi oscillation. At intermediate delay, there is a destructive interference between the two pulses causing reduced transmission. . . 30

2.9 Switching performance for different pulse durations. (a) Total cavity transmission integrated over time as a function of the delay between two pulses. Pulses with different pulse-durations are considered in different curves. An increased transmission is observed at zero time-delay. The minimum transmission at a non-zero time delay is due to a destructive interference between two pulses caused by the Rabi oscillation. (b) The effect of pure QD dephasing. With increasing QD dephasing, Rabi oscillations are suppressed, the destructive interference becomes ineffective, and the minimum transmission increases with pure QD dephasing rates. (c) The on-off ratio (defined as the ratio of time-integrated cavity transmission between zero delay and large delay) as a function of the pulse duration. Increasing on-off-ratio with increasing pulse duration is due to reduced bandwidth of the pulses. (d) Ratio between maximum and minimum transmission as a function of the pulse duration. 31

2.10 (a) Transmission spectra of coupled cavity-QD system for two different QD-cavity detunings. The blue arrow shows the wavelength of the laser whose transmission is being modified. (b) Normalized steady state transmission with different QD detunings. The laser is resonant with the cavity. We used the following parameters: $g/2\pi = \kappa/2\pi = 20$ GHz; $\gamma = \kappa/80$; the pure dephasing rate is assumed to be zero for this analysis ($\gamma_d/2\pi = 0$). 35
2.11 The frequency response of the switch for different (a) κ. ($g/2\pi$) is kept constant at 20 GHz and (b) g. ($\kappa/2\pi$) is kept constant at 20 GHz. For both simulations $\Omega = 1$ GHz; $\Delta\omega_0/2\pi = 10$ GHz; $\gamma_d/2\pi = \gamma/2\pi = 0.1$ GHz. 37
2.12 (a) Cut-off frequency of the modulator as a function of g and κ. In the color scheme, the maximum cutoff frequency of $\sim$ 90 GHz is red and the minimum cut-off frequency of $\sim$ 10 GHz is blue; (b) On-off ratio of the modulator at a modulating frequency of $\omega_e/2\pi = 5$ GHz as a function of g and κ. For both plots $\Delta\omega_0/2\pi = 5$ GHz; $\gamma_d/2\pi = 0.1$ GHz; $\Omega = 1$ GHz. 38
2.13 Normalized output signal for two different maximal QD detunings $\Delta\omega_0$. (a) $\Delta\omega_0/2\pi = 2$ GHz. (b) $\Delta\omega_0/2\pi = 40$ GHz. For both simulations the frequency of the electrical signal is $\omega_e/2\pi = 20$ GHz, $\kappa/2\pi = g/2\pi = 20$ GHz and $\Omega = 1$ GHz. 39
2.14 Ratio of the second and third harmonic to the first harmonic of the modulated signal, as a function of the maximum frequency shift of the QD, scaled by a factor of g^2/κ. The first harmonic is proportional to the actual signal. For the simulation we assumed that the modulation is working in the passband ($\omega_e/2\pi = 20$ GHz); $\kappa/2\pi = g/2\pi = 20$ GHz and the dephasing rate $\gamma_d/2\pi = 0$. 41
2.15 Step response of the single QD electro-optic modulator. The parameters used for the simulation are: $\kappa/2\pi = 5$ GHz; $g/2\pi = 20$ GHz; $\Delta\omega_0/2\pi = 20$ GHz; $\Omega = 1$ GHz. 42

2.16 Ratio between the third and first harmonic of the modulated signal for different QD-cavity coupling g and maximum QD detuning $\Delta\omega_0$. The cavity decay rate $\kappa/2\pi = 20$ GHz and the modulation frequency $\omega_e/2\pi = 5$ GHz. 43

2.17 (a) Normalized steady state transmission of the laser resonant with the dot (i.e., $\Delta\omega_a = 0$) with pure dephasing rate $\gamma_d/2\pi$. Parameters used are: $g/2\pi = \kappa/2\pi = 20$ GHz; $\gamma = \kappa/80$; (b) On-off ratio of the modulated signal as a function of the dephasing rate, for $\kappa/2\pi = g/2\pi = 20$ GHz. The modulation frequency $\omega_e/2\pi = 5$ GHz and the amplitude of the change in resonance frequency $\Delta\omega_0/2\pi = 10$ GHz. . 44

3.1 Cross-polarized reflectivity setup: the cavity is kept at a 45^o angle. The probe light is vertically polarized, but we collect only the horizontal light at the output. Thus we collect only the light which interacted with the cavity, and get rid of the background. 46

3.2 The normalized cavity transmission for different pulse duration. The pulse duration is changed from 5 ps to 50 ps. We observe oscillation in the cavity output, although the oscillation frequency decreases with increasing pulse-width. This can be explained by the reduced overlap between the pulse and the coupled dot-cavity system in frequency domain. 47

3.3 Experimentally measured time resolved transmission of 40ps pulses through a strongly coupled dot-cavity system for three different powers (averaged over the pulse repetition period): (a)0.1 nW; (b) 0.23 nW; (c) 1 nW. The powers are measured in front of the objective lens in the confocal microscopy setup. For this specific system cavity field decay rate $\kappa/2\pi = 29$ GHz and coherent dot-cavity coupling strength $g/2\pi = 25$ GHz. Clear oscillations are observed in the cavity transmission, consistent with the the theoretical predictions. We also observe decreasing oscillation with increasing laser power due to QD saturation. 48

3.4 (a) Scanning electron micrograph of the photonic crystal cavity. (b) In the experiment, a combination of pulsed control laser (frequency ω_c), non-resonant pulsed or continuous wave pump laser at ω_e above the QD exciton line, and pulsed or continuous-wave signal laser (ω_s) is employed. The cavity is backed by a distributed Bragg reflector, effectively creating a single-sided cavity[1]. A cross-polarized confocal microscope configuration reduces the laser background that is reflected from the sample without coupling to the cavity, which is polarized at 45° to the incident laser polarization. The measurement is effectively a transmission measurement from the horizontal (H) into the vertical (V) polarization. (c) Anticrossing observed in the PL as the QD single exciton (X) is temperature-tuned through the cavity. The QD is pumped through higher-order excited states by optical excitation at ω_e corresponding to a wavelength of $\lambda_e = 878$ nm. (d) The transmitted intensity of a broad-band light source (in the cross-polarized setup) shows the mode splitting of the strongly coupled QD-cavity system (this signal is resolved on a spectrometer). (e) PL lifetime ~ 17 ps when the QD is tuned into the cavity and pulsed excitation is at wavelength $\lambda_e = 878$ nm. The emission that is expected theoretically, based on the system parameters in (d) and a 10-ps relaxation time into the single exciton state, is shown in the solid line. 50

3.5 All-optical switching of the CW signal beam by a pulsed control beam through the strongly coupled QD/cavity system. (a) Cavity transmission when the signal and control are tuned to the cavity, which is resonant with the QD (panel 1). The transmitted cavity output is normalized w.r.t. the maximum cavity transmission. As the signal and control input powers are increased (panels 2 and 3), the QD saturates and results in a net-positive nonlinear transmission. For the three panels, the CW signal powers are 12 nW, 168 nW and 240 nW, respectively; the pulsed control powers are 0.2 nW, 1.6 nW and 3.8 nW, respectively (all measured before the objective lens). (b) Plots of the theoretically estimated intracavity photon number $\langle a^\dagger a \rangle$, which gives the transmission by $T = 2\kappa \langle a^\dagger a \rangle$. We plot the calculated intracavity photon number for the control beam intracavity photon number $n(c)$, signal and control $n(s+c)$, and the differential photon number $\Delta n = n(s+c) - n(s) - n(c)$. 53

3.6 All-optical switching between two weak laser pulses interacting via a strongly coupled QD-cavity system. (a) Time-delay setup for producing pulses at a separation of Δt. (b) Simulated interaction of two laser pulses, represented by the instantaneous intracavity photon number $\langle a^\dagger a \rangle$ as a function of the time delay Δt between the two 40 ps long Gaussian pulses. Curves are calculated for a set of different rates of pure QD dephasing [2], γ_d, which causes a reduction of the transmission dips before and after the peak. Pure dephasing also causes a blurring of the spectral normal mode splitting [2], which in turn raises the transmission for increasing γ_d. (c) Pump-power dependence of the cavity transmission for coincident pulses repeating at 80 MHz. Different curves correspond to the average power of each of the pulses used in the experiment (averaged over 13 ns, the pulse repetition period). (d) Signal observed when the cavity-QD system is probed with two 40 ps long pulses as a function of their delay. When the two pulses have a temporal overlap inside the cavity (i.e., delay approaches zero), the QD saturates and the overall cavity transmission increases. The power in the single of the two pulses corresponds roughly to the 3.4nW trace in (c). Best agreement is found with the theoretical plot for a pure dephasing rate $\gamma_d/2\pi \sim 5$ GHz (the solid red line). 55

4.1 (a) Scanning electron microscope image of the photonic crystal cavity and the metallic electrode placed within $1\mu m$ from the center of the cavity. (b) Schematic representation of the experimental setup (not drawn to scale). A cross-polarized confocal microscope setup composed of a polarizing beam splitter(PBS), half wave plate (HWP) and objective lens (OL) was used for photoluminescence and reflectivity measurements. The voltage on the chip was controlled using a function generator (FG) and the output signal was detected using a single-photon counting module (SPCM). A flip mirror (M) switched the signal from spectrometer to SPCM. The time domain measurements were performed using a picosecond time analyzer(PTA).(c) Photoluminescence spectra taken for different cavity/QD detunings by increasing the temperature of the sample (indicated for each spectrum). The avoided crossing of the polaritons (marked by the red lines as a guide to the eye) indicates that QD1 is strongly coupled. 59

4.2 (a) Photoluminescence spectra as a function of increasing control voltage (V) from 0V to 10V. At 0V the quantum dot was tuned on resonance with the cavity (T=48K). The PL intensity decreases and the QD red shifts for $V > 8V$. The shift is much smaller than the one observed in broadband reflectivity because of the screening induced by free carriers. (b)Broadband reflectivity spectra while changing V from 0V to 10V (T=48K). The QD red shifts for $V > 4V$. 60

4.3 Change in QD frequency and coupling strength g with bias voltage (a) Stark shift of the quantum dot with applied bias. (b) Experimental data and fit indicating the quadratic dependence of the quantum dot shift with electric field. (c) Dependence of the cavity/QD coupling g with applied voltage, as inferred from the fit to experimental data (d) Broadband reflectivity taken at T=46K such that the QD was resonant with the cavity at high electric fields. As the voltage approaches 8V, the signature of the quantum dot in the spectrum vanished, most probably due to the loss in the quantum dot confinement due to high electric field. More information about the nature of this effect could be inferred by a QD spectroscopy method where the energy of all the QD orbitals are monitored while varying the field. 62
4.4 Fast electrical switching of a continuous wave laser beam (a) CW reflectivity for bias voltages of 0V, 10V and 14V. During the time-domain switching experiment the laser was set at the wavelength marked by the vertical dashed line and a 0-10V signal was applied. (b) Switching of the coupled laser at the electrical QD driving frequency of 150MHz. 64
4.5 The details of the p-n-i-n wafer with doping densities. 68
4.6 Vertical electric field applied to a quantum dot in p-i-n diode: (a) Fabrication steps for contacts and photonic crystal devices enabling electrical control in a p-i-n junction. Here, p-GaAs, n-GaAs and i-GaAs indicate p-doped, n-doped and intrinsic gallium arsenide, respectively. (b) QD resonance as a function of the applied potential in p-i-n diode. (c) Photoluminescence spectra as a function of the applied potential. A discrete jump of the QD resonance is observed, which indicates a discrete charging event of the QD. 69

5.1 (a) Schematic representation of a single emitter coupled to an optical resonator. The optical resonator has mirrors with different reflection coefficients ($R_{in} >> R_{out}$) such that most of the field coupled into the cavity is emitted at the output port. (b) Schematic representation of the energy eigenstates for a strongly coupled cavity-emitter system. . 72

5.2 (a) Non-classical state generation via pulsed-operation in photon blockade. The properties of the laser pulse coupled at the input port are controlled such that the output field has primarily a single-photon component. (b) Normalized Fock-state coefficients ($|c_0|^2$ for vacuum state, $|c_1|^2$ for single photon state, and $|c_{multi}|^2 = \sum_{n=2}^{\infty} |c_n|^2$ for multi photon probability) for the output field as the intensity of the laser pulse Ω_0 is modified and the pulsewidth is kept constant at $\tau = 0.45/\kappa$. The ground state and one of the first order eigenstates form an effective two level system so Rabi oscillations are observed in the single photon character of the output field. The system has parameters $\kappa/2\pi = 1GHz$, $\gamma/2\pi = 0.1GHz$, $g/2\pi = 40GHz$. (c) Fock-state coefficients for the output field as the duration of the laser pulse (τ) is modified while $\Omega_0 = 10GHz$ was kept constant. The system has parameters $\kappa/2\pi = 1GHz$, $\gamma/2\pi = 0.1GHz$, $g/2\pi = 40GHz$. (d) The same simulation as in the panel **b** for a system with $\kappa/2\pi = 5GHz$, $g/2\pi = 30GHz$ 74

5.3 (a) Second order correlation correlation function of the output field, for the case $\kappa/2\pi = 1GHz$, $g/2\pi = 40GHz$. (b) Second order correlation correlation function for $\kappa/2\pi = 5GHz$, $g/2\pi = 30GHz$. 78

5.4 Ratio of single photon to multi-photon probability in the output field of the non-classical source with $\kappa/2\pi = 1GHz$ $g/2\pi = 40GHz$ as a function of mean photon number per pulse. The results are compared with a coherent pulsed laser source of the same brightness. 79

5.5 (a) Operation principle for non-classical state generation using a continuous wave input and fast control of the dipole frequency using an electric field. (b) Detuning of the dipole frequency with time. The cavity resonance is constant and zero detuning means dipole resonant with the cavity. (c) Normalized Fock-state coefficients ($|c_0|^2$ for vacuum state, $|c_1|^2$ for single photon state, and $|c_{multi}|^2 = \sum_{n=2}^{\infty} |c_n|^2$ for multi photon probability) for the output field with varying intensity of the continuous wave input field (Ω_0). The system has parameters $\kappa/2\pi = 1GHz$, $\gamma/2\pi = 0.1GHz$, $g/2\pi = 40GHz$. (d) Normalized Fock-state coefficients for a system with $\kappa/2\pi = 5GHz$, $\gamma/2\pi = 0.1GHz$, $g/2\pi = 30GHz$ 80

5.6 (a) The anharmonic ladder structure: when the laser is detuned from the polariton, then the coupling of the first photon is difficult, but two photons together can reach the second order manifold, and the output light will have more two photon character. 82

5.7 Numerically calculated photon statistics at the output of the QD-cavity system driven by Gaussian pulses with duration $\tau_p \sim 24$ ps. The simulation parameters are $g = 2\pi \times 40$ GHz, $\kappa = 2\pi \times 4$ GHz, and $\mathcal{E}_o = 2\pi \times 9$GHz; pure QD dephasing is neglected. (a) $P(n)$, probability of generating an n photon state at the CQED system output as a function of laser-cavity detuning Δ_c. (b) The ratios r_1 and r_2 as a function of Δ_c. $r_m = \frac{P(m)^2}{P(m-1)P(m+1)}$, where $P(m)$ is the probability of having m photons in the light. The dotted lines show the expected values of the ratios from a classical coherent state. (c) Second order auto-correlation $g^{(2)}(0)$ as a function of Δ_c. The red dashed line shows the expected $g^{(2)}(0)$ for a coherent state. (d) Second order differential correlation $C^{(2)}(0)$ as a function of Δ_c. (e) $C^{(2)}(0)$ as a function of the laser-cavity detuning Δ_c for different values of the peak laser field $\mathcal{E}_o/2\pi$ (in units of GHz). Every plot is normalized by the maximum $C^{(2)}(0)$, so that the peak value becomes 1 for all the plots. We observe that the peak in the $C^{(2)}(0)$ occurs at $\Delta_c = 0.7g$ for weaker excitation (where the second order manifold is excited resonantly via two photons). However, with increasing excitation power, the peak positions shifts towards $\Delta_c = 0$, due to excitation of higher manifolds. 85

5.8 Numerically calculated photon statistics for pulsed driving of our current QD-cavity system: (a)The probability $P(n)$ of n photon states in the output light, as a function of $\mathcal{E}_o$, when the laser is resonant with the cavity. (b) $g^{(2)}(0)$ and $C^{(2)}(0)$ as a function of $\mathcal{E}_o$. The minimum $\mathcal{E}_o$ used is 0.1 in the plot. (c) $P(n)$ for n photon state as a function of laser-cavity detuning Δ. (d) $g^{(2)}(0)$ and $C^{(2)}(0)$ as a function of Δ. The simulation parameters are $g \approx \kappa = 2\pi \times 20$ GHz, $\mathcal{E}_o = 2\pi \times 9$GHz and and the system is driven with Gaussian pulses with $\tau_p \sim 24$ ps. . 87

5.9 Experimental observations of photon induced tunneling and blockade under pulsed excitation ($\tau_p \sim 24$ ps pulses with 80 MHz repetition frequency). (a) Coincidence measurement obtained when the laser is tuned to the dip between polaritons. Increased coincidence counts at $t = 0$ indicate the photon induced tunneling regime. (b) Coincidence measurement obtained when the laser is tuned to the polariton (in this case, the one at lower frequency). The reduced coincidence counts at $t = 0$ indicate the photon blockade regime. The average laser power for the measurement is $P_{avg} = 0.2$nW. 89

5.10 (a) The transmission spectrum of a strongly coupled QD-cavity system showing two polaritons. (b) Second order coherence function at $t = 0$, $g^{(2)}(0)$ as a function of the laser detuning from the empty cavity frequency. The system is excited with $\tau_p = 24$ ps Gaussian pulses, with 80 MHz repetition frequency. The dashed grey (solid black) line results from a numerical simulation based on the system's experimental parameters and no (with) QD blinking. The average laser power for the measurement is $P_{avg} = 0.2$nW. For the simulations we use a QD dephasing rate $\gamma_d/2\pi = 1$ GHz. 90

5.11 (a) Normalized differential correlation function $C^{(2)}(0)$ as a function of the laser detuning. The dashed red line shows the result of a numerical simulation based on the system's experimental parameters. (b) $g^{(2)}(0)$ in the tunneling regime ($\Delta_c = 0$) as a function of laser power P_{avg} measured in front of the objective lens. The solid line shows the result of numerical simulation including the effects of QD blinking, while the inset plots the numerically simulated $g^{(2)}(0)$ in the absence of blinking. For the simulations we use a QD dephasing rate $\gamma_d/2\pi = 1$ GHz. . . 90

5.12 The effect of pure QD dephasing on the tunneling and blockade regime: (a) In the blockade regime $g^{(2)}(0)$ remains lower than 1, but increases with increasing dephasing rate. (b) In the tunneling regime, $g^{(2)}(0)$ remains higher than 1, but decreases with increasing dephasing rate. . 93

5.13 The effect of pure QD dephasing on the Fock state generation: (a) Probability $P(n)$ of generating n photon states as a function of Δ/g. No QD dephasing is included. (b) $P(n)$ as a function of Δ/g, with a pure QD dephasing rate $\gamma_d/2\pi = 1$ GHz. For all the simulations: $\kappa/2\pi = 4$ GHz and $g/2\pi = 40$ GHz. 94

5.14 (a) Schematic of a QD coupled to a single mode cavity, with a coupling strength of g. (b) Schematic of a bimodal cavity with a coupled QD. The two cavity modes are not directly coupled to each other. However, both of them are coupled to the QD with interaction strengths g_a and g_b. (c) The cavity output $\kappa\langle a^\dagger a\rangle$ as a function of the driving laser detuning Δ from the empty cavity resonance both for a single mode cavity (dashed line) and the bimodal cavity (solid line). The split resonance observed is due to the coupled QD. (d) Second order autocorrelation $g^{(2)}(0)$ function calculated for the collected output of the driven mode for a single mode (thick dashed line) and bimodal cavity (solid line). The green dashed line marks the Poissonian statistics of a coherent state (always 1). For single mode cavities at $\Delta \sim \pm 1.5g$ and for bimodal cavities at $\Delta \sim \pm 1.8g$, we observe a weakly sub-Poissonian light ($g^{(2)}(0)$ slightly less than 1). However, for bimodal cavity a strong sub-Poissonian light is generated when $\Delta = 0$. For bimodal cavities we assumed identical interaction strengths and cavity decay rates for two modes. Parameters used for the simulations: QD-cavity interaction strength $g/2\pi = g_a/2\pi = g_b/2\pi = 10$ GHz, cavity field decay rate $\kappa/2\pi = 20$ GHz, dipole decay rate $\gamma/2\pi = 1$ GHz, and driving laser strength $\mathcal{E}\sqrt{\kappa}/2\pi = 1$ GHz. 98

5.15 (a) Transmitted output $\kappa\langle b^\dagger b\rangle$ from the undriven cavity mode b as a function of g and κ. For both modes the same g and κ are assumed. (b) Second order autocorrelation $g^{(2)}(0)$ for the bimodal cavity as a function of g and κ. The light is always sub-Poissonian, and results from the resonant QD excitation via mode a, and collection of the output photons via mode b. This is similar to a conventional single photon source under resonant excitation of the QD. 100

5.16 (a) Second order autocorrelation $g^{(2)}(0)$ for the conventional photon blockade in a single mode cavity as a function of the QD-cavity coupling strength g and cavity field decay rate κ. $g^{(2)}(0)$ decreases with increasing value of g/κ, as expected, as a result of reduced overlap of energy eigenstates in the anharmonic ladder. (b) $g^{(2)}(0)$ for the bimodal cavity as a function of g and κ. $g^{(2)}(0)$ is calculated for the output of mode a, i.e., for photons leaking from the mode a. We observe that $g^{(2)}(0) \rightarrow 1$ (Poissonian output) when $g/\kappa \rightarrow 0$ or ∞. However, we can observe very low $g^{(2)}(0)$ even when the QD is not strongly coupled to the two cavity modes ($g < \kappa/2$). (c) $g^{(2)}(0)$ as a function of the ratio κ/g for different g showing sub-Poissonian light generation in the bimodal cavity even in the weak coupling regime. For all the simulations $\mathcal{E}/2\pi = 0.1$ GHz such that the QD is not saturated. 101

5.17 (a) Cavity output for an empty cavity β and another cavity α coupled to a QD with a coupling strength of $\sqrt{2}g$. The combined output of these two replicates the output from the bimodal cavity a (Fig. 5.14). (b) $g^{(2)}(0)$ for these three cases: the empty cavity β gives Poissonian light; the cavity α with coupled QD gives super-Poissonian light due to photo-induced tunneling [3] (the black curve goes to infinity at $\Delta = 0$); the combined output a provides sub-Poissonian light. Parameters for the simulation: $g/2\pi = 10$ GHz, $\kappa/2\pi = 20$ GHz, $\gamma/2\pi = 1$ GHz and $\mathcal{E}\sqrt{\kappa}/2\pi = 1$ GHz. 103

5.18 (a) Second order autocorrelation $g^{(2)}(0)$ of the cavity transmission, as a function of the relative detuning Δ_{ab} between two cavity modes for different cavity field decay rates $\kappa = \kappa_a = \kappa_b$. The quality of the sub-Poissonian photon stream in the transmitted output degrades with increasing detuning, which can be compensated by increasing κ, thereby maintaining low $g^{(2)}(0)$. For these simulations we assume $g_a/2\pi = g_b/2\pi = 10$ GHz and $\mathcal{E}/2\pi = 0.1$ GHz. (b) Second order autocorrelation $g^{(2)}(0)$ of the cavity transmission as a function of the ratio g_b/g_a for different g_a. The transmitted light behaves like a coherent state at high g_b/g_a ratio and like a super-Poissonian state generated via photo-induced tunneling at low g_b/g_a ratio. In between, when $g_b/g_a \sim 1$, we observe strong sub-Poissonian output. Here, $\kappa/2\pi = 20$ GHz for both cavity modes. 106

5.19 Scanning electron micrographs of fabricated photonic crystal cavities that can support degenerate modes: (a) $H1$ cavity, where the central hole is removed; (b) "calzone" cavity, where the central hole and half of the next layer of holes are removed; (c) $H2$ cavity, where the central hole and the first layer of surrounding holes are removed. (d) Photoluminescence spectrum of an $H1$ cavity showing moderate quality factors and moderate degeneracy of the two modes. Black dots correspond to experimental data points; the red lines are Lorentzian fits. 107

5.20 (a), (b) PL spectrum of the bimodal (H2) cavity and a coupled QD at two different temperatures 20K (a) and 30K (b). The two modes are denoted as M1 and M2 and the QD is denoted as D1. (c),(d) Polarization dependence of the cavity modes (red and black plots) and the QD (green plot) at two different temperatures: 20K (a) and 30K (b). 108

6.1 Numerically calculated cavity transmission spectra when the QD resonance is tuned across the two cavity resonances. (a) Anticrossing is observed between the quantum dot and both cavity modes when the two cavities are coupled (coupling rate between the two cavities is $J/2\pi = 80$ GHz). (b) When the two cavities are not coupled ($J = 0$), we observe anti-crossing in only one cavity. Parameters used for the simulation: cavity decay rate $\kappa/2\pi = 20$ GHz (for both cavities); QD dipole decay rate $\gamma/2\pi$=1 GHz; dot-cavity coupling rate of $g/2\pi = 10$ GHz; intrinsic detuning between the bare cavity modes $\Delta_o/2\pi = 40$ GHz for (a) and 120 GHz for (b). The plots are vertically offset for clarity. The horizontal axis corresponds to the detuning of the probe laser frequency ω_p from the cavity a resonance ω_0 in units of cavity field decay rate. 114

6.2 Photoluminescence spectra of the coupled cavities for different hole spacings between two cavities: (a) the cavities are diagonally placed and separated at an angle of 60^o (see the inset for a scanning electron micrograph (SEM)); (b) the cavities are laterally separated (see the inset for SEM). A decrease in the wavelength separation between two cavity modes is observed with increasing spatial separation between the cavities (i.e., with increasing number of holes inserted in between the two cavities). For the diagonally placed cavities the holes are counted along the 60^o direction. A much larger separation is observed in (a) when the cavities are coupled at an angle compared to the lateral coupling (b). 115

6.3 Normalized PL intensity plotted when we tune the QD across the cavity resonance by temperature: (a) before nitrogen deposition (i.e., the QD is temperature tuned across the longer wavelength resonance), and (b) after nitrogen deposition (which red-shifts the cavity resonances and allows us to temperature tune the QD across the shorter wavelength resonance). Clear anti-crossings between the QD and the cavity are observed for both super-modes. In both cases, the temperature is increased from bottom to top (the plots are vertically offset for clarity). In the inset the resonances of the two anti-crossing peaks (as extracted from curve-fitting) are plotted. Since nitrogen tuning affects only cavity resonances (not QD), the same QD is tuned across both super-modes. Red arrow in figure (a) shows another blue-shifted QD that enters this spectral range during the temperature tuning, but it is only weakly coupled to the lower super-mode, as explained in the text, and does not affect experimental results. 117

6.4 QD-photonic molecule spectrum, (a) when the QD is resonant with super-mode sm2 and (b) when the QD is resonant with super-mode sm1. From the fit we extract the system parameters (see text). Numerically simulated (c) second order autocorrelation $g^2(0)$ and (d) transmission from cavity b, as a function of laser frequency, with the experimental system parameters that were extracted from the fits. 119

6.5 (a) Cavity transmission for two cases: bimodal cavity and photonic molecule. (b) Second order autocorrelation $g^{(2)}(0)$ for these two cases. Parameters used for the simulations: QD-cavity interaction strengths $g/2\pi = g_a/2\pi = g_b/2\pi = 10$ GHz; cavity field decay rates $\kappa_a/2\pi = \kappa_b/2\pi = 20$ GHz; coupling strength for the photonic molecule $J/2\pi = 40$ GHz; dipole decay rate $\gamma/2\pi = 1$ GHz. 119

7.1 (a),(b) Energy levels of the coupled QD/cavity system where the QD is blue (a) and red (b) detuned from the cavity. A laser drives the quantum dot (transition between ground state (1) and excited state (2)) resonantly. The excited state (2) can decay via two paths: the first is by direct decay back to the ground state (1) via the spontaneous emission; the second is by indirect decay via the emission (Fig. 7.1 a) or absorption (Fig. 7.1 b) of a phonon (transition (2) to (3)) and subsequent emission of a photon at the cavity frequency (transition (3) to (1)). (c), (d) Emission $S(\omega)$ as a function of frequency ω for a resonantly driven QD, that is blue (c) and red (d) detuned from the cavity, where ω_l is the laser frequency. Three different cases are considered: without any dephasing; with pure dephasing and with a cavity enhanced phonon process. We observe the Mollow triplet at the QD frequency in all three cases. The insets of (c) and (d) show an enlarged view of the emission at the cavity frequency. For the simulation we assume $g/2\pi = \kappa/2\pi = 20$ GHz; $\gamma/2\pi = 1$ GHz; $\Omega/2\pi = 6$ GHz; QD-cavity detuning $\Delta = \pm 6\kappa$. 124

7.2 Resonance fluorescence I collected from the cavity for a blue-detuned QD ($\Delta > 0$). (a) $log_e(I)$ as a function of the rates γ_d and γ_r (for two models, respectively). $\Delta/\kappa = 10$. (b) $log_e(I)$ as a function of the cavity linewidth κ, when the dot-cavity detuning $\Delta = 10\kappa$. (c) QD linewidth as a function of the rates γ_d and γ_r for pure dephasing and the cavity enhanced phonon process, respectively. In both cases, $\Omega/2\pi = 1$ GHz and $\Delta = 12\kappa$. The solid black line shows the theoretical estimates of the QD linewidth when the laser excitation power is very low and the QD is not significantly perturbed by the cavity. (Parameters used for all the simulations are $g/2\pi = \kappa/2\pi = 20$ GHz; $\gamma/2\pi = 1$ GHz.) . . . 130

7.3 Theoretical resonance fluorescence I collected from the cavity and QD linewidth for a blue-detuned QD ($\Delta > 0$): (a) Normalized cavity fluorescence as a function of the Rabi frequency Ω of the laser for two models. Saturation of the cavity emission is observed. (b) Power broadened QD linewidth (read through the cavity, as in [4]) vs laser Rabi frequency Ω for QD-cavity detuning $\Delta/2\pi = 6$ GHz. (c) Dependence of the saturated cavity emission I_{sat} on the dot-cavity detuning Δ. (d) Dependence of the intrinsic QD linewidth $\Delta\omega_0$ on dot-cavity detuning Δ. $\Delta\omega_0/2\pi$ approaches $2(\gamma+\gamma_d)/2\pi$ or $2(\gamma+\gamma_r)/2\pi$ (both chosen to be 4 GHz) with large Δ. (Parameters used for all the simulations are: $\kappa/2\pi = g/2\pi = 20$ GHz; $\gamma/2\pi = 1$ GHz.) 132

7.4 (a) The difference in QD linewidths measured via collected emission through the off-resonant cavity for a blue ($\Delta\omega_+$) and a red ($\Delta\omega_-$) detuned QD for different values of the excitation laser Rabi frequency Ω as a function of the bath temperature T. (b) Ratio of the cavity intensity for an off-resonant QD blue (I_+) and red (I_-) detuned from the cavity as a function of the bath temperature T. For all the simulations, the absolute value of the QD-cavity detuning is kept at 10κ. 133

7.5 Experimentally observed off-resonant cavity emission as a function of the detuning Δ between the resonantly driven QD and the cavity. Data are fit with a model $\Delta^{-\alpha}$. Extracted values of α for the different curves are shown. 134

7.6 (a) Cross-polarized confocal microscope setup. (b) E_y field in the L3-cavity structure. The structure is perturbed at the sites indicated by dashed circles, as described in Ref.[5]. (c) Scanning electron micrograph of fabricated structure. (d) Energy levels of the coupled QD/cavity system showing the two polarization states of the single exciton (X,Y) and the biexciton state (XX). The table lists the system parameters derived from the measurements, where g, κ, γ^* are the vacuum Rabi frequency, cavity field decay rate, and dipole dephasing rate, respectively. The dipole decay rate γ is estimated from the lifetime of uncoupled QDs. (e) The photoluminescence (PL) shows the QD/cavity anticrossing as the QD is temperature-tuned through the cavity. (f) Vacuum Rabi splitting observed in the reflectivity from the strongly coupled QD/cavity system. For comparison, we show the reflectivity of an empty cavity. 136

7.7 (a) Resonant QD excitation at 10K. For the autocorrelation measurements, the cavity emission is isolated from the pump using a grating filter providing 17 dB of isolation at $\delta = -1.2$ nm detuning. The laser is operated in continuous wave here so that is has low overlap with the cavity. (b) Autocorrelation histogram of cavity emission when the QD is pumped resonantly with 40-ps pulses (spectrum not shown). (c) Time-resolved resonant pumping of the quantum dot and emission into the cavity mode. A theoretical fit to the cavity emission yields an estimate of the pure dephasing rate. 138

7.8 QD spectroscopy through cavity mode at 10K. (a) Intensity on spectrometer when the pump wavelength λ_p is scanned across the detuned QD/cavity system (the laser has a weak red-detuned side band; power is 12 nW before the objective lens). When λ_p is resonant with the dot (cavity), the cavity (QD) intensity rises. (b) Spectrum when QD is pumped (the middle peak corresponds to the laser side mode) (c) spectrum when cavity is pumped. In (b) and (c), we model the driving mechanism by a pure dephasing process with $\gamma^* = 0.1g$. The model agrees well with the emission through the cavity (QD) when the QD (cavity) is pumped. (d) The integrated cavity emission as a function of the pump wavelength λ_p shows the single exciton absorption resolved to 3 GHz. (e) The integrated QD emission. 140

7.9 (a) Dependence of integrated cavity emission on QD detuning when the QD is resonantly pumped. (b) Pump power dependence: at a pump power of 200 nW, a second line becomes visible at a pump wavelength $\lambda_p = 919.87$ nm. (The lines are slightly shifted since the temperature was, for technical reasons, raised to 18 K). (c) Integrated cavity emission as λ_p is scanned. *Inset:* The power dependence of the two lines suggests exciton (X) and biexciton (XX) states; in this inset, a background of 40 was subtracted. 141

7.10 (a) Cavity emission when the QD is resonantly excited. (b) QD emission when the cavity is resonantly excited. Experiments to obtain (a) and (b) are performed at 55 K. The cavity wavelength is 931.2 nm. The QD resonances are at (a) 933.15 nm and (b) 931.9 nm. Emission from the QD at 933.15 nm is very weak under resonant excitation of the cavity. Hence, for (b) another QD at 931.9 nm is used. (c) Integrated cavity emission as a function of the pump laser wavelength when the QD is resonantly excited [as in (a)]. The solid line is a Lorentzian fit (with a linewidth of 0.075 nm, i.e., $\Delta\omega/2\pi \approx 25$ GHz). (d) Integrated QD emission as a function of laser wavelength for the case of resonant cavity excitation [as in (b)]. The solid line is a Lorentzian fit (with a linewidth of 0.1517 nm, i.e., $\Delta\omega/2\pi \approx 52$ GHz). 146

7.11 (a),(c),(e): Integrated cavity emission as a function of the excitation power of the laser resonantly pumping the QD, for the three QD-cavity systems studied. (c.c. stands for CCD count.) The solid lines are fits to the data using the model given by Eq. 7.38. (b),(d),(f): Corresponding measured linewidths [as in Fig. 7.10 (c)] as a function of the laser excitation power. The solid lines are fits to the data using the model given by Eq. 7.40. The excitation laser power is measured in front of the objective lens. 148

7.12 (a),(c): Integrated QD emission as a function of the excitation power of the laser resonantly pumping the cavity, for the two QD-cavity systems studied (see Table 7.2). (c.c. stands for CCD count.) The solid lines are fits to the data using model given by Eq. 7.38. (b),(d): The difference between the cavity linewidth $\Delta\omega_c$ measured by observing the QD emission and the cavity linewidth $\Delta\omega_{c0}$ obtained from the cavity reflectivity measurements, as a function of the laser power. The solid line is a linear fit to the difference. The excitation laser power is measured in front of the objective lens. 149

7.13 Experimental setup and numerical simulations. (a) The schematic shows the relative position of the QD and the cavity on a wavelength axis. For the particular QD-cavity system considered, the QD is red detuned from the cavity, though off-resonant coupling is observed for both red and blue detuned QDs. In experiments, a strong pump laser dresses the QD while a weak probe laser is scanned across the QD. QD emission is incoherently coupled to the cavity. The cavity emission is monitored as a function of probe laser wavelength λ_p. (b) The experimental setup is a confocal cross-polarization setup. The PBS (polarizing beam splitter) is used to perform cross-polarized reflectivity measurements, as in previous work [1]. The powers are measured in front of the objective lens (OL). The output is dispersed in a single-grating monochromator and measured by a nitrogen-cooled CCD. We employ a linear three hole defect PC cavity (a scanning electron micrograph is shown in the inset). (c) Normalized off-resonant cavity emission obtained by numerical simulation is plotted as a function of $\lambda_p - \lambda_{QD}$, λ_{QD} and λ_p being the QD resonance and probe laser wavelengths, respectively, for different pump powers P (normalized units) while the probe power is kept at 1. The pump laser is resonant with the QD. (d) For a pump power of $P = 25$, the cavity emission is plotted as a function of $\lambda_p - \lambda_{QD}$ for different pump-QD detunings $\Delta\lambda_{pump}$ (nm). In both (c) and (d), spectra are vertically offset for clarity. . . 155
7.14 Power dependence of the peaks and dips in the cavity emission spectra and effect of coherent dot-cavity interaction strength g: (a) The separation between the two peaks (as shown in Fig. 7.13 c) as a function of the laser Rabi frequency. The slope of the linear fit is ~ 4. (b) The separation between the two dips (as shown in Fig. 7.13 c) as a function of the laser Rabi frequency. The slope of the linear fit is ~ 2(c) Cavity emission as a function of probe laser wavelength, for different dot-cavity coupling g. 156

7.15 (Characterization of the QD-cavity system in photoluminescence (PL) and probing of the off-resonant dot-cavity coupling. (a) PL spectrum of the system. From the Lorentzian fit to the cavity we estimate a cavity linewidth $\Delta\lambda_{cav} = 0.1$ nm. (b) The laser is scanned across the QD-cavity system. Emission from the cavity is observed when the laser is resonant with the QD. Similarly, emission from the QD is observed when the laser is resonant with the cavity. (c),(d) The QD (cavity) linewidth is measured by monitoring the cavity (QD) emission as a function of the probe wavelength λ_p. 158

7.16 Coherent interaction between the QD and the laser observed through cavity emission. (a) Normalized cavity emission as a function of the probe laser wavelength for different pump powers (measured before the objective lens). We observe that a single QD resonance splits into two peaks. The splitting is linearly proportional to the Rabi frequency of the pump laser. Each peak is fit with a Lorentzian. (b) Rabi frequency Ω of the laser (estimated from the splitting) as a function of the square root of the pump power P. A linear relation exists between Ω and $\sqrt{P}$. (c) Normalized cavity emission for a pump power of 190 nW for two different QD-cavity detunings $\Delta\lambda = 0.22$ and 0.4 nm. (d) Cavity emission for a pump power of 290 nW at two different QD-cavity detunings $\Delta\lambda = 0.26$ and 0.4 nm. We observe that the splitting increases for smaller detuning (i.e., when the pump laser is closer to the cavity), which suggests that the input laser power is enhanced by the presence of the cavity. For all experiments the probe laser power is kept constant at 20 nW. The QD-cavity detuning is defined as $\Delta\lambda = \lambda_{QD} - \lambda_{cav}$. In (a), (c), (d) the spectra are vertically offset for clarity. 163

7.17 Dependence of the result on pump-QD detuning. Off-resonant cavity emission as a function of the probe laser wavelength for different pump-QD detunings $\Delta\lambda_{pump} = \lambda_{pump} - \lambda_{QD}$. We observe that the QD linewidth broadens when the pump is present and detuned from the QD resonance. As the pump is tuned through the QD resonance, we observe the emergence of two peaks in the cavity emission spectrum. This two-peak spectrum is consistent with the observation of the anti-crossing of Rabi sidebands. The pump and probe power are kept at 290 nW and 20 nW, respectively. The spectra are offset for clarity. . 164

7.18 Simple level diagrams of the off-resonantly coupled QD-cavity system for a blue (a) and a red (b) detuned QD. The ground state a and excited state b of the QD are coupled via a laser. The excited state can decay to the ground state with a rate γ, and to the virtual state with a rate γ_t. The cavity couples the virtual state to the ground state, and the cavity decay rate is κ. In our experiment we measure the population in the virtual state, or, $c(t)$. 166

7.19 Time resolved measurement of the off-resonant cavity emission. The QD is resonantly excited with a 40 ps pulse, and the time-resolved measurement of the higher energy off-resonant cavity emission is performed. The inset plots the fall times of the cavity emission (extracted from the exponential fits) against the system's temperature. 167

7.20 (a) Illustration of the phonon assisted inter-dot coupling. QD1 is resonantly driven with a pump laser. The excitation is transferred to QD2 via the cavity. (b) Experimental cross-polarized confocal microscopy setup. PBS: polarizing beam splitter, OL: objective lens. (c) Numerically calculated power spectral density $S(\omega)$ of the cavity output for different QD2-phonon coupling strengths γ_{r2} and QD2-cavity mode coupling g_2. QD1 is resonantly excited (i.e., $\omega_l = \omega_{d1}$) and QD1-cavity coupling is $g_1/2\pi = 20$ GHz, while QD1-phonon coupling rate is $\gamma_{r1}/2\pi = 0.5$ GHz. The cavity field decay rate is $\kappa/2\pi = 20$ GHz. Inset shows a zoom-in of the emission at the QD2 frequency. 171

7.21 (a), (b) Calculated $S(\omega)$ when QD1(a) and QD2(b) are resonantly excited, and the dot-cavity detunings are changed. In other words, $\omega_l = \omega_{d1}$ for (a) and $\omega_l = \omega_{d2}$ for (b). QD1 and QD2 resonances are tuned together, as in the experiment. When QD1 is resonantly driven (a), we observe anti-crossing between QD2 and the cavity in the higher energy off-resonant emission. On the other hand, when QD2 is resonantly driven (b), we observe an increase in QD1 emission when QD2 is resonant with the cavity. For (a) and (b) parameters used for the simulations were: $\gamma_1/2\pi = \gamma_2/2\pi = 1$GHz, $\gamma_{r1}/2\pi = \gamma_{r2}/2\pi = 0.5$ GHz, $g_1/2\pi = g_2/2\pi = 20$ GHz, $\kappa/2\pi = 20$ GHz, detuning between two dots 5κ, driving laser strength $\Omega_0/2\pi = 5$ GHz. Inset of a(b), shows the QD1(2) linewidth measured via monitoring QD2(1) emission. The simulation result is fit with a Lorentzian to estimate the linewidths. . 172

7.22 Measurement of the emission from the off-resonant cavity and QD1, under resonant excitation of QD2. We observe anti-crossing between QD1 and the cavity when the temperature of the system is changed. Natural log of the count from the spectrometer CCD is plotted. Inset zooms into the cavity emission showing the anti-crossing between the QD1 and the cavity. The plots are vertically offset for clarity. 173

7.23 Experimental demonstration of the phonon mediated inter-dot coupling: we observe the emission from a lower energy QD1, when a higher energy quantum dot QD2 is resonantly excited (blue). Similarly, under resonant excitation of a lower energy QD1, emission from a higher energy QD2 is observed (red). Natural log of the count from the spectrometer CCD is plotted. Inset zooms into the QD emission (the actual spectrometer ccd counts are plotted). QD linewidths are estimated by fitting Lorentzians. Measured linewidths of the higher and lower energy QDs, respectively, are ~ 0.03 nm and ~ 0.013 nm. The cavity is at ~ 935 nm, close to the higher energy QD2. 175

7.24 Comparison of the linewidths measured in direct off-resonant dot emission (Fig. 7.23) and from resonant spectroscopy of the QDs: (a),(b) the off-resonant QD emission (same as the inset of Fig. 7.23). QD linewidths are estimated by fitting Lorentzians. Linewidths of the higher and lower energy QDs, respectively, are ~ 0.03 nm and ~ 0.013 nm. The cavity is at ~ 935 nm, close to the higher energy QD. (c),(d) the off-resonant dot emission as a function of the pump laser wavelength λ_p. In this experiment, a laser is scanned across one QD and emission is collected from the other QD as a function of the laser wavelength, same as in Ref. [4]. By fitting Lorentzians, we estimate the linewidths of the higher and lower energy QDs to be ~ 0.024 nm and ~ 0.008 nm, respectively. The y-axis plots the photon counts obtained in the spectrometer CCD. 176

7.25 Effects of temperature on dot to dot coupling and the resulting frequency conversion of the pump. In the experiments, the wavelength of the pump, λ_p, is scanned through one QD and the peak intensity of the other QD is monitored. In (a), the pump is scanned through the higher energy QD and the down-converted light from the lower energy QD is collected and plotted. In (b), we plot the up-converted light emitted from the higher energy QD as the pump is scanned through the lower energy QD. All plots are separately normalized by the maximum QD emission intensity in each plot and are vertically offset for clarity. . . 178

8.1 The cross-polarized confocal microscopy setup used to probe the coupled QD-cavity system. The inset shows a scanning electron micrograph of the fabricated PC cavity. OL and PBS stand for objective lens and polarizing beam splitter, respectively. 183

8.2 (a) Effect of the above-band (AB) laser on the transmission spectrum of a strongly coupled QD-cavity system. The arrow shows the wavelength of the other (resonant) CW laser, whose transmission is modulated by the AB laser in (b) and (c). Inset shows numerically simulated plots of a cavity with and without two strongly coupled QDs. The theoretical results qualitatively match the experimental data well. (b) The transmitted laser power in steady state when the AB laser is turned on and off manually, at intervals of several 10s. This shows the DC characteristics of the modulation. (c) The temporal dynamics of the QD-cavity system: the transmitted laser output as a function of time (black plot). The shown modulation signal (red) is used to modulate the above-band laser. From exponential fits (green) we estimate a time constant of ~ 22 ns, which is obtained as the inverse of the total diffusion rate (equal to the sum of the rates for the rising edge, i.e., carrier capture, and the falling edge, i.e., carrier release). (d) The on-off ratio of the transmitted laser as a function of the modulation frequency. 185

8.3 QD spectroscopy by off-resonant dot-cavity coupling: (a) The spectrum showing the laser resonantly driving the QD and the emission from an off-resonant cavity. A logarithmic scale is used to show both the strong laser and the weak cavity emission. (b) Cavity emission as a function of the power of the laser that is driving the QD resonantly. (c) QD linewidth $\Delta\omega$ measured by monitoring the cavity emission by scanning the laser across the QD. $\Delta\omega$ is plotted as a function of the excitation laser power. We find that the standard power broadening model over-estimates the measured QD linewidth (the dashed line). However, the model provides better agreement with experimental results when spectral diffusion is taken into account (solid line). 189

8.4 Effect of the AB laser on the QD spectrum as measured though off-resonant cavity emission. In the absence of the AB laser, we observe a broad QD linewidth. However, in the presence of this laser, a significant linewidth narrowing is observed. The increased background with the AB laser on is caused by the PL generated by the AB laser. The inset shows the QD linewidth measured as a function of the AB laser power. 190

8.5 (a) Off-resonant cavity emission as a function of the laser power driving the QD resonantly for two cases: with and without the additional, weak above band laser. (b) Extracted QD linewidth as a function of the resonant driving laser power. A much narrower linewidth is observed in the presence of the AB laser at lower excitation powers. Also, the QD linewidth follows a simple power broadening with the excitation laser power when the AB laser is present. In the absence of the AB laser, we observe an additional power independent broadening, which can be explained by spectral diffusion of the QD. 191

9.1 SEM of a coupled cavity array in photonic crystal. This particular structure contains 16 cavities. 194

9.2 (a)SEM of a photonic crystal cavity with metallic grating on the side. (b) SEM of a metallic grating fabricated for generating surface acoustic wave. 195

9.3 Energy-level diagrams of a single electron spin confined in QD under magnetic field (in the Voigt configuration). The two ground states are electron spin up and down. These two constitute the stable basis for the matter qubit. The two excited states are trion states. 196

Chapter 1

Introduction

A single quantum dot (QD) coupled to a photonic crystal micro-cavity constitutes an integrated nano-photonic platform for probing solid state cavity quantum electrodynamic (CQED) effects [6]. Apart from the fundamental interest involving the coupled system, there are two major practical applications that can potentially take advantage of the strong light-matter interaction: long distance quantum communication and optical interconnects.

1.1 Long distance quantum communication

For any long distance communication, the signal from the transmitter to the receiver will be attenuated due to the losses in the channel. To counteract those losses a classical communication system uses repeaters in the intermediate locations to amplify the attenuated signals. Because of the no cloning theorem [7], this approach cannot be used for long distance quantum telecommunications, and thus sending quantum information over a long distance appears to be almost impossible at the first sight.

This predicament is addressed by so called quantum repeaters, and in past decade scientists have come up with numerous schemes for implementing such repeaters [8, 9, 10]. Although quantum repeater proposals are different in many aspects and protocols, the basic principle behind them is sharing entangled photon pairs between two adjacent nodes placed apart at a distances at which attenuation is small and creating an entangled state between these nodes. Initially it was thought that to have entanglement between two particles, one needs to have a shared history between them. This turns out not to be true and one can entangle two qubits without any prior shared history, by exploiting entanglement swapping [11]. This is one of the essential steps for achieving remote entanglement. Another important requirement is entanglement purification [12], where one starts with M entangled pair of qubits with not very high purity, but can create $N < M$ entangled qubits with almost 100% fidelity. Exploiting such entanglement purification and swapping one can achieve entanglement over large distance, and hence a successful quantum communication. Additionally, most of the quantum repeater proposals rely on the availability of quantum memory that would allow storage and retrieval of the quantum state of a photon. This in turn can be achieved by mapping the quantum state of the photon on the quantum state of a quantum emitter; however for this to happen efficiently, strong interaction between the photon and the emitter is needed. Additionally, entanglement purification requires simple quantum computing, which is simpler to perform with matter than photonic qubits. Hence one needs to use a matter qubit, which is much easier to manipulate. In general, the polarization degrees of freedom (horizontal or vertical) are used to specify a photon qubit(used for quantum communication), and spins of quantum emitters are employed as matter qubits.

We note that, not just for quantum communication, but also for quantum computing one needs coherent mapping between the light and matter qubits, which requires very strong light-matter interaction [13]. Such a quantum computing architecture, known as a flying qubit architecture, is similar in many ways to a classical computing architecture, where the information is carried by metallic wires connecting the transistors. The physical bit used for carrying information in classical computing is also an electromagnetic wave, but at a much smaller frequency than the photons used in quantum computing. Similarly, in transistors, the computation is performed via electrons and holes. Of course the mapping between the electromagnetic wave and the electron/ holes states in classical computing is not as delicate as required by the quantum computing. In fact, in classical computing one does not need a coherent mapping between them, as one deals only with the eigen-states. However, quantum computing relies on the superposition of the eigen-states and hence a coherent mapping is essential.

1.2 Optical interconnects

Another motivation to study light-matter interaction is to combine the electronics and photonics in the same device. The modern electronics industry is facing a serious problem as the energy required to transfer signal at high frequencies is increasing. One solution for this is to transmit signal via optical interconnects [14, 15]. Using optical interconnects in parallel with the electronics used for computing is not a new idea, and fiber optic cable is already used for sending signals over long distances.

For using optical interconnects with electronic components, one needs to convert the electrical signal to an optical signal in the transmitter and reconvert the optical signal back to the electrical signal in the receiver. However, all these energy conversion processes are power-hungry [14]. As optical interconnects are used to bridge shorter and shorter distances, the energy efficiency of the electro-optical signal conversion becomes increasingly important. Such efficient conversion requires very strong light-matter interaction. The figures of merit are the speed and energy consumption per bit, and the current estimates are that the optical interconnect devices are needed that operate at the speeds of 10's of GHz and consume less than 1 fJ/bit [14]. The requirement of such conversion with low energy is also important from an environment-friendliness point of view. One might think that the energy required for personal computing is much smaller than the energy required in the common household appliances. However, the increasing amount of data processing required in data centers in companies like Google or Facebook poses a serious problem in terms of energy consumption. Moreover, the energy dissipated in these data-centers is so high that they require cooling by water. The large amount of water required is also a big question in terms of sustainability.

Optical computing is one of the holy grails for the optical physicists [16], but its implementation is currently limited by the size of conventional optical components and availability of significant optical non-linearities accessible with low power signals. For any computing one needs to change an input signal by applying a control signal. This requires a nonlinearity, as the system (or switch) depends on the control power. However, optical nonlinearity appears at very high optical power. Hence, the optical computing is significantly more energy consuming than the current electronic switches made of Si-CMOS technology. Also, the optical components are much larger than the electronic components. Nanophotonics may be able to address the latter issue and provide a compact integrated platform for optical circuits. At the same time, CQED provides a platform for achieving optical non-linearities at very small optical power. In fact, the Jaynes Cummings nonlinearity that can be obtained in CQED is a unique optical nonlinearity, that is present only at very low optical power and disappears at higher power.

1.3 Quantum dots and photonic crystal cavities

Our solid state CQED experiments are based on self-assembled quantum dots coupled to photonic crystal cavities [17]. In general, QDs can be roughly classified into three categories: electrically defined QD [18], self-assembled QD [17] and nanocrystals or colloidal QD [19]. In electrically defined QDs, either an electron or a hole is confined with a set of nanofabricated electrodes, but the system is not suitable for interaction with light. To attain optical addressability one needs to confine both the electron and the hole at the same spatial location. Colloidal QDs are somewhat similar to self-assembled QDs in terms of optical properties. However, colloidal QDs have smaller electric dipole moment and larger homogeneous broadening than self-assembled QD, which makes them less suitable for single emitter CQED experiments (the inhomogeneous linewidth of the the colloidal QD can be controlled by filtering the size). We use self-assembled, epitaxially grown InAs (bandgap 0.36 eV) QDs embedded in the GaAs (1.43 eV) substrate (see Figs. 1.1 a, b). The difference in the bandgap in two materials provides the necessary confinement for electrons and holes. Such a three dimensional confinement gives rise to delta-function-like density of states in the QD, making it an attractive candidate for an artificial atom. For our QDs, however, the carriers are not confined at high temperature. Although the bandgap difference between InAs and GaAs is large (~ 1 eV) due to quantum confinement the energy difference between the QD exciton and GaAs bandgap is much smaller. At around 4K, the energy difference between the QD exciton (wavelength ~ 920 nm) and the GaAs bandgap (wavelength ~ 820 nm) is only 164 meV. Hence with increasing temperature the carriers can get thermally excited from the QD (and in our case, the QD loses confinement at around 60 K). Quantum dots are self-assembled and thus randomly positioned within a slab, as can be seen in Figure 1.1 b. We work with sparse QDs, typically with densities below 100 per $1\mu m^2$. Additionally, QDs suffer from inhomogeneous broadening of around 60 nm in their exciton wavelengths, resulting from the discrepancy in their sizes and shapes (see Fig. 1.2 b).

In our experiments, this QD is embedded in a photonic crystal cavity. We use a two-dimensional slab of photonic crystal, where a defect (cavity) is introduced by removing holes. This defect then forms an optical cavity (resonator) in which light gets confined in-plane by distributed Bragg reflection and out-of-plane by total internal reflection (see Fig. 1.1). In our experiment, the 160nm GaAs membrane used to fabricate the photonic crystal is grown by molecular beam epitaxy on top of a GaAs (100) wafer. The GaAs membrane sits on a 918 nm sacrificial layer of $\mathrm{Al_{0.8}Ga_{0.2}As}$. Under the sacrificial layer, a 10-period distributed Bragg reflector, consisting of a quarter-wave AlAs/GaAs stack, is used to increase the collection into the objective lens. The photonic crystal was fabricated using electron beam lithography, dry plasma etching, and wet etching of the sacrificial layer in hydrofluoric acid (6%). We rely on probabilistic coupling of the QD with the cavity, meaning that we fabricate a regular array of photonic crystal cavities and end up with resonant QDs located inside of some of them. The fraction of cavities containing a single resonant QD is small (at most 10% for a perfect fabrication run), because of the sparse QDs and their inhomogeneous broadening.

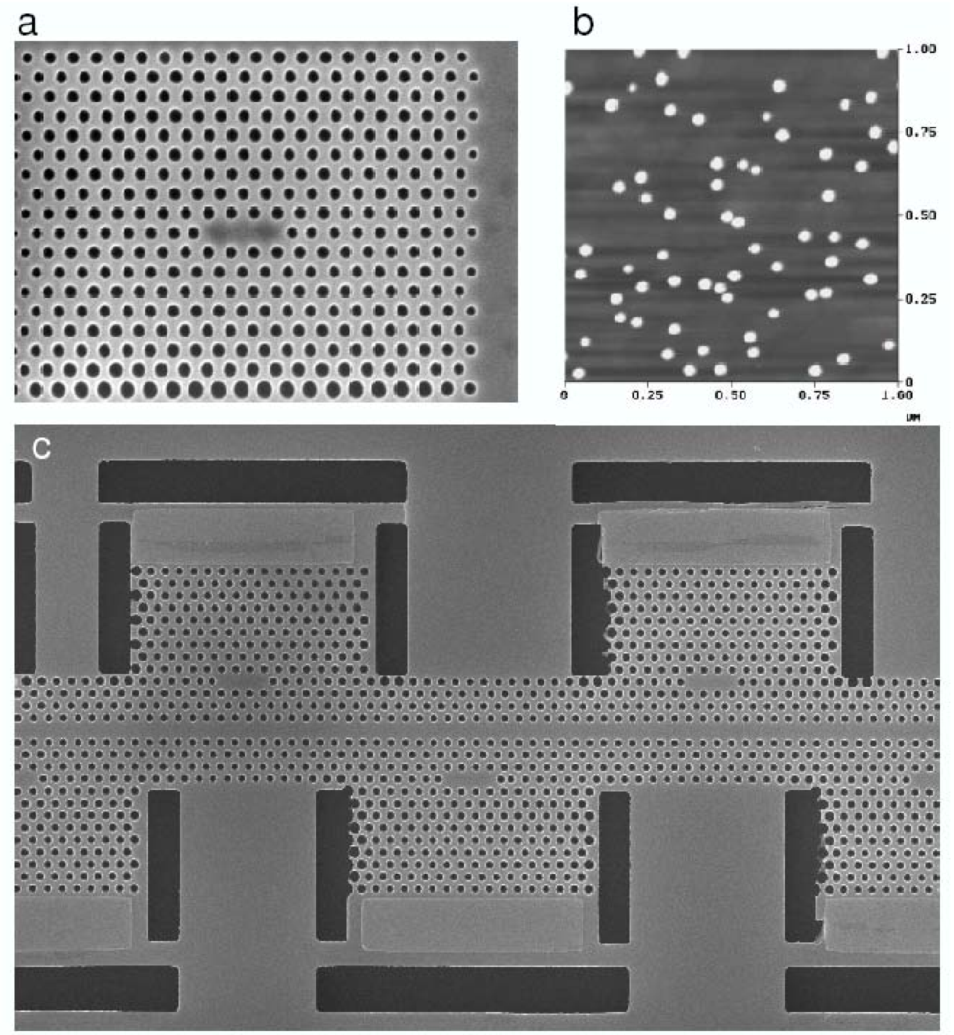

Figure 1.1: (a)Scanning electron microscope image of the fabricated photonic crystal cavity, (b) Atomic Force Microscopy (AFM) image of a $1\mu m^2$ array of self-assembled InAs/GaAs QDs (courtesy of Bingyang Zhang, Stanford University). (c) Scanning electron micro-graph of a hypothetical integrated nano-photonic structure made of photonic crystal cavities and wave-guides.

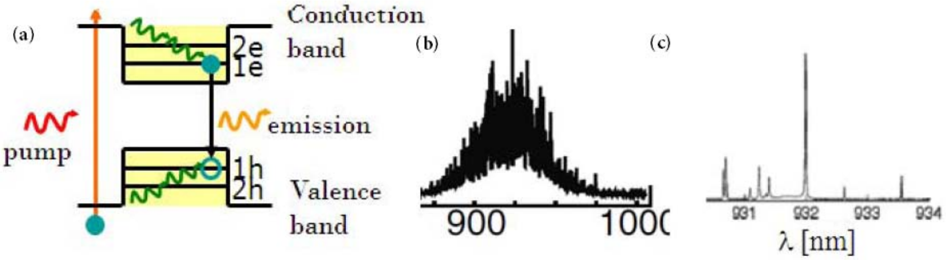

Figure 1.2: (a) The QD energy levels. Difference in bandgap between two materials give rise to the barriers for the electrons and the holes; (b) The inhomogeneous broadening of the quantum dots; (c) Single QD lines: delta function like density of states in quantum dot gives rise to very narrow spectral lines in QD photoluminescence.

1.4 Cavity quantum electrodynamics

Optical cavities can confine light in a small mode volume, which in turn can lead to high electric field intensity inside the cavity. Hence, by embedding matter inside the cavity one can achieve very strong light-matter interactions. When the interaction strength is smaller than the system losses, then the coupling between the emitter and the cavity field is weak, and one can use perturbation theory to explain the system dynamics. However, when the interaction strength is larger than the system losses, the strong coupling regime is reached. In that regime, one cannot apply simple perturbation theory, as the eigen-states of strongly coupled system are entangled states consisting of the QD state and the cavity field. These eigen-states are called the polaritons, hybridized states of matter and light [20].

Initial studies of CQED were mostly based on laser-cooled atoms trapped inside Fabry Perot cavities [21]. An unprecedented amount of control over light-matter interactions has been achieved in experiments based on such systems, and proof of principle demonstrations of novel technologies, such as quantum information processing and long distance quantum telecommunication, have been reported [22, 23, 24]. Atomic CQED in combination with technologies like laser cooling and Bose Einstein condensation remains a promising platform for exploring fundamental physics and precision metrology. However, the macroscopic size of Fabry-Perot cavities and the need for atom cooling and trapping infrastructure make these systems difficult to scale or develop into integrated devices.

Advancement in nanofabrication technologies in last few decades has enabled implementation of CQED systems in an integrated semiconductor platform. In such systems, one uses quantum confined structures such as quantum wells or quantum dots (QD) as the matter, and nanophotonic cavities to confine the light [25, 1]. This semiconductor technology has a huge promise of scalability. Additionally the huge dipole moment of a QD ($\sim 30D$) is much larger than an atom ($\sim 1D$) and a nanophotonic cavity can have a mode-volume below $\sim (\lambda/n)^3$, which is much smaller than the mode volumes achievable with Fabry-Perot cavities (typically of the order of $100-1000\ \lambda^3$ [21]). The cavity mode-volume V_m signifies the volume in which the electromagnetic wave (light) is confined, and is given by

$$V = \frac{\int d^3 r \epsilon(r)|E(r)|^2}{max(\epsilon(r)|E(r)|^2)} \tag{1.1}$$

Here, ϵ is the relative permittivity of the system, and E is the electric field amplitude. The QD-cavity interaction strength is proportional to the QD dipole moment μ, and is given by

$$g = \frac{1}{\hbar}\sqrt{\frac{\hbar\omega}{2V_m}}\mu \tag{1.2}$$

(when the QD is placed at the position of the maximum $\epsilon|E|^2$). For our system parameters, the value of $g/2\pi$ is $\sim$ 40 GHz, but experimentally we observe $g/2\pi \sim 10-25$ GHz (resulting from the spatial misalignment between the QD and the cavity field). Consequently, scalable devices based on this platform can potentially operate at speeds exceeding $\sim$ 10 GHz, which exceeds the speeds possible in conventional atomic CQED by two to three orders of magnitude.

The downside of the semiconductor platform is that at the current state-of-the-art technology, there is not much control over the growth of QD. As described in the previous section, the QDs are grown via a self-assembly process, which results in non-deterministic spatial locations of the QDs [17]. Similarly, the size of the QDs cannot be fully controlled, which results in variation in the QD resonances and leads to a rather large inhomogeneous broadening of the QD (the linewidth of the QD ensemble is $\sim 40nm$). This randomness presents challenges to the scalability of the

QD-CQED platform, as it makes it difficult to position the QDs deterministically at the preferred locations, and to spectrally align the QDs to cavity resonance. Although the large inhomogeneous broadening of the QD presents a significant challenge to the scalability of the solid state platform, there are several interesting avenues to overcome that problem, such as, phonon-mediated coupling to circumvent the detuning between QD and cavity [2]; or using nonlinear optics in a very small mode volume cavity to achieve the nonlinear interaction [26]. Apart from this, the QD interacts with its semiconductor environment, and hence the effects of phonons and other sources of dephasing become important in QD-CQED. However, these effects also give rise to new physics previously unexplored in atomic CQED systems [4, 2]. Finally, another technical problem currently faced in QD-CQED is the necessity of cryogenic temperature operation needed for the confinement of charge carriers in the QD.

Initial experiments in solid state CQED focused on using quantum wells in DBR cavities [27]. Although strong coupling can be observed in such a system, its behavior does not exhibit non-linearity in the presence of smaller number of photons (explained in more details in chapter 3). To obtain nonlinearity at single or few photon level one needs to use single quantum emitters, such as a QD, an NV center in diamond [28], an atom [21], an ion, other impurities in a semiconductor [29], a single molecule [30] etc. However, reaching the strong coupling regime with such single quantum emitters is much harder than with a quantum well, as a result of a smaller overall dipole moment. To enhance the coupling strength between the emitter and the optical field, one needs to fabricate cavities with very small mode volume. With semiconductor nano-cavities [31] one can realize the strong coupling between a single QD and an optical cavity [25, 1, 32, 33], which opens up a new avenue for doing optical CQED. We note that the coupling of the single quantum emitter to an optical cavity can be well described by the Jaynes-Cummings Hamiltonian (see chapter 2).

The figure of merit for the cavities used in CQED is given by Q/V, where $Q = \omega_o/\Delta\omega$ is the quality factor of cavity ($\Delta\omega$ is the cavity line-width and ω_o is the resonance frequency), and V is the mode volume of the cavity. We note that in this thesis, κ is used to denote the cavity field decay rate, where $\Delta\omega = 2\kappa$.

Photonic crystal (PC) cavities provide a platform with the highest achievable Q/V ratio among all the nanophotonic cavities. In particular, PC cavities benefit from very small mode volume $V \sim (\lambda/n)^3$ (where λ is the free space resonance wavelength of the cavity and n is the refractive index of the material in the cavity). We also note that, although the figure of merit for a cavity is Q/V or Q^2/V for some applications, increasing Q decreases the speed of operation, which is crucial for information processing. Hence, reducing V to improve the cavity performance is definitely a better strategy than increasing Q, at least for the information processing applications. Apart from this, a photonic crystal confines light in-plane, which allows the implementation of planar, on-chip integrated photonic circuits.

1.5 Outline of the thesis

Chapter 2 provides an overview of the theoretical tools used in this PhD work to describe the coupled CQED system. We use these techniques to solve the problems of all-optical switching and electro-optical modulation in a strongly coupled dot-cavity system. Then in chapter 3 we describe experiments showing the non-linear nature of the system. Such nonlinearity can be used to perform all-optical switching with the coupled system. The results presented in the chapter 3 are mostly based on the References [34, 35]. In chapter 4 we describe our experiments in which the QD-cavity system is used an electro-optic modulator. We show that we can achieve electro-optic modulation with light-matter interaction at the most fundamental limit. These results are published in the References [36, 37]. Chapter 5 presents studies of the quantum nature of the system by measuring photon correlations in the light transmitted through the cavity, where we show that in the strong coupling regime, the system can produce non-classical photon states. These results are based on the references [38, 39, 3]. Chapter 6 extends our CQED work from a single QD coupled to a single cavity to CQED with a QD coupled to coupled cavities, also called a photonic molecule. Such a system can be considered to be the first step towards building a coupled cavity network with embedded single quantum emitters. These results are reported in the reference [40]. Chapter 7 explores a new phenomenon observed in the QD-CQED system, known as phonon-mediated off-resonant dot-cavity coupling. We use this coupling to perform resonant QD spectroscopy. The results on such phonon-mediated coupling are reported in the references [2, 4, 41, 42]. From such spectroscopic measurements we find a signature of large spectral diffusion in the coupled dot-cavity system, most likely coming from the proximity of the QD to the etched surfaces (chapter 8). This result is also published in [43]. Chapter 9 describes the future research directions and the prospects for this solid state CQED platform.

Chapter 2

Theoretical study of the quantum dot-cavity QED system

In this chapter, we present the theoretical framework for analyzing the dynamics of the coupled QD-cavity system. The theory employed to analyze this CQED system can be applied to any other CQED system, namely, atomic systems in the optical or microwave domain, [44] or superconducting circuit QED [45]. However, the superconducting CQED might reach a new regime known as ultra-strong coupling, where the vacuum Rabi frequency is of the same order of magnitude as the photon frequency - the regime in which the following theoretical formalism breaks down. Therefore, as long as photon frequency is much larger than all the rates in the system, we can use the theoretical approach presented in this chapter. More detailed description of the presented theory can be found elsewhere [46, 47, 48]. Using this theoretical approach, we also analyze the basic physics of our cavity QED system, which is experimentally studied in subsequent chapters.

2.1 Hamiltonian dynamics

The lossless dynamics of the quantum system is governed by the Hamiltonian dynamics. In the rotating wave approximation, the quantum-mechanical Hamiltonian

$\mathcal{H}$ describing the coherent dynamics of the coupled QD-cavity system is given by [46]:

$$\mathcal{H} = \omega_a \sigma^\dagger \sigma + \omega_c a^\dagger a + ig(a\sigma^\dagger - a^\dagger \sigma) \tag{2.1}$$

Here, ω_c and ω_a are, respectively, the resonance frequencies of the cavity and the QD; a is the annihilation operator for the cavity mode; $\sigma = |g\rangle\langle e|$ is the lowering operator for the QD with excited state $|e\rangle$ and ground state $|g\rangle$; g is the coherent interaction strength between the QD and the cavity and $\hbar$ is set to 1. In general the interaction term is given by $(a + a^\dagger)(\sigma + \sigma^\dagger)$. However, rotating wave approximation (RWA) gets rid of the non energy-conserving terms (also known as anti-Jaynes-Cummings terms) $a^\dagger\sigma^\dagger$ and $a\sigma$. It should be noted that, such RWA is not valid when the photon energies are comparable to the rate parameters, as is true in the ultra-strong coupling regime. When this system is coherently driven by a laser pulse with an electric field amplitude envelope $\mathcal{E}(t) = \mathcal{E}_o p(t)$ and a center frequency ω_l, the driven Hamiltonian is

$$\mathcal{H}_d = \omega_a \sigma^\dagger \sigma + \omega_c a^\dagger a + ig(a\sigma^\dagger - a^\dagger \sigma) + i\sqrt{\kappa}\mathcal{E}(t)(ae^{-i\omega_l t} - a^\dagger e^{+i\omega_l t}) \tag{2.2}$$

This Hamiltonian, in a frame rotating at the frequency ω_l is given by (the formal procedure is shown below)

$$\mathcal{H}_{rot} = \Delta\omega_c a^\dagger a + \Delta\omega_a \sigma^\dagger \sigma + ig(a^\dagger \sigma - a\sigma^\dagger) + i\sqrt{\kappa}\mathcal{E}(t)(a - a^\dagger) \tag{2.3}$$

Here, $\Delta\omega_c$ and $\Delta\omega_a$ are the detuning of the cavity and the QD resonance from the laser frequency; $\mathcal{E}_0$ is the maximum laser strength and $p(t)$ is proportional to the envelope of the laser electric field.

When we switch to a frame rotating with a frequency ω_o, the new Hamiltonian $\mathcal{H}_{rot}$ becomes:

$$\mathcal{H}_{rot} = T^\dagger \mathcal{H} T + i\frac{\partial T^\dagger}{\partial t} T \tag{2.4}$$

where T is given by

$$T = e^{-i\omega_o t a^\dagger a} e^{-i\omega_o t \sigma^\dagger \sigma} \tag{2.5}$$

The new hamiltonian H_{rot} becomes:

$$T^\dagger(\omega_c a^\dagger a)T \quad = \quad \omega_c a^\dagger a \tag{2.6}$$

$$\begin{aligned} T^\dagger(\omega_a\sigma^\dagger\sigma)T &= \omega_a\sigma^\dagger\sigma && (2.7)\\ i\frac{\partial T^\dagger}{\partial t}T &= -\omega_o(a^\dagger a+\sigma^\dagger\sigma) && (2.8)\\ T^\dagger(a)T &= e^{-i\omega_o t}a && (2.9)\\ T^\dagger(a^\dagger)T &= e^{i\omega_o t}a^\dagger && (2.10)\\ T^\dagger(\sigma)T &= e^{-i\omega_o t}\sigma && (2.11)\\ T^\dagger(\sigma^\dagger)T &= e^{i\omega_o t}\sigma^\dagger && (2.12)\end{aligned}$$

$$\begin{aligned} \mathcal{H}_{rot} &= \hbar(\omega_c-\omega_o)a^\dagger a+\hbar(\omega_a-\omega_o)\sigma^\dagger\sigma && (2.13)\\ &+ \hbar g(a^\dagger\sigma+a\sigma^\dagger)+i\hbar\sqrt{\kappa}\mathcal{E}(t)(ae^{i(\omega_l-\omega_o)t}-a^\dagger e^{-i(\omega_l-\omega_o)t}) \end{aligned}$$

Using $\omega_l=\omega_o$, the Hamiltonian in rotating frame becomes ($\hbar=1$)

$$\mathcal{H}_{rot}=\Delta\omega_c a^\dagger a+\Delta\omega_a\sigma^\dagger\sigma+ig(a^\dagger\sigma-a\sigma^\dagger)+i\sqrt{\kappa}\mathcal{E}(t)(a-a^\dagger). \tag{2.14}$$

2.2 Master equation for lossy dynamics

All CQED systems are dissipative. These systems are inherently non-equilibrium systems where a steady-state is reached by a balance between the drive and dissipation. However, the Hamiltonian dynamics explained before ignores any effect of loss. One way to incorporate the effect of loss is to use the quantum optical master equation. For the specific system of coupled QD-cavity, there are two major sources of loss: dissipation of the cavity field to the environment with a decay rate $\kappa=\omega_c/2Q$ (Q is the quality factor of the resonator) and a dipole spontaneous emission rate γ. The dynamics of the QD-cavity system, in presence of losses, are determined by the master equation [47]:

$$\frac{d\rho}{dt}=-i[H,\rho]+2\kappa\mathcal{L}[a]+2\gamma\mathcal{L}[\sigma] \tag{2.15}$$

where ρ is the density matrix of the coupled QD-cavity system. $\mathcal{L}[D]$ is the Lindblad operator corresponding to a collapse operator D to model the incoherent decays and is given by:

$$\mathcal{L}[D]=D\rho D^\dagger-\frac{1}{2}D^\dagger D\rho-\frac{1}{2}\rho D^\dagger D \tag{2.16}$$

In this thesis, the Master equation is solved using numerical integration routines provided in quantum optics toolbox, truncating the photon states to ≈ 20 photons [49]. This method is completely quantum mechanical, and no approximation (other than the standard Born-Markov approximation and truncation of Fock state basis) is made.

2.2.1 Quantum and semiclassical description

Although, the master equation provides a complete description of the coupled system, it is computationally expensive, and in general, analytically intractable. A semi-classical description of the coupled system [36] can be derived by using the relation

$$\frac{d\langle D\rangle}{dt} = Tr\left[D\frac{d\rho}{dt}\right] \tag{2.17}$$

valid for any operator D. These mean field dynamical equations for the coupled QD-cavity system can then be written as

$$\begin{aligned}
\frac{\mathrm{d}\langle a\rangle}{\mathrm{d}t} &= -\kappa\langle a\rangle + g\langle\sigma\rangle - \sqrt{\kappa}\mathcal{E}(t) && (2.18)\\
\frac{\mathrm{d}\langle\sigma\rangle}{\mathrm{d}t} &= -\gamma\langle\sigma\rangle + g\langle a\sigma_z\rangle && (2.19)\\
\frac{\mathrm{d}\langle\sigma_z\rangle}{\mathrm{d}t} &= -2\gamma(\langle\sigma_z\rangle + 1) - 2g(\langle a^\dagger\sigma\rangle + \langle a\sigma^\dagger\rangle) && (2.20)
\end{aligned}$$

where, $\sigma_z = |e\rangle\langle e| - |g\rangle\langle g|$. We note that this set of equations is not complete; for an exact solution we need to find the equations describing all the other higher order moments, namely $\langle a\sigma_z\rangle$ and $\langle a\sigma^\dagger\rangle$. However, in the low excitation regime (no more than 1 photon in the system), the QD will remain mostly in its ground state and we can approximate $\langle\sigma_z\rangle \approx -1$ and replace $\langle a\sigma_z\rangle = -\langle a\rangle$. The resulting set of equations

$$\begin{aligned}
\frac{\mathrm{d}\langle a\rangle}{\mathrm{d}t} &= -\kappa\langle a\rangle + g\langle\sigma\rangle - \sqrt{\kappa}\mathcal{E} && (2.21)\\
\frac{\mathrm{d}\langle\sigma\rangle}{\mathrm{d}t} &= -\gamma\langle\sigma\rangle - g\langle a\rangle && (2.22)
\end{aligned}$$

is identical to the set of equations describing the dynamics of two coupled linear classical oscillators. Although this approximation neglects the nonlinear nature of the

QD, it matches the actual output quantitatively at low excitation power. However, with increasing drive intensities $\mathcal{E}_0$, this model fails completely, as the approximation $\langle \sigma_z \rangle \approx -1$ becomes invalid. For sufficiently high drive intensities, though one can approximate, $\langle \sigma_z \rangle \to 0$, and equation (2.19) simplifies to

$$\frac{\mathrm{d}\langle \sigma \rangle}{\mathrm{d}t} = -\gamma \langle \sigma \rangle \tag{2.23}$$

Alternatively, we can retain the dynamics of the σ_z term, while making the set of equations (2.18), (2.19), and (2.20) complete by using the approximations $\langle a\sigma_z \rangle \approx \langle a \rangle \langle \sigma_z \rangle$ and $\langle a^\dagger \sigma \rangle \approx \langle a^\dagger \rangle \langle \sigma \rangle$ [50]. While this approach neglects the coherence of the system while analyzing the mean-field dynamical equations, the nonlinear behavior of the QD is taken into account.

2.3 Quantum trajectory

Another way to incorporate the lossy dynamics is to use quantum trajectory method. In quantum trajectory method, one can calculate information about both the density matrix and the wave-function. The methods are known as stochastic master equation (when one calculates information about the density matrix) and stochastic wave-equation method (for just the wave-function). For a density matrix type of calculation one still needs to compute $O(N^2)$ elements where N is the size of the Hilbert space. On the other hand, when one calculates the wave function, one needs to compute only $O(N)$ elements. Hence we obtain significant reduction in total computations.

For the Monte Carlo simulation using quantum trajectory method [47] the Schrӧdinger equation is:

$$i\frac{d\psi}{dt} = H_{eff}(t)\psi \tag{2.24}$$

where H_{eff} is given by:

$$H_{eff}(t) = H(t) - \frac{i}{2}\sum_k D_k^\dagger D_k \tag{2.25}$$

where, $H(t)$ is the system Hamiltonian without loss and D_k is the collapse operator corresponding to the k^{th} dissipation channel. In the experiment considered here, there are mainly two decay channels: the spontaneous emission of the QD $D_1 = \sqrt{\gamma}|g\rangle\langle e|$ and the cavity decay $D_2 = \sqrt{\kappa}a$. For running the Monte Carlo simulations, the total time-interval of interest is divided into small steps, such that in each step we can have either one detection event or no detection. At each step, with certain probability we collapse the wave-function as $\psi(t_{n+1}) = D_k\psi(t_n)$ and then propagate the wave-function with the effective Hamiltonian. Several trajectories are run and ensemble average is taken to get the result.

2.4 Strong coupling

From the master equation as well as from the semi-classical description one can derive that the eigen-values of the coupled system consisting of a single QD (atom) and a single photon are given by

$$\omega_{\pm} = \frac{\omega_c + \omega_a}{2} - i\frac{\kappa + \gamma}{2} \pm \sqrt{g^2 + \frac{1}{4}\left(\delta - i(\kappa - \gamma)\right)^2} \tag{2.26}$$

where $\delta = \Delta\omega_c - \Delta\omega_a$ is the dot-cavity detuning. In the dot-cavity system the QD dipole decay rate γ is very small. Hence, when $g > \kappa/2$, the expression under the square root is positive. In this case, the system is in strong coupling regime: there are two distinct solutions for real part of $\omega_{\pm}$, which are exhibited as the split resonance appearing in the cavity transmission spectrum (Fig. 2.1 a). On the other hand, without a coupled QD, a single Lorentzian peak is observed in the spectrum of the cavity transmission (Fig. 2.1 a). The two peaks correspond to the entangled states of the QD and the cavity, known as polaritons. They are also called dressed states, and the splitting between these two polaritons is twice the QD-cavity coupling strength g, also known as the vacuum Rabi frequency.

The solutions given by equation 2.26 are the two lowest order eigenstates of the strongly coupled QD-cavity system. In this strong coupling regime, energy eigenstates are grouped into two-level manifolds with eigen-energies given by $n\omega_c \pm g\sqrt{n}$ (for $\omega_a = \omega_c$), where n is the number of energy quanta in the cavity-QD system (shown

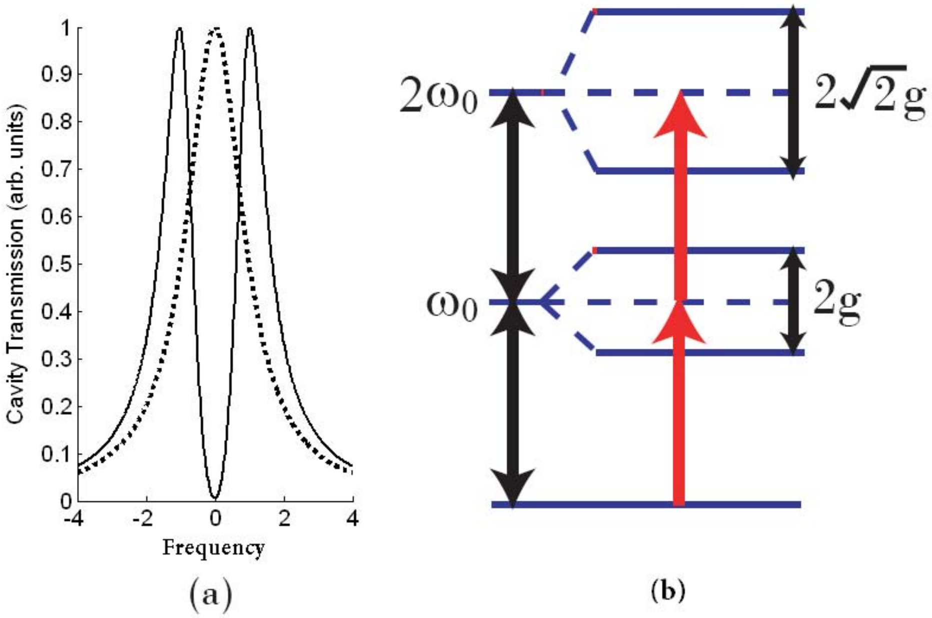

Figure 2.1: (a) The transmission spectrum of a strongly coupled QD-cavity system (split resonance) and and empty cavity (single Lorentzian line); (b) The anharmonic dressed state ladder structure.

in Fig. 2.1 b). The eigenstates can be written as:

$$|n, \pm\rangle = \frac{|g, n\rangle \pm |e, n-1\rangle}{\sqrt{2}} \tag{2.27}$$

As the splitting between the energy eigenstates in each manifold has a non-linear dependence on n, the eigen-structure of the coupled system is anharmonic (as opposed to an empty cavity which is described by a harmonic oscillator, as shown in the left part of the Fig. 2.1 b). This anharmonicity is crucial for understanding the effect like photon blockade and tunneling (see chapter 5) as well as for implementing devices like all-optical switch (see chapter 3) or elecro-optic modulator (see chapter 4).

2.5 Temporal dynamics of dot-cavity system

While the signature of the strong coupling regime in frequency domain is the splitting of the cavity resonance into two peaks (see Fig. 2.1 a), in time domain this corresponds to Rabi oscillation between the original eigenstates of the uncoupled system (e.g., $|e,0\rangle$ and $|g,1\rangle$ for the first ladder manifold). In this section, we theoretically analyze the temporal dynamics of strongly coupled quantum dot-cavity system driven by a resonant laser pulse and observe the signature of Rabi oscillation in the time resolved response of the system (i.e., in the numerically calculated cavity output). The experimental data on such dynamics is reported in chapter 3. First, we study the temporal dynamics of the coupled dot-cavity system driven by a short laser pulse (Fig. 2.2 a) using a full quantum optical numerical simulation. The oscillatory behavior of the cavity output (Fig. 2.2 b), which is caused by the vacuum Rabi splitting, is analyzed at low, intermediate, and high intensity of the driving laser. Specifically, we show that under weak driving, the coupled QD-cavity system follows the same dynamics as a set of two classical linear coupled oscillators. Following this, we describe an improved, non-linear semi-classical model, that mimics the quantum optical model very well for both very low and high peak intensity of the driving pulse. However, the non-linear semi-classical model deviates from the quantum optical description at intermediate peak intensities of the drive pulse, and we show that this discrepancy arises from the coherence present in the quantum optical system. Finally, we present a study of the temporal dynamics as a function of the major parameters describing the cavity-QD system.

2.5.1 Semiclassical equation of motion

A quantum optical and semi-classical description of the system can be derived by the method outlined above. When driven very weakly ($\sigma_z = -1$ as explained above), the dynamics of the coupled QD-cavity system is identical to the set of equations describing the dynamics of two coupled linear classical oscillators. The dynamics of two classical coupled oscillators, with resonance frequency ω_0 and decay rates Γ_1 and Γ_2, are governed by

$$\frac{d^2x_1}{dt^2} + \Gamma_1\frac{dx_1}{dt} + \omega_0^2 x_1 + G(x_1 - x_2) = \Omega(t)e^{i\omega_0 t} \tag{2.28}$$

and

$$\frac{d^2x_2}{dt^2} + \Gamma_2\frac{dx_2}{dt} + \omega_0^2 x_2 + G(x_2 - x_1) = 0, \tag{2.29}$$

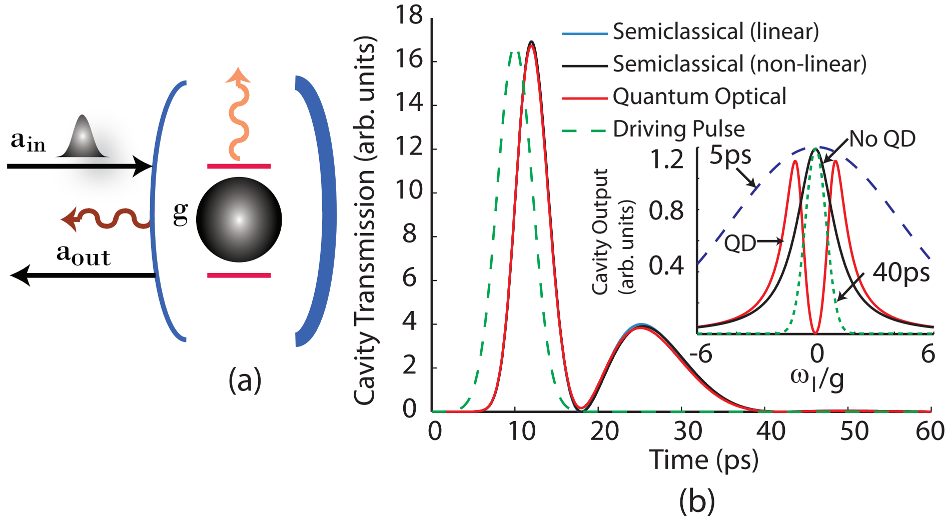

Figure 2.2: (a) The schematic of the coupled QD-cavity system. It is driven by a laser pulse, and the cavity output is monitored. (b) The cavity transmission calculated by three different models: the quantum optical (red), semi-classical linear (blue) and non-linear (black) model at low ($\Omega_0/2\pi = 1$ GHz) peak intensity of the driving pulse. All three models match quite well. The input pulse is also shown (green dashed line). The oscillation in the cavity output is due to Rabi oscillation of the photon between the QD and the cavity. Inset shows the cavity transmission spectrum in presence and in absence of the strongly coupled QD. The split resonances are separated approximately by twice the coherent dot-cavity interaction strength g. The spectral shape of laser pulses with pulse-length 5 ps (blue dashed line) and 40 ps (green dashed line) is also shown. Parameters used for the simulations are $g/2\pi = 25$ GHz, $\kappa/2\pi = 29$ GHz and $\gamma/2\pi = 1$ GHz.

where G denotes the coupling strength between the oscillators. One of the oscillators is driven resonantly with driving strength $\Omega(t)$, as the cavity is driven by a laser. We assume a solution of the form $x_1(t) = X_1(t)e^{i\omega_0 t}$ and $x_2(t) = X_2(t)e^{i\omega_0 t}$, where $X_1(t)$ and $X_2(t)$ are slowly varying envelopes of the actual oscillator outputs. Then we can write

$$\begin{aligned} \frac{dx_1}{dt} &= i\omega_0 X_1 e^{i\omega_0 t} + \left(\frac{dX_1}{dt}e^{i\omega_0 t}\right) \\ \frac{d^2x_1}{dt^2} &= 2i\omega_0 \frac{dX_1}{dt}e^{i\omega_0 t} - \omega_0^2 X_1 e^{i\omega_0 t} + \left(\frac{d^2X_1}{dt^2}e^{i\omega_0 t}\right) \end{aligned}$$

For x_2 we can find similar equations. Using the slowly varying envelope approximation ($\frac{dX_1}{dt} << i\omega_0 X_1$ and $\frac{d^2X_1}{dt^2} << i\omega_0\frac{dX_1}{dt}, \omega_0^2 X_1$), we remove the bracketed terms and obtain the following equations for the un-driven coupled oscillator system:

$$\frac{dX_1}{dt} = -\left(\frac{\Gamma_1}{2} + \frac{G}{2i\omega_0}\right)X_1 + \frac{G}{2i\omega_0}X_2 + \Omega(t) \tag{2.30}$$

and

$$\frac{dX_2}{dt} = -\left(\frac{\Gamma_2}{2} + \frac{G}{2i\omega_0}\right)X_2 + \frac{G}{2i\omega_0}X_1 \tag{2.31}$$

Alternatively, by retaining the dynamics of the σ_z term we can derive nonlinear semi-classical equations (as explained above). Fig. 2.2b compares the time-resolved cavity transmission in the low-excitation limit ($\Omega_0/2\pi = 1$) when calculated by the three different models: (i) semi-classical in the linear approximation, (ii) semi-classical in the non-linear approximation; (iii) and the numerical Master equation solution up to truncated fock state basis $n = 15$. For the numerical simulation, we used a Gaussian pulse with full-width half-maximum (FWHM) of 5 ps to drive the dot-cavity system with a pulse with bandwidth higher than the coupled system (as shown in the inset of Fig. 2.2b). In this low-excitation limit, all three models closely agree, and exhibit an oscillation in the cavity transmission. This oscillation is due to the coherent Rabi oscillation of the photons between the QD and the cavity and vanishes when $g \rightarrow 0$. Note that further oscillations are quenched by the decay of the cavity field. To intuitively understand the origin of the oscillation, one can consider the eigenvalues of the lossy coupled system (see chapter 2). When the cavity is driven with a short pulse with bandwidth larger than that of the coupled system, the cavity output is modulated at the frequency difference between the polaritons. i.e., $2\sqrt{g^2 + \frac{1}{4}\left(\delta - i(\kappa - \gamma)\right)^2}$.

Although the non-linear semi-classical model allows QD saturation, it neglects the quantum mechanical coherence between the QD and the cavity. Fig. 2.3 compares the semiclassical and quantum optical simulations of the coupled dot-cavity system. We find that the results match well both at low (when the QD excited state population is almost zero and $\langle \sigma_z \rangle \sim -1$) and high intensities of the driving field (when the QD is saturated and $\langle \sigma_z \rangle \sim 0$). As expected, the nonlinear semi-classical approach deviates for intermediate intensities. As a measure of the coherence, we plot the quantity $C = (\langle a^\dagger \sigma \rangle - \langle a^\dagger \rangle \langle \sigma \rangle)/\Omega_0^2$ integrated over time as a function of the driving strength Ω_0 in the inset of Fig. 2.3. C is zero in absence of any coherence, and is much smaller for low and high excitation powers than in the intermediate excitation regime. Note that the onset of the increase in the higher excitation power is due to numerical errors caused by the truncated Fock state basis.

2.5.2 Dependence on the system parameters

We are now in a position to characterize the temporal cavity transmission as a function of four relevant parameters describing the coupled dot-cavity system: dot-cavity detuning δ, the dot-cavity coupling rate g, the cavity field decay rate κ and pure QD dephasing rate γ_d. Fig. 2.4a shows that the time interval between two peaks decreases as the QD-cavity coupling rate, g, increases. This observation is consistent with the oscillation period as predicted by the simple linear analysis. At the same time, the oscillation period depends only weakly on κ (Fig. 2.4b). We note an increasing cavity output with increasing cavity decay rate κ, which is due to the increasing overlap between the input pulse and the cavity spectrum. The oscillation frequency increases with increasing detuning between the dot and the cavity; when the QD is detuned too far from the cavity, the oscillation almost disappears. This is expected, as with large enough detuning, the input pulse is not affected by the QD (Fig. 2.4c).

An important effect in solid-state cavity QED is pure QD dephasing, which destroys the coherence of the system, without affecting the population of the quantum

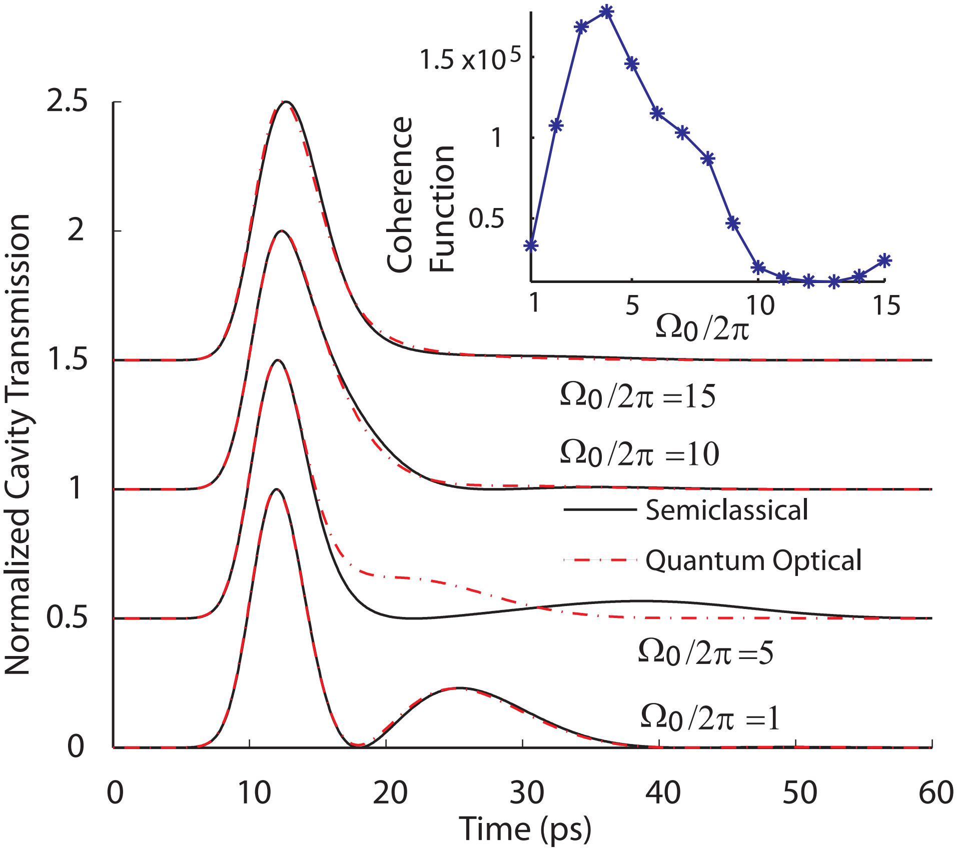

Figure 2.3: (a) Comparison between the temporal cavity transmission obtained via quantum optical (red dashed line) and the semi-classical non-linear (black solid line) models. The cavity transmission is normalized by the maximum cavity transmission and plots are vertically offset for clarity. The two models match quite well at low and high driving power, but at intermediate power, they differ. Inset shows the coherence calculated as $(\langle a^\dagger\sigma\rangle - \langle a^\dagger\rangle\langle\sigma\rangle)/\Omega_0^2$ integrated over time as a function of the driving strength Ω_0. We observe that quantity increases in the intermediate driving power. Parameters used for the simulations: $g/2\pi = 25$ GHz and $\kappa/2\pi = 29$ GHz.

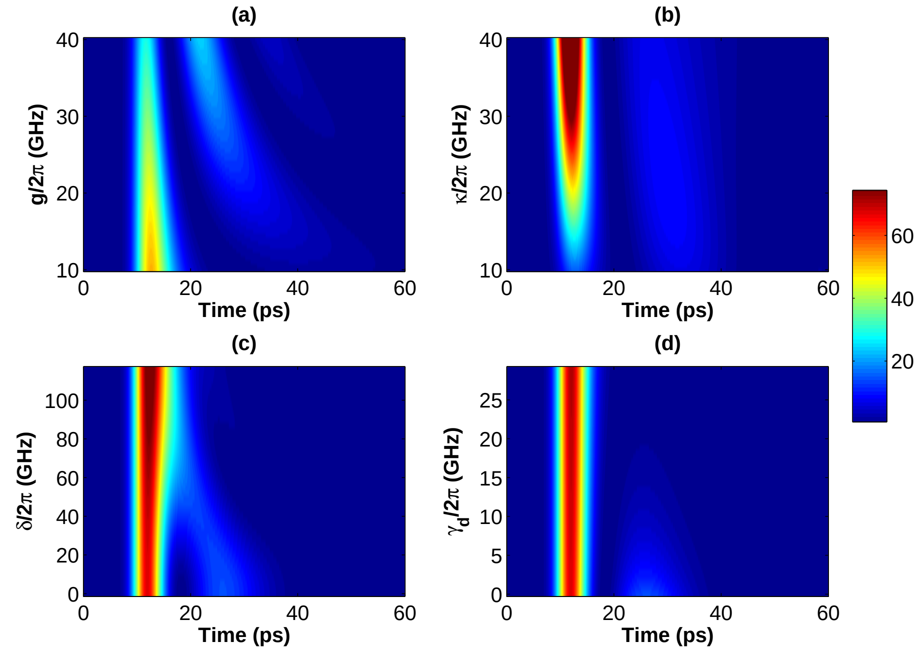

Figure 2.4: The temporal cavity output obtained from the full quantum optical simulation as a function of (a) the dot-cavity coupling strength g (here $\kappa/2\pi = 20$ GHz; $\delta = 0$ and $\gamma_d = 0$), (b) the cavity field decay rate κ (here $g/2\pi = 20$ GHz; $\delta = 0$ and $\gamma_d = 0$), (c) the dot cavity detuning δ (here $g/2\pi = \kappa/2\pi = 20$ GHz and $\gamma_d = 0$) and (d) the pure QD dephasing rate γ_d (here $g/2\pi = \kappa/2\pi = 20$ GHz and $\delta = 0$). For all the simulations a low excitation power ($\Omega_0/2\pi = 2$) is assumed.

dot states. The effect of pure QD dephasing can be incorporated by adding the term $2\gamma_d\mathcal{L}(\sigma^\dagger\sigma)$ in the Master equation [2, 41], where γ_d is the pure QD dephasing rate. Fig. 2.4d plots the cavity output as a function of the pure QD dephasing rate γ_d, indicating that the oscillation eventually disappears when the dephasing rate is large.

2.6 All-optical switching with quantum dot-cavity QED system

In the previous section, we analyzed the transmission of a single pulse through the cavity and observed significant optical nonlinearity. Here we theoretically analyze the performance of an all-optical switch, which exploits such optical nonlinearity. We present numerical simulation results showing both the detailed temporal behavior of such a switch and the time-integrated light transmission through the cavity.

2.6.1 Static response

The switching characteristic of the all-optical switch is first calculated using a continuous wave (CW) driving laser. The cavity output $\propto \langle a^\dagger a\rangle$ (normalized by an empty cavity transmission) is calculated as a function of the laser power. Figure 2.5 shows the non-linear transmission characteristic of the coupled QD-cavity system. This can be thought of as the DC behavior of the switch. Figure 2.5a shows the cavity transmission as a function of the laser frequency, for a resonant dot-cavity system (i.e., detunings of the laser from both the QD and the cavity mode are equal: $\Delta\omega_c = \Delta\omega_d = \Delta$). We find that the dip between the polaritons (induced by the strongly coupled QD) is reduced when the incident laser power increases. This is caused by saturation of the QD.

An important aspect of the solid-state quantum emitter is pure QD dephasing, caused by the constant interaction of the quantum emitter with the phonons in the surrounding crystal lattice [41]. This pure QD dephasing destroys the coherence of the system without affecting the population. This can be modeled by adding another Lindblad term in the Master equation, $2\gamma_d\mathcal{L}(\sigma^\dagger\sigma)$. The pure QD dephasing reduces the dip in the transmission spectrum of the coupled QD-cavity system. Fig. 2.5b plots the transmission of a resonant laser through the QD-cavity system with and without pure dephasing as a function of the incident laser power. For both cases, the transmission of the system increases with increasing laser power due to saturation of the QD. However, we observe increased transmission of the laser at low power when pure dephasing is included.

Finally, we analyze the performance of the system as a function of the QD-cavity interaction strength g and cavity decay rate κ. In absence of any control, only signal (with a driving strength $\mathcal{E}$) interacts with the coupled system. However, in presence

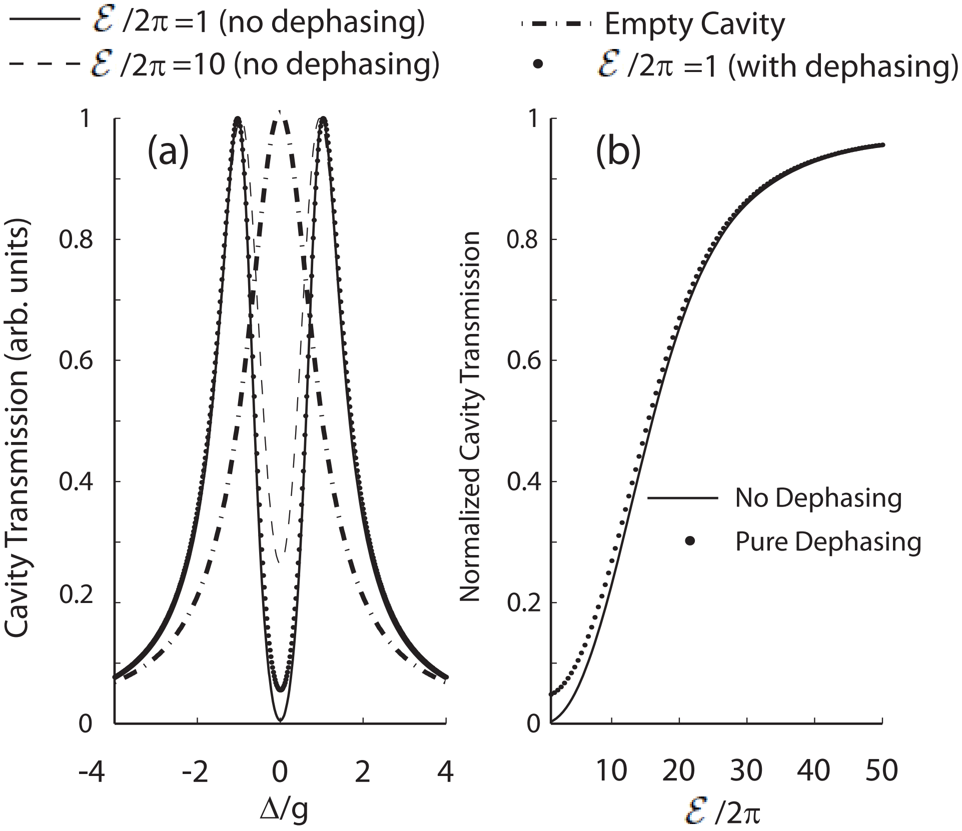

Figure 2.5: DC transmission characteristics of the all-optical switch made of a strongly coupled QD-cavity system system. The system is on resonance ($\omega_c = \omega_d$), and thus driving laser detunings from both QD and cavity mode are equal $\Delta = \Delta\omega_c = \Delta\omega_d$. (a) The transmission spectra for four different cases. An empty cavity shows a single Lorentzian peak. A strongly coupled QD-cavity system shows two peaks in the transmission, corresponding to the polaritons. The dip reduces both due to the pure QD dephasing, and at high laser power. The change in the dip at different driving laser power $\mathcal{E}$ is due to the QD saturation. The units of $\mathcal{E}/2\pi$ are in GHz. (b) The transmission on resonance with an empty cavity, i.e., at $\Delta\omega_c = 0$ (normalized by the empty cavity transmission) as a function of the driving laser strength.

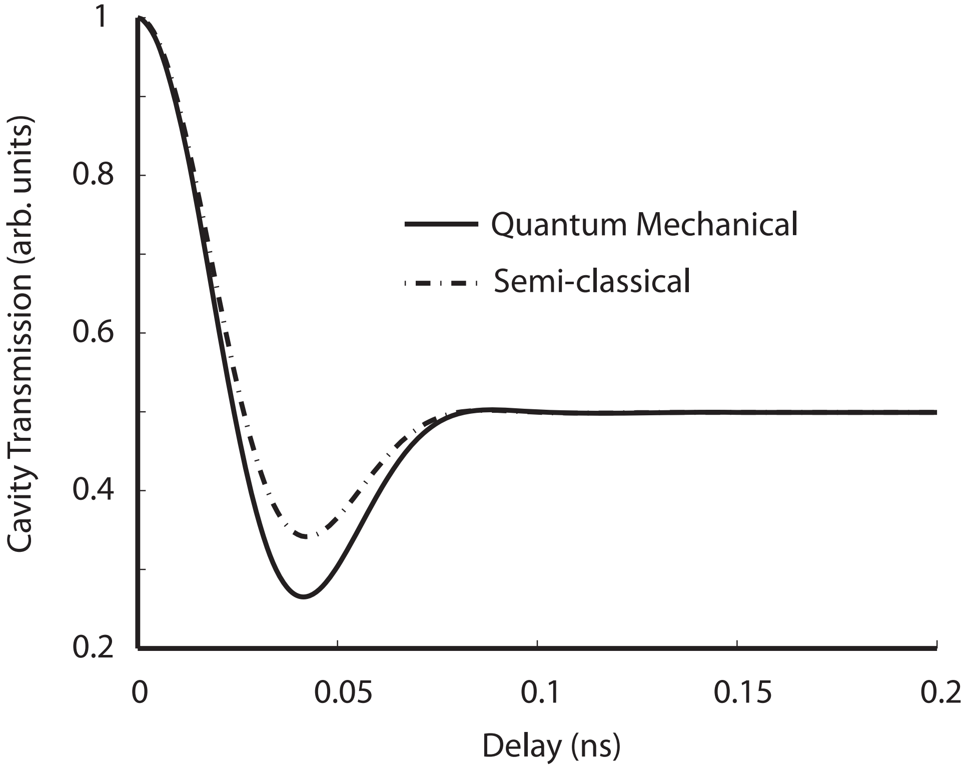

Figure 2.6: Comparison between two methods: quantum optical and semi-classical. The integrated cavity transmission is plotted as a function of the delay between two pulses. The two methods match quite well at zero and large time delay. However, they differ at the minimum transmission due to destructive interference between two pulses.

of a control, the total driving strength becomes $2\mathcal{E}$, assuming the control and the signal are of same strength. We define the on-off ratio of the switch as $T(2\mathcal{E})/4T(\mathcal{E})$, where $T(\mathcal{E})$ is the cavity transmission at a driving laser strength of $\mathcal{E}$. If the system is completely linear, the factor $T(2\mathcal{E})/4T(\mathcal{E})$ will always be 1. Figure 2.7a shows the on-off ratio as a function of g and κ, maintaining the same cavity transmission for different κ. We note that the on-off-ratio is not a strong function of g or κ. Figure 2.7b shows the on-off-ratio as a function of the ratio g/κ for several different values of κ. We observe that, increasing both g and κ improves the on-off ratio. This is because with increasing g the separation between the two polaritons increases, which reduces the transmission of single pulses resonant with the bare cavity. On the other hand, increasing κ reduces the power needed to saturate the QD, which again causes the on-off ratio to increase.

2.6.2 Dynamic response

For any switch, the speed of switching is a very important quantity. To estimate the switching speed we numerically calculate the dynamics of the coupled dot-cavity system.

Fig. 2.6 shows the integrated cavity transmission as a function of delay between two pulses. This is the type of signal observed in the recently published experiments [35, 51], in which a low speed detector was used. The two curves were obtained using the quantum optical and semi-classical approaches. At zero delay and large delay two methods agree quite well. An interesting feature in the integrated transmission of the switch is the dip that appears at small delay between the two pulses and we will explain its origin in the next paragraphs. Note that the semi-classical approach underestimates the amplitude of this dip.

Fig. 2.8a shows the temporal cavity output when two pulses interact with the coupled system, for different delays between the pulses and pulse duration of 40ps. For each input pulse, we observe two pulses at the output, as can be seen from the temporal cavity output at large delay. This is a signature of Rabi oscillation between the QD and the cavity in time domain, as analyzed in the previous section. Fig. 2.9

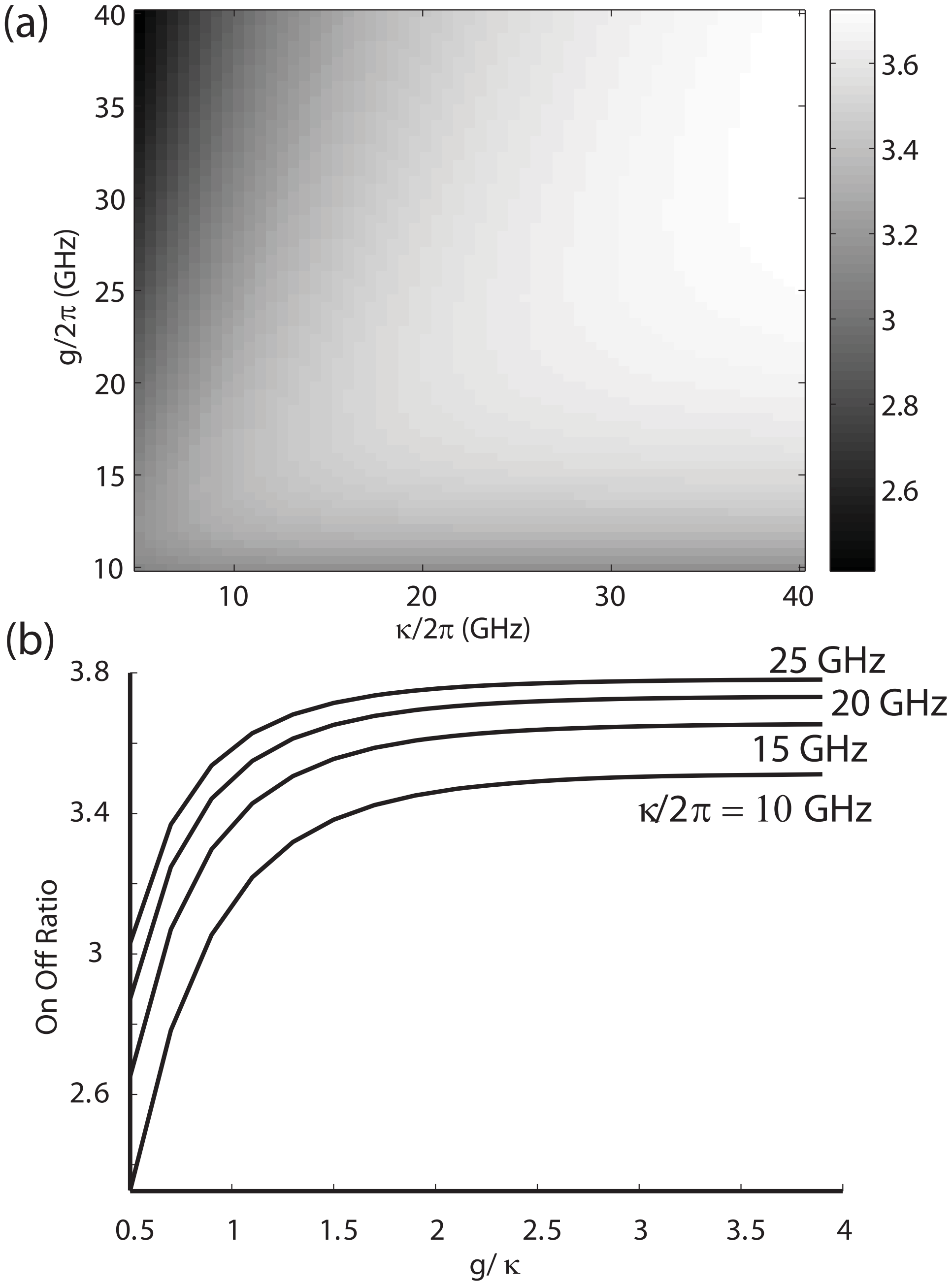

Figure 2.7: (a) Figure showing the on-off ratio (as defined in the text) under CW driving, as a function of g and κ. (b) On-off ratio as a function of the ratio g/κ for different κ. An increase in on-off ratio is observed with increase in both g and κ. For, this simulation $\mathcal{E}/2\pi = 0.1$ GHz.

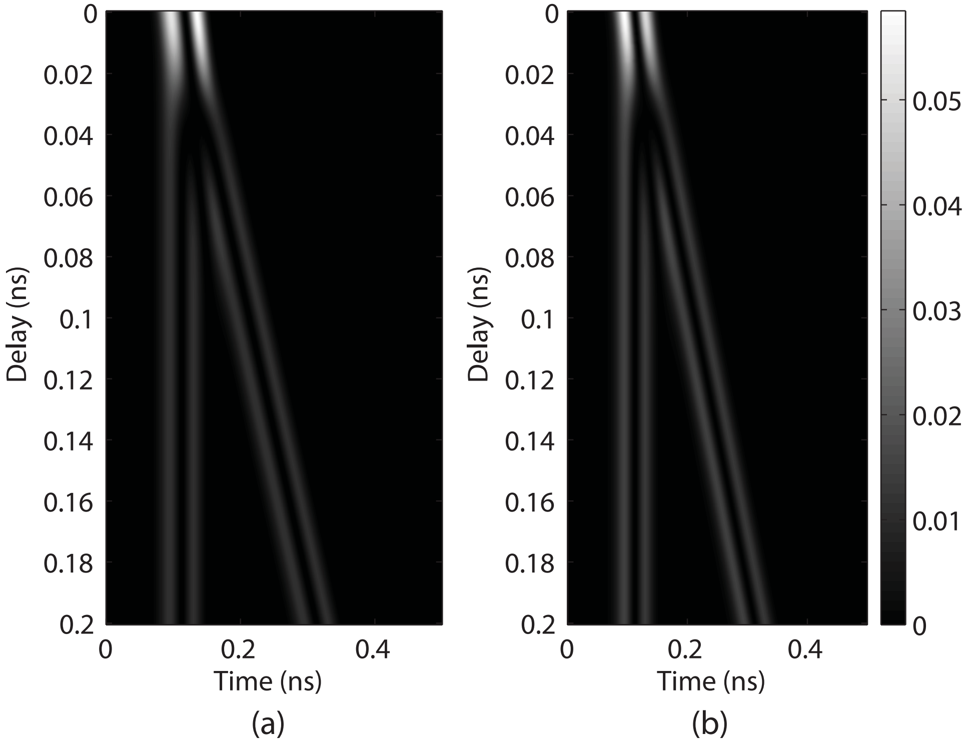

Figure 2.8: The cavity transmission as a function of time (horizontal axis) when two pulses interact with the coupled QD-cavity system, for different delays between two pulses (vertical axis). We present both results obtained by full quantum optical calculation (a) and semi-classically (b). The pulse-length is 40ps and $\mathcal{E}/2\pi = 1$ GHz. For this weak excitation limit, the two approaches yield nearly identical results. At small delay between the two pulses, the pulses overlap, and they behave as a single pulse. At larger delay, two pulses do not meet, and propagate independently of each other. For each input pulse we obtain two output pulses due to Rabi oscillation. At intermediate delay, there is a destructive interference between the two pulses causing reduced transmission.

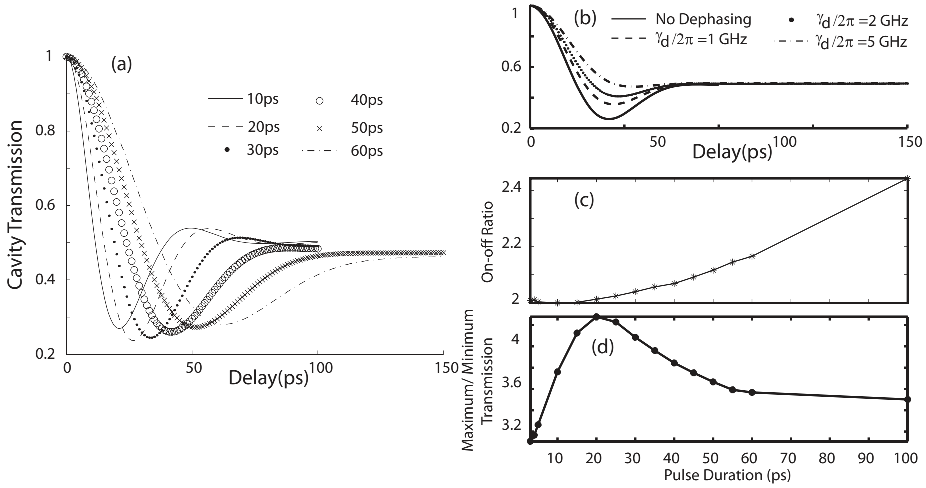

Figure 2.9: Switching performance for different pulse durations. (a) Total cavity transmission integrated over time as a function of the delay between two pulses. Pulses with different pulse-durations are considered in different curves. An increased transmission is observed at zero time-delay. The minimum transmission at a non-zero time delay is due to a destructive interference between two pulses caused by the Rabi oscillation. (b) The effect of pure QD dephasing. With increasing QD dephasing, Rabi oscillations are suppressed, the destructive interference becomes ineffective, and the minimum transmission increases with pure QD dephasing rates. (c) The on-off ratio (defined as the ratio of time-integrated cavity transmission between zero delay and large delay) as a function of the pulse duration. Increasing on-off-ratio with increasing pulse duration is due to reduced bandwidth of the pulses. (d) Ratio between maximum and minimum transmission as a function of the pulse duration.

a shows the integrated cavity transmission as a function of the delay between the two pulses for several pulse-lengths. As expected, an increase in cavity transmission is observed, when the two pulses arrive simultaneously (delay = 0). This is due to the saturation of the QD, which gives rise to the nonlinear behavior of the switch. As expected, when the two pulses are delayed relative to each other, the cavity transmission is low.

Numerical simulations also reveal an interesting effect of suppressed transmission that happens at a finite non-zero time delay. This can be explained by a destructive interference between the two pulses at a finite delay. We observe that effect more clearly in the temporal cavity output in Fig. 2.8a. When the two pulses overlap in time, they behave almost like a single pulse. At large delay between two pulses, the two pulses are independent of each other and we see four peaks, corresponding to two output peaks from each input pulse due to Rabi oscillation. At an intermediate delay between the pulses, the second peak from the first input pulse destructively interferes with the first peak from the second input pulse, and we observe only two peaks. At this delay the integrated transmission is minimal. In addition, we observe that this minimum transmission increases with increasing pure QD dephasing rate (Fig. 2.9 b).

Next, we study the dependence of the switching performance on pulse duration. Fig. 2.9 c shows the on-off ratio (defined as the ratio of the time-integrated cavity transmission at zero and large time delay, i.e., the ratio of the values in the curves in Fig. 2.9a at delay$= 0$ and as delay tends to ∞) as a function of the pulse length. We observe an increase in the on-off-ratio with increasing pulse length. With short pulses, the spectral bandwidth of the pulses exceeds the width of the dip induced by the QD. Consequently, the effective transmission of the pulse increases. Lastly, in Fig. 2.9d we examine the ratio between the maximum and minimum transmission through the coupled QD-cavity system as a function of the pulse length (practically, we plot the ratio between the maximum and minimum values of the plots in Fig. 2.9a).

The initial increase in the ratio with an increase in the pulse length can be ascribed to reduction in the pulse bandwidth. However, as the pulse length keeps increasing, complete destructive interference and cancelation of the middle peaks (see Fig. 2.8) cannot be achieved, which leads to a decrease in the plotted values. We note that, in this switch, we do not have a control-to-output isolation (i.e., the control goes to the output, and one cannot distinguish the control and signal), as generally required in a practical switch [52]. This can be achieved if one has access to both the polarizations of the quantum dot, and thus distinguishes the signal and the control by polarization. The other possibility is to use slightly frequency detuned signal and control pulses [35, 51, 53]. However, in both of these cases signal and control are not interchangeable, as is needed for realistic optical computing. Nevertheless, our simulation clearly shows the presence of an optical non-linearity almost at a single photon level, which can be exploited to make an optical switch.

2.7 Theory of electro-optic modulation

In the previous two sections, we exploited the low power optical nonlinearity for potential optical information processing. However, the properties of the QD can also be drastically changed by applying an electrical signal, and hence the coupled dot-cavity system can also be used as an electro-optic modulator. Here we analyze the performance of such an electro-optic modulator, where the electrical control of the quantum dot frequency is achieved via the quantum confined Stark effect (QCSE). Using realistic system parameters, we show that modulation speeds of a few tens of GHz are achievable with this system. In addition, we study the non-linear distortion, and the effect of pure quantum dot dephasing on the performance of the modulator.

We can use the previously described quantum optical Master equation to solve the dynamics of the system. However, that method is computationally expensive. Therefore we find the mean-field equations (also described previously in this chapter) for the coupled cavity/QD system (assuming the laser is resonant with the cavity frequency, i.e., $\Delta\omega_c = 0$):

$$\frac{d\langle X\rangle}{dt} = A\langle X\rangle + i\Omega B \tag{2.32}$$

and

$$\frac{d\langle Y\rangle}{dt} = C\langle Y\rangle + i\Omega D\langle X\rangle \tag{2.33}$$

where

$$X = \begin{bmatrix} a & \sigma & a^\dagger & \sigma^\dagger \end{bmatrix}^T \tag{2.34}$$

$$Y = \begin{bmatrix} a^\dagger a & \sigma^\dagger\sigma & a^\dagger\sigma & a\sigma^\dagger \end{bmatrix}^T \tag{2.35}$$

$$A = \begin{bmatrix} -\kappa & g & 0 & 0 \\ -g & \Gamma & 0 & 0 \\ 0 & 0 & -\kappa & g \\ 0 & 0 & -g & \Gamma^* \end{bmatrix} \tag{2.36}$$

$$B = \begin{bmatrix} -1 & 0 & 1 & 0 \end{bmatrix}^T \tag{2.37}$$

$$C = \begin{bmatrix} -2\kappa & 0 & g & g \\ 0 & -2\gamma & -g & -g \\ -g & g & \Gamma-\kappa & 0 \\ -g & g & 0 & \Gamma^*-\kappa \end{bmatrix} \tag{2.38}$$

$$D = \begin{bmatrix} 1 & 0 & -1 & 0 \\ 0 & 0 & 0 & 0 \\ 0 & 1 & 0 & 0 \\ 0 & 0 & 0 & -1 \end{bmatrix} \tag{2.39}$$

where $\Gamma = -(\gamma + \gamma_d + i\Delta\omega_a)$. These equations are similar to the Maxwell-Bloch equations (MBE). In deriving the MBEs, we assume that under low excitation, the system stays mostly in the lowest manifolds (single quantum of energy) and hence $\langle a\sigma_z\rangle \approx -\langle a\rangle$ and $\langle a^\dagger a\sigma_z\rangle \approx -\langle a^\dagger a\rangle$ [54].

When operating as a modulator, the cavity/QD system modulates the transmission of the laser driving the cavity (laser amplitude $\mathcal{E}$ and frequency ω_l). The system is modulated using an electrical signal which changes the QD resonance frequency via the quantum confined Stark effect (QCSE). In our analysis, we assume that the optical signal is always resonant with the bare cavity ($\omega_l = \omega_c$) and only the QD resonance frequency changes. We note that applying electric field across the QD reduces the overlap between the electron and the hole wavefunctions and consequently

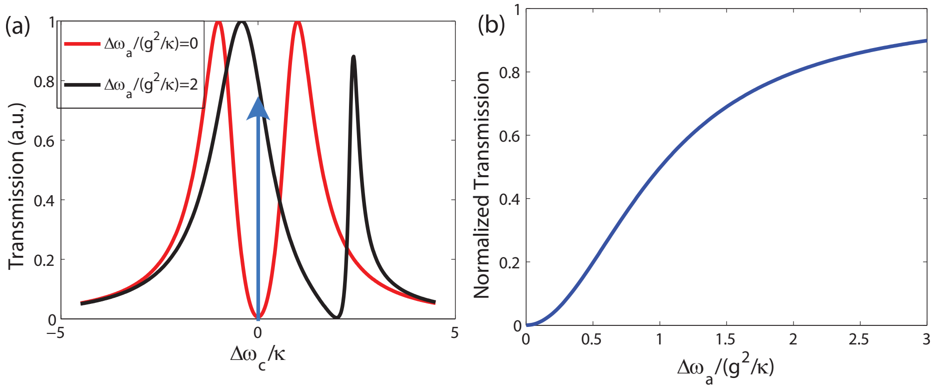

Figure 2.10: (a) Transmission spectra of coupled cavity-QD system for two different QD-cavity detunings. The blue arrow shows the wavelength of the laser whose transmission is being modified. (b) Normalized steady state transmission with different QD detunings. The laser is resonant with the cavity. We used the following parameters: $g/2\pi = \kappa/2\pi = 20$ GHz; $\gamma = \kappa/80$; the pure dephasing rate is assumed to be zero for this analysis ($\gamma_d/2\pi = 0$).

reduces the dipole moment of the QD and the coherent coupling strength g. However the reduction in g is due to the change in the spatial overlap of the eigen-states of the perturbed Hamiltonian (the Hamiltonian describing the confining potential of the QD), while the change in the QD resonance frequency is due to the modification of eigenvalues of the perturbed Hamiltonian. The perturbation in eigen-states due to QCSE is a higher order effect than the change in eigenvalues. Hence the reduction in g is much less prominent than the change in the QD resonance frequency and we preserve strong coupling even with the applied electric field [37]. However, there is a finite probability for the electron or the hole to tunnel out of the QD, when a large electric field E_{tun} is applied. For successful operation of the electro-optic modulator, the applied electric field must be smaller than E_{tun} and here we assume that this condition is satisfied.

The detuning of the quantum dot due to the application of an electric field causes dramatic changes in the transmission spectrum of the strongly coupled dot-cavity system (Fig. 2.10(a)). This directly affects the transmitted intensity of a laser tuned at the bare cavity resonance [shown by an arrow in Fig. 2.10(a)]. Figure 2.10(b) shows the steady-state transmission (normalized by the transmission through an empty cavity) for different values of QD-cavity detuning. This has been derived by solving the MBEs (Eqs. 2.32, 2.33) at steady-state (in absence of pure dephasing, i.e., $\gamma_d/2\pi = 0$), which gives that the ratio of the maximum to the minimum transmission through the cavity is $(1 + g^2/\kappa\gamma)^2$. To relate our theory to current state of the art technology where values of $\kappa/2\pi = g/2\pi \approx 20$ GHz ($\kappa/2\pi = 20$ GHz corresponds to a cavity quality factor of ~ 8000) can be easily achieved [1], we mainly analyze the system performance for both $\kappa/2\pi$ and $g/2\pi$ ranging between 10 to 40 GHz.

2.7.1 Frequency response

The foremost criterion of a good electro-optic modulator is its speed of operation. In this electro-optic modulator, the modulation speed is determined by two different time scales. One time scale depends on how fast the QD can be modulated by applying an electric field. This depends on the drift velocity of electrons and holes in the semiconductor, and the electrical capacitance of the modulator. As the active area of the modulator is very small (dimensions of a QD $\sim 10 \times 10 nm^2$), this time scale is extremely short and thus does not limit the modulator speed. The other time scale is due to the optical bandwidth of the system, i.e., the finite bandwidths of the cavity spectrum and the dip induced by the strong coupling of the dipole to the cavity. The cavity has a finite bandwidth, which limits how fast the modulator can operate. This optical bandwidth limits the speed of operation of the electro-optical modulator described here. To estimate the bandwidth of modulation, one can consider the cavity transmission spectrum [as shown by the red line in Fig. 2.10 (a)] as the filter response of the modulator; for successful operation, the pulse band-width should not exceed the splitting obtained due to the strong coupling. Following this argument, the bandwidth of the pulse that can be modulated via this electro-optic modulator is approximately g^2/κ.

However, to obtain the modulation speed more rigorously, we apply a sinusoidal change in the QD resonance frequency: $\Delta\omega_a(t) = \frac{1}{2}\Delta\omega_0(1 - cos(\omega_e t))$; where $\Delta\omega_0$ is the maximum detuning of the QD resonance (this is proportional to the amplitude of

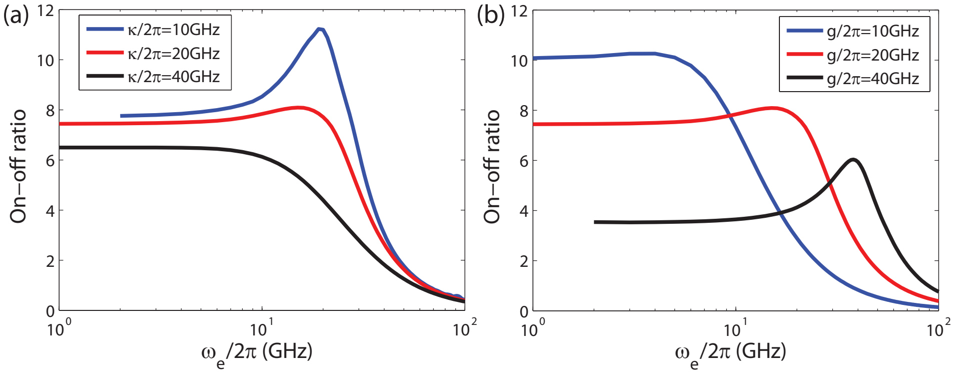

Figure 2.11: The frequency response of the switch for different (a) κ. $(g/2\pi)$ is kept constant at 20 GHz and (b) g. $(\kappa/2\pi)$ is kept constant at 20 GHz. For both simulations $\Omega = 1$ GHz; $\Delta\omega_0/2\pi = 10$ GHz; $\gamma_d/2\pi = \gamma/2\pi = 0.1$ GHz.

the electrical signal applied to tune the QD) and ω_e is the frequency of the modulating electrical signal and hence also the frequency of the change in the QD resonance. The system performance is determined by analyzing the change in the cavity output (i.e. $\kappa\langle a(t)^\dagger a(t)\rangle$) as a function of ω_e . The on/off ratio is defined as the ratio of the maximum to minimum cavity output during sinusoidal driving. The Rabi frequency Ω of the driving laser is chosen such that the QD is not saturated. The effect of free carriers generation in the semiconductor surrounding the QD by two photon absorption of the driving laser is not included in our analysis as at low Ω (that is, at low intensity of the driving laser) this effect is very small. The pure dephasing rate $\gamma_d/2\pi$ of the QD is assumed to be 0.1 GHz.

Figure 2.11 shows the on-off ratio of the output signal as a function of frequency of modulating signal for different κ and g. We observe that the modulator behaves like a second order low pass filter with a roll-off of -20 dB/decade. Figure 2.12 shows the cut-off frequency and the on-off ratio at low frequency as a function of different g and κ. The cut-off frequency of the filter increases with the coupling strength g. Similarly, reduction in κ increases the cut-off frequency. However when $\kappa < g$, the change in cut-off frequency is not significant and g plays the dominant role. At the same time, the on-off ratio decreases with g, which occurs because we kept the maximum detuning $\Delta\omega_0/2\pi$ fixed at 5 GHz. By increasing $\Delta\omega_0/2\pi$ the on-off ratio

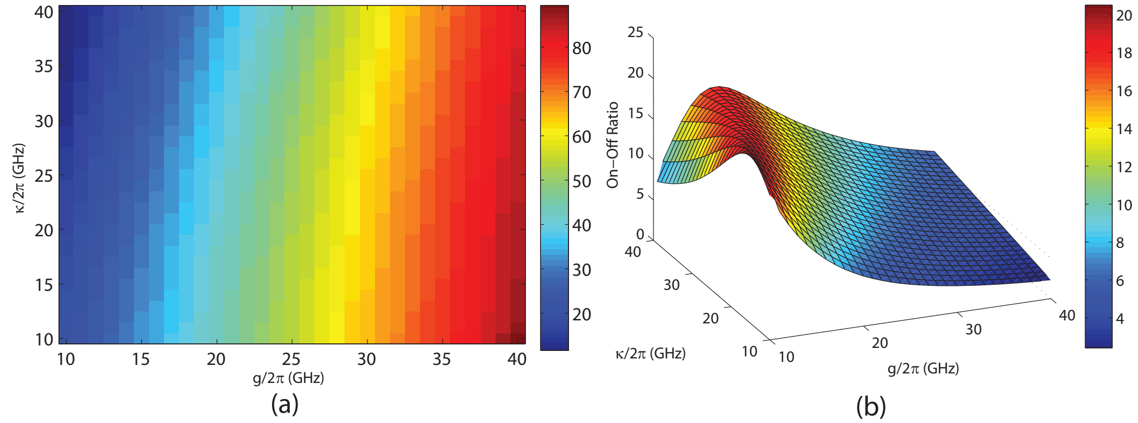

Figure 2.12: (a) Cut-off frequency of the modulator as a function of g and κ. In the color scheme, the maximum cutoff frequency of ~ 90 GHz is red and the minimum cutoff frequency of ~ 10 GHz is blue; (b) On-off ratio of the modulator at a modulating frequency of $\omega_e/2\pi = 5$ GHz as a function of g and κ. For both plots $\Delta\omega_0/2\pi = 5$ GHz; $\gamma_d/2\pi = 0.1$ GHz; $\Omega = 1$ GHz.

can be increased for higher values of g.

2.7.2 Nonlinear distortion of signal

Another important property of good modulators is that the modulated optical output should closely resemble the shape of the modulating electrical signal. If the modulator does not operate in the linear regime, the output signal contains spurious higher harmonics. Figure 2.13 shows the optical output signal for two different values of maximal QD detuning $\Delta\omega_0$. For small values of the electrical input (i.e., for small $\Delta\omega_0$), the output follows exactly the variation of the QD resonance frequency, as shown in Fig. 2.13(a). However, distortions appear for higher amplitudes of $\Delta\omega_0$ [Fig. 2.13(b)]. Here we observe ripples at a frequency different from the modulating frequency ω_e. These ripples do not arise only because of the finite bandwidth of the system, but are also due to the nonlinearity of the system with respect to $\Delta\omega_0$. A more detailed analysis of these ripples is described below, when we analyze the step response of the modulator. The value of $\Delta\omega_0$ also affects the visibility of the modulated signal. The on-off ratio (i.e., the desired output) is proportional to the

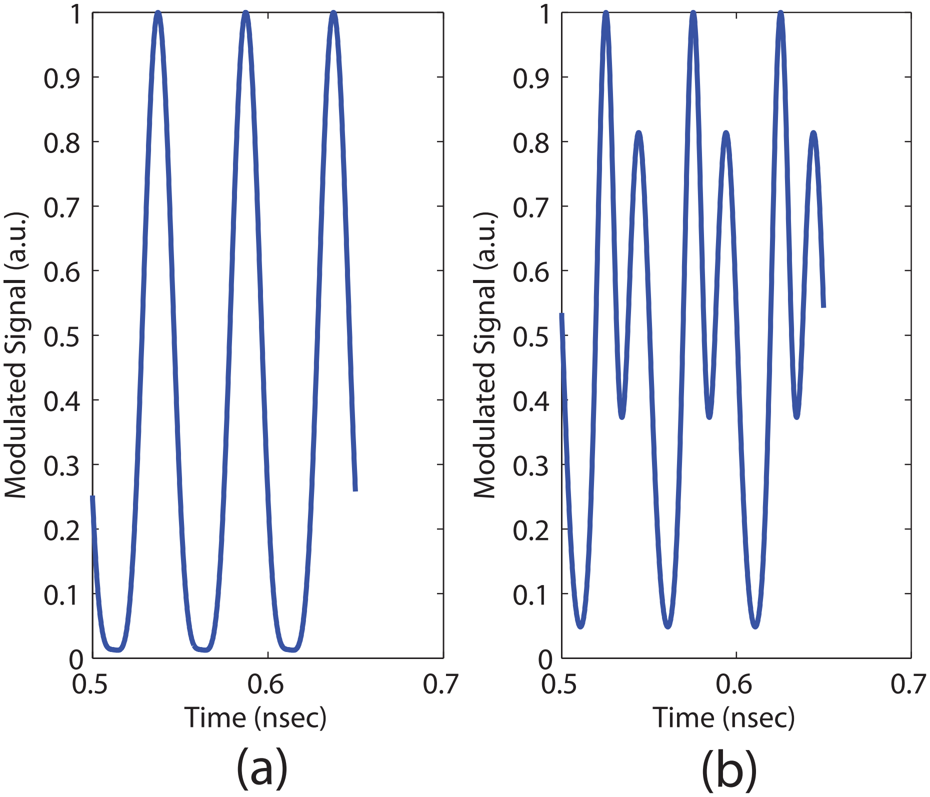

Figure 2.13: Normalized output signal for two different maximal QD detunings $\Delta\omega_0$. (a) $\Delta\omega_0/2\pi = 2$ GHz. (b) $\Delta\omega_0/2\pi = 40$ GHz. For both simulations the frequency of the electrical signal is $\omega_e/2\pi = 20$ GHz, $\kappa/2\pi = g/2\pi = 20$ GHz and $\Omega = 1$ GHz.

first harmonic of the modulated output signal. Figure 2.14 shows the ratio of second and third harmonics to the first harmonic of the output signal as a function of $\Delta\omega_0$. As expected, the higher order harmonics increase with increase in QD detuning $\Delta\omega_0$.

We note that by employing a differential detection method, one can get rid of the even order harmonics. For differential detection, one uses two electro-optic modulators, but the electrical signals applied to the modulators are out of phase. Let us assume that the desired signal, when the modulator is in linear regime, is $x(t) = Asin(\omega t)$. Due to nonlinearity the distorted signal is $x_d(t) = A_1 sin(\omega t) + A_2 sin^2(\omega t) + A_3 sin^3(\omega t) + \cdots$, where A_1,A_2, A_3 are the amplitudes of different harmonics. In differential detection, we apply two out of phase signals and then subtract the modulated optical signals to remove the even order harmonics, which are unaffected by the phase change. Hence the performance of the modulator is primarily determined by the third order harmonics.

2.7.3 Step response

The step response gives information about both the bandwidth of the system and the nonlinear distortion. To analytically calculate the step response we consider two situations: (1) when the electrical signal goes from on to off (that is the QD detuning goes from $\Delta\omega_0 \longrightarrow 0$); and (2) when the electrical signal goes from off to on (that is the QD detuning goes from $0 \longrightarrow \Delta\omega_0$). For low excitation and small dephasing rate, the average value of cavity output $\kappa|\langle a(t)^\dagger a(t)\rangle|$ is approximately given by $\kappa|\langle a(t)\rangle|^2$, where $\langle a(t)\rangle$ is

$$\langle a(t)\rangle_{\Delta\omega_0\to 0} = r(0)e^{-\alpha(0)t}cos(\beta(0)t + \phi(0)) + SS(0) \tag{2.40}$$

and

$$\langle a(t)\rangle_{0\to\Delta\omega_0} = r(\Delta\omega_0)e^{-\alpha(\Delta\omega_0)t}cos(\beta(\Delta\omega_0)t + \phi(\Delta\omega_0)) + SS(\Delta\omega_0) \tag{2.41}$$

where the switching happens at $t = 0$ and

$$\alpha(\omega) \quad = \quad \frac{\kappa + \gamma + i\omega}{2}$$

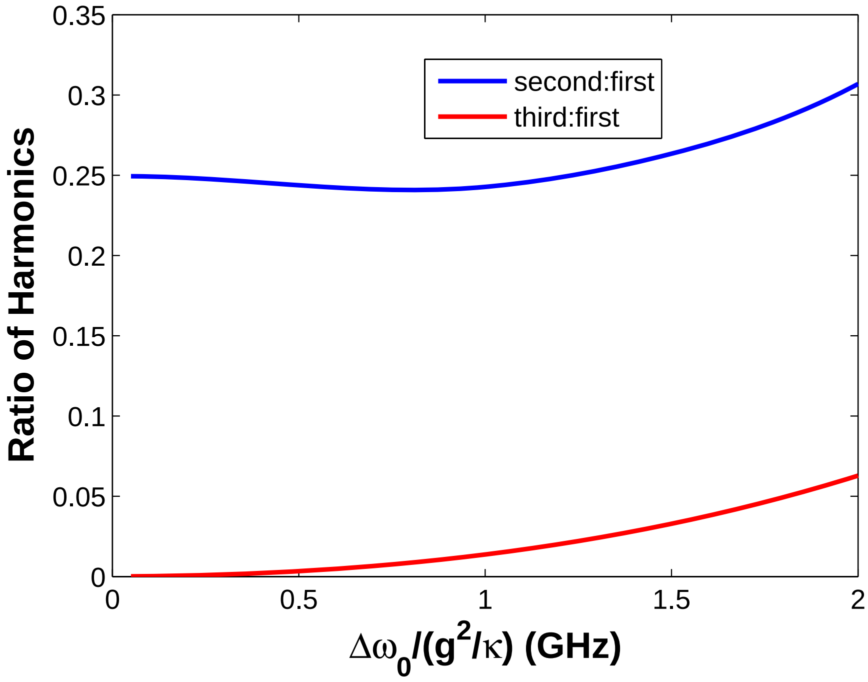

Figure 2.14: Ratio of the second and third harmonic to the first harmonic of the modulated signal, as a function of the maximum frequency shift of the QD, scaled by a factor of g^2/κ. The first harmonic is proportional to the actual signal. For the simulation we assumed that the modulation is working in the passband ($\omega_e/2\pi = 20$ GHz); $\kappa/2\pi = g/2\pi = 20$ GHz and the dephasing rate $\gamma_d/2\pi = 0$.

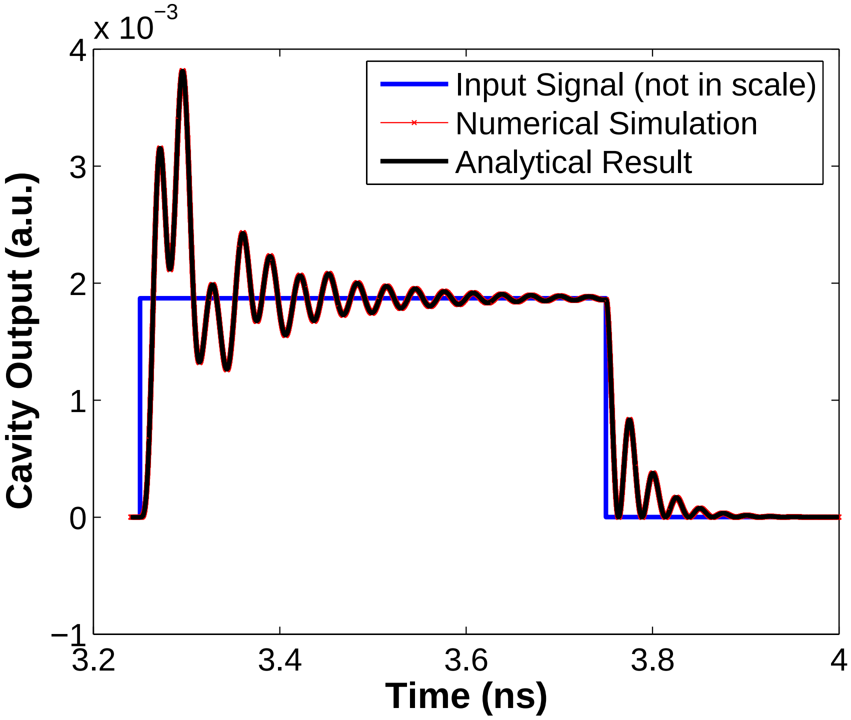

Figure 2.15: Step response of the single QD electro-optic modulator. The parameters used for the simulation are: $\kappa/2\pi = 5$ GHz; $g/2\pi = 20$ GHz; $\Delta\omega_0/2\pi = 20$ GHz; $\Omega = 1$ GHz.

$$\begin{aligned}
\beta(\omega) &= \frac{\sqrt{4g^2 - (\kappa - \gamma - i\omega)^2}}{2} \\
SS(\omega) &= \frac{i\Omega(\gamma + i\omega)}{g^2 + \kappa(\gamma + i\omega)} \\
\phi(\omega) &= tan^{-1}\left(\frac{\alpha(\omega)}{\beta(\omega)}\right) \\
r(0) &= \frac{SS(\Delta\omega_0) - SS(0)}{cos(\phi(0))} \\
r(\Delta\omega_0) &= \frac{SS(0) - SS(\Delta\omega_0)}{cos(\phi(\Delta\omega_0))}
\end{aligned}$$

Figure 2.15 shows the step response of the modulator. The numerical simulation of MBEs and the analytical expression for the step response show excellent agreement. We see the oscillations in step response because the system needs finite time to relax. Due to non-linearity of the system, this relaxation time depends on $\Delta\omega_0$. Hence in

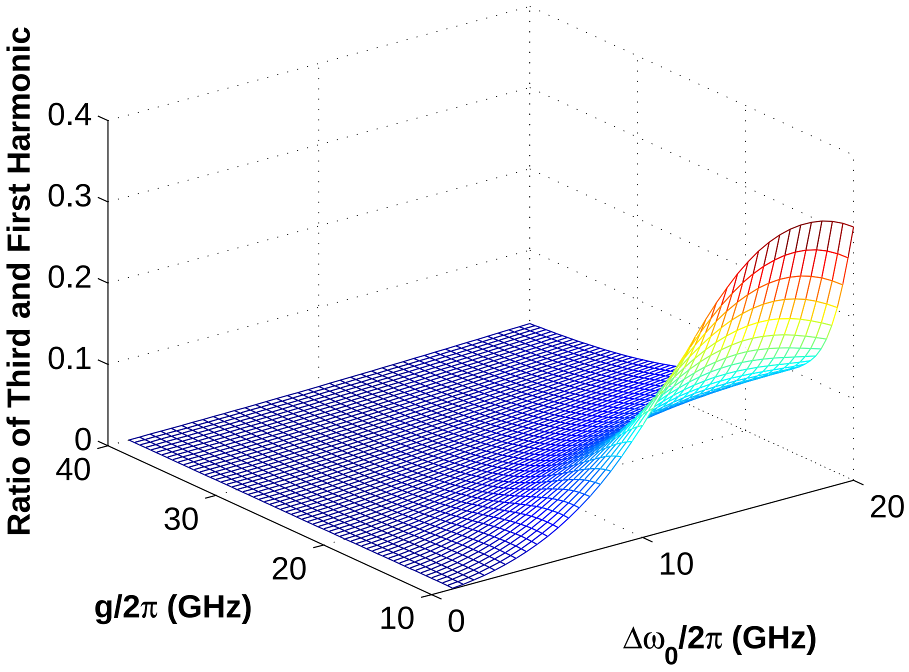

Figure 2.16: Ratio between the third and first harmonic of the modulated signal for different QD-cavity coupling g and maximum QD detuning $\Delta\omega_0$. The cavity decay rate $\kappa/2\pi = 20$ GHz and the modulation frequency $\omega_e/2\pi = 5$ GHz.

Fig. 2.13 we observe ripples only for high values of $\Delta\omega_0$.

Following previous analysis, we observe that with high amplitude of electrical signal ($\Delta\omega_0$), the on-off ratio of the modulator increases, but the modulated signal becomes distorted. In fact, when QD-cavity coupling g is large, one needs high $\Delta\omega_0$ to achieve good on-off ratio (Fig. 2.12). However, it should be noted that in a system with high g, the amplitude of electrical signal causing distortion is also high. Figure 2.16 shows the ratio between the third and first harmonic of the modulated signal for different g and $\Delta\omega_0$. We observe that for same amplitude of electrical signal (i.e., $\Delta\omega_0$), the distortion is larger for a system with smaller g.

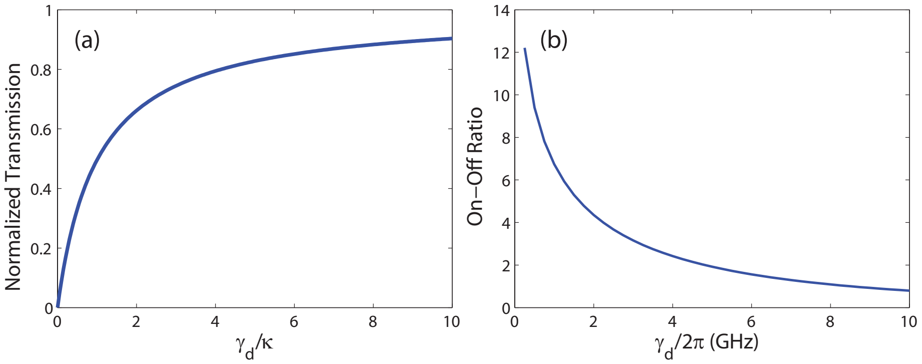

Figure 2.17: (a) Normalized steady state transmission of the laser resonant with the dot (i.e., $\Delta\omega_a = 0$) with pure dephasing rate $\gamma_d/2\pi$. Parameters used are: $g/2\pi = \kappa/2\pi = 20$ GHz; $\gamma = \kappa/80$; (b) On-off ratio of the modulated signal as a function of the dephasing rate, for $\kappa/2\pi = g/2\pi = 20$ GHz. The modulation frequency $\omega_e/2\pi = 5$ GHz and the amplitude of the change in resonance frequency $\Delta\omega_0/2\pi = 10$ GHz.

2.7.4 Effect of dephasing on performance of the single QD modulator

One of the major problems in CQED with a QD is the dephasing of the QD, caused by interaction of the QD with nearby nuclei and phonons. The dip in transmission through the cavity in presence of a coupled QD is caused by the destructive interference of the incoming light and the light absorbed and re-radiated by the QD [54]. Due to the dephasing of the QD, the light scattered from the QD is not exactly out-of-phase with the incoming light. This affects the destructive interference thus causing the cavity not to be fully reflective. Figure 2.17(a) shows the steady state transmission through a coupled cavity/QD system (normalized by the transmission through an empty cavity) of a laser resonant with the cavity and the QD, as a function of the QD dephasing rate. It is clear that, the performance of the modulator is strongly affected by dephasing. Figure 2.17(b) shows the on-off ratio as a function of the dephasing rate $\gamma_d/2\pi$ of the QD. As expected the on-off ratio falls off with increased dephasing rate.

Chapter 3

Temporal dynamics and all optical switching with QD-CQED system: Experiment

In the previous chapter, we have theoretically shown how a QD-CQED system can provide strong optical nonlinearity that could be employed in classical optical switching, where a control pulse can change the transmission of the signal pulse through the coupled dot-cavity system. We have also theoretically studied dynamics of the QD-CQED system and the predicted transmission of an optical pulse through it, exhibiting features coming from vacuum Rabi oscillation. In this chapter, we present experimental results of these effects too. First, we present experimental data showing the cavity transmission for a single pulse. We observe vacuum Rabi oscillation, which depends on the excitation laser power. Then we present cavity transmission for two pulses, and show the signature of optical switching.

3.1 Temporal Rabi Oscillation

First, we provide the experimental data to test the validity of our numerical simulations of the dynamics of a strongly coupled dot-cavity system driven by a short pulse (see chapter 2). We note that temporal Rabi oscillations were previously reported

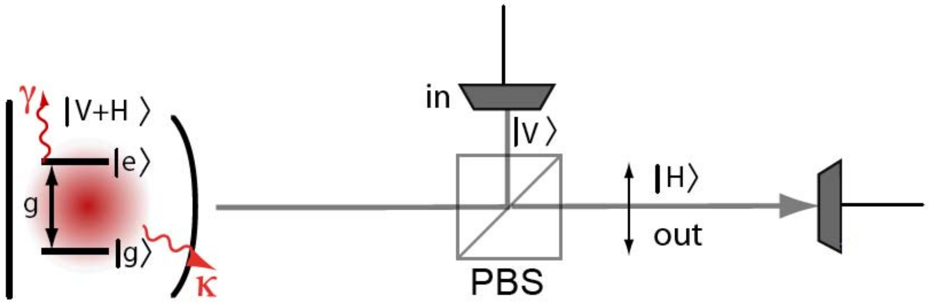

Figure 3.1: Cross-polarized reflectivity setup: the cavity is kept at a 45^o angle. The probe light is vertically polarized, but we collect only the horizontal light at the output. Thus we collect only the light which interacted with the cavity, and get rid of the background.

in atomic CQED system with a single atom [55], but very recently by our group with a single solid-state quantum emitter [34]. In the solid state system, much larger dipole-cavity interaction strength is possible due to the large QD dipole moment and tight confinement of the light field inside the small mode-volume cavity (the vacuum Rabi frequency is on the order of ~ 10 GHz, compared to MHz in atomic CQED systems) [2, 1]. As a result, the temporal dynamics is much faster than that previously reported in the atomic system [55]. We also note that time-resolved Rabi oscillations were previously analyzed theoretically [56] and experimentally [57] with quantum well excitons embedded in planar microcavities. However, that system is very different from a single quantum emitter (e.g., single quantum dot) embedded in a nanocavity.

A cross-polarized reflectivity setup (Fig. 3.1) was used to obtain the transmission of light through the coupled system and the cavity transmission was monitored with a Hamamatsu streak camera. In cross-polarized reflectivity, the probe light is linearly polarized (say, vertical polarization). The linearly polarized cavity is kept at a 45^o angle, i.e., at a polarization $\frac{1}{\sqrt{2}}(H+V)$. However, only horizontal polarized light is collected at the output. Hence, we collect only the light, that is reflected from the cavity. The experimental parameters of the probed dot-cavity system are $g/2\pi = 25$ GHz and $\kappa/2\pi = 29$ GHz [35]. We did not observe the predicted oscillations in the initial experiments measuring the transmission of 5 ps pulses through the cavity,

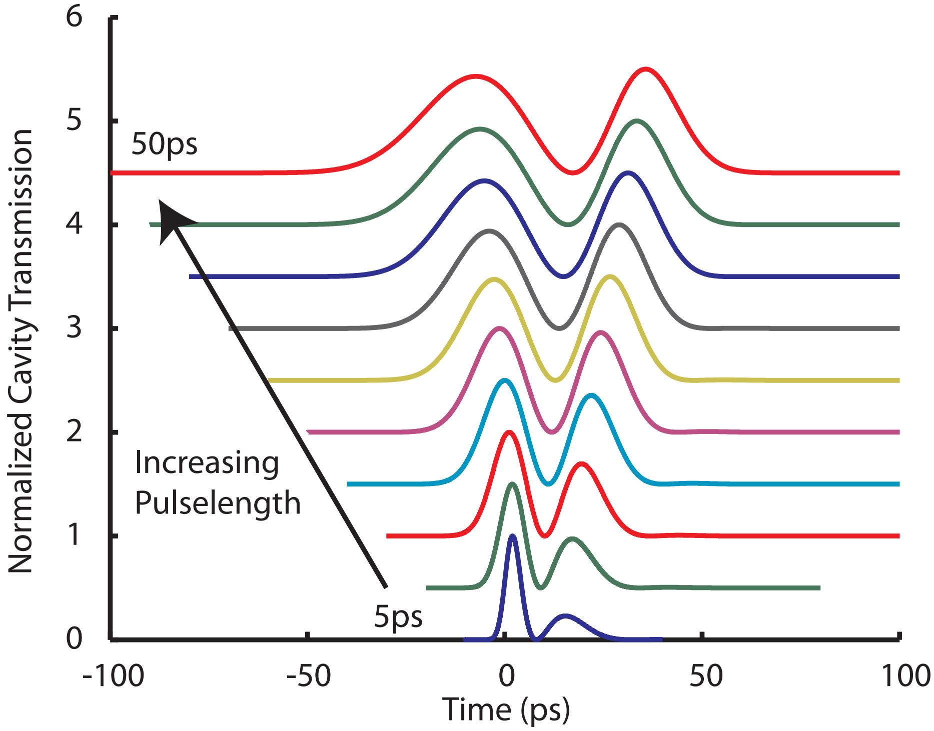

Figure 3.2: The normalized cavity transmission for different pulse duration. The pulse duration is changed from 5 ps to 50 ps. We observe oscillation in the cavity output, although the oscillation frequency decreases with increasing pulse-width. This can be explained by the reduced overlap between the pulse and the coupled dot-cavity system in frequency domain.

most likely because of the limited time resolution of our detector. Subsequently the experiment was performed with a longer pulse (40 ps Full Width Half Maximum (FWHM)). As shown in chapter 2, we theoretically analyze the dependence of the cavity transmission on the pulse duration (Fig. 3.2). When the pulse duration is changed from 5 ps to 50 ps, we observe a decreasing oscillation frequency. This can be explained by the reduced overlap between the input pulse and the coupled dot-cavity system with reduction in pulse bandwidth. In other words, a long pulse does not have sufficient bandwidth to excite both the polaritons and the oscillation frequency in the cavity output deviates more from $2g$.

Fig. 3.3 a,b,c show the experimentally obtained cavity output for three different

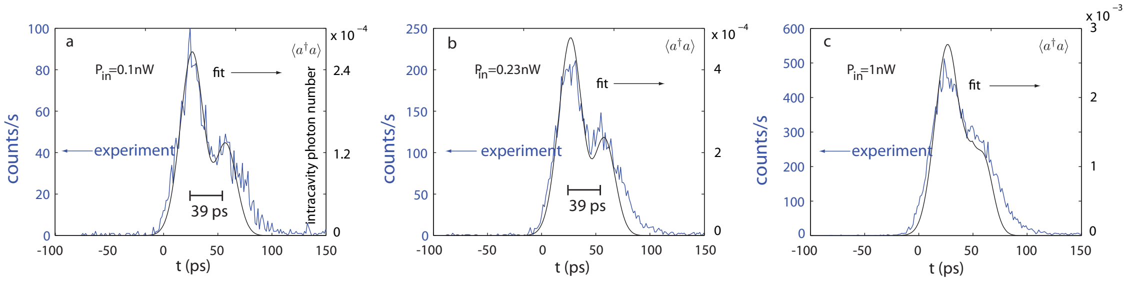

Figure 3.3: Experimentally measured time resolved transmission of 40ps pulses through a strongly coupled dot-cavity system for three different powers (averaged over the pulse repetition period): (a)0.1 nW; (b) 0.23 nW; (c) 1 nW. The powers are measured in front of the objective lens in the confocal microscopy setup. For this specific system cavity field decay rate $\kappa/2\pi = 29$ GHz and coherent dot-cavity coupling strength $g/2\pi = 25$ GHz. Clear oscillations are observed in the cavity transmission, consistent with the the theoretical predictions. We also observe decreasing oscillation with increasing laser power due to QD saturation.

excitation powers. The experimental data match qualitatively the predictions from the numerical simulation and clear oscillation is observed in the cavity output. This oscillation disappears with increasing laser power, as expected from the QD saturation. The oscillation period is estimated to be 25 GHz, corresponding to time difference of 39 ps between the two peaks. We note that the numerically obtained plots in Fig. 3.2 are calculated with very small excitation power. However, the experiment cannot be performed with such low excitation power as the detected signal is too low. Hence, in the experiment, the coupled system is driven close to the QD saturation, and the oscillations are less visible. Another reason is that the extinction of the cross-polarized cavity transmission measurement is not perfect, so the signal will be detected together with light reflected from the surface of the sample that did not interact with the QD-cavity system. Additionally, possible charging of the QD moves the dot far out of resonance and will blur the predicted oscillatory cavity transmission with the non-oscillating spectrum for $g = 0$.

3.2 All-optical switch

Once we understand the transmission of a single pulse, we study dynamics of the interaction between two weak light beams mediated by a strongly coupled quantum dot-photonic crystal cavity system. Optical nonlinearity observable with low power light is a necessary requirement for efficient all-optical switching. Though cavities can be used to enhance the bulk optical nonlinearity of a material, the enhancement is often not sufficient for operation of a practical device. In recent years, several experiments (including several experiments by our group) have demonstrated optical non-linearities at single-photon level, showing potential for implementation of ultra-low power and high-speed all-optical gates and switches for classical information processing [58, 53, 1, 37, 33]. In particular, the strongly coupled dot-cavity system seems very promising for such switching. The advantages of these systems include their small footprint and compatibility with standard nanofabrication procedures, in addition to an optical nonlinearity that is, in the ideal limit, observable with a single photon.

The parameters of the emitter-cavity system used in the experiment (obtained by fitting the spectrum of coupled QD-cavity system at resonance as shown in Fig. 3.4 d) are $g/2\pi = 25$ GHz and $\kappa/2\pi = 27$ GHz. The spectrum of the coupled QD-cavity system does not depend strongly on the QD dipole decay rate γ, as it is much smaller compared to g and κ. However, this parameter is estimated from the time-resolved measurements of the uncoupled QD emission and from QD linewidth measurements in off-resonant dot-cavity coupling [4] to be equal to $\gamma/2\pi \sim 1$ GHz.

We characterize the system in a cross-polarized confocal microscope setup in a He flow cryostat (Fig. 3.4(b)). The photoluminescence (PL) scans in Fig. 3.4(c) show the anticrossing between the QD-like states and the cavity-like states as the temperature is raised from 36K to 42 K, giving the polariton energies. The cavity transmission, obtained using a broad-band light source at 930 ± 20 nm in the cross-polarized configuration [1] shown in Fig. 3.4(b), shows the same mode splitting in Fig. 3.4(d). We also characterize the system by time-resolved photoluminescence after the QD is quasi-resonantly excited with 3.5 ps pulses at 878 nm. As shown in

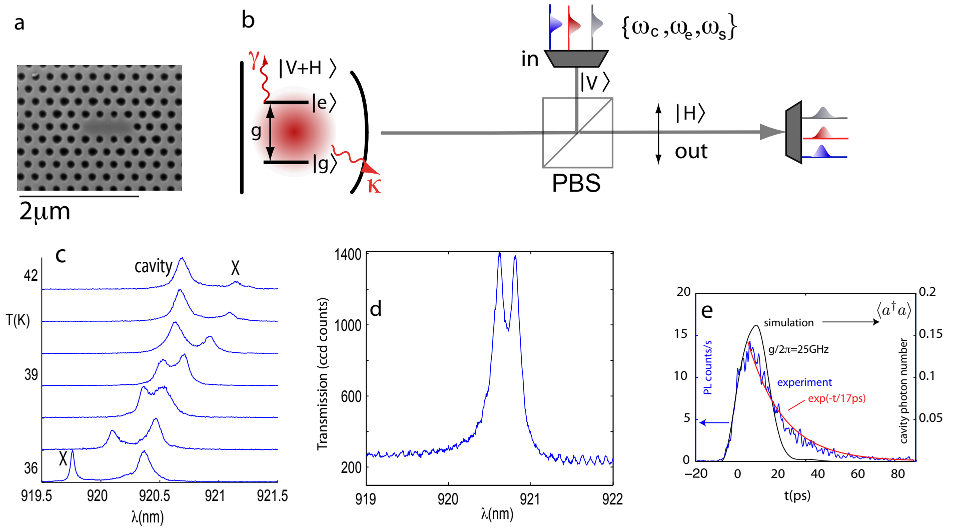

Figure 3.4: (a) Scanning electron micrograph of the photonic crystal cavity. (b) In the experiment, a combination of pulsed control laser (frequency ω_c), non-resonant pulsed or continuous wave pump laser at ω_e above the QD exciton line, and pulsed or continuous-wave signal laser (ω_s) is employed. The cavity is backed by a distributed Bragg reflector, effectively creating a single-sided cavity[1]. A cross-polarized confocal microscope configuration reduces the laser background that is reflected from the sample without coupling to the cavity, which is polarized at 45° to the incident laser polarization. The measurement is effectively a transmission measurement from the horizontal (H) into the vertical (V) polarization. (c) Anticrossing observed in the PL as the QD single exciton (X) is temperature-tuned through the cavity. The QD is pumped through higher-order excited states by optical excitation at ω_e corresponding to a wavelength of $\lambda_e = 878$ nm. (d) The transmitted intensity of a broad-band light source (in the cross-polarized setup) shows the mode splitting of the strongly coupled QD-cavity system (this signal is resolved on a spectrometer). (e) PL lifetime ~ 17 ps when the QD is tuned into the cavity and pulsed excitation is at wavelength $\lambda_e = 878$ nm. The emission that is expected theoretically, based on the system parameters in (d) and a 10-ps relaxation time into the single exciton state, is shown in the solid line.

Fig. 3.4(e), the PL decays with a characteristic time of 17 ps, as measured using a streak camera with 3 ps timing resolution. This decay closely matches a theoretical model of the cavity field and coupled QD system. Very weak above-band laser power (1 nW measured before the objective lens) is used in this measurement, in order to avoid generation of multi-excitonic complexes which may affect the measured lifetime [59].

The coupled QD-cavity system enables a strong interaction between two weak laser fields. This was previously demonstrated by our group for two slightly frequency detuned continuous-wave (CW) beams[53]. However, for practical applications of this effect, it is important to demonstrate such interaction with ultrafast optical pulses. Moreover, for practical applications it is critical that signal and control beams are at the same frequency, in order to enable cascading of the switches [52]. In both experiments presented below we used signal and control beams of the same frequency. We first study the time-resolved dynamics of this interaction between CW 'signal' and pulsed 'control' beams, both within the linewidth of the cavity resonance. In the experiment, with the QD resonant with the cavity and the control and signal beams tuned to the bottom of the transmission dip (shown in Fig. 3.4d), we measure the time-resolved transmission of the control $T(c)$, the signal $T(s)$, and the signal and control $T(s+c)$ on the streak camera. The system temperature is set to 30 K for this experiment. This measurement was taken on the same system from Fig. 3.4, but on a different day when the QD-cavity became resonant at lower temperature than in Fig. 3.4c.

We first set the signal and control fields resonant with the tuned QD-cavity system and attenuate the power so that the average intracavity photon number is nearly zero; this corresponds to 12 nW for the CW beam and $\sim$ 0.2 nW average power for the pulsed control (40ps pulses, 13ns repetition period), both measured before the objective lens. Considering a coupling efficiency into the cavity of $\eta \sim 3\%$ [1], this corresponds to an average intracavity photon number of $\langle a^\dagger a \rangle \sim 0.005$ for the CW signal beam and up to 0.025 (per pulse) for the pulsed control beam. Here the intracavity photon number is estimated as $\eta P_{in}/(2\kappa\hbar\omega_r)$ for CW beam , where P_{in} is the average input power measured before the objective lens [1]. For a pulsed beam this expression is multiplied by a factor 325, corresponding to the ratio between the repetition period and the pulse duration. In the following figures $\langle a^\dagger a \rangle$ corresponds to the *instantaneous* cavity photon number. Fig. 3.5(a), panel 1, plots the curves $T(c), T(s), T(s+c)$, as well as the difference $\Delta T = T(c+s) - T(c) - T(s)$, which provides a measure of the nonlinear response of the system. Measurements for two additional sets of curves with higher powers in signal (168 nW and 240 nW, respectively) and control (1.6 and 3.8 nW, respectively), are shown in panels 2 and 3 of Fig. 3.5(a). We observe that the difference ΔT increases with increasing laser power, as the QD is driven closer to saturation. We note that, for the three sets of data, the collection efficiency and integration time of collection are different, due to mechanical instability of the system. A stochastic simulation of the quantum master equation yields the cavity transmission, which is proportional to the intracavity photon numbers $n(c), n(c+s)$, and $n(s)$, as well as the nonlinear signal Δn, all plotted in Fig. 3.5b and showing good agreement with the experiment in Fig. 3.5a. In fitting the data, the intensities of the pulsed and CW beams were not free parameters, but were fixed by the experimentally measured optical powers, using the same coupling efficiency η. We note that in these simulations we did not include the effect of pure QD dephasing [2], as the role of these particular simulations is to just qualitatively show the expected system dynamics. However, we do include the effect of dephasing in the simulations of the actual optical switching between two pulses described below. As previously reported [36], dephasing reduces the switching contrast, which can be alleviated by performing the experiment at lower temperature.

Finally, we perform the actual all-optical switching experiment between two weak, 40ps optical pulses, by interacting them in a strongly coupled QD-cavity system. The pulses are resonant with the cavity and have a relative delay of Δt. The pulse pair is generated using the delay setup of Fig. 3.6(a). The pulses are therefore at the same frequency, but to eliminate interference between the two pulses, we detune them by 40 MHz and average measurement over many pulse pairs (this detuning is very small compared to the pulse bandwidth). Same as in the experiments in Fig. 3.5, numerical integration of the Master equation predicts an increased transmission when both pulses are simultaneously coupled to the cavity. This is shown for a particular

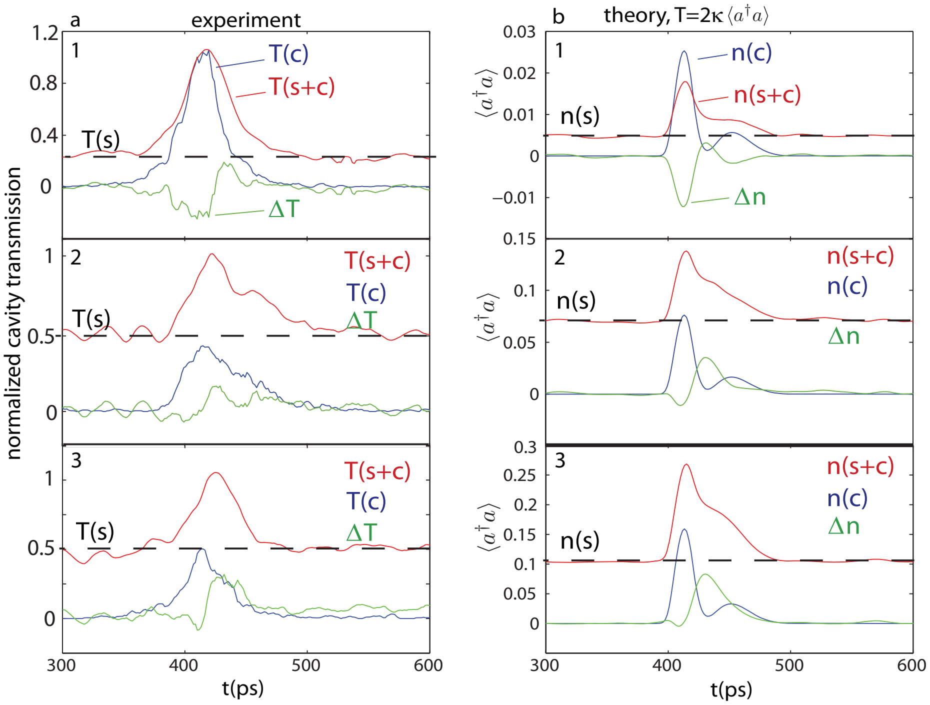

Figure 3.5: All-optical switching of the CW signal beam by a pulsed control beam through the strongly coupled QD/cavity system. (a) Cavity transmission when the signal and control are tuned to the cavity, which is resonant with the QD (panel 1). The transmitted cavity output is normalized w.r.t. the maximum cavity transmission. As the signal and control input powers are increased (panels 2 and 3), the QD saturates and results in a net-positive nonlinear transmission. For the three panels, the CW signal powers are 12 nW, 168 nW and 240 nW, respectively; the pulsed control powers are 0.2 nW, 1.6 nW and 3.8 nW, respectively (all measured before the objective lens). (b) Plots of the theoretically estimated intracavity photon number $\langle a^\dagger a \rangle$, which gives the transmission by $T = 2\kappa \langle a^\dagger a \rangle$. We plot the calculated intracavity photon number for the control beam intracavity photon number $n(c)$, signal and control $n(s+c)$, and the differential photon number $\Delta n = n(s+c) - n(s) - n(c)$.

choice of powers in Fig. 3.6(b).

This experiment is performed on a different QD-cavity system with similar parameters $\{\kappa, g, \gamma\}/2\pi = \{27.2, 21.2, 1\}$ GHz while the temperature of the system is kept at 38K. Photon statistics measurements on the system showed non-classical behavior confirming only a single QD is coupled to the cavity and result in the effects of photon blockade and photon induced tunneling, confirming quantum nature of the system [3]. Fig. 3.6(c) plots the time-averaged cavity transmitted signal observed on a spectrometer for coincident pump pulses with average power of both pulses increasing from 0.3 nW to 9.2 nW before the objective lens. It is evident that for powers beyond $\sim$ 9 nW, the polariton mode splitting disappears as the QD is saturated. This suggests that the QD-cavity system acts as a highly nonlinear system that increases its transmission for coincident pulses. Based on the result of Fig. 3.6c, we choose average powers of individual pulses to be 3.4 nW, as it is evident that the presence of two such pulses saturates the system leading to maximum cavity transmission. This pulse power corresponds to an intracavity photon number of 0.4 for each pulse ($\eta = 3\%$). Then we perform optical switching experiment by tuning the delay between two such pulses, as shown in Fig. 3.6(d): the cavity transmission rises by 22% when the pulses are coincident at $\Delta t = 0$. This transmission peak agrees with the theoretical prediction as shown by the red curve. In the theory plot, we also observe reduced transmission at a non-zero time delay. We find that by including a pure QD dephasing term into the master equation model, the transmission dips are diminished (Fig. 3.6 b), as observed in the experimental results. The best fit to experimental data is found for a dephasing rate of $\gamma_d/2\pi \approx 5$ GHz.

In conclusion, we demonstrated the ultrafast all-optical switching between the pulsed control beam and a CW or pulsed signal beam via a strongly coupled QD/cavity system. A strong nonlinear response exists at low powers corresponding to mean intracavity photon numbers below one. The large nonlinearity may be of use in classical all-optical signal processing[58] – for example, for the implementation of all-optical logic gates operating at the single- or few-photon level. In addition, it may be beneficial for quantum information processing with optical nonlinearities [44, 60]. Moreover,

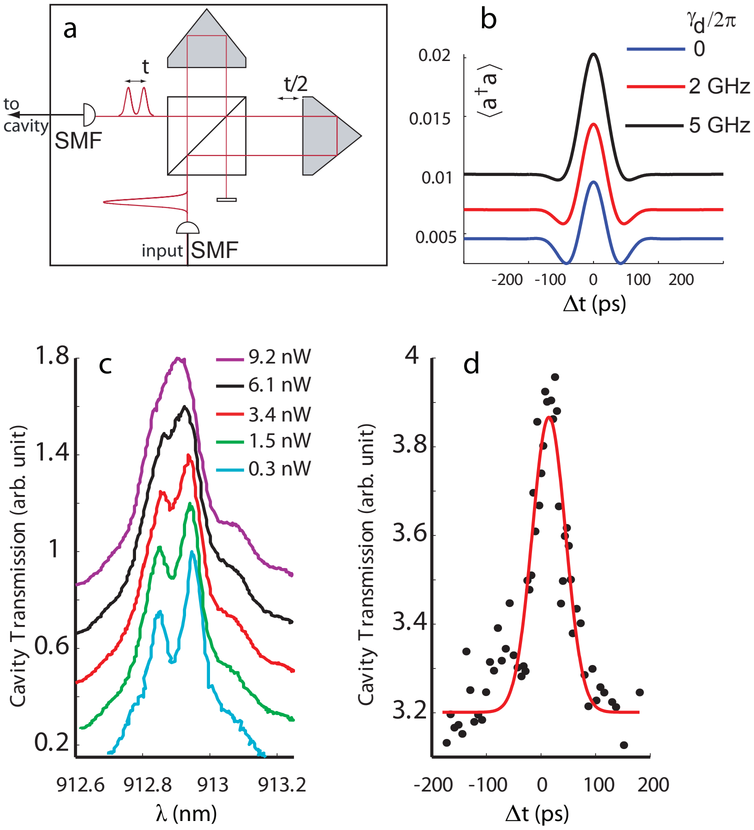

Figure 3.6: All-optical switching between two weak laser pulses interacting via a strongly coupled QD-cavity system. (a) Time-delay setup for producing pulses at a separation of Δt. (b) Simulated interaction of two laser pulses, represented by the instantaneous intracavity photon number $\langle a^\dagger a \rangle$ as a function of the time delay Δt between the two 40 ps long Gaussian pulses. Curves are calculated for a set of different rates of pure QD dephasing [2], γ_d, which causes a reduction of the transmission dips before and after the peak. Pure dephasing also causes a blurring of the spectral normal mode splitting [2], which in turn raises the transmission for increasing γ_d. (c) Pump-power dependence of the cavity transmission for coincident pulses repeating at 80 MHz. Different curves correspond to the average power of each of the pulses used in the experiment (averaged over 13 ns, the pulse repetition period). (d) Signal observed when the cavity-QD system is probed with two 40 ps long pulses as a function of their delay. When the two pulses have a temporal overlap inside the cavity (i.e., delay approaches zero), the QD saturates and the overall cavity transmission increases. The power in the single of the two pulses corresponds roughly to the 3.4nW trace in (c). Best agreement is found with the theoretical plot for a pure dephasing rate $\gamma_d/2\pi \sim 5$ GHz (the solid red line).

the QD-cavity system is ideal for on-chip integration and can easily operate with repetition rates up to a tens of GHz.

Chapter 4

Fast electrical control of a single quantum dot-cavity system

In this chapter, we present experimental results of electro-optic modulation of an input laser beam using a single QD strongly coupled to a photonic crystal cavity. Theoretical analysis of such a system was presented in chapter 2. For electro-optic modulation we employed a lateral electric field. In the last section, we describe an experiment on vertical electrical control of a QD in cavity, where the QD is embedded in a p-n-i-n diode.

4.1 Electro-optic modulation: lateral electrical control

In this section, we present the experimental study of the electro-optic modulation by a single QD strongly coupled to the cavity. The resonance frequency of the InAs quantum dot strongly coupled to a GaAs photonic crystal cavity was electrically controlled via quadratic quantum confined Stark effect. Stark shifts up to 0.3 meV were achieved using a lateral Schottky electrode that created a local depletion region at the location of the quantum dot. We report switching of a probe laser coherently coupled to the cavity up to speeds as high as 150MHz, limited by the RC constant of the transmission line used to feed electrical signal into the cryostat. The coupling strength g and the magnitude of the Stark shift with electric field were investigated while coherently probing the system.

The device consists of an InAs quantum dot coupled to a linear three hole defect photonic crystal cavity fabricated in a 160nm thick GaAs membrane (Fig.4.1(a)), similar to the devices reported in the previous chapters. The electrical control was achieved by applying a lateral electric field across the quantum dot and thus shifting its resonant frequency via QCSE[61, 62]. The field was created in the depletion layer of a Schottky contact (20nm Cr/25nm Au on GaAs) deposited in the vicinity of the quantum dot[63]. A scanning electron microscope image of the photonic crystal resonator integrated with the laterally positioned electrode is shown in Fig.4.1(a). Another Schottky contact, located on the surface of the chip a few hundred microns away from the photonic crystal, was used to set the ground potential.

One challenge in designing the device is the small extent of the depletion layer in the vicinity of the Schottky contact. For typical undoped GaAs grown by molecular beam epitaxy, there is still a dopant concentration of $\sim 10^{16}/cm^3$ that limits the size of the depletion layer to a few microns for a 10V bias voltage. This requires the contact to be brought into a proximity of a few microns from the quantum dot embedded in the photonic crystal cavity. Since metals introduce high optical losses, the device was designed such that the metal electrode, located within $\sim 1\mu m$ from the center of the resonator, had a minimum overlap with the optical mode. The fundamental mode of the resonator extends mainly in a direction that makes an angle of $\sim 30^o$ with the cavity axis (x) and has a small extent in the y direction[64]. To minimize the optical loss, the electrode was brought in the proximity of the resonator along the y direction and no significant degradation of the quality factor was observed. On the same chip, we measured electrically controlled resonators with quality factors as high as 17000, similar to cavities without the metal electrode. The cavity studied in this letter had a lower quality factor ($Q \sim 4000$) because it was integrated with a grating structure that allows efficient resonant in/out coupling from the resonator, as discussed in [2].

The measurements were done at cryogenic temperatures using a cross-polarized optical setup as shown in Fig.4.1(b). First, a photoluminescence (PL) measurement

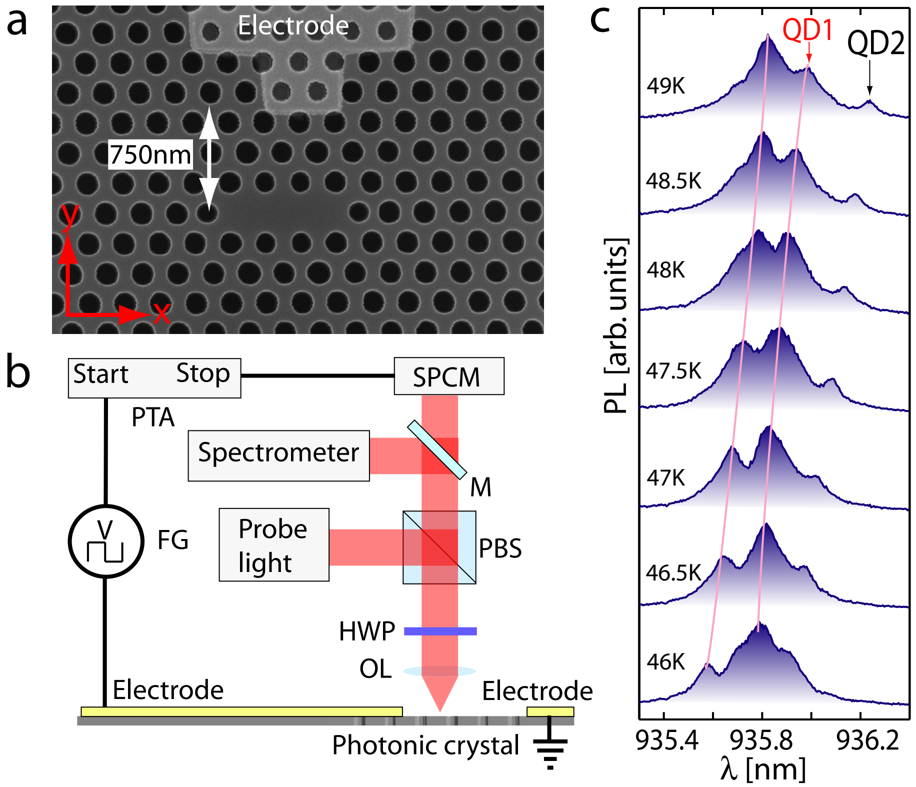

Figure 4.1: (a) Scanning electron microscope image of the photonic crystal cavity and the metallic electrode placed within $1\mu m$ from the center of the cavity. (b) Schematic representation of the experimental setup (not drawn to scale). A cross-polarized confocal microscope setup composed of a polarizing beam splitter(PBS), half wave plate (HWP) and objective lens (OL) was used for photoluminescence and reflectivity measurements. The voltage on the chip was controlled using a function generator (FG) and the output signal was detected using a single-photon counting module (SPCM). A flip mirror (M) switched the signal from spectrometer to SPCM. The time domain measurements were performed using a picosecond time analyzer(PTA).(c) Photoluminescence spectra taken for different cavity/QD detunings by increasing the temperature of the sample (indicated for each spectrum). The avoided crossing of the polaritons (marked by the red lines as a guide to the eye) indicates that QD1 is strongly coupled.

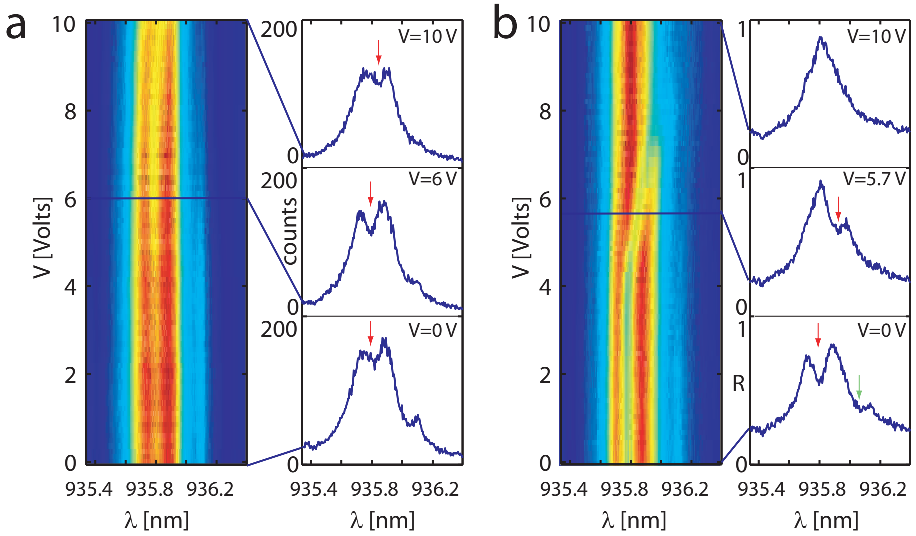

Figure 4.2: (a) Photoluminescence spectra as a function of increasing control voltage (V) from 0V to 10V. At 0V the quantum dot was tuned on resonance with the cavity (T=48K). The PL intensity decreases and the QD red shifts for $V > 8V$. The shift is much smaller than the one observed in broadband reflectivity because of the screening induced by free carriers. (b)Broadband reflectivity spectra while changing V from 0V to 10V (T=48K). The QD red shifts for $V > 4V$.

was performed to identify a strongly coupled QD. The signature of strong coupling is the vacuum Rabi splitting, observed (Fig.4.1(c)) as an avoided crossing of the eigenstates of the system when the quantum dot is tuned into resonance with the cavity [65]. From the PL spectra one could identify two quantum dots with frequencies close to the cavity resonance, labeled as QD1 and QD2 in (Fig.4.2(a)). Only QD1 showed the avoided crossing, thus indicating strong coupling. All the measurements reported here were done using QD1, but the signature of QD2 was still visible in some of the data sets. For clarity, QD1 was marked with a red arrow in some of the figures. The experimental data indicated a cavity quality factor $Q \sim 4000$, corresponding to a field decay rate $\kappa/2\pi \sim 40GHz$), and a quantum dot cavity coupling strength $g/2\pi \sim 20GHz$. Since $g \geq \kappa/2$ and $g >> \gamma$, (quantum dot spontaneous emission rate $\gamma/2\pi$ on the order of 0.1GHz), the system operated on the onset of the strong coupling regime.

The vacuum Rabi splitting was also observed in the transmission function of the resonator, as measured using a cross-polarized reflectivity measurement(Fig.4.2(b))[1]. Two types of resonant probing were used in this experiment. In one case, a continuous wave (CW) laser beam was scanned through the cavity resonance and the output was monitored with a photodetector. This measurement is referred as “CW reflectivity”. In the second case, a broadband light source was coupled into the resonator and the entire reflectivity spectrum was monitored on a spectrometer. This measurement is referred to as “broadband reflectivity”.

With the quantum dot and the cavity brought into resonance (temperature set to $T = 48K$), the effect of the electric field was first studied in PL by changing the bias voltage from 0V to 10V. As the bias approached $\sim 10V$, the total PL intensity decreased and the quantum dot showed a red shift of only $\sim 0.03nm$ ($0.04meV$) as shown in Fig.4.2(a). The shift in the QD resonance was due to the QCSE, and the reduction in the PL intensity was caused by the carriers being swept away before recombining in the QD. The Stark shift and the PL reduction were only observed when using low powers of the excitation laser (tuned at 875nm). By increasing the intensity of the laser, more carriers were excited in the cavity and thus screened the electric field.

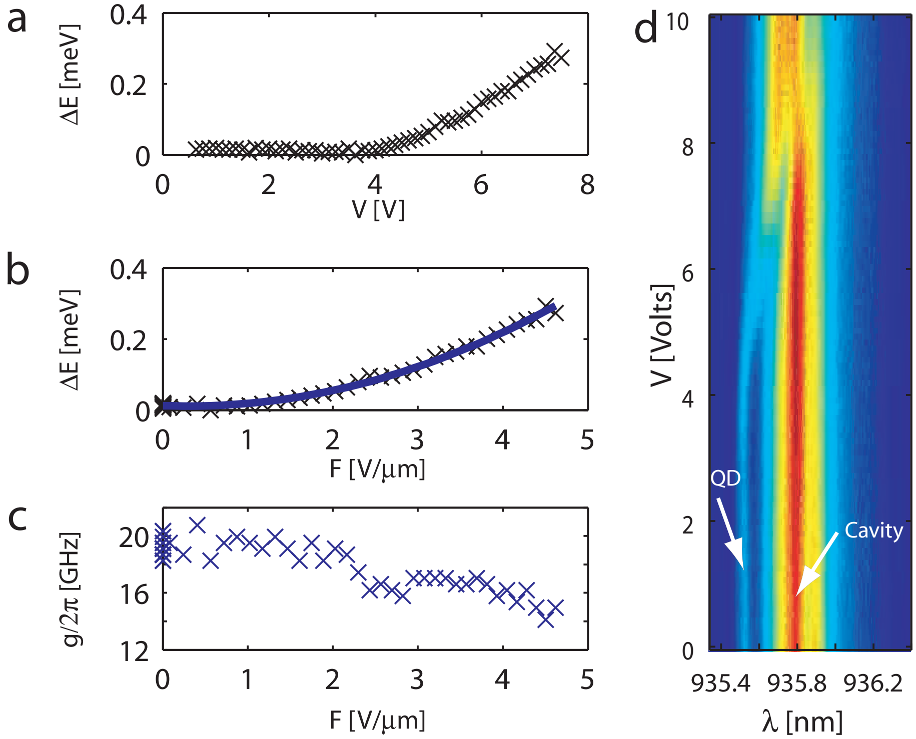

Figure 4.3: Change in QD frequency and coupling strength g with bias voltage (a) Stark shift of the quantum dot with applied bias. (b) Experimental data and fit indicating the quadratic dependence of the quantum dot shift with electric field. (c) Dependence of the cavity/QD coupling g with applied voltage, as inferred from the fit to experimental data (d) Broadband reflectivity taken at T=46K such that the QD was resonant with the cavity at high electric fields. As the voltage approaches 8V, the signature of the quantum dot in the spectrum vanished, most probably due to the loss in the quantum dot confinement due to high electric field. More information about the nature of this effect could be inferred by a QD spectroscopy method where the energy of all the QD orbitals are monitored while varying the field.

To test the effect of the electric field under resonant probing, the system was measured using broadband reflectivity. A superluminescent diode with broad emission around 935nm was used as the light source, thus minimizing free carrier generation because of it's low spectral power density. The broadband reflectivity spectra shown in Fig.4.2(b), indicate two local minima (marked by the red arrow for the strongly coupled dot and green arrow for the weakly coupled dot) thus confirming that two quantum dots were coupled to the cavity. The effect of the bias voltage on the QD wavelength was more pronounced than in the PL measurement. The Stark shift could be observed for bias voltages larger than $V \sim 4V$, and for voltages exceeding $V \sim 7V$ the quantum dot was completely detuned from the cavity. As seen from Fig.4.2(c), by applying the electric field the transmission at the cavity resonance is switched from a local minimum to a local maximum.

The dependence of the quantum dot Stark shift with the applied bias voltage is shown in Fig.4.3(a). The quantum dot frequency was determined by fitting the spectra in Fig.4.2(b), as described in ref.[1]. The Stark shift is only observed for voltages larger than $V \sim 4V$, which corresponds to the depletion layer extending to the location of the quantum dot. The magnitude of the electric field in the center of the cavity was inferred by modeling the Schottky contact. The size of the depletion layer ($x_d(V)$) and the electric field in the cavity ($F(V)$) are given by $x_d = \sqrt{2\epsilon_0\epsilon_{GaAs}(V-\phi)/(eN_d)}$ and $F = -eN_d(x_d - \Delta x)H(x_d - \Delta x)/(\epsilon_0\epsilon_{GaAs})$. Here, $\Delta x = 750nm$ is the distance between the electrode and the center of the cavity, $N_d = 9 \times 10^{15}/cm^3$ is the doping concentration, $\phi = 0.36V$ is the potential barrier of the Schottky contact, e is the electron charge, $\epsilon_{GaAs} = 12.9$ is the dielectric constant of GaAs at low temperatures, ϵ_0 is the electrical permittivity of vacuum, and $H(x)$ is the unit-step function. The effect of the surface states were not considered when estimating the electric field. The dependence of the energy shift with electric field is shown in Fig.4.3(b). The shift was quadratic in electric field, since the perturbation of the energy levels due to electric field is a second order effect. The data was fit using[63] $\Delta E = pF - \beta F^2$ with $\beta = -0.015meV\mu m^2/V^2 = -2.4 \times 10^{-36}J/(V/m)^2$ and $p = -0.009meV\mu m/V = -1.4 \times 10^{-30}Cm$. These values are within an order of magnitude but lower than previously measured by other research groups [63]. We believe that the lower value that we estimate is caused by the QD not being located exactly in the middle of the cavity, as we assumed.

The confining potential of the quantum dot could be perturbed by the influence of the electric field. For the data set shown in Fig.4.2(b) (taken at $T = 48K$) the QD became completely off resonant with the cavity for $V > 7V$ so the reflectivity spectrum at high electric field yielded little information about the quantum dot. For a better investigation of the QD behavior at large electric fields, another data set was taken at $T = 46K$ (Fig.4.3(d)) such that the QD was resonant with the cavity for $V > 7V$. Under bias voltage, the electron and hole wave functions were deformed and pulled in opposite directions thus reducing their overlap. One consequence is diminished QD oscillator strength. The overall result is in a reduction of the cavity/QD coupling g. The fits to the data showed that $g/2\pi$ decreased from $\sim 20GHz$ to $\sim 15GHz$ when a bias of $\sim 7V$ was applied. For $V > 8V$, the influence of the electric field was strong enough to completely erase the signature of the quantum dot from the broadband reflectivity spectrum. This could be either due to reduced g, or high tunneling rate of the electron-hole pairs out of the quantum dot placed in the electric field.

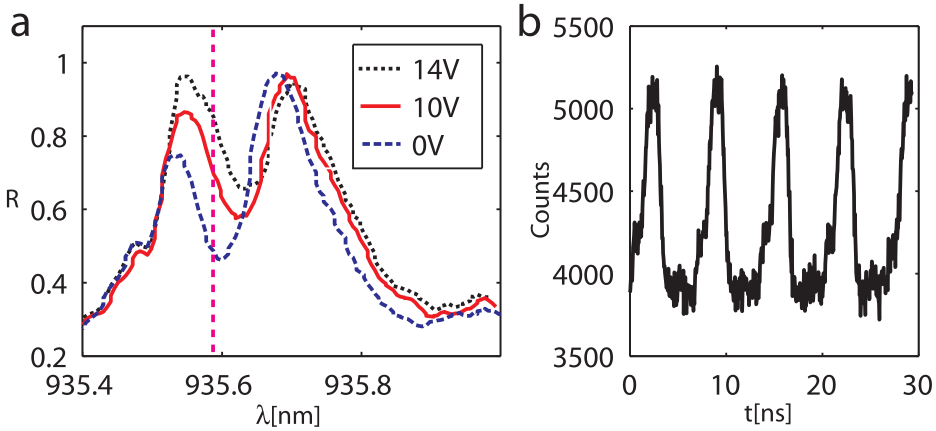

Figure 4.4: Fast electrical switching of a continuous wave laser beam (a) CW reflectivity for bias voltages of 0V, 10V and 14V. During the time-domain switching experiment the laser was set at the wavelength marked by the vertical dashed line and a 0-10V signal was applied. (b) Switching of the coupled laser at the electrical QD driving frequency of 150MHz.

The CW reflectivity spectra for different values of the bias voltage are shown in Fig.4.4(a). The Stark shift was still present but its magnitude was smaller compared to the broadband reflectivity measurement ($0.04meV$ for $V \sim 10V$), most probably due to an increased number of carriers that screen the electric field. We believe that, unlike the broadband source, the CW laser was more efficient in generating excitons in the quantum dot because of increased spectral power density and long coherence length. Due to the bias voltage, these electron-hole pairs could tunnel out of the quantum dot and become free carriers that screened the electric field [66]. Alternatively, since more than one quantum dot was present in the cavity, the screening could also be caused by excitons created in the neighboring off resonant quantum dots. It has already been shown that these excitons could be created through the off resonant energy transfer between the photonic crystal resonator and the coupled quantum dots[2, 32]. The screening of the electric field became more pronounced with increasing laser intensity, thus affecting the device performance. The effect of the QD on the transmission function of the resonator can be observed for coupled probe powers as high as tens on nW (as previously shown in[1]), but manipulation of the QD via QCSE at those probe power levels still needs to be demonstrated and may be limited by electric field screening. The CW reflectivity spectra in Fig.4.4(a) indicated that an on/off switching ratio of $\sim 1.5:1$ was achievable with this system when driven between 0V and 10V (on/off ratio of 2:1 achievable for 0V to 14V driving). Although on:off ratios of 100:1 are theoretically expected with this system, the experimentally observed on/off ratio was limited by the properties of the quantum dot, especially operation at the onset of the strong coupling regime, decoherence[2] and QD blinking[67].

The time domain measurement was performed by setting the probe laser at the QD frequency (marked by the vertical dashed line in Fig.4.4(a)) and by controlling the voltage using a function generator. The modulated output was monitored using a single photon counting module (SPCM) and a dual channel picosecond time analyzer(PTA) synchronized to the function generator. To minimize the amount of screening due to coherently excited carriers, the probe laser power was set to $\sim 10pW$. The switching behavior at 150MHz is shown in Fig.4.4(b), with an on/off ratio of

$\sim 1.3:1$. This is smaller than the expected $\sim 1.5:1$ because of the 3dB cutoff in the transmission line at 100MHz. An on/off ratio of 1.45:1 was observed when driving the system at 80MHz, close to the value expected from the DC measurement.

The performance of the proof of concept device reported in this section is limited by the experimental setup and the non-ideality of the strongly coupled system. All-optical measurements on similar devices showed that speeds up to 10GHz could be achieved with this type of system[2]. This was also predicted with theoretical analysis presented in chapter 2. With improved engineering, similar speeds should be achievable in electrical operation. Theoretically, when operating with $g, \kappa >> \gamma$ (i.e. strong coupling regime or high Purcell factor regime) as is the case for quantum dots in photonic crystals, the maximum bandwidth is limited to $min(g/\pi, \kappa/\pi)$ in the strong coupling regime and $g^2/(\pi\kappa)$ in the weak coupling regime. Regarding the energy required to shift the QD, it is fundamentally limited by the energy density of the electric field required to shift the quantum dot inside the active volume. Considering an active volume the size of the resonator ($V_a \sim 1\mu m \times 1\mu m \times 200nm$), and an electric field $F \sim 5 \times 10^4 V/cm$, this translates into a switching energy of $\sim 1fJ$, much lower than state of the art devices[68, 69, 70, 71]. Confining the electric field over such a small volume is not trivial, but suitable technological solutions may be found in the future. This type of device can be integrated in a on-chip optical or quantum network [72] and will be an essential building block for future optoelectronic devices for classical and quantum information processing devices operating at ultra-low energies, where fine and fast tuning of the quantum dot resonance is required.

4.1.1 Switching power

For most of the modern optoelectronic devices, the energy required per switching operation is one of the most important figures of merit [14]. For the type of devices presented here the fundamental limit for the control energy per switching operation is given by the energy density of the electric field required to detune the QD inside the active volume. To estimate the control energy we use the experimental parameters as presented in [37]. When the electrode is placed laterally at a distance of $1\mu m$, the active region of the cavity/QD system has a volume of $V \sim 1\mu m \times 1\mu m \times 200nm$. Since the electric field to tune the quantum dot is on the order of $F \sim 5 \times 10^4$ V/cm, the energy per switching operation is on the order of $E = \epsilon_0 \epsilon_r F^2 V/2 \sim 0.5$ fJ ($\epsilon_r \sim 13$). This translates into an operating power of $\sim 5\mu$ W at 10 GHz. The same order of magnitude estimation is obtained by modeling the device as a parallel plate capacitor with width $w \sim 1\mu m$, thickness $t \sim 200nm$ and spacing $L \sim 1\mu m$ and taking into account fringing effects. Since the energy consumption has a quadratic dependence on the applied voltage, the operating power can be lowered significantly by bringing the electrode closer to the quantum dot. In case the active volume could be reduced to the size of the quantum dot itself ($\sim 25 \times 25 \times 25$ nm^3), the switching energy can be lowered below 0.1 aJ. These energy scales are of the same order of magnitude as all other optical switching devices operating at single photon level [1, 53], and are orders of magnitude lower than the current state of the art electro-optic modulators [69, 68]. However, this electro-optic modulator cannot be used to modulate high power optical signal, as high optical power will saturate the QD.

4.2 Vertical electrical control

In the previous experiment, the electric field was applied in the lateral direction (in plane) of the QD. However, the QD is larger (less confined) in this direction whereas it is more confined in the vertical direction, along the growth axis. Therefore to efficiently control and to potentially charge the QD on demand, the QD should be embedded in a p-i-n diode. To achieve this, we grow a p-i-n junction embedded in a photonic crystal slab, where QDs are located in the i-region at the center of the slab. The description of the p-i-n membrane with doping is shown in the Figure 4.5. Such a structure is also useful for QD charging with a single electron, which is needed in order to build a 3-level lambda system necessary to implement a spin-photon interface [13].

The fabrication procedure essentially remains the same as previously, except now p and n contacts have to be deposited (Fig. 4.6a) after photonic crystal fabrication to allow application of voltage across the p-i-n diode. Fig. 4.6b shows the vertical

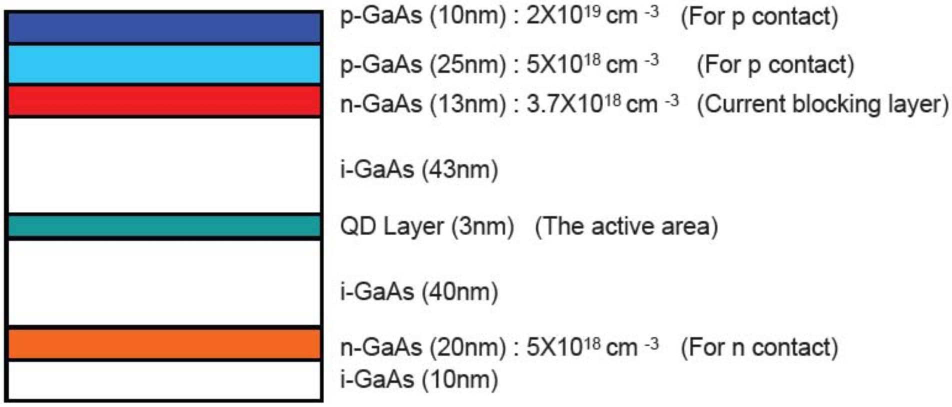
p-GaAs (10nm) : 2X10^{19} cm^{-3} (For p contact)
p-GaAs (25nm) : 5X10^{18} cm^{-3} (For p contact)
n-GaAs (13nm) : 3.7X10^{18} cm^{-3} (Current blocking layer)
i-GaAs (43nm)
QD Layer (3nm) (The active area)
i-GaAs (40nm)
n-GaAs (20nm) : 5X10^{18} cm^{-3} (For n contact)
i-GaAs (10nm)

Figure 4.5: The details of the p-n-i-n wafer with doping densities.

Stark shift of the QD transition, when a forward bias is applied to the p-i-n diode. The QD senses an electric field even in the absence of any applied voltage due to the built-in potential of the p-i-n diode. Under forward bias, the electric field across the QD decreases, and we observe a blue-shift. At a high forward voltage, the flat-band condition is achieved, and we do not see any more changes in the QD resonance. We also observe discrete jumps of the QD resonances (shown by a dashed arrow in Fig. 4.6c), which are due to the charging of the QD with additional carriers [6].

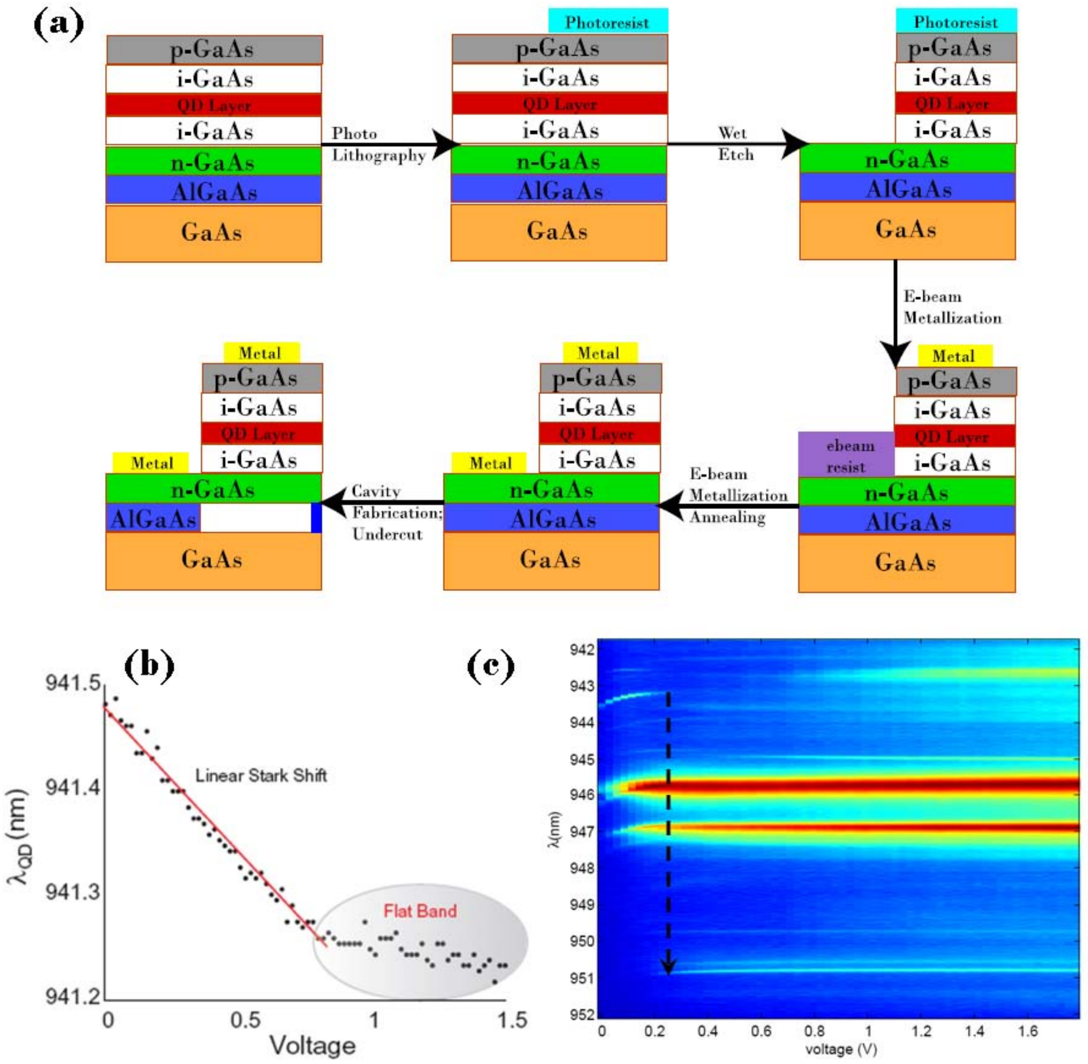
(a)
p-GaAs
i-GaAs
QD Layer
i-GaAs
n-GaAs
AlGaAs
GaAs
Photo Lithography
Photoresist
Wet Etch
E-beam Metallization
Metal
ebeam resist
E-beam Metallization Annealing
Cavity Fabrication; Undercut
(b)
941.5
941.4
941.3
941.2
λ_{QD} (nm)
Linear Stark Shift
Flat Band
0
0.5
1
1.5
Voltage
(c)
942
943
944
945
946
947
948
949
950
951
952
λ(nm)
0
0.2
0.4
0.6
0.8
1
1.2
1.4
1.6
voltage (V)

Figure 4.6: Vertical electric field applied to a quantum dot in p-i-n diode: (a) Fabrication steps for contacts and photonic crystal devices enabling electrical control in a p-i-n junction. Here, p-GaAs, n-GaAs and i-GaAs indicate p-doped, n-doped and intrinsic gallium arsenide, respectively. (b) QD resonance as a function of the applied potential in p-i-n diode. (c) Photoluminescence spectra as a function of the applied potential. A discrete jump of the QD resonance is observed, which indicates a discrete charging event of the QD.

Chapter 5

Photon blockade and photon assisted tunneling

In this chapter, we introduce the effects of the photon induced tunneling and blockade, and explore the possibility of employing them for non-classical light generation and probing of higher order dressed states in the solid state CQED system consisting of a single QD coupled to a photonic crystal cavity. We start by giving an introduction into these effects, and then we provide numerical simulation data showing that the single photon generation in the photon blockade regime can be improved by choosing a proper pulse shape. More specifically, we show that the single photon probability in the cavity transmitted light oscillates as the excitation pulse amplitude is changed. Then, we show that photon induced tunneling can be used to preferentially generate specific multi-photon states. Following this, we present experimental data demonstrating the transition from blockade to tunneling regime in such a system and show the signature of higher order dressed states observed in the measured photon statistics. Finally, we present theoretical results demonstrating that a QD coupled to a bimodal cavity can be used to generate strong sub-Poissonian light even in the presence of large cavity loss.

5.1 Photon blockade

Single photons at optical frequencies are commonly used in quantum key distribution systems[73], and play a fundamental role in proposed devices for quantum information processing [23, 74]. While the majority of quantum cryptography systems currently in use are based on coherent light sources, most of the proposals for more advanced quantum information devices are based on non-classical states of light, mainly single photon states. One way to generate single photons is by parametric down conversion or attenuation of coherent laser beams such that the probability of having multi-photon states is considerably diminished. However, this causes increased probability of the vacuum state, so most of the time there are no photons in the light source. To make a good single photon source one has to ensure suppression of both the multi-photon states as well as the zero-photon state. There are several proposals for making on demand single photon sources, like above-band or resonant excitation of solid state single emitters [75] or adiabatic state transfer in single atoms [76].

Non-classical states of light that closely resemble the single photon states can be generated in the photon blockade regime[77] with a single emitter strongly coupled to an optical resonator. The experiments on atomic system [78] as well as in semiconductor CQED [67] demonstrated photon anti-bunching caused by photon blockade, a signature of enhanced probability of the single photon states at the output. There are a few advantages for using photon blockade for single photon generation. First, the produced single photons are free of jitter, as the quantum emitter is resonantly excited [79]. Second, the collection efficiency of the photons is very high due to the presence of a cavity. However, for on demand single photon generation, the source must be operated in pulsed regime and only one photon should be generated for each pulse. The latter requirement was not satisfied in any experiments performed so far on photon blockade.

5.1.1 Photon blockade in pulsed operation of the driving field

As explained before, the studied optical system consists of a single emitter (QD) strongly coupled to a cavity (coherently driven by a laser), as shown in Fig.5.1. The

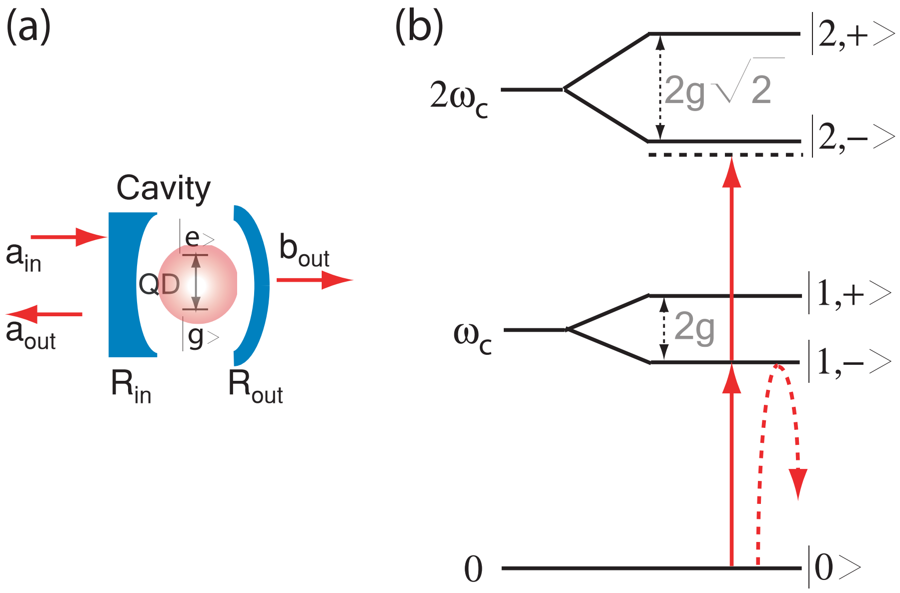
(a)
Cavity
a_{in}
a_{out}
b_{out}
|e>
QD
|g>
R_{in}
R_{out}
(b)
$2\omega_c$
ω_c
0
|2,+>
|2,−>
$2g\sqrt{2}$
|1,+>
|1,−>
2g
|0>

Figure 5.1: (a) Schematic representation of a single emitter coupled to an optical resonator. The optical resonator has mirrors with different reflection coefficients ($R_{in} >> R_{out}$) such that most of the field coupled into the cavity is emitted at the output port. (b) Schematic representation of the energy eigenstates for a strongly coupled cavity-emitter system.

anharmonic ladder structure of this coupled system (see chapter 2) gives rise to the effect of photon blockade, where the presence of one photon in the cavity blocks the coupling of subsequent photons. For example, the system could be driven by a coherent light source (see Fig.5.1) with frequency resonant with one of the polaritons (say $|1,-\rangle$). Once a photon is coupled, the system is excited into the state $|1,-\rangle$, so the coupling of another photon with energy $\omega_c - g$ would require the system to transition to energy state $2(\omega_c - g)$. However, the system does not have an eigenstate at this energy, the closest being at $2\omega_c - g\sqrt{2}$. For this reason, the probability of coupling the second photon is reduced. This effect is refereed to as the photon blockade - as the presence of one photon in the system prevents coupling of another photon, similar to Coulomb blockade.

A typical experimental configuration for observing photon blockade is depicted in Fig.5.1(a) where light can be coupled into the cavity containing a strongly coupled quantum emitter via the input port a_{in} and the output can be collected at the port b_{out}. The resonator is represented by two mirrors with reflection coefficients R_{in} and R_{out}.

For on demand generation of non-classical states of light, it is desirable that the state is delivered at the output port at times that can be chosen deterministically. This means that the interaction between the input beam and the cavity/QD system is controlled in time domain. One way to achieve this is by driving the system with light pulses with controlled shape, as illustrated schematically in Fig.5.2(a). In this section, we investigate how the non-classical state of light observed at the output depends on the properties of the laser pulse at the input.

To simulate the system we use quantum trajectory method [47], as explained in the chapter 2. The dephasing rate of the QD and any non-radiative decay is neglected. As the non-classical state is collected from one of the output modes of the cavity (b_{out}), only the collapse operator corresponding to the cavity decay is monitored.

The driving term $\Omega(t)$ in the Hamiltonian (see chapter 2) is assumed to be of the form $\Omega(t) = \Omega_o p(t)$, where Ω_o is the amplitude and the time dependence is described by $p(t)$. For the simulation we assume a Gaussian shape for $p(t)$:

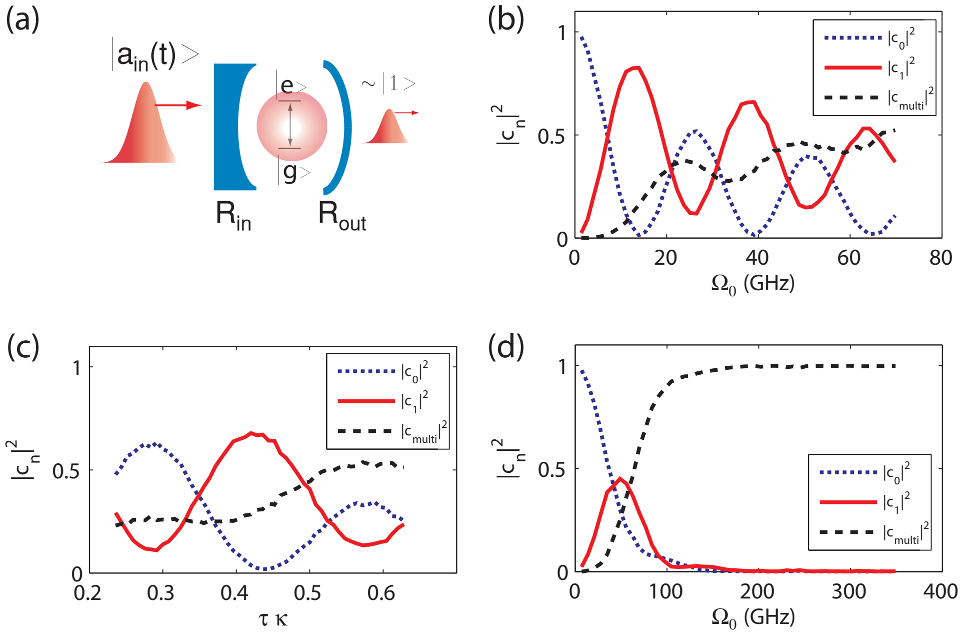

Figure 5.2: (a) Non-classical state generation via pulsed-operation in photon blockade. The properties of the laser pulse coupled at the input port are controlled such that the output field has primarily a single-photon component. (b) Normalized Fock-state coefficients ($|c_0|^2$ for vacuum state, $|c_1|^2$ for single photon state, and $|c_{multi}|^2 = \sum_{n=2}^{\infty} |c_n|^2$ for multi photon probability) for the output field as the intensity of the laser pulse Ω_0 is modified and the pulsewidth is kept constant at $\tau = 0.45/\kappa$. The ground state and one of the first order eigenstates form an effective two level system so Rabi oscillations are observed in the single photon character of the output field. The system has parameters $\kappa/2\pi = 1GHz$, $\gamma/2\pi = 0.1GHz$, $g/2\pi = 40GHz$. (c) Fock-state coefficients for the output field as the duration of the laser pulse (τ) is modified while $\Omega_0 = 10GHz$ was kept constant. The system has parameters $\kappa/2\pi = 1GHz$, $\gamma/2\pi = 0.1GHz$, $g/2\pi = 40GHz$. (d) The same simulation as in the panel **b** for a system with $\kappa/2\pi = 5GHz$, $g/2\pi = 30GHz$

$$p(t) = exp\left(-\left(\frac{t-t_0}{\tau}\right)^2\right), \tag{5.1}$$

where t_0 is the time when the pulse reaches its maximum value and τ is the pulse-width. In principle, the input laser pulse can have any specific waveform. To limit the number of free parameters, we analyze the configuration where the system is driven with Gaussian pulses. In this case, the free parameters are the length, intensity and the center frequency of the pulse.

The non-classical state of light emitted at the output is analyzed using an ideal single photon detector. Exact modeling of the non-ideality of the detectors requires stochastic master equation, where the whole density matrix needs to be monitored. This is because although one can ensure that the initial state is a pure state, the non-ideality of the detector makes the state mixed. However, the error generated by the assumption of ideal detector is not significant, and stochastic wave function can also be used to model non-ideal detectors. For each quantum trajectory, a laser pulse is coupled to the cavity and the number of clicks detected at the output is monitored. Ideally, for a deterministic single photon source, a single click should be registered by the detector every time the device is operated. However, the output field is not in a pure single photon state, and in a Fock state basis, it can be expressed as:

$$|b_{out}\rangle = \sum_{n=0}^{\infty} \varphi_n |n\rangle \tag{5.2}$$

where the φ_n is the coefficient of the Fock state $|n\rangle$. Here we write the output state as a pure state considering that the dephasing rate of the system is negligible. The normalized value ($|c_n|^2$) of the coefficients $|\varphi_n|^2$ can be estimated from the number of detected photons at the output when running a large number of trajectories. For example, $|c_n|^2 = \frac{|\varphi_n|^2}{\sum_i |\varphi_i|^2}$ is well estimated by the relative number of trajectories for which n counts were detected at the output. If the desired output state should be as close as possible to a single photon state, then the simulation parameters should be optimized such that $|c_1|^2$ is maximized.

The experimental configuration considered here is as shown in Figure 5.2(a). The cavity has two mirrors, with decay rates κ_1 and κ_2 such that $\kappa_1 << \kappa_2$. Effectively, the total decay rate of the cavity is $\kappa \approx \kappa_1$. The driving laser is incident on the mirror with higher reflectivity and the output field is mainly collected from the lossier mirror. This configuration allows for efficient collection of the non-classical field at the cavity output.

To illustrate the behavior of the system operating in photon blockade under pulsed driving, we first analyze a system with parameters $\kappa/2\pi = 1GHz$, $\gamma/2\pi = 0.1GHz$, $g/2\pi = 40GHz$. The value $\kappa/2\pi = 1GHz$ corresponds to a cavity with a quality factor of $Q = 160000$. This is about 5 times larger than the state of the art values of Q observed in GaAs cavities with coupled InAs quantum dots operating around 930 nm, but still within the theoretical limit for this material [80]. Regarding the coupling rate g, the typical values measured so far are around $g/2\pi = 25GHz$[2]. However, with further improvements in the material system and the fabrication techniques it is expected that higher values for Q and g, as considered here, will be achievable. For this simulation, the cavity and the quantum dot are assumed to be on resonance ($\omega_c = \omega_a$). The center frequency of the driving field is set on resonance with the transition to the first order manifold ($\omega_c + g$) and the pulse width is set to $\tau = 0.45/\kappa$. Figure 5.2(b) shows the zero-photon, single photon as well as multi-photon population ($|c_{multi}|^2 = \sum_{n=2}^{\infty} |c_n|^2$) as a function of the amplitude of a driving pulse. The values for the coefficients $|c_n|^2$ are inferred from the number of detection events detected over multiple (3000) quantum trajectories.

As shown in Fig.5.2(b), the probability of obtaining a single photon at the output has a strong oscillatory dependence on the intensity on the incoming pulse. When operating in blockade regime, the successful blocking of the second photon depends on how well the first photon is coupled to the QD-cavity system. One could consider the ground state and the state $|1, -\rangle$ to constitute an effective two-level system. Under pulsed excitation, the population in $|1, -\rangle$ Rabi oscillates with the pulse area (Fig. 5.1(b)). For optimum operation, one would choose the pulse area such that the system transitions completely from $|0\rangle$ to $|1, -\rangle$ so one photon is coupled into the system and then is released at the output port. At the operation point with maximum single photon state probability, the output field has $\sim 83\%$ single photon, $\sim 1\%$ vacuum state and $\sim 15\%$ multi-photon state character (i.e. $|c_0|^2 = 0.01$,

$|c_1|^2 = 0.83$, $|c_{multi}|^2 = \sum_{n=2}^{\infty} |c_n|^2 = 0.16$).

The oscillations of the single photon population in the output field can also be observed when the maximum field intensity is kept constant and the pulse length is changed. This is shown in Fig.5.2(c), where the pulse intensity was chosen as the intensity that gave the maximum single photon output in Fig.5.2(c) ($\Omega_0 = 10GHz$).

A similar but less prominent effect can be observed in a system with $\kappa/2\pi = 5GHz$, $g/2\pi = 30GHz$, parameters that are very close to those already achieved experimentally [2, 80]. For this set of parameters the maximum achievable single photon probability is $\sim 45\%$, with $\sim 30\%$ vacuum state and $\sim 25\%$ multi photon state, as shown in Fig.5.2(d).

One of the parameters most commonly used to characterize single photon source, is the second order correlation function $g^{(2)}(0)$. For single photon sources it is desired that $g^{(2)}(0) = 0$, which means that the source emits either zero or one photon but never multiple photons. However, the second order correlation does not give any information about the efficiency of emitting a single photon each time the source is operated. Starting from the coefficients $|c_n|^2$, one may compute $g^{(2)}(0) = (\sum_{n=1}^{\infty}(n-1)(n-2)|c_n|^2)/(\sum_{n=1}^{\infty}(n-1)|c_n|^2)^2$, and the results are shown in Fig.5.3(a,b). For the case $\kappa/2\pi = 1GHz$, $g/2\pi = 40GHz$, $g^{(2)}(0)$ can be as small as 0.12, while for $\kappa/2\pi = 5GHz$, $g/2\pi = 30GHz$ the minimum value is $g^{(2)}(0) = 0.64$.

These sources of non-classical light could improve the speed of generating secure quantum keys, compared to current systems that use coherent laser sources. Compared to coherent laser pulses of the same brightness, the ratio of single photon pulses to multi-photon pulses could be up to ten times higher in the case of non-classical light sources operating in photon blockade as shown in Fig.5.4.

5.1.2 Non-classical state generation via fast control of dipole frequency

Here we present an alternative method for on demand generation of non-classical light that is based on ultra-fast control of the QD dipole. The principle is depicted in Fig.5.5(a), where a continuous wave field is incident on the input port and the

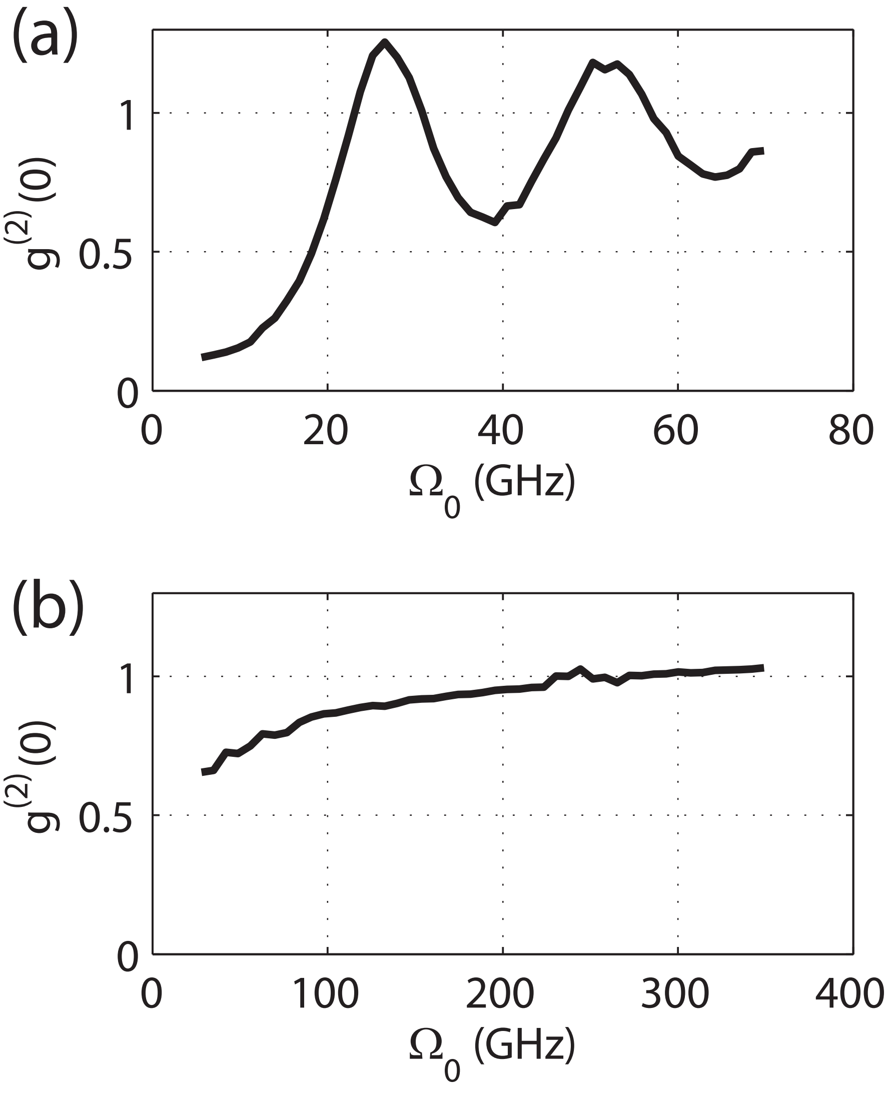

Figure 5.3: (a) Second order correlation correlation function of the output field, for the case $\kappa/2\pi = 1GHz$, $g/2\pi = 40GHz$. (b) Second order correlation correlation function for $\kappa/2\pi = 5GHz$, $g/2\pi = 30GHz$.

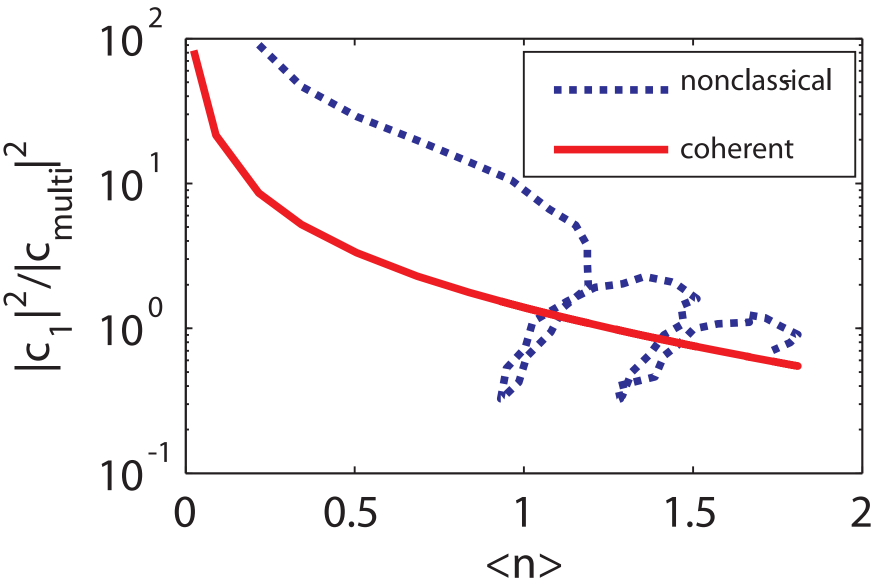

Figure 5.4: Ratio of single photon to multi-photon probability in the output field of the non-classical source with $\kappa/2\pi = 1GHz$ $g/2\pi = 40GHz$ as a function of mean photon number per pulse. The results are compared with a coherent pulsed laser source of the same brightness.

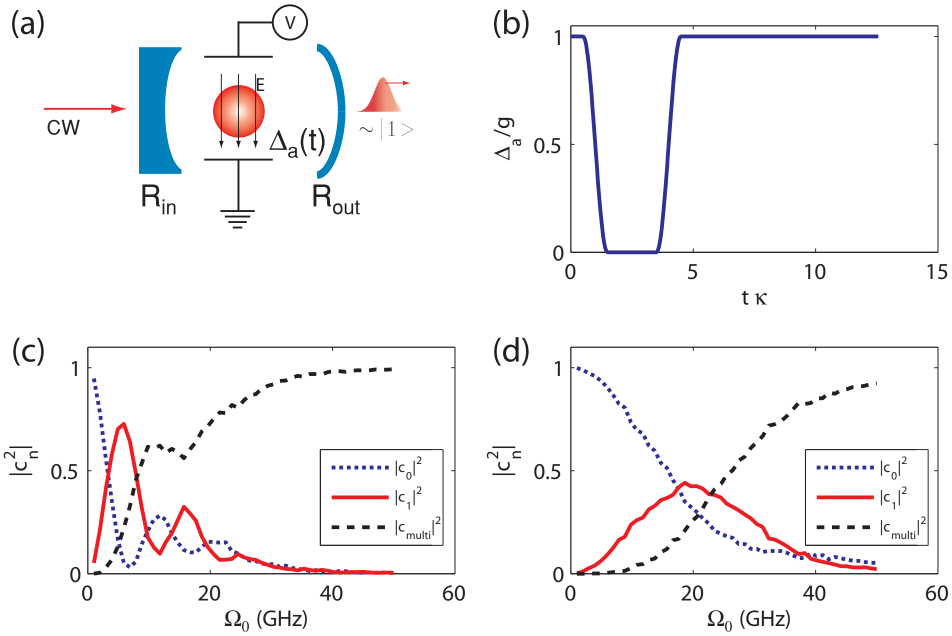

Figure 5.5: (a) Operation principle for non-classical state generation using a continuous wave input and fast control of the dipole frequency using an electric field. (b) Detuning of the dipole frequency with time. The cavity resonance is constant and zero detuning means dipole resonant with the cavity. (c) Normalized Fock-state coefficients ($|c_0|^2$ for vacuum state, $|c_1|^2$ for single photon state, and $|c_{multi}|^2 = \sum_{n=2}^{\infty} |c_n|^2$ for multi photon probability) for the output field with varying intensity of the continuous wave input field (Ω_0). The system has parameters $\kappa/2\pi = 1GHz$, $\gamma/2\pi = 0.1GHz$, $g/2\pi = 40GHz$. (d) Normalized Fock-state coefficients for a system with $\kappa/2\pi = 5GHz$, $\gamma/2\pi = 0.1GHz$, $g/2\pi = 30GHz$

frequency of the dipole (Δ_a) is controlled at time-scales comparable to the cavity decay rate. One method to achieve this kind of ultra-fast control in solid-state systems is by using an electric-field to shift the frequency of a quantum dot via quantum confined Stark effect, as we described in the previous chapter [37, 81].

In this configuration, the cavity frequency is kept constant and the electric field controls the cavity - quantum dot detuning. With the quantum dot and the cavity on resonance, the input laser is tuned to the frequency of one of the first order eigenstates (say $|1,-\rangle$). Shifting the resonance of the quantum dot causes an energy shift of both first order eigenstates. To generate single photon states, one should start with the quantum dot detuned from the cavity such that no light is transmitted to the output. Then the quantum dot is brought into resonance with the cavity such that $|1,-\rangle$ becomes resonant with the input laser beam. The QD is kept resonant with the cavity so only one photon is coupled and transmitted through the system, and then it is detuned back as shown in Fig.5.5(b). In this case, the coherent driving term in the Hamiltonian Ω_0 (dependent on the driving laser power), and cavity-laser detuning Δ_c is kept constant, but the dot-laser detuning $\Delta_a(t)$ is time dependent, and is the fixed detuning between the cavity and the driving laser.

The quantum statistics of the output field as a function of Ω_0 is shown in Fig. 5.5(c-d) for different parameters of the strongly coupled system. The quantum dot frequency is detuned by up to g, as shown in in Fig. 5.5(b). Similar to the optical time domain pulse shaping, oscillations are observed in the magnitude of the single photon state for $\kappa/2\pi = 1GHz$, $g/2\pi = 40GHz$ (Fig.5.5(c)). For optimal operation parameters, $|c_0|^2 = 0.05$, $|c_1|^2 = 0.73$, $\sum_{n=2}^{\infty} |c_n|^2 = 0.22$. The results for $\kappa/2\pi = 5GHz$, $g/2\pi = 30GHz$ are shown in Fig. 5.5(d), and indicate an 44% single photon, 35% vacuum state, and 21% multi photon Fock states at the point of maximum single photon state probability.

5.2 Multi-Fock state generation

In this section we investigate the photon induced tunneling phenomena in a the same strongly coupled dot-cavity system. We theoretically analyze how this tunneling

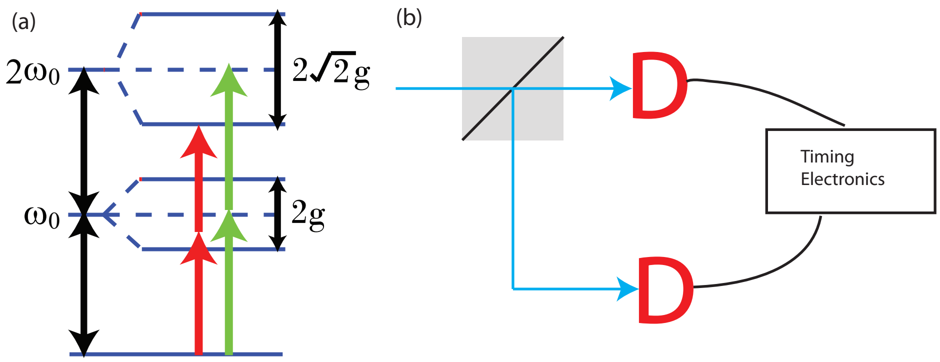

Figure 5.6: (a) The anharmonic ladder structure: when the laser is detuned from the polariton, then the coupling of the first photon is difficult, but two photons together can reach the second order manifold, and the output light will have more two photon character.

can be used to generate photon states consisting mainly of a particular Fock state (in contrast to single photon state as explained in last section). Additionally, we study experimentally the second order auto-correlation $g^{(2)}(0)$ in the photon-induced tunneling regime as a function of the frequency and the power of the probe laser and observe signs of higher manifolds of the Jaynes-Cummings Hamiltonian in the frequency-dependent photon-statistics of the transmitted light, as well as the strong power dependence of $g^{(2)}(0)$, distinguishing this effect clearly from bunching occurring in a thermal light source.

As explained in last section, the anharmonic ladder structure gives rise to phenomenon of the photon blockade, when the laser is tuned to the polariton frequency. A very different regime is achieved when the laser is detuned from the polariton (see Fig. 5.6 a). As shown in the Fig. 5.6 a, due to slight detuning between the laser and the polariton, the coupling of the initial photon is difficult, but two photons simultaneously can reach the second order manifold, and thus the transmitted light will have more two photon character. This is called photon-induced tunneling. In contrast to blockade, in the tunneling regime, the coupling of initial photons into the system is inhibited by the absence of the dressed states at this frequency. However, once the initial photon is coupled, the probability of coupling subsequent photons is increased as higher order manifolds in the ladder of dressed states are reached via multiphoton processes. In our system, as a result of broadening of the dressed states, at the empty cavity resonance one can excite multiple higher order manifolds. Hence, the light transmitted through a cavity in the photon-induced tunneling regime is a superposition of Fock states with small photon numbers and a strong presence of the vacuum state. As a result, the photon statistics of this light is super-Poissonian [3].

As explained in the last section, signatures of the photon blockade and photon-induced tunneling tunneling can be detected through photon-statistics measurements, such as the second-order coherence function at time delay zero $g^{(2)}(0) = \frac{\langle a^\dagger a^\dagger a a\rangle}{\langle a^\dagger a\rangle^2}$. Another important statistical quantity is n^{th} order differential correlation function $C^{(n)}(0) = \langle a^{\dagger n} a^n\rangle - \langle a^\dagger a\rangle^n$, which provides a clearer measure of the probability to create n photons at once in the cavity [82]. Second order differential correlation function can also be expressed as $C^{(2)}(0) = [g^{(2)}(0) - 1]n_c^2$, where $n_c = \langle a^\dagger a\rangle$ is the average intra-cavity photon number. Particularly for a weakly driven system ($n_c \ll 1$), $C^{(2)}(0)$ becomes positive only when the probability of two-photon state becomes significant compared to that of a single-photon state, while a peak in $C^{(2)}(0)$ indicates maximum probability of a two-photon state inside the cavity.

We note that $g^{(2)}(0)$ is measured in the experiment by means of Hanbury Brown Twiss (HBT) setup as shown in the Fig. 5.6b. In the HBT setup the light is split into paths via a beam-splitter and sent to two detectors. The clicks in the detectors are monitored via a timing electronics. If the incoming light is single photon, then when the light is split into two paths, the single photon can go in one of the two paths, but not in both paths. Hence no coincidence can be observed between the two detectors. Such a coincidence measurement is in effect similar to the second order auto-correlation $g^{(2)}(0)$ measurement.

5.2.1 Numerical simulation

Although the photon blockade and tunneling phenomena can be observed under continuous wave (CW) excitation in a numerical simulation, for practical consideration it is important to analyze the response of the cavity-QD system to a pulsed driving field. In particular, the ability to measure the photon statistics of the system's output during the actual experiment is determined by the time resolution capabilities of the single photon counters in the HBT setup, which in practice do not allow for $g^{(2)}$ measurement of a CW-driven cavity-QD system. A common way to overcome this limitation is to drive the strongly coupled cavity-QD system with a train of weak, coherent pulses of sufficiently narrow bandwidth [67]. We use quantum trajectory method [47, 83] to analyze the pulsed driving of the coupled QD-cavity system and find the resulting photon statistics [38]. As the non-classical state is collected from the cavity, only the collapse operator corresponding to the cavity decay (a) is monitored. A histogram is calculated based on the photon counts in the cavity decay channel, and probability $P(n)$ for having exactly n photons in the system is found. The driving term $\mathcal{E}(t)$ in the Hamiltonian is assumed to be of the form $\mathcal{E}(t) = \mathcal{E}_o exp(-\frac{t^2}{2\tau_p^2})$, where $\mathcal{E}_o$ is the peak amplitude of the pulse. We set $\tau_p = 24.4$ ps (i.e., full width at half maximum - FWHM of 34 ps), which satisfies the narrow-band condition and corresponds to our experimental parameters.

Figure 5.7 shows the behavior of the system with better than current state of the art [84] but achievable experimental parameters (assuming QD dipole moment of 30 Debye embedded in a linear three holes defect cavity with mode volume $\sim 0.7(\lambda/n)^3$) resulting in $g = 2\pi \times 40$GHz and $\kappa = 2\pi \times 4$ GHz . The results in Fig. 5.7a show that such a cavity-QD system can be employed to deterministically and preferentially generate a non-classical state with a high fraction of a particular Fock state inside the cavity (no pure QD dephasing is included in the simulation). The detuning values ($1.1g$, $0.9g$ and $0.7g$) are different from what one intuitively expects from a lossless strongly coupled QD-cavity system under CW driving (g, $g/\sqrt{2}$ and $g/\sqrt{3}$, corresponding to the excitation of first, second and third order manifold, respectively) because of both the losses and the pulsed driving of the system [67]. We note that, in presence of pure QD dephasing, $P(n)$ for n photon states decreases. We also note that even for a coherent state $|\alpha\rangle = \sum_n \frac{\alpha^n}{\sqrt{n!}}|n\rangle$, it is possible to have a particular Fock state $|m\rangle$ to be the state with the highest probability $P(m)$ of occurrence by choosing α such that $m + 1 > \alpha^2 > m$. However, for a coherent state the ratio $r_m = \frac{P(m)^2}{P(m-1)P(m+1)} = 1 + 1/m$ does not depend on α, and that cannot be increased by

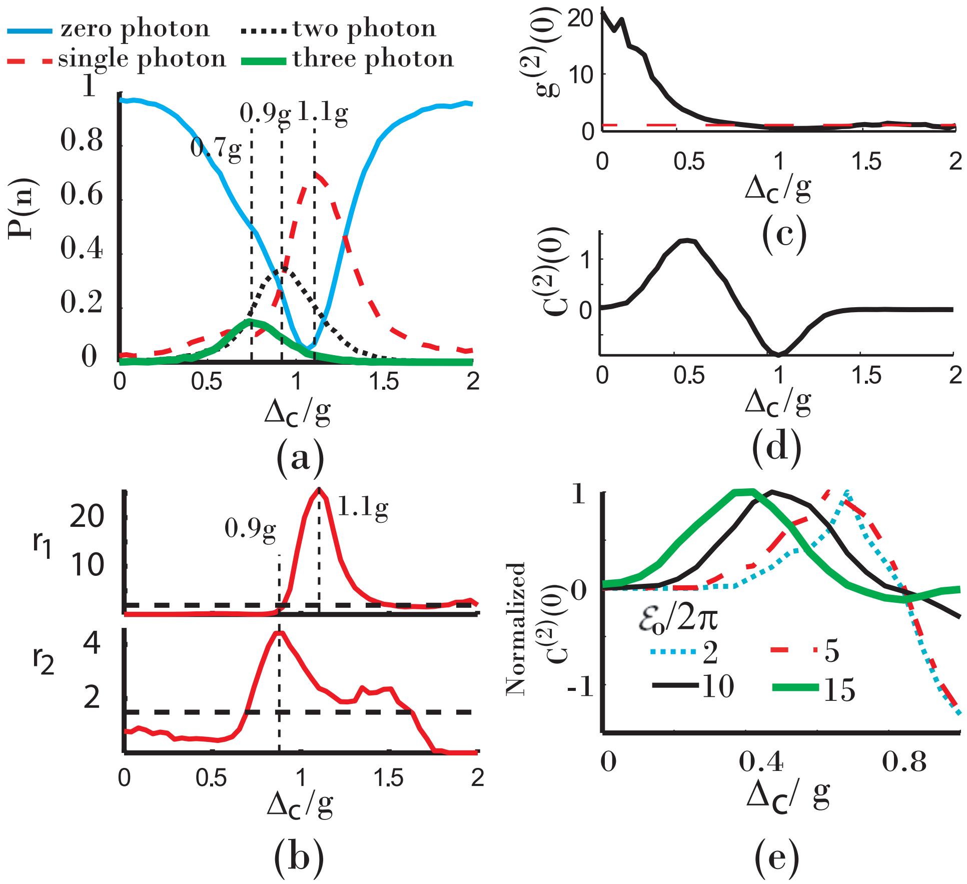

Figure 5.7: Numerically calculated photon statistics at the output of the QD-cavity system driven by Gaussian pulses with duration $\tau_p \sim 24$ ps. The simulation parameters are $g = 2\pi \times 40$ GHz, $\kappa = 2\pi \times 4$ GHz, and $\mathcal{E}_o = 2\pi \times 9$GHz; pure QD dephasing is neglected. (a) $P(n)$, probability of generating an n photon state at the CQED system output as a function of laser-cavity detuning Δ_c. (b) The ratios r_1 and r_2 as a function of Δ_c. $r_m = \frac{P(m)^2}{P(m-1)P(m+1)}$, where $P(m)$ is the probability of having m photons in the light. The dotted lines show the expected values of the ratios from a classical coherent state. (c) Second order auto-correlation $g^{(2)}(0)$ as a function of Δ_c. The red dashed line shows the expected $g^{(2)}(0)$ for a coherent state. (d) Second order differential correlation $C^{(2)}(0)$ as a function of Δ_c. (e) $C^{(2)}(0)$ as a function of the laser-cavity detuning Δ_c for different values of the peak laser field $\mathcal{E}_o/2\pi$ (in units of GHz). Every plot is normalized by the maximum $C^{(2)}(0)$, so that the peak value becomes 1 for all the plots. We observe that the peak in the $C^{(2)}(0)$ occurs at $\Delta_c = 0.7g$ for weaker excitation (where the second order manifold is excited resonantly via two photons). However, with increasing excitation power, the peak positions shifts towards $\Delta_c = 0$, due to excitation of higher manifolds.

changing power in the coherent state. However, using the strongly coupled QD-cavity system, one can preferentially generate Fock states with probabilities that exceed this classical ratio achievable in a coherent state. This is shown in Fig. 5.7b, where we compare the ratio r_m for 1 and 2 photon Fock state for a classical coherent state and the non-classical state generated by the coupled QD-cavity system. We clearly see a large increase in the ratio $r_1(r_2)$ for QD-cavity system at a detuning $\sim 1.1g$ ($\sim 0.9g$) showing that at those detunings we are preferentially generating 1 and 2 photon Fock states.

From the probability distribution of the different Fock states we can find the wavefunction of the overall photon state $|\psi\rangle = \sum\limits_n c_n|n\rangle$ with $P(n) = |c_n|^2$, the second order coherence function $g^{(2)}(0) = \frac{\langle\psi|a^\dagger a^\dagger aa|\psi\rangle}{\langle\psi|a^\dagger a|\psi\rangle^2} = \frac{\sum\limits_n n(n-1)P(n)}{\left(\sum\limits_n nP(n)\right)^2}$ and second order differential correlation function $C^{(2)}(0) = \langle\psi|a^\dagger a^\dagger aa|\psi\rangle - \langle\psi|a^\dagger a|\psi\rangle^2 = \sum\limits_n n(n-1)P(n) - \left(\sum\limits_n nP(n)\right)^2$, which we can measure experimentally. Figure 5.7c shows $g^{(2)}(0)$ as a function of Δ_c, the laser detuning from the empty cavity. The dashed line indicates the expected $g^{(2)}(0)$ for a coherent state. Figure 5.7d shows $C^{(2)}(0)$ as a function of Δ_c. $C^{(2)}(0)$ transitions from negative to positive value with decreased detuning at $\Delta_c \sim 0.9g$, thanks to the excitation of the second manifold in the ladder when two photons are simultaneously coupled into the cavity-QD system. Fig. 5.7e shows $C^{(2)}(0)$ as a function of Δ_c for different laser excitation powers. We note that, the peak position changes depending on the excitation laser power and at lower driving power we observe the peak at $\Delta_c \sim 0.7g$, where the second order manifold is excited via two photons. With increasing power, the higher (third and more) manifolds starts being populated, and the peak in $C^{(2)}(0)$ subsequently shifts to smaller values of detuning. In Fig.5.7d, the peak in $C^{(2)}(0)$ is at a detuning of $\Delta_c \sim 0.5g$.

Figure 5.8a shows the probability $P(n)$ for different photon numbers as a function of the peak amplitude of the drive pulse $\mathcal{E}_o$ of the laser for $\kappa \approx g \approx 2\pi \times 20$GHz, which correspond to typical experimental parameters of our current system. The system is driven with Gaussian pulses with $\tau_p \sim 24$ ps. Figure 5.8b shows the dependence of $g^{(2)}(0)$ and $C^{(2)}(0)$ on the coherent driving amplitude $\mathcal{E}_o$. We assume that the laser

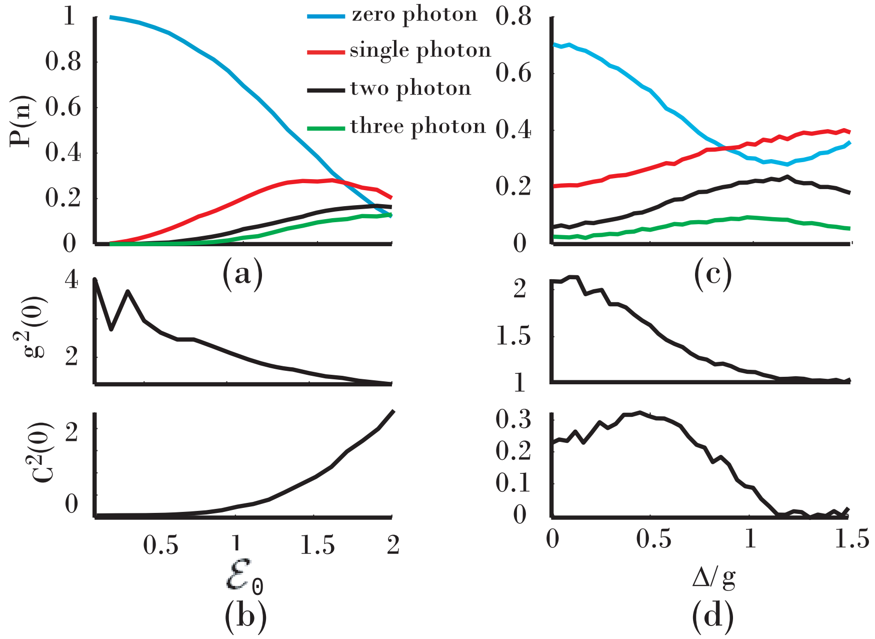

Figure 5.8: Numerically calculated photon statistics for pulsed driving of our current QD-cavity system: (a)The probability $P(n)$ of n photon states in the output light, as a function of $\mathcal{E}_o$, when the laser is resonant with the cavity. (b) $g^{(2)}(0)$ and $C^{(2)}(0)$ as a function of $\mathcal{E}_o$. The minimum $\mathcal{E}_o$ used is 0.1 in the plot. (c) $P(n)$ for n photon state as a function of laser-cavity detuning Δ. (d) $g^{(2)}(0)$ and $C^{(2)}(0)$ as a function of Δ. The simulation parameters are $g \approx \kappa = 2\pi \times 20$ GHz, $\mathcal{E}_o = 2\pi \times 9$GHz and and the system is driven with Gaussian pulses with $\tau_p \sim 24$ ps.

is resonant with the empty cavity frequency ($\Delta = 0$), and hence the coupled system is in the tunneling regime.

We repeat these calculations with $\mathcal{E}_o$ fixed while the laser-cavity detuning Δ is being changed. Figures 5.8c and 5.8d show the probabilities of different photon states at the output, $g^{(2)}(0)$, and $C^{(2)}(0)$ as a function of Δ for a driving laser with peak amplitude $\mathcal{E}_o = 2\pi \times 9$ GHz, which roughly corresponds to the laser power used in our experiment.

5.2.2 Experimental result

We confirm our theoretical predictions by performing experiment with InAs QDs coupled to a linear three hole defect GaAs photonic crystal cavity. We measure laser transmission through the system (using the same cross-polarized reflectivity setup described previously in this thesis, in chapter 3) and observe anti-crossing between the QD and cavity (by changing temperature) signifying the system is in the strong coupling regime. At resonance, the QD and cavity mix to generate two polaritons, seen as two Lorentzian peaks in Figure 5.10a. By fitting the spectrum at resonance we estimate the system parameters as $\kappa/2\pi = 27$ GHz (corresponding to $Q \approx 6,000$) and $g/2\pi = 21$ GHz. To drive the cavity-QD system, we use a mode-locked Ti-Sapphire laser, that generates 3 ps pulses at a repetition rate of $f_{rep} = 80$ MHz. These 3 ps pulses are passed through a monochromator to elongate the pulse in time domain, which results in pulses with approximately Gaussian temporal profile of 34 ps FWHM, corresponding to $\tau_p = 24.44$ ps (as in our theoretical analysis). We determine the amplitude of the coherent driving field using $\mathcal{E}_o = \sqrt{\frac{\eta P_{avg}}{4\pi^{\frac{1}{2}} Q \tau_p f_{rep} \hbar}}$, where P_{avg} is the average optical power of the pulse train measured before the objective lens and $\eta \sim 0.03$ [67] is the coupling efficiency of the incident light into the cavity including all the optics losses. For our experimental parameters, $\mathcal{E}_o \approx 2\pi\sqrt{P_{avg}(nW)} \times 9.3\text{GHz}$.

All the photon statistics measurement were performed using the HBT setup. We measure the histograms corresponding to the coincidences between two counters. We tune the pulsed laser to the dip in the transmission spectrum (between two polaritons) and perform second-order correlation measurement on light transmitted through the cavity. Figure 5.9a shows the histogram, where the coincidence counts at zero time delay are increased compared to the non-zero time delays. This is a signature of photon bunching, and indication of photon-induced tunneling. Similar experiment with the laser tuned slightly above the polariton frequency results in anti-bunching, where the coincidence count at zero time delay is smaller than the coincidence counts at non-zero time delay (Figure 5.9 b). This is the signature of photon blockade. We estimate $g^{(2)}(0)$ as the ratio of the coincidence counts at zero-time delay and non-zero time delay. The second order auto-correlation $g^{(2)}(0)$ is measured as a function of excitation laser frequency (Figure 5.10b) to observe transition from photon blockade to photon induced tunneling regime. The measurement setup has a timing resolution of 100 ps. We estimate $g^{(2)}(0)$ as the ratio of the coincidence counts at zero-time delay and at a time delay much larger than the timescale of the system dynamics

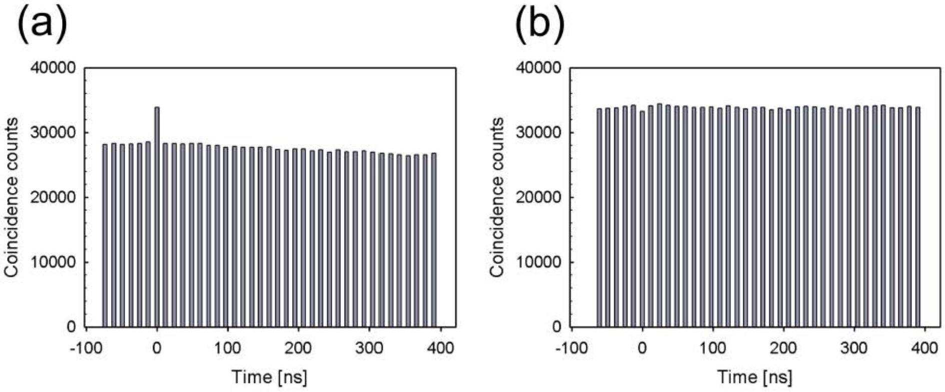

Figure 5.9: Experimental observations of photon induced tunneling and blockade under pulsed excitation ($\tau_p \sim 24$ ps pulses with 80 MHz repetition frequency). (a) Coincidence measurement obtained when the laser is tuned to the dip between polaritons. Increased coincidence counts at $t = 0$ indicate the photon induced tunneling regime. (b) Coincidence measurement obtained when the laser is tuned to the polariton (in this case, the one at lower frequency). The reduced coincidence counts at $t = 0$ indicate the photon blockade regime. The average laser power for the measurement is $P_{avg} = 0.2$nW.

($\sim 1ns$).

Following this we calculate the second order differential correlation function $C^{(2)}(0)$ for the coupled-QD cavity system as a function of the laser-cavity detuning (Fig. 5.11a). We observe the transition of $C^{(2)}(0)$ from negative to positive values. Simulations with our system parameters are shown by the dashed line in Fig. 5.11a and the onset of a peak at $\Delta_c \sim 0.5g$ corresponding to the excitation of the higher order dressed states is observed. The absence of such a clear peak in the experimental data can be ascribed to QD blinking. As explained before, the peak in $C^{(2)}(0)$ does not correspond exactly to the resonant excitation of the second order manifold via two photon process, because of the additional excitation of the higher order manifolds. All the measurements are performed at 14 K. We note that, in the simulation, $g^{(2)}(0)$ in the tunneling regime is much larger than the experimentally measured value as a result of QD blinking, which causes the experimentally collected data to be a weighted average of transmission through an empty cavity and a cavity with strongly coupled QD; in other words, blinking effectively pulls the $g^{(2)}(0)$ curve towards $g^{(2)}(0) = 1$

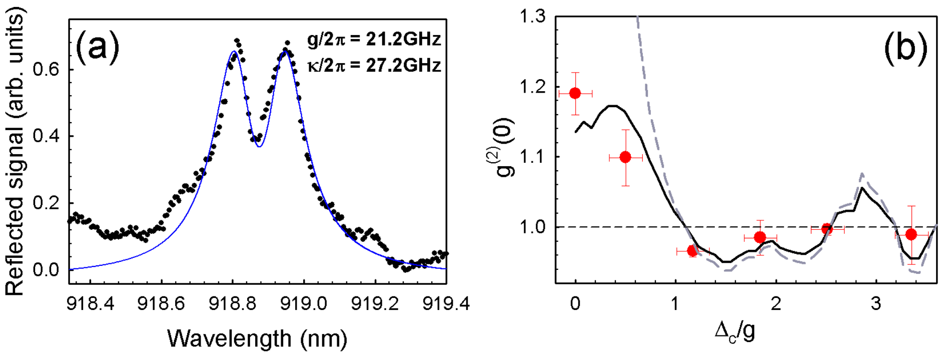

Figure 5.10: (a) The transmission spectrum of a strongly coupled QD-cavity system showing two polaritons. (b) Second order coherence function at $t = 0$, $g^{(2)}(0)$ as a function of the laser detuning from the empty cavity frequency. The system is excited with $\tau_p = 24$ ps Gaussian pulses, with 80 MHz repetition frequency. The dashed grey (solid black) line results from a numerical simulation based on the system's experimental parameters and no (with) QD blinking. The average laser power for the measurement is $P_{avg} = 0.2$nW. For the simulations we use a QD dephasing rate $\gamma_d/2\pi = 1$ GHz.

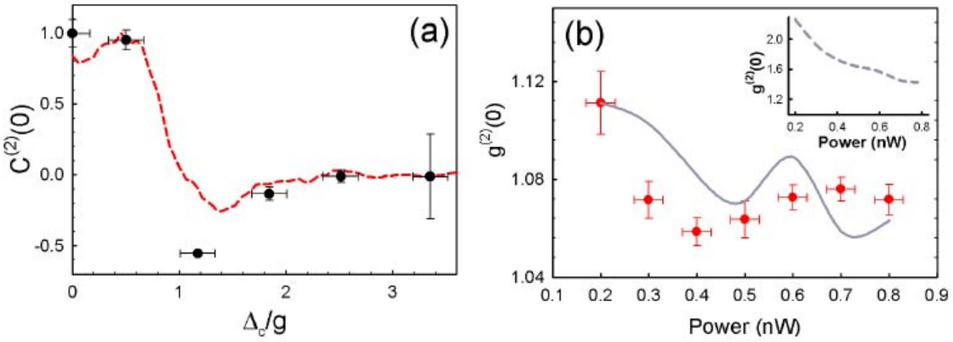

Figure 5.11: (a) Normalized differential correlation function $C^{(2)}(0)$ as a function of the laser detuning. The dashed red line shows the result of a numerical simulation based on the system's experimental parameters. (b) $g^{(2)}(0)$ in the tunneling regime ($\Delta_c = 0$) as a function of laser power P_{avg} measured in front of the objective lens. The solid line shows the result of numerical simulation including the effects of QD blinking, while the inset plots the numerically simulated $g^{(2)}(0)$ in the absence of blinking. For the simulations we use a QD dephasing rate $\gamma_d/2\pi = 1$ GHz.

[67]. We model the blinking behavior of the QD by assuming that during a unit time interval the QD is active for a fraction r and inactive for $(1-r)$ of the time. Thus the $g^{(2)}(0)$ measured in the experiment will be a statistical mixture of the coherent photon state (when QD is inactive, i.e., QD-cavity coupling $g=0$) and the correlated photons from the coupled QD-cavity system. The quantum mechanical description of the state is a mixed state $(1-r)|\alpha\rangle\langle\alpha| + r|\psi\rangle\langle\psi|$, where the QD is active during the fraction of the time given by r. In the simulation we calculate $g^{(2)}(0)$ for two different cases: $g_a^{(2)}(0)$ when the QD is active ($g \neq 0$) and $g_d^{(2)}(0)$ when the QD is inactive or dark ($g=0$). Hence we can find that the combined $g^{(2)}(0)$ (for a mixed state) is given by

$$g^{(2)}(0) = \frac{r g_a^{(2)}(0)\langle a^\dagger a\rangle_a^2 + (1-r) g_d^{(2)}(0)\langle a^\dagger a\rangle_d^2}{r\langle a^\dagger a\rangle_a^2 + (1-r)\langle a^\dagger a\rangle_d^2} \tag{5.3}$$

where, $\langle a^\dagger a\rangle_a$ and $\langle a^\dagger a\rangle_d$ are respectively, the square of the cavity transmission for an active and a dark QD. We obtain good fit to our experimental data with $r = 0.65$. The vertical error bars in all the figures are calculated from the uncertainties in the fit of the histogram data sets. The horizontal error bars are given by the uncertainty in the measurement of the laser wavelength or the laser power.

Finally, Fig. 5.11 b shows $g^{(2)}(0)$ as a function of excitation laser power in the tunneling regime ($\Delta_c = 0$). This data is taken with the same CQED system on a different day, when the cavity is red-shifted compared to the previous measurements. For this particular experiment, the QD and the cavity are resonant at 26 K. This slightly higher temperature might cause more QD dephasing, leading to a worse value of $g^{(2)}(0)$ (1.12 as opposed to 1.2 from the previous measurement). Overall, $g^{(2)}(0)$ decreases with increasing laser power as expected from the intuitive picture of QD saturation at high driving power and the numerical simulation. This clearly shows that the photon bunching observed in tunneling regime is coming solely from the quantum mechanical nature of the QD-cavity system, and not from a classical effect. We also observe interesting oscillatory behavior in $g^{(2)}(0)$ as a function of power. An oscillatory behavior is also observed in the simulation that includes the effects of QD blinking. Without any QD blinking, the simulation results show a mostly monotonically decreasing $g^{(2)}(0)$ with increasing laser power (inset of Fig. 5.11b).

We would like to point out that these measurements have been performed at the lowest $P_{avg} = 0.2$ nW that we can reliably use, corresponding to $\mathcal{E}_o \approx 2\pi \times 4.2$GHz. This roughly corresponds to the red plot in the theoretical Fig. 5.7e, where the peak in $C^{(2)}(0)$ is near $\sim 0.5g$. This lower power limit is caused by the limited mechanical stability of the cryostat and the low overall efficiency with which we can couple the cavity photons into the single photon counters in our HBT setup. The time needed to perform the second-order coherence measurement increases quadratically with decreasing P_{avg} and for low powers the cavity drifts out of focus before we can collect sufficient number of coincidence counts.

5.2.3 Effect of dephasing on blockade and tunneling

Pure QD dephasing turns out to be a very important quantity, for solid state CQED with quantum dot [2]. The effect of pure QD dephasing can be modeled by adding a term $2\gamma_d\mathcal{L}(\sigma^\dagger\sigma)$ in the Master equation. With increasing dephasing rate, the $g^{(2)}(0)$ spectrum tends to the one expected from just a coherent state ($g^{(2)}(0) = 1$ for all the detunings) (Figure 5.12). However the qualitative nature of the tunneling and blockade in the spectrum remains same.

We also investigate the effect of pure QD dephasing on the Fock-state generation. Figure 5.13 shows the probability $P(n)$ of generating n photon Fock state for two different situations: no dephasing and with a pure QD dephasing rate of $\gamma_d/2\pi = 1$ GHz. We observe that the qualitative nature of the Fock state generation remains same even in the presence of the pure dephasing. However, the corresponding probabilities are diminished. In fact at very large dephasing, the system produces only a coherent state.

5.3 Sub-Poissonian light generation with a bimodal cavity

In previous sections, the system studied involved a single mode cavity. In this section, we propose an implementation of a source of strongly sub-Poissonian light in a

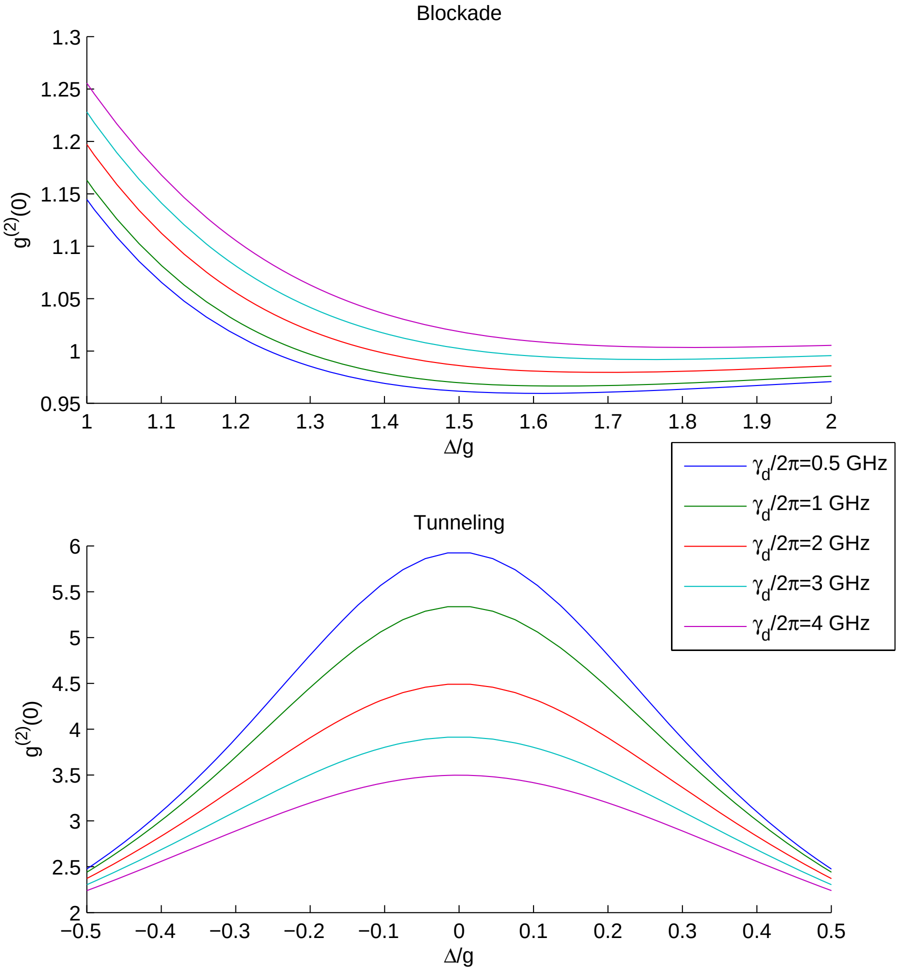

Figure 5.12: The effect of pure QD dephasing on the tunneling and blockade regime: (a) In the blockade regime $g^{(2)}(0)$ remains lower than 1, but increases with increasing dephasing rate. (b) In the tunneling regime, $g^{(2)}(0)$ remains higher than 1, but decreases with increasing dephasing rate.

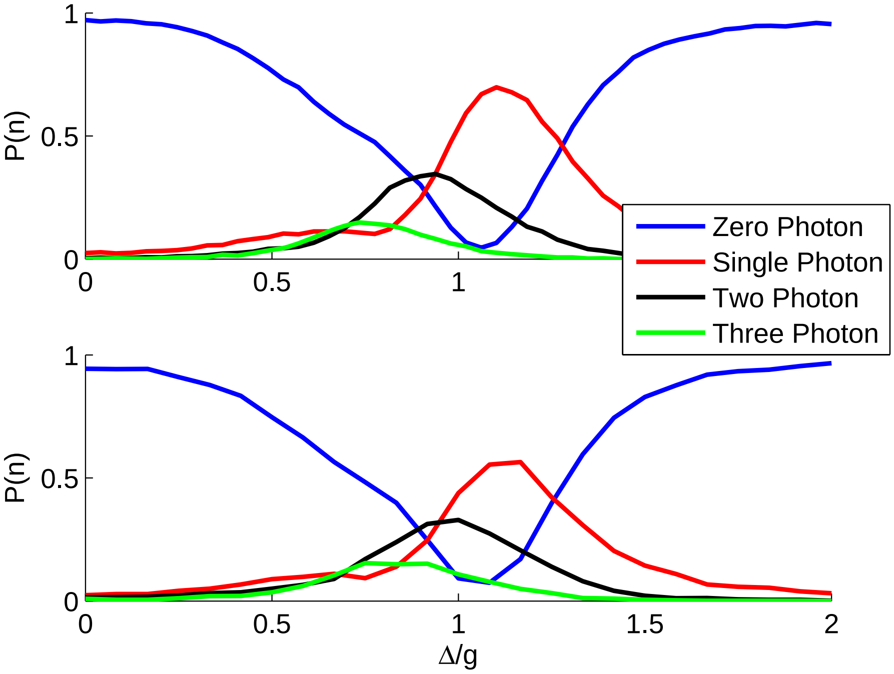

Figure 5.13: The effect of pure QD dephasing on the Fock state generation: (a) Probability $P(n)$ of generating n photon states as a function of Δ/g. No QD dephasing is included. (b) $P(n)$ as a function of Δ/g, with a pure QD dephasing rate $\gamma_d/2\pi = 1$ GHz. For all the simulations: $\kappa/2\pi = 4$ GHz and $g/2\pi = 40$ GHz.

system consisting of a quantum dot coupled to both modes of a lossy bimodal optical cavity [39]. When one mode of the cavity is resonantly driven with coherent light, the system will act as an efficient single photon filter, and the transmitted light will have a strongly sub-Poissonian character. In addition to numerical simulations demonstrating this effect, we present a physical explanation of the underlying mechanism. In particular, we show that the effect results from an interference between the coherent light transmitted through the resonant cavity and the super-Poissonian light generated by photon-induced tunneling. Peculiarly, this effect vanishes in the absence of the cavity loss.

While most of the recent experiments focus on photon blockade with a single two level system and a single cavity [78, 67, 3, 85], there have been several theoretical proposals predicting similar effects and sub-Poissonian light generation in systems based on multi-level atoms in a cavity [77] and on a quantum dot interacting with a pair of proximity-coupled nanocavities [86, 87] or wave-guides [88].

The cavity QED systems in which photon blockade can be studied depend on three important rate quantities: the coherent coupling strength between the atomic system and the cavity g, the cavity field decay rate κ and the dipole decay rate γ (as explained earlier in the thesis). In all aforementioned proposals, the photon blockade occurs in the strong coupling regime, when the coherent interaction strength is larger than the loss rates in the system. In fact, the limit of $g/\kappa, g/\gamma \to \infty$ results in vanishing overlap between the energy eigen-states of the anharmonic ladder, which in turn leads to a perfect photon blockade ($g^{(2)}(0) = 0$). In a solid state optical system based on a photonic-crystal cavity with an embedded single QD as the two-level system, the condition $g \gg \gamma$ is generally easy to satisfy. However, achieving the condition of $g \gg \kappa$, which requires a high quality (Q) factor of the cavity, is generally difficult due to fabrication challenges. As a result, even the best photon blockade with a QD embedded in a solid-state nanocavity reported so far in the literature gives a second order correlation $g^{(2)}(0) \sim 0.75$ [85]. Though a proposal based on a QD interacting with a photonic molecule (a pair of coupled cavities) predicts efficient blockade even for cavities with easily achievable Q factors [86, 87](also analyze din the following chapter), the suggested scheme requires both individual addressability of each cavity and a large coupling strength between the two cavities. Since nanophotonic cavities are generally coupled via spatial proximity, large coupling poses a major challenge for achieving individual addressability.

In this section, we propose a different approach for generation of strongly antibunched light which employs a bimodal cavity with both of its modes coupled to a QD. We will show that in this approach the cavity loss is actually crucial for achieving the effect, as opposed to photon blockade systems introduced so far in which the cavity loss plays a negative role. Specifically, the effect does not occur in our system in the limit of $g/\kappa \rightarrow 0$, which is intuitively expected, as this is the case of an infinitely large loss (and this is what also happens for the cases of blockade with a single QD strongly coupled to a single cavity and in previous photonic molecule proposals). However, for $g/\kappa \rightarrow \infty$ (zero loss, i.e., an infinite cavity Q-factor), the proposed system fails to generate sub-Poissonian light, in contrast with the single cavity with a strongly coupled QD, where perfect photon blockade occurs in such a limit. Here, we provide an intuitive explanation of how a balance between the coherent QD-cavity interaction and the decay of the cavity field is required to achieve a strong sub-Poissonian output photon stream. Second order auto-correlation of such a bimodal cavity was analyzed before experimentally [89] and theoretically [90] in the context of semiconductor micro-disk cavities, where the right and left hand circularly polarized cavity modes are degenerate. However, the unusual dependence of the sub-Poissonian light on g/κ ratio was not reported before. Additionally, we analyze the nanophotonic platform for possible experimental realization of this effect. We note that the role of cavity loss in generation of entanglement between two cavity modes was previously studied in Ref. [91].

5.3.1 Theory

In a conventional strongly coupled QD-cavity system, a QD interacts with a single cavity mode (Fig. 5.14a). In the bimodal cavity, the QD is coupled to both cavity modes (described with photon annihilation operators a and b) although there is no direct coupling between the two modes (Fig. 5.14b). Assuming the cavity modes are degenerate and the QD is resonant with both of them, the Hamiltonian $\mathcal{H}$ describing such a system (in a frame rotating at the frequency of the laser driving the cavity mode a) is:

$$\begin{aligned}\mathcal{H} = \Delta(a^\dagger a &+ \sigma^\dagger\sigma + b^\dagger b) + g_a(a^\dagger\sigma + a\sigma^\dagger) \\ &+ g_b(b^\dagger\sigma + b\sigma^\dagger) + \mathcal{E}\sqrt{\kappa}(a + a^\dagger)\end{aligned} \tag{5.4}$$

Here, σ is the QD lowering operator, g_a and g_b are the coupling strengths between the QD and the two cavity modes,κ is the cavity field decay rate, $\mathcal{E}$ denotes strength of the driving laser and Δ is the detuning between the driving laser and the cavity modes. The loss in the system is incorporated in the usual way by using the Master equation. Fig. 5.14c shows the transmitted light collected from the driven cavity ($\kappa\langle a^\dagger a\rangle$) for both single (dashed line) and double mode cavities (solid line). The cavity output is qualitatively similar for both cases, and the split resonance is caused by coupling of the QD to the cavity and creation of polaritons. For the single mode cavity, the two polaritons are separated by $2g$, while for the bimodal cavity, the separation is $2\sqrt{2}g$ due to the presence of two modes, as will be explained later. Increased cavity transmission at $\Delta = 0$ for the bimodal case is also due to the presence of two modes. However, the second-order autocorrelation functions of the cavity transmission $g^{(2)}(0)$ are strikingly different for two cases (Fig. 5.14d). For the single mode cavity, one observes photon blockade ($g^{(2)}(0) < 1$), when the driving laser is tuned close to the frequency of the polariton, $\Delta \approx \pm 1.5g$. For the bimodal cavity, sub-Poissonian statistics are observed at three different detunings: $\Delta \approx \pm 1.8g$ and $\Delta = 0$. A slight deviation from the polariton frequencies (for single mode cavity $\Delta \approx \pm g$ and for bimodal cavity $\Delta \approx \pm\sqrt{2}g$) is due to the losses in the system. The weak sub-Poissonian light ($g^{(2)}(0) \sim 0.95$) at $\Delta \approx \pm\sqrt{2}g$ is comparable to that observed in the single mode cavity, and it arises from the same mechanism. At $\Delta = 0$, the sub-Poissonian character is much stronger ($g^{(2)}(0) \sim 0.4$), and it is this regime in the bimodal cavity that we will focus on. Note that the sub-Poissonian character observed at this frequency of the driving laser cannot be explained by the anharmonic nature of the ladder alone. In fact, in the energy structure of the coupled QD and the bimodal cavity, we always find an available eigen-state at this empty cavity frequency.

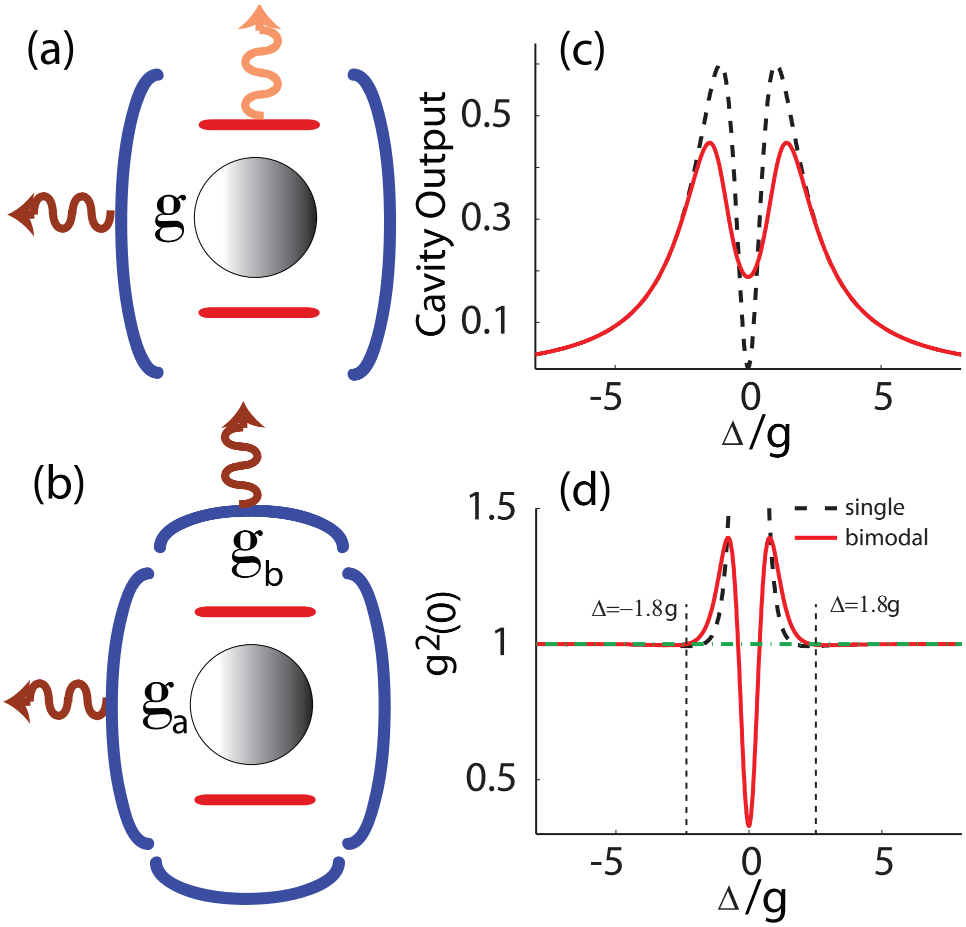

Figure 5.14: (a) Schematic of a QD coupled to a single mode cavity, with a coupling strength of g. (b) Schematic of a bimodal cavity with a coupled QD. The two cavity modes are not directly coupled to each other. However, both of them are coupled to the QD with interaction strengths g_a and g_b. (c) The cavity output $\kappa\langle a^\dagger a\rangle$ as a function of the driving laser detuning Δ from the empty cavity resonance both for a single mode cavity (dashed line) and the bimodal cavity (solid line). The split resonance observed is due to the coupled QD. (d) Second order autocorrelation $g^{(2)}(0)$ function calculated for the collected output of the driven mode for a single mode (thick dashed line) and bimodal cavity (solid line). The green dashed line marks the Poissonian statistics of a coherent state (always 1). For single mode cavities at $\Delta \sim \pm 1.5g$ and for bimodal cavities at $\Delta \sim \pm 1.8g$, we observe a weakly sub-Poissonian light ($g^{(2)}(0)$ slightly less than 1). However, for bimodal cavity a strong sub-Poissonian light is generated when $\Delta = 0$. For bimodal cavities we assumed identical interaction strengths and cavity decay rates for two modes. Parameters used for the simulations: QD-cavity interaction strength $g/2\pi = g_a/2\pi = g_b/2\pi = 10$ GHz, cavity field decay rate $\kappa/2\pi = 20$ GHz, dipole decay rate $\gamma/2\pi = 1$ GHz, and driving laser strength $\mathcal{E}\sqrt{\kappa}/2\pi = 1$ GHz.

To further illustrate the difference between the photon blockade in a single mode cavity and the effect we observe in a bimodal cavity, we perform numerical simulations for a range of coupling strengths g and cavity field decay rates κ in both systems. Using these simulations, we obtained the values of $g^{(2)}(0)$ for the transmitted light for a single mode cavity (laser tuned to one of the polaritons, i.e., $\Delta = g$) and for a double mode cavity (the laser tuned to the bare cavity frequency, i.e., $\Delta = 0$). Fig. 5.16a,b shows $g^{(2)}(0)$ as a function of g and κ. For a single mode cavity, blockade appears at high g and low κ, as generally expected for any photon blockade system (Fig. 5.16a). However, for a bimodal cavity (when excited at $\Delta = 0$), the effect disappears and the transmitted photon output becomes Poissonian whenever g and κ are disproportionate (i.e., $g/\kappa \to 0$ or $g/\kappa \to \infty$). A strongly sub-Poissonian output can be observed from a bimodal cavity when g and κ are comparable. Fig. 5.16c plots the $g^{(2)}(0)$ as a function of the ratio κ/g for different g demonstrating sub-Poissonian light in the bimodal cavity even in the weak coupling regime. We stress again that this result cannot be explained just by the anharmonicity of the ladder of energy eigenstates. We note that for the bimodal cavity when pumped at $\Delta \approx \sqrt{2}g$, the light is sub-Poissonian only at high g and low κ, consistent with conventional photon blockade. We now briefly discuss the light state from the undriven cavity mode b. Mode b is not directly coupled to mode a, and the only way it can receive photons is via the QD. Hence the amount of light collected from mode b is very small, but the light is sub-Poissonian. However, there is no photon blockade present in the mode b, and the sub-Poissonian character of light in mode b is similar to the single photons generated by resonant excitation of a QD. Fig. 5.15 a,b shows the transmitted cavity (b) output and second order autocorrelation $g^{(2)}(0)$ as a function of g and κ.

To understand the origin of the strongly sub-Poissonian light transmitted through a bimodal cavity, we transform the system's Hamiltonian to a different cavity mode basis: $\alpha = (a+b)/\sqrt{2}$ and $\beta = (a-b)/\sqrt{2}$. The Hamiltonian $\mathcal{H}$ can be written (assuming $g_a = g_b = g$) as $\mathcal{H} = \mathcal{H}_1 + \mathcal{H}_2$ with

$$\mathcal{H}_1 = \Delta(\alpha^\dagger\alpha + \sigma^\dagger\sigma) + \sqrt{2}g(\alpha^\dagger\sigma + \alpha\sigma^\dagger) + \frac{\mathcal{E}\sqrt{\kappa}}{\sqrt{2}}(\alpha + \alpha^\dagger) \tag{5.5}$$

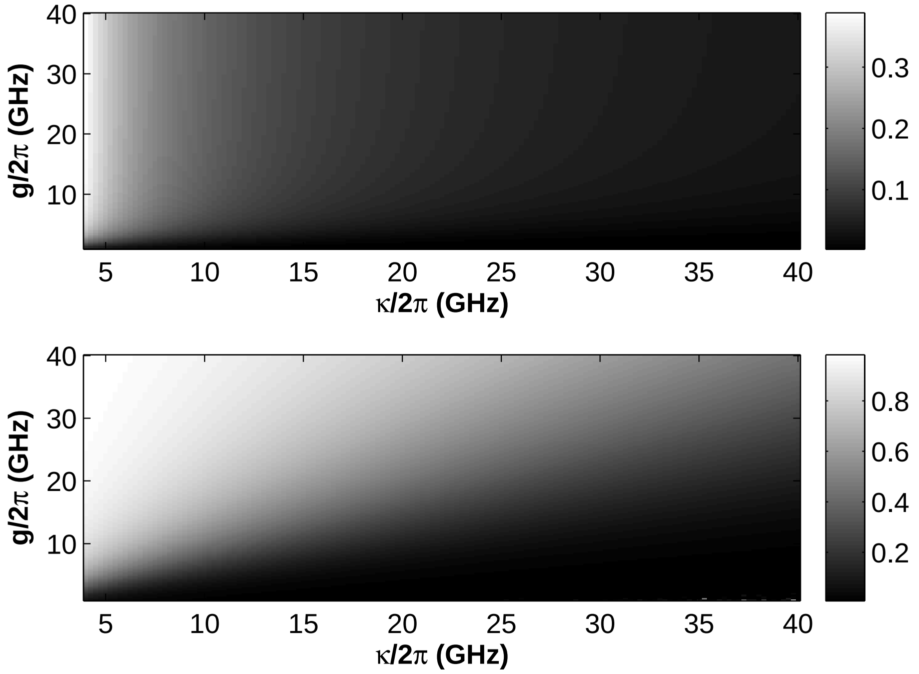

Figure 5.15: (a) Transmitted output $\kappa\langle b^\dagger b\rangle$ from the undriven cavity mode b as a function of g and κ. For both modes the same g and κ are assumed. (b) Second order autocorrelation $g^{(2)}(0)$ for the bimodal cavity as a function of g and κ. The light is always sub-Poissonian, and results from the resonant QD excitation via mode a, and collection of the output photons via mode b. This is similar to a conventional single photon source under resonant excitation of the QD.

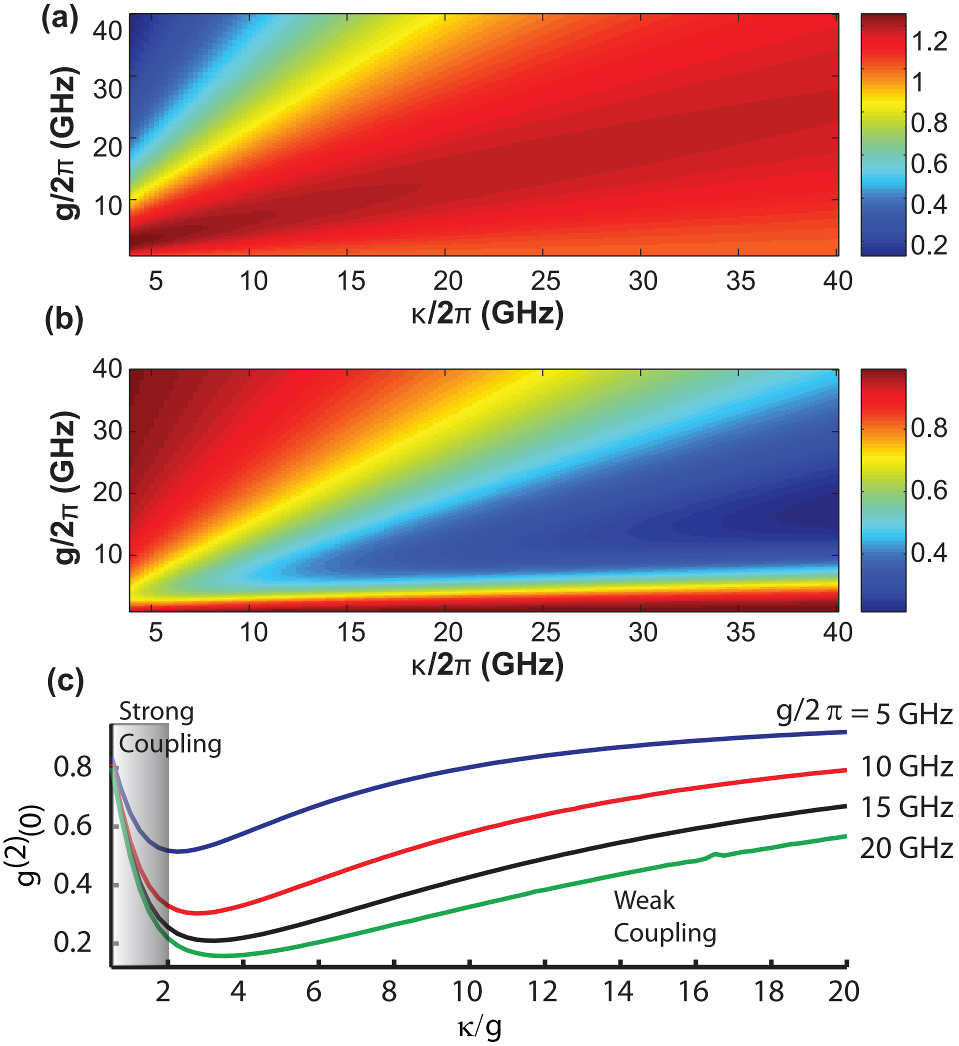

Figure 5.16: (a) Second order autocorrelation $g^{(2)}(0)$ for the conventional photon blockade in a single mode cavity as a function of the QD-cavity coupling strength g and cavity field decay rate κ. $g^{(2)}(0)$ decreases with increasing value of g/κ, as expected, as a result of reduced overlap of energy eigenstates in the anharmonic ladder. (b) $g^{(2)}(0)$ for the bimodal cavity as a function of g and κ. $g^{(2)}(0)$ is calculated for the output of mode a, i.e., for photons leaking from the mode a. We observe that $g^{(2)}(0) \rightarrow 1$ (Poissonian output) when $g/\kappa \rightarrow 0$ or ∞. However, we can observe very low $g^{(2)}(0)$ even when the QD is not strongly coupled to the two cavity modes ($g < \kappa/2$). (c) $g^{(2)}(0)$ as a function of the ratio κ/g for different g showing sub-Poissonian light generation in the bimodal cavity even in the weak coupling regime. For all the simulations $\mathcal{E}/2\pi = 0.1$ GHz such that the QD is not saturated.

describing a driven single mode cavity coupled to a QD with a strength of $\sqrt{2}g$ and

$$\mathcal{H}_2 = \Delta\beta^\dagger\beta + \frac{\mathcal{E}\sqrt{\kappa}}{\sqrt{2}}(\beta + \beta^\dagger) \tag{5.6}$$

describing a driven empty cavity mode. Both cavities are driven at the bare cavity resonances. We monitor $a = (\alpha+\beta)/\sqrt{2}$ which, in the transformed basis, is equivalent to the output from two cavities: one with a coupled QD (α) and the other empty (β), combined on a beam-splitter. Fig. 5.17a shows the transmitted cavity output for three different cases: cavity α alone, cavity β alone and the combined output. Note the polariton peaks in the combined output at $\pm\sqrt{2}g$ and increased transmission of light at zero detuning due to the empty cavity.

The cavity transmission with a strongly coupled QD driven at the cavity resonance is super-Poissonian due to photon-induced tunneling, as explained earlier in this chapter(α in Fig. 5.17b). On the other hand, the empty cavity transmission (β in Fig. 5.17 b) is a purely Poissonian coherent state. When the outputs of these two cavities are combined on a beam-splitter ($a = (\alpha + \beta)/\sqrt{2}$ in Fig. 5.17 b), the output shows sub-Poissonian character. We note that similar interference effect was previously reported in [89]. However, for efficient generation of sub-Poissonian light, one needs comparable transmitted light intensity from both cavities, which calls for a balance between the cavity loss κ and the QD-cavity nonlinear interaction strength g. Using this effective model, the somewhat unusual dependence of $g^{(2)}(0)$ on g and κ can now be explained. When $g/\kappa \to 0$, the coupled system is linear and both of the equivalent cavities transmit just coherent light. On the other hand, although photon-induced tunneling does happen in the limit $g/\kappa \to \infty$, the amount of super-Poissonian light transmitted through the cavity α is so small (as the dressed states separation in the ladder is so large that it is impossible to couple photons at energies between them) that its interference with the coherent light from the empty cavity β will still result in light with Poissonian statistics. To generate enough super-Poissonian light via photon-induced tunneling in cavity (α) which can affect the coherent light from the empty cavity (β), comparable values of dot-cavity interaction strength g and cavity decay rate κ are required.

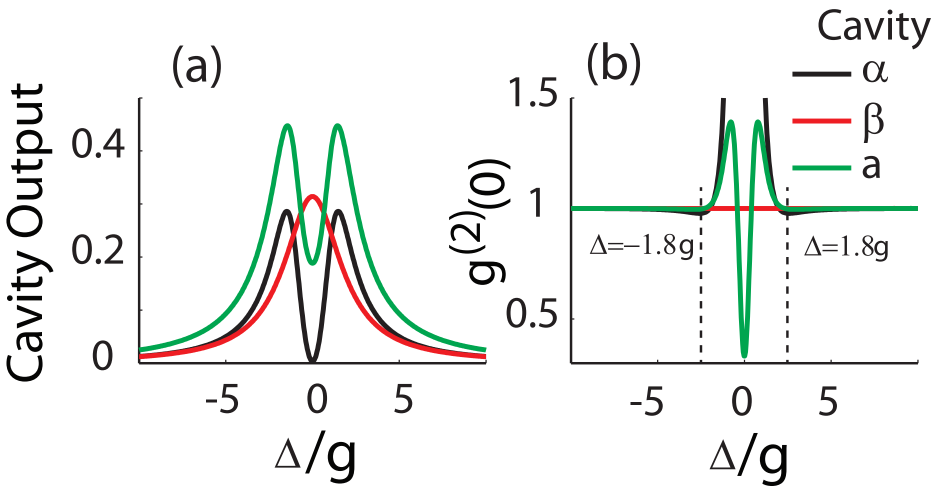

Figure 5.17: (a) Cavity output for an empty cavity β and another cavity α coupled to a QD with a coupling strength of $\sqrt{2}g$. The combined output of these two replicates the output from the bimodal cavity a (Fig. 5.14). (b) $g^{(2)}(0)$ for these three cases: the empty cavity β gives Poissonian light; the cavity α with coupled QD gives super-Poissonian light due to photo-induced tunneling [3] (the black curve goes to infinity at $\Delta = 0$); the combined output a provides sub-Poissonian light. Parameters for the simulation: $g/2\pi = 10$ GHz, $\kappa/2\pi = 20$ GHz, $\gamma/2\pi = 1$ GHz and $\mathcal{E}\sqrt{\kappa}/2\pi = 1$ GHz.

5.3.2 Proposed experiment and preliminary experimental data

Finally, we discuss the nanophotonic platform that can be used to implement our proposal. A photonic-crystal cavity with C_6 symmetry can support two degenerate cavity modes with orthogonal polarizations [92]. The two cavity modes are thus not coupled to each other (since their polarizations are orthogonal), and can be easily addressed independently by a laser. At the same time, a QD can be coupled to both cavity modes, if it is placed spatially at the center of the cavity with its dipole moment aligned at a 45^o-angle to the polarizations of both modes.

Two potential issues can arise from fabrication imperfections in a realistic system: a frequency difference Δ_{ab} between the two cavity modes and a mismatch between the QD coupling strengths g_a and g_b to each mode. These issues can be seen in the preliminary experimental results shown below. To examine the robustness of the proposed scheme against these imperfections, we plot their effects on $g^{(2)}(0)$ in Fig. 5.18. Fig. 5.18a shows the numerically calculated $g^{(2)}(0)$ as a function of the detuning between the two cavity modes Δ_{ab}. We observe that the sub-Poissonian character of the transmitted light vanishes when $\Delta_{ab} \geq \kappa$. This negative effect of frequency difference of the two modes can be balanced simply by increasing the cavity decay rate κ, i.e., by lowering the cavity quality factor. This results in an increase of the frequency overlap between the two modes and makes the degeneracy of the two modes more robust. The effects of this improvement outweigh the penalty incurred on the system's performance by reducing the g/κ ratio, and we can see in Fig. 5.18a that a strong sub-Poissonian output can still be produced.

Additionally, we analyze the performance of the system as a function of the ratio g_b/g_a, where g_b and g_a are the QD coupling strengths with the cavity modes a and b assuming mode a is coherently driven. It can be shown from the effective model that at a large g_b/g_a ratio, we essentially drive only the empty cavity β and the photon statistics is Poissonian. Similarly, at a small g_b/g_a ratio, we drive only the cavity α with coupled QD and the photon statistics is super-Poissonian due to photo-induced tunneling. This can be explained by looking at the effective model for different g_a and g_b, which is described previously only for the $g_a = g_b$ case. To understand the nature of the effect resulting in transmission of sub-Poissonian light, we make the following transformation:

$$\alpha = \frac{g_a a + g_b b}{\sqrt{g_a^2 + g_b^2}} \tag{5.7}$$

$$\beta = \frac{g_b a - g_a b}{\sqrt{g_a^2 + g_b^2}} \tag{5.8}$$

Under this transformation, we can rewrite the total Hamiltonian as

$$\mathcal{H} = \mathcal{H}_1 + \mathcal{H}_2 \tag{5.9}$$

with

$$\mathcal{H}_1 = \Delta(\alpha^\dagger \alpha + \sigma^\dagger \sigma) + \sqrt{g_a^2 + g_b^2}(\alpha \sigma^\dagger + \alpha^\dagger \sigma) + \sqrt{\kappa}\frac{\mathcal{E}}{\sqrt{1+r^2}}(\alpha + \alpha^\dagger) \tag{5.10}$$

$$\mathcal{H}_2 = \Delta \beta^\dagger \beta + \sqrt{\kappa}\frac{r\mathcal{E}}{\sqrt{1+r^2}}(\beta + \beta^\dagger), \tag{5.11}$$

where $r = g_b/g_a$. For $g_a = g_b$, we recover the result reported in the main text. When $r \to 0$, there is no light in the uncoupled cavity, and all the light output is from the coupled QD-cavity system. That light is super-Poissonian due to photo-induced tunneling. On the other hand, when $r \to \infty$, the coupled QD-cavity does not get any light. Hence the output light is just in a coherent state, which means its photon statistics will be Poissonian.

When $g_b/g_a \sim 1$, we meet the optimal condition of interference between the coherent state and super-Poissonian state to generate light with sub-Poissonian photon statistics. This can be seen in the numerical simulations of $g^{(2)}(0)$ as a function of g_b/g_a in Fig. 5.18b. The system performance is insensitive to the actual value of g_a for a relatively large range, as long as the ratio g_b/g_a is maintained. At the same time, we can see that the lowest value of $g^{(2)}(0)$ is achieved for the ratio of coupling strengths $g_b/g_a \sim 0.8$. We note that this ratio depends on the driving strength of the laser, and can be related to the requirement for similar transmission from the cavities α and β.

Now we will describe some initial experimental results showing the signature of QD-cavity coupling in a bimodal cavity, and comment on the feasibility of implementing our theoretical method in this system. Fig. 5.19 a,b,c show the scanning electron

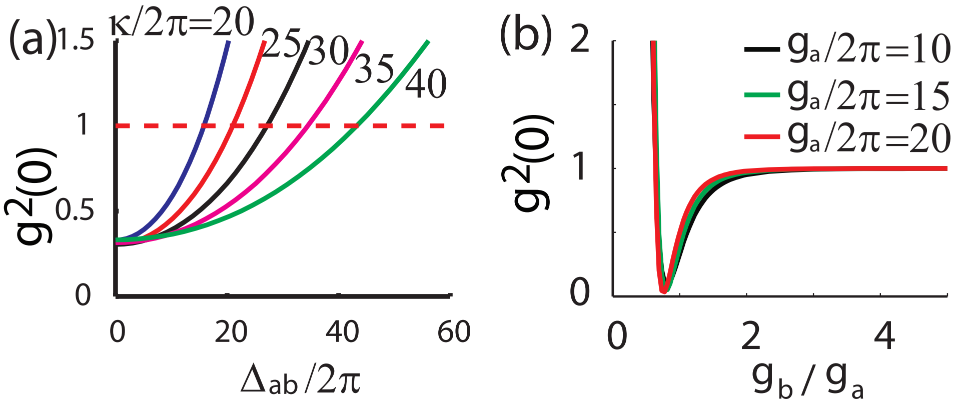

Figure 5.18: (a) Second order autocorrelation $g^{(2)}(0)$ of the cavity transmission, as a function of the relative detuning Δ_{ab} between two cavity modes for different cavity field decay rates $\kappa = \kappa_a = \kappa_b$. The quality of the sub-Poissonian photon stream in the transmitted output degrades with increasing detuning, which can be compensated by increasing κ, thereby maintaining low $g^{(2)}(0)$. For these simulations we assume $g_a/2\pi = g_b/2\pi = 10$ GHz and $\mathcal{E}/2\pi = 0.1$ GHz. (b) Second order autocorrelation $g^{(2)}(0)$ of the cavity transmission as a function of the ratio g_b/g_a for different g_a. The transmitted light behaves like a coherent state at high g_b/g_a ratio and like a super-Poissonian state generated via photo-induced tunneling at low g_b/g_a ratio. In between, when $g_b/g_a \sim 1$, we observe strong sub-Poissonian output. Here, $\kappa/2\pi = 20$ GHz for both cavity modes.

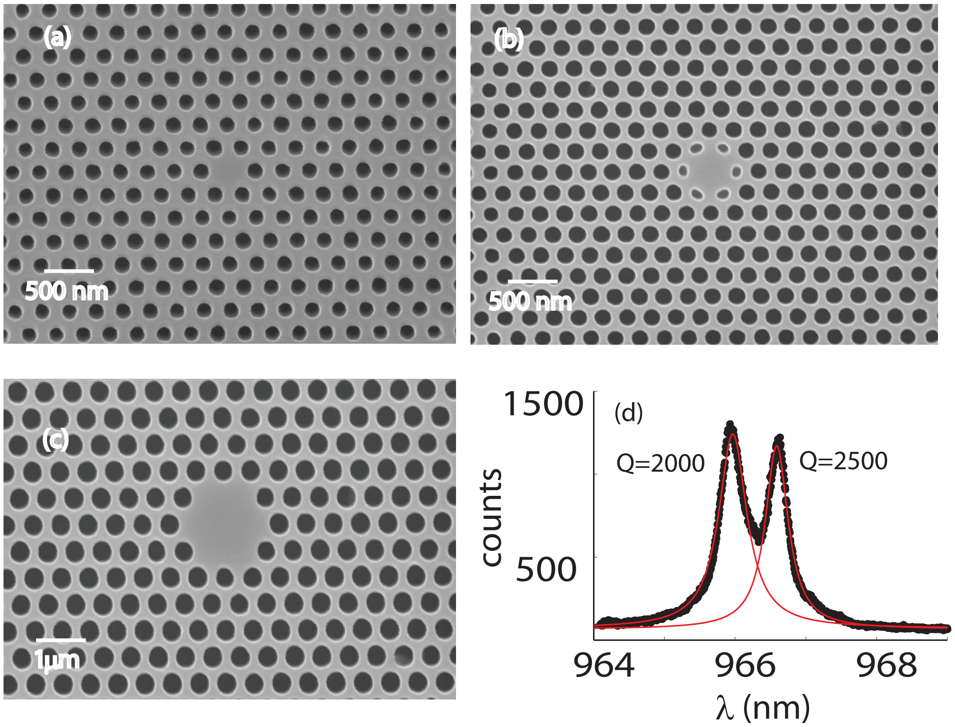

Figure 5.19: Scanning electron micrographs of fabricated photonic crystal cavities that can support degenerate modes: (a) $H1$ cavity, where the central hole is removed; (b) "calzone" cavity, where the central hole and half of the next layer of holes are removed; (c) $H2$ cavity, where the central hole and the first layer of surrounding holes are removed. (d) Photoluminescence spectrum of an $H1$ cavity showing moderate quality factors and moderate degeneracy of the two modes. Black dots correspond to experimental data points; the red lines are Lorentzian fits.

microscope images of three different photonic crystal cavities designed to support degenerate cavity modes. Fig 5.19d shows the photoluminescence (PL) spectrum from an $H1$ (Fig. 5.19a) cavity. We have so far achieved quality factors of $2000 - 2500$ with this cavity design while maintaining significant overlap between the two modes. For this particular system the separation between the two peaks is ~ 0.5 nm.

Lastly, we study the effects of the drive laser polarization to verify that the QD can couple to both cavity modes, and to examine the polarization properties of the two cavity modes. Fig. 5.20a,b show the PL spectrum of the bimodal cavity system (mode M1 and M2), with a coupled QD (D1) at two different temperatures 20K and

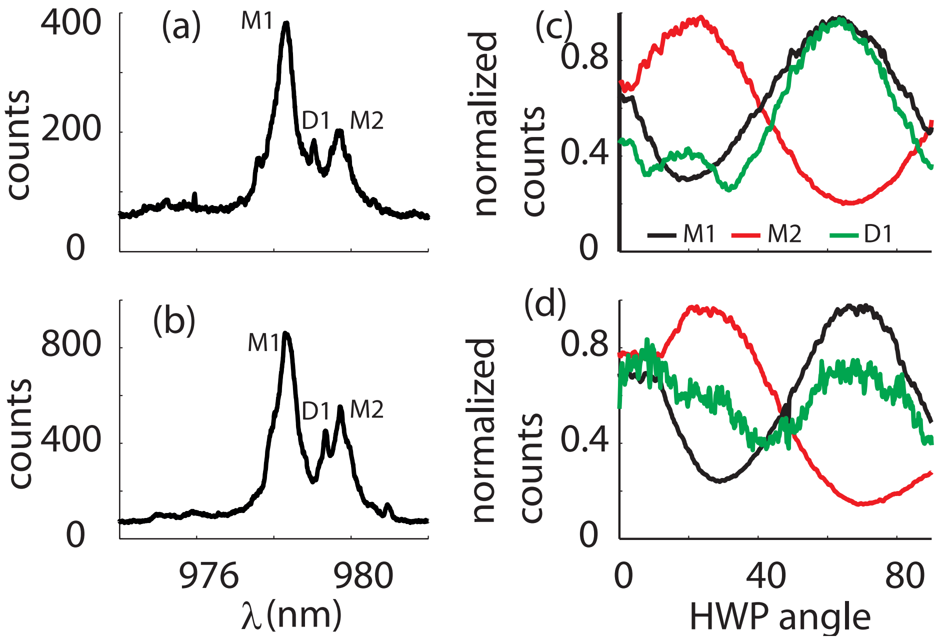

Figure 5.20: (a), (b) PL spectrum of the bimodal (H2) cavity and a coupled QD at two different temperatures 20K (a) and 30K (b). The two modes are denoted as M1 and M2 and the QD is denoted as D1. (c),(d) Polarization dependence of the cavity modes (red and black plots) and the QD (green plot) at two different temperatures: 20K (a) and 30K (b).

30K. Fig. 5.20c,d show the polarization dependence of the two modes and the QD. At both temperatures, the cavities are of orthogonal polarizations. However, in Fig. 5.20c the QD D1 mostly follows cavity mode M1. With increasing temperature, the QD moves closer to mode M2, and the polarization dependence of D1, follows both modes M1 and M2 (Fig. 5.20d).

Based on these preliminary results, we expect that modest fabrication improvements increasing the frequency overlap of the two modes or implementation of in-situ frequency tuning of the two modes will allow us to implement the proposed scheme.

In summary, we introduced a scheme for generation of sub-Poissonian light in a CQED system with a bimodal cavity and provided a theoretical and numerical analysis of its performance. For similar system parameters, the bimodal cavity can provide a much better sub-Poissonian character of the transmitted photon stream ($g^{(2)}(0) \sim 0.1$) compared to a single mode cavity ($g^{(2)}(0) \sim 0.9$). We also introduce an equivalent model which explains the effect as an interference between a coherent state and a super-Poissonian state generated by photon-induced tunneling, and a balance between the nonlinearity and the loss of the system is required to observe it. Moreover, the effect disappears in the absence of the cavity loss ($g/\kappa \to \infty$). This interplay between loss and nonlinearity has great potential to be exploited for the design of realistic coupled cavity arrays for efficient quantum simulation.

Chapter 6

Cavity QED with a Single Quantum Dot in a Photonic Molecule

In this chapter, we demonstrate cavity QED effects for a quantum dot coupled to a photonic molecule, consisting of a pair of coupled photonic crystal cavities. We show anti-crossing between the quantum dot and the two super-modes of the photonic molecule, signifying achievement of the strong coupling regime. From the anti-crossing data, we estimate the contributions of both mode-coupling and intrinsic detuning to the total detuning between the super-modes. Such a configuration is useful both for nonclassical light generation and for quantum simulation of exotic many-body systems.

6.1 Introduction

As described in the previous chapters, a single QD coupled to a PC cavity is an important building block for integrated nanophotonic quantum information processing devices [6]. However, all of the CQED effects demonstrated so far in this system involve a single cavity. Although numerous theoretical proposals employing multiple cavities coupled to quantum dots exist in the literature [93, 94, 95], experimental development in this direction is rather limited. Recently it has been reported that strongly sub-Poissonian light can be generated from a pair of coupled cavities containing a single QD [86, 87]. This double cavity, also called a photonic molecule, coupled to a single QD forms the first step towards building an integrated cavity network with coupled QDs. Photonic molecules made of PC cavities were studied previously [96, 97] to observe mode-splitting due to coupling between the cavities. In those studies, a high density of QDs was used merely as an internal light source to generate photoluminescence (PL) under above-band excitation and no quantum properties of the system were studied. In another experiment, a photonic molecule consisting of two micropost cavities was used along with a single QD to generate entangled photons via exciton-biexciton decay, but the QD-cavity system was in the weak coupling regime and the Purcell enhancement was the only CQED effect observed [98].

In this chapter, we demonstrate strong coupling of a photonic molecule with a single QD. We show clear anti-crossing between the QD and two super-modes formed in the photonic molecule. In general, the exact coupling strength between two cavities in a photonic molecule is difficult to calculate, as the observed separation between the two modes has contributions both from the cavity coupling strength as well as from the mismatch between the two cavities due to fabrication imperfections. However, by monitoring the interaction between a single QD and the photonic molecule we can exactly calculate the coupling strength between the cavities and separate the contribution of the bare detuning due to cavity mismatch. In fact, without any coupling between two cavities, one cannot have strong coupling of the QD with both of the observed modes. Hence, the observed anti-crossing of the QD with both modes clearly indicates coupling between the cavities.

6.2 Theory

Let us consider a photonic molecule consisting of two cavities with annihilation operators for their bare (uncoupled) modes denoted by a and b, respectively. We assume that a QD is placed in and resonantly coupled to the cavity described by operator a.

The Hamiltonian describing such a system is:

$$\mathcal{H} = \Delta_o b^\dagger b + J(a^\dagger b + a b^\dagger) + g(a^\dagger \sigma + a\sigma^\dagger) \tag{6.1}$$

where Δ_o is the detuning between the two bare cavity modes; J and g are, respectively, the inter-cavity and dot-cavity coupling strength; σ is the QD lowering operator; and the resonance frequency ω_0 of the cavity with annihilation operator a is assumed to be zero. We now transform this Hamiltonian by mapping the cavity modes a and b to the bosonic modes α and β introduced as $a = \cos(\theta)\alpha + \sin(\theta)\beta$ and $b = \sin(\theta)\alpha - \cos(\theta)\beta$. We note that this mapping maintains the appropriate commutation relations between operators a and b. Under these transformations we can decouple the two cavity modes (α and β) for the following choice of θ:

$$\tan(2\theta) = -\frac{2J}{\Delta_o} \tag{6.2}$$

Under this condition the transformed Hamiltonian becomes:

$$\begin{aligned} \mathcal{H} &= \alpha^\dagger\alpha(\Delta_o \sin^2(\theta) + J\sin(2\theta)) + g\cos(\theta)(\alpha^\dagger\sigma + \alpha\sigma^\dagger) \\ &+ \beta^\dagger\beta(\Delta_o \cos^2(\theta) - J\sin(2\theta)) + g\sin(\theta)(\beta^\dagger\sigma + \beta\sigma^\dagger) \end{aligned}$$

Therefore, a QD coupled to a photonic molecule has exactly the same eigen-structure as two detuned cavities with the QD coupled to both of them (from the equivalence of the two expressions above for the Hamiltonian $\mathcal{H}$). The super-modes of the transformed Hamiltonian α and β will be separated by $\Delta = \sqrt{\Delta_o^2 + 4J^2}$ (obtained by subtracting the terms multiplying $\alpha^\dagger\alpha$ and $\beta^\dagger\beta$, under the conditions of Eq.6.2) and the interaction strength between the QD and the super-modes will be $g_1 = g\cos(\theta)$ and $g_2 = g\sin(\theta)$. If the two cavities are not coupled ($J = 0$ and $\theta = 0$), we can still observe two different cavity modes in the experiment due to Δ_o, the intrinsic detuning between two bare cavities. However, if we tune the QD across the two cavities in this case, we will observe QD-cavity interaction only with one cavity mode (in this case α, as the term coupling β to the QD in the transformed Hamiltonian will vanish, as a result of $\sin(\theta) = 0$). In other words, in this case the QD is spatially located in only one cavity and cannot interact with the other, spatially distant and decoupled cavity. Fig. 6.1 shows the numerically calculated cavity transmission spectra (proportional to $\langle a^\dagger a\rangle + \langle b^\dagger b\rangle$) when the QD is tuned across the two cavity resonances. When the two cavities are coupled ($J \neq 0$), we observe anti-crossing between each cavity mode and the QD (Fig. 6.1a). However, only one anti-crossing is observed when the cavities are not coupled (Fig. 6.1b).

6.3 Characterization of photonic molecule

The actual experiments are performed with self-assembled InAs QDs embedded in GaAs. We fabricated two different types of coupled cavities: in one case, the two cavities are offset at a 30^o angle (inset of Fig. 6.2a) and in the other the two cavities are laterally coupled (inset of Fig. 6.2b). In the first case the coupling between the cavities is stronger as the overlap between the electromagnetic fields confined in the cavities is larger along the 30^o angle. Figs. 6.2a,b show the typical PL spectra of these two different types of coupled cavities for different spacing between the cavities. A clear decrease in the frequency separation between the cavities is observed with increasing spatial separation. Note that the consistency of this trend between different fabrication runs already indicates that this frequency separation cannot be purely due to the fabrication-related intrinsic detuning between the two cavities. Nevertheless, it is very difficult to quantify how much of the separation is due to coupling (J), and how much is due to intrinsic detuning (Δ_o) of the cavity resonances. However, we will show that by observing the anti-crossing between the QD and the two modes we can conclusively determine both J and Δ_o.

6.4 Strong coupling between a single QD and a photonic molecule

First, we investigate the strong coupling between a single QD and the photonic molecule. For this particular experiment, we used a photonic molecule consisting of cavities separated by 4 holes along the 60^o angle. In practice it is not trivial to

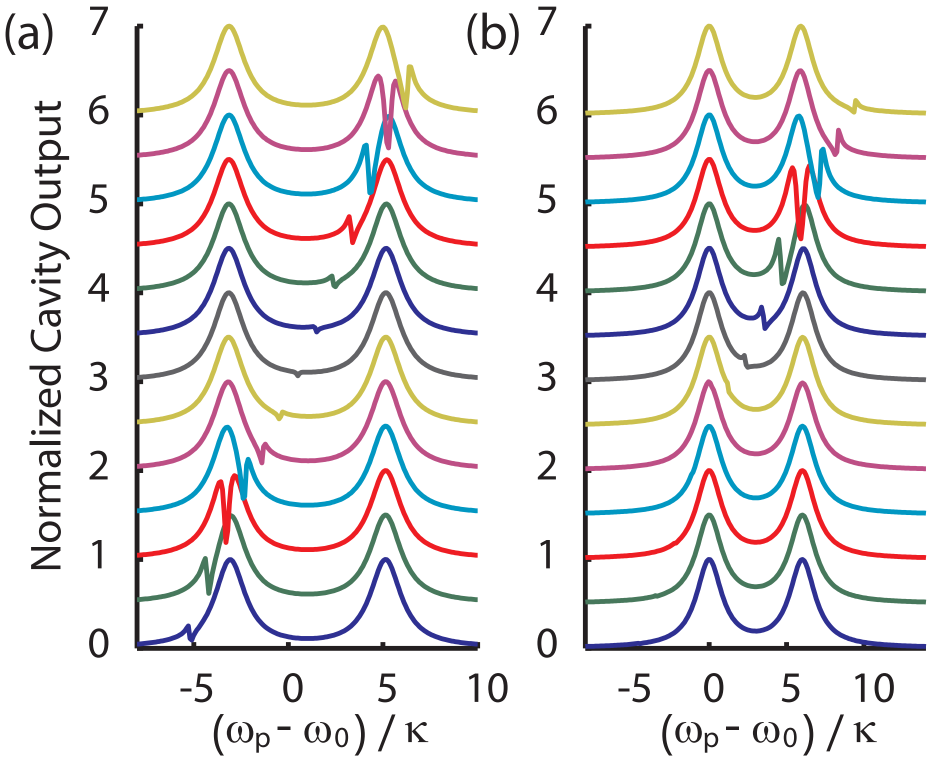

Figure 6.1: Numerically calculated cavity transmission spectra when the QD resonance is tuned across the two cavity resonances. (a) Anticrossing is observed between the quantum dot and both cavity modes when the two cavities are coupled (coupling rate between the two cavities is $J/2\pi = 80$ GHz). (b) When the two cavities are not coupled ($J = 0$), we observe anti-crossing in only one cavity. Parameters used for the simulation: cavity decay rate $\kappa/2\pi = 20$ GHz (for both cavities); QD dipole decay rate $\gamma/2\pi$=1 GHz; dot-cavity coupling rate of $g/2\pi = 10$ GHz; intrinsic detuning between the bare cavity modes $\Delta_o/2\pi = 40$ GHz for (a) and 120 GHz for (b). The plots are vertically offset for clarity. The horizontal axis corresponds to the detuning of the probe laser frequency ω_p from the cavity a resonance ω_0 in units of cavity field decay rate.

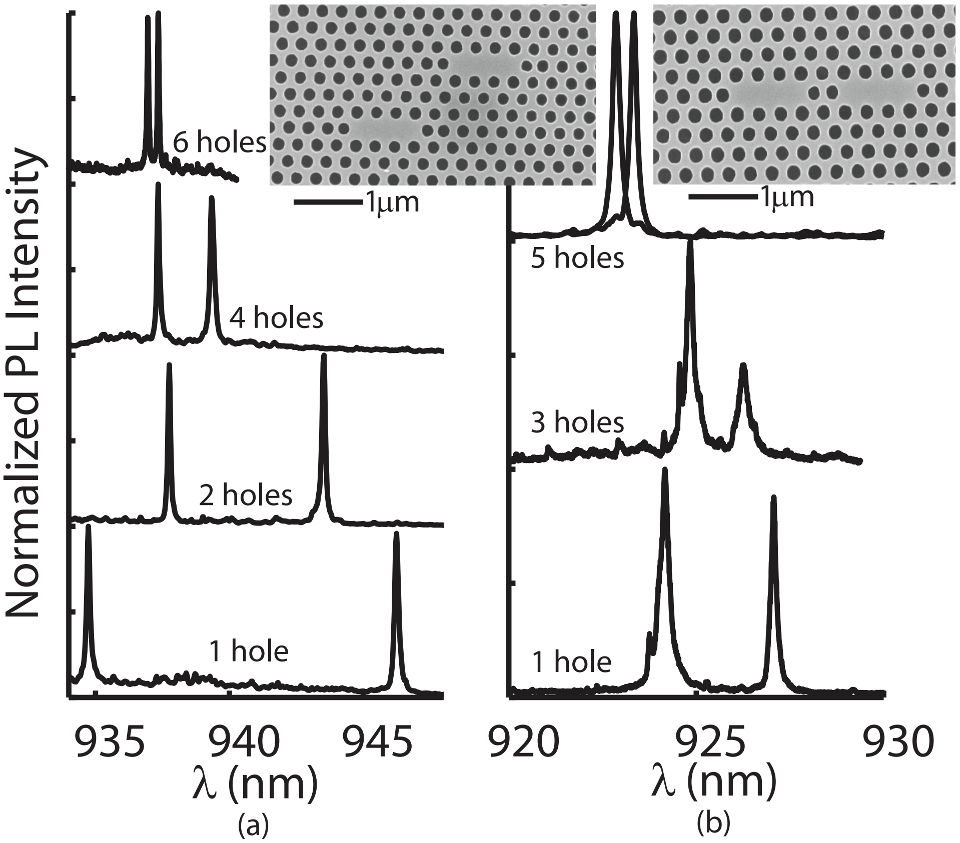

(a)

(b)

Figure 6.2: Photoluminescence spectra of the coupled cavities for different hole spacings between two cavities: (a) the cavities are diagonally placed and separated at an angle of 60^o (see the inset for a scanning electron micrograph (SEM)); (b) the cavities are laterally separated (see the inset for SEM). A decrease in the wavelength separation between two cavity modes is observed with increasing spatial separation between the cavities (i.e., with increasing number of holes inserted in between the two cavities). For the diagonally placed cavities the holes are counted along the 60^o direction. A much larger separation is observed in (a) when the cavities are coupled at an angle compared to the lateral coupling (b).

tune the QD over such a long wavelength range as required by the observed separation of the two cavity peaks. Hence we use two different tuning techniques: we tune the cavity modes by depositing nitrogen on the cavity [99], and then tune the QD resonance across the cavity resonance by changing the temperature of the system. We observe clear anti-crossings for both the modes as shown in Figs. 6.3a,b. Fig. 6.3a is obtained by temperature-tuning the QD across the longer-wavelength cavity mode before nitrogen deposition. We then perform the nitrogen deposition to red-shift the cavity resonances, and repeat the temperature tuning to scan QDs across cavities. Since nitrogen tuning does not shift QDs and shifts only cavities, we always scan the same QD through cavity resonances. Fig. 6.3b shows the anti-crossing between the QD and the shorter-wavelength cavity mode. The nitrogen and the temperature tuning do not cause a significant change in the coupling and the detuning between the cavities, as confirmed in the experiments described below.

We perform curve-fitting for the PL spectra when the QD is resonant to the cavity super-modes and estimate the system parameters (Figs. 6.4a,b). The super-mode at shorter (longer) wavelength is denoted as sm1 (sm2). As the detuning between the super-modes is much larger than the vacuum Rabi spitting caused by the QD, we can assume that when the QD is resonant to sm1(2), its interaction with sm2(1) is negligible. Therefore, we can fit the PL spectra of sm1 (sm2) modes exhibiting Rabi splitting individually. For sm1, we extract from the fit the field decay rate $\kappa_1/2\pi = 22.4$ GHz and the QD-field interaction strength $g_1/2\pi = 14.2$ GHz (Fig. 6.4b); for sm2, $\kappa_2/2\pi = 16.7$ GHz and $g_2/2\pi = 23.7$ GHz (Fig. 6.4a). We note that we can achieve very high quality factors ($\sim 7,000 - 10,000$) of the coupled cavity modes as seen from the extracted κ values. We also estimate the total detuning between two observed modes as $\Delta/2\pi = 0.7$ and 0.72 nm before and after nitrogen tuning. This minimal difference in Δ resulting from the nitrogen tuning does not impact our further analysis, and we take Δ to be the average of these two values. The change in the cavity field decay rates arising from the nitrogen deposition is also minimal. From these data, we use the relations $\theta = \arctan(g_2/g_1)$, $\tan(2\theta) = -2J/\Delta_o$ and $\Delta = \sqrt{4J^2 + \Delta_o^2}$ to obtain: $J/2\pi \approx 110$ GHz and $\Delta_o/2\pi \approx 118$ GHz.

We now numerically simulate the performance of such a QD-photonic molecule

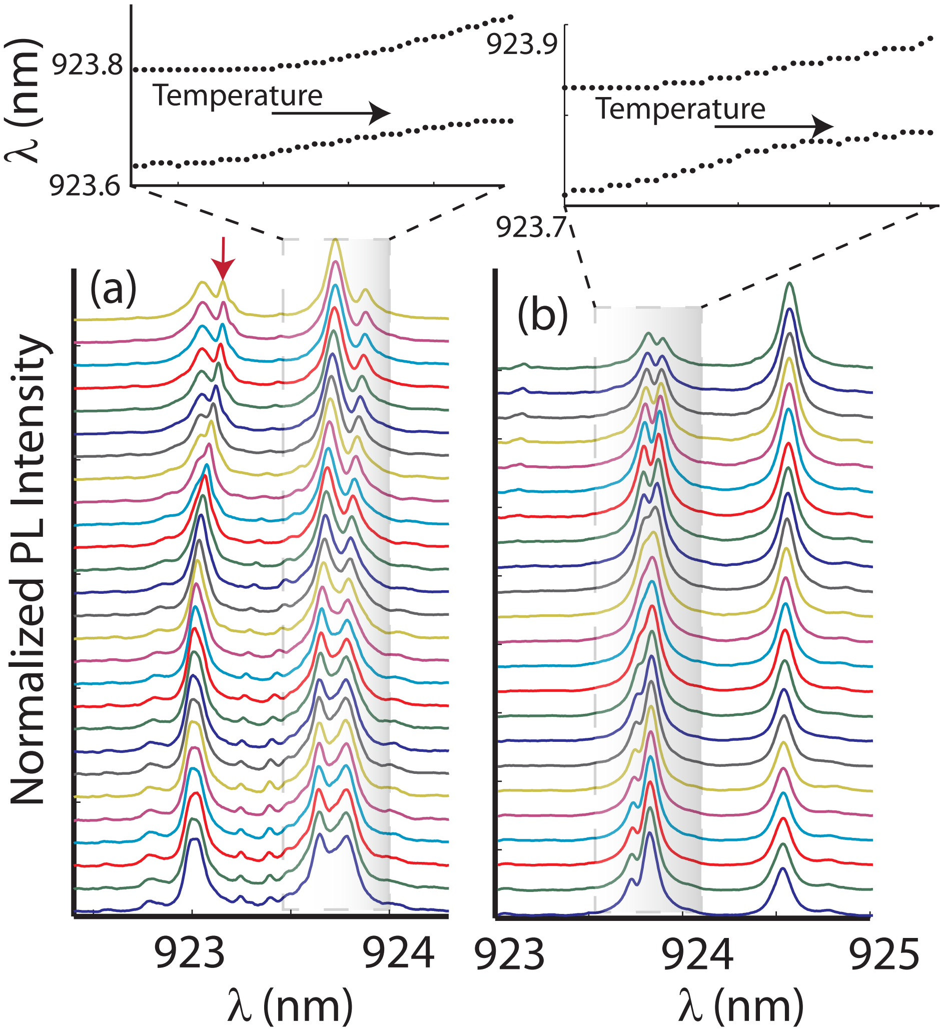

Figure 6.3: Normalized PL intensity plotted when we tune the QD across the cavity resonance by temperature: (a) before nitrogen deposition (i.e., the QD is temperature tuned across the longer wavelength resonance), and (b) after nitrogen deposition (which red-shifts the cavity resonances and allows us to temperature tune the QD across the shorter wavelength resonance). Clear anti-crossings between the QD and the cavity are observed for both super-modes. In both cases, the temperature is increased from bottom to top (the plots are vertically offset for clarity). In the inset the resonances of the two anti-crossing peaks (as extracted from curve-fitting) are plotted. Since nitrogen tuning affects only cavity resonances (not QD), the same QD is tuned across both super-modes. Red arrow in figure (a) shows another blue-shifted QD that enters this spectral range during the temperature tuning, but it is only weakly coupled to the lower super-mode, as explained in the text, and does not affect experimental results.

for generation of sub-Poissonian light using the quantum optical master equation approach [41]. Two bare cavity modes are separated by $\Delta_o/2\pi = 118$ GHz; a QD is resonant and strongly coupled to one of the modes (a) with interaction strength $g/2\pi = 27.6$ GHz ($g = \sqrt{g_1^2 + g_2^2}$, where g_1 and g_2 are the two values of QD-cavity interaction strengths obtained by fitting the PL spectra); mode b is the empty cavity. The mode b is driven and the second order autocorrelation $g^2(0) = \frac{\langle b^\dagger b^\dagger b b\rangle}{\langle b^\dagger b\rangle^2}$ of the transmitted light through cavity b is calculated [87]. We also assume the two cavities to have the same cavity decay rate, which is an average of the cavity decay rates measured from the two super-modes. Note however that, having slightly different decay rates does not significantly affect the performance of the system. The numerically simulated cavity b transmission and $g^2(0)$ of the transmitted light is shown in Figs. 6.4c,d. We note that with our system parameters we can achieve strongly sub-Poissonian light with $g^2(0) \sim 0.03$. Unfortunately, in practice it is very difficult to drive only one cavity mode without affecting the other mode due to the spatial proximity of two cavities. This individual addressability is critical for good performance of the system [87] and to retain such a capability in a photonic molecule the cavities should be coupled via a waveguide [100].

6.5 Comparison with bimodal cavity

We note that generation of sub-Poissonian light with photonic molecule is somewhat related to the proposal of generating sub-Poissonian light in a bimodal cavity as described in the previous chapter. Figure 6.5 a,b shows the transmitted cavity output and $g^{(2)}(0)$ for two different cases: the photonic molecule and the bimodal cavity. We observe that the performance for both cases are comparable. However, for the photonic molecule, we need to maintain both individual addressability and high coupling strength between the cavities. In the nanophotonics platform this requirement is challenging, as generally the inter-cavity coupling is achieved by spatial proximity. Although, wave-guide coupling can be employed to mitigate the problem [100], that solution brings the added complexity of engineering the cavity-to-waveguide coupling.

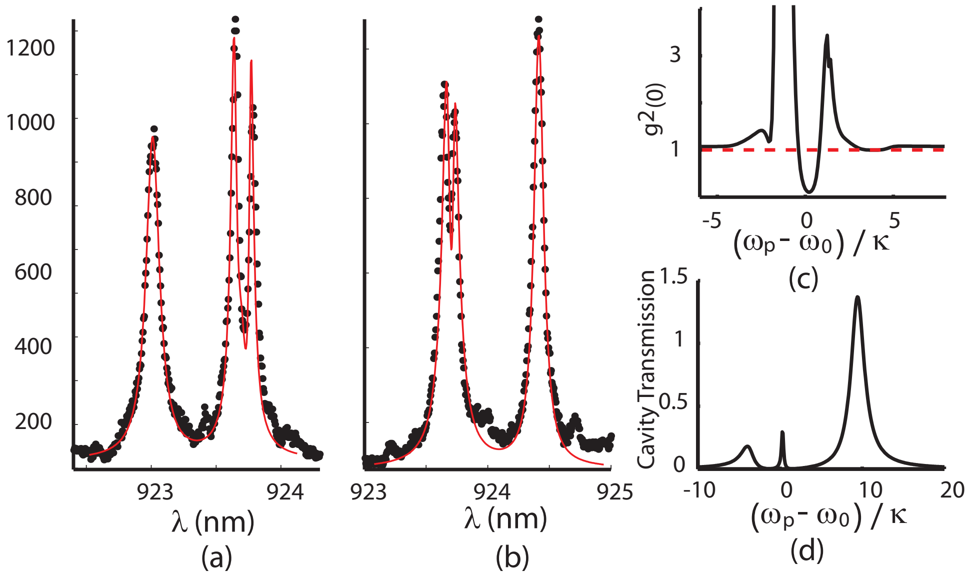

Figure 6.4: QD-photonic molecule spectrum, (a) when the QD is resonant with super-mode sm2 and (b) when the QD is resonant with super-mode sm1. From the fit we extract the system parameters (see text). Numerically simulated (c) second order autocorrelation $g^2(0)$ and (d) transmission from cavity b, as a function of laser frequency, with the experimental system parameters that were extracted from the fits.

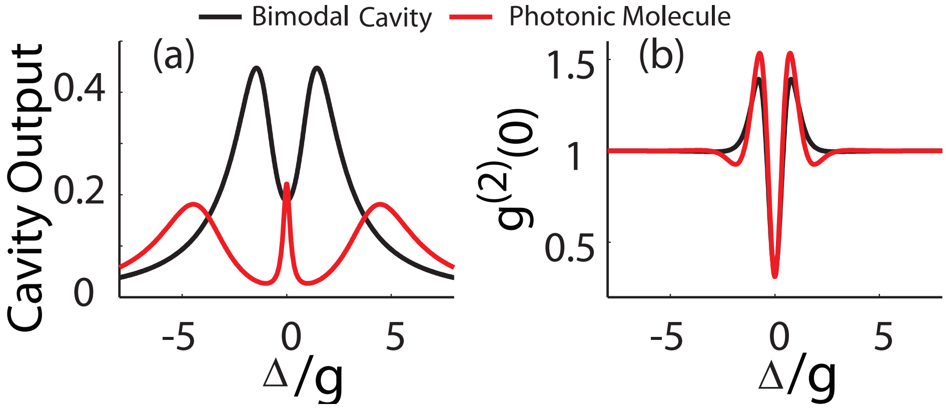

Figure 6.5: (a) Cavity transmission for two cases: bimodal cavity and photonic molecule. (b) Second order autocorrelation $g^{(2)}(0)$ for these two cases. Parameters used for the simulations: QD-cavity interaction strengths $g/2\pi = g_a/2\pi = g_b/2\pi = 10$ GHz; cavity field decay rates $\kappa_a/2\pi = \kappa_b/2\pi = 20$ GHz; coupling strength for the photonic molecule $J/2\pi = 40$ GHz; dipole decay rate $\gamma/2\pi = 1$ GHz.

Chapter 7

Phonon-mediated off-resonant interaction in a quantum dot-cavity system

Phonon-mediated coupling between a self-assembled semiconductor quantum dot (QD) and a semiconductor microcavity is a recently discovered phenomenon unique to solid state cavity quantum electrodynamics. The physical effects described in the previous chapters (like photon blockade, electro-optic modulation or all-optical switching) can be well explained assuming that the QD behaves just like a two level atomic system, but explaining this new off-resonant interaction requires a deeper understanding of the role that phonons play in the solid state. The prospect of strongly enhanced light-matter interactions between a QD and an optical field has served as a focal point in integrating QDs with high quality factor (Q) optical cavities, with maximum enhancement occurring when the QD and the cavity are resonant and the QD is spatially aligned to the cavity mode. Since achieving this maximum enhancement is difficult due to limitations in growth and fabrication techniques, the recently observed coupling between a single QD and a detuned optical cavity mode [2, 101] has spurred considerable theoretical [102, 41] and experimental interest in determining the physical mechanism behind such coupling as well as in possible applications. This phenomenon has been observed both in photoluminescence studies under above-band pumping [32, 103, 104, 105, 106] and under resonant excitation of the QD [2, 101]. The coupling observed via photoluminescence is attributed to several phenomena including the electron-phonon interactions [102, 107, 108, 109, 110, 111], multi-exciton complexes [59] and charges in the vicinity of the QD [112]. To isolate the role of phonons in off-resonant QD-cavity coupling, studies employing resonant excitation of the QD are preferable as they avoid possible complications arising from multi-excitonic complexes and nearby charges generated via above band pumping. A recent experiment, although performed in photoluminescence, eliminated possible multi-excitonic processes by novel QD growth techniques [113]. Apart from the fundamental interest in identifying the mechanism behind this off-resonant coupling [113, 59, 102, 107, 108, 109], this effect can be used to probe the coherent interaction of the QD with a strong laser [42] as well as the cavity-enhanced AC stark shift of a QD [114]. These results demonstrate that the off-resonant cavity constitutes an efficient read-out channel for the QD states.

In this chapter, we theoretically and experimentally investigate off-resonant dot-cavity coupling under resonant excitation of the QD. First we provide a theoretical framework to explain such coupling. We model this coupling as an incoherent phonon-mediated channel. Then we present experimental results showing some applications of this off-resonant coupling, namely, making a single photon source with photon frequency controlled by the cavity resonance, as well as using it for resonant QD spectroscopy. Finally, we show the signature of such phonon-mediated coupling between two off-resonant QDs.

7.1 Theory

In this section, we propose a model for phonon mediated off-resonant quantum dot-cavity coupling and use it to successfully explain the observed results from resonant QD spectroscopy. We first theoretically model the coupling via pure QD dephasing. Then, we propose a new model where the phonon-mediated coupling is enhanced by the cavity. We compare these two models and find that they predict qualitatively similar signatures in resonant QD spectroscopic studies, such as power broadening and QD saturation [4, 115] (explained later in this chapter). However, in the cavity-enhanced model, the coupling is maintained even at very large QD-cavity detunings (~ 3 meV). Thus our results demonstrate that phonon mediated processes effectively extend the detuning range in which off-resonant QD-cavity coupling may occur beyond that given by pure dephasing processes. Simulated QD spectroscopy results also exhibit an inherent asymmetry between phonon emission and absorption rate, depending on whether the QD is red or blue detuned from the cavity. To contrast the two theoretical models, we experimentally study several QDs that are off-resonantly coupled to a photonic crystal cavity mode. Analysis of the detuning dependence of the off-resonant coupling shows that pure QD dephasing is incapable of describing experimentally observed results. The phonon-mediated model, on the other hand, provides an experimentally consistent and intuitive picture that accurately accounts for the persistence of off-resonant coupling at large QD-cavity detunings.

7.1.1 Theory with pure QD dephasing

In addition to system losses (the cavity and the QD decay), phonons in the solid state system destroy the coherence of the exciton. This is generally modeled by adding an additional incoherent decay term $2\gamma_d\mathcal{L}[\sigma^\dagger\sigma]$ to the master equation, where $2\gamma_d$ is the pure dephasing rate of the QD. This term destroys the polarization of the QD without affecting the population of the QD. The dissipations of the QD polarization and population ($\sigma_z = [\sigma^\dagger, \sigma]$) is described by the mean-field equations:

$$\frac{d\langle\sigma\rangle}{dt} = -(\gamma+\gamma_d)\langle\sigma\rangle \tag{7.1}$$

$$\frac{d\langle\sigma_z\rangle}{dt} = -2\gamma(1+\langle\sigma_z\rangle) \tag{7.2}$$

The linewidth of the QD, at the zero excitation power limit, is $2(\gamma+\gamma_d)$. However, in this model, the effect of phonons is embedded in the phenomenological pure dephasing rate γ_d, which affects only the QD and does not include any cavity effects.

7.1.2 Theory with cavity enhanced phonon process

We now propose a different model for off-resonant dot-cavity coupling, where the phonon-mediated coupling strength is affected by both the cavity and the QD. In this case, the effect of phonons can be modeled by adding two additional incoherent decay terms to the master equation. For a blue-detuned QD (Fig. 7.1 a) the master equation has the form

$$\begin{aligned} \frac{d\rho}{dt} &= -i[H,\rho] + 2\kappa\mathcal{L}[a] + 2\gamma\mathcal{L}[\sigma] \\ &\quad +2\gamma_r\bar{n}\mathcal{L}(\sigma^\dagger a) + 2\gamma_r(\bar{n}+1)\mathcal{L}(\sigma a^\dagger) \end{aligned} \tag{7.3}$$

where $2\gamma_r$ is the effective decay rate of the QD exciton states via the emission of a phonon and a photon at the off-resonant cavity frequency and $\bar{n}(\Delta,T) = (e^{\hbar\Delta/k_B T} - 1)^{-1}$ is the average number of phonons at the dot-cavity detuning Δ, which are present in the system at thermal equilibrium with the reservoir at a temperature T. The analysis for a QD red detuned from the cavity (Fig. 7.1 b) can be carried out in a similar manner by replacing the final two terms of Eqn. 7.3 with $2\gamma_r\bar{n}\mathcal{L}(\sigma a^\dagger)$ and $2\gamma_r(\bar{n}+1)\mathcal{L}(\sigma^\dagger a)$.

We use the level diagram as shown in Fig. 7.1 a to model the effect of phonons explicitly. The Hamiltonian of the system is given by

$$H = H_0 + H_I \tag{7.4}$$

where,

$$H_0 = \omega_1|1\rangle\langle 1| + \omega_2|2\rangle\langle 2| + \omega_3|3\rangle\langle 3| + \omega a^\dagger a + \sum_j \nu_j b_j^\dagger b_j \tag{7.5}$$

and

$$H_I = g_v(a|3\rangle\langle 1| + a^\dagger|1\rangle\langle 3|) + \sum_j g_{23}^j(b_j^\dagger|3\rangle\langle 2| + b_j|2\rangle\langle 3|) \tag{7.6}$$

where, $|i\rangle\langle i|$ is the population operator for i^{th} level; a is the annihilation operator for the cavity mode; b_j is the annihilation operator for a phonon in the j^{th} mode. ω_i , ω and ν_j are the frequencies of the i^{th} energy level, cavity resonance and a phonon in the j^{th} mode. g_v signifies the interaction strength between the cavity and the virtual

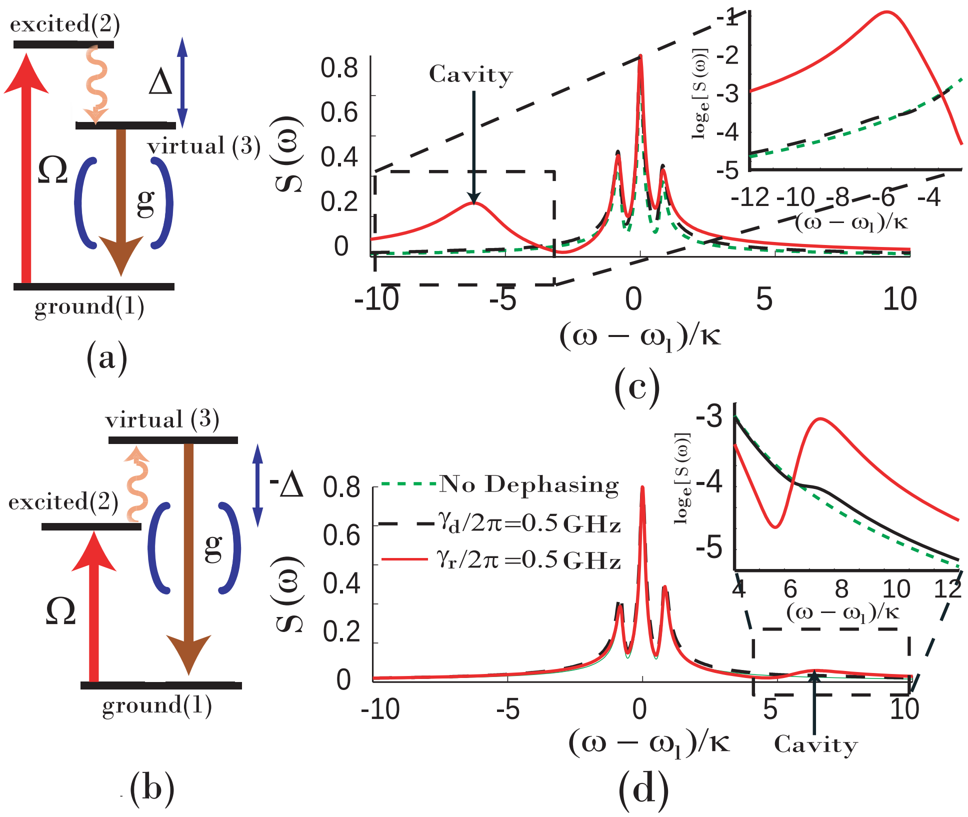

Figure 7.1: (a),(b) Energy levels of the coupled QD/cavity system where the QD is blue (a) and red (b) detuned from the cavity. A laser drives the quantum dot (transition between ground state (1) and excited state (2)) resonantly. The excited state (2) can decay via two paths: the first is by direct decay back to the ground state (1) via the spontaneous emission; the second is by indirect decay via the emission (Fig. 7.1 a) or absorption (Fig. 7.1 b) of a phonon (transition (2) to (3)) and subsequent emission of a photon at the cavity frequency (transition (3) to (1)). (c), (d) Emission $S(\omega)$ as a function of frequency ω for a resonantly driven QD, that is blue (c) and red (d) detuned from the cavity, where ω_l is the laser frequency. Three different cases are considered: without any dephasing; with pure dephasing and with a cavity enhanced phonon process. We observe the Mollow triplet at the QD frequency in all three cases. The insets of (c) and (d) show an enlarged view of the emission at the cavity frequency. For the simulation we assume $g/2\pi = \kappa/2\pi = 20$ GHz; $\gamma/2\pi = 1$ GHz; $\Omega/2\pi = 6$ GHz; QD-cavity detuning $\Delta = \pm 6\kappa$.

transition and g_{23}^{j} is the interaction strength between the QD exciton and a j^{th} mode phonon. We note that this interaction Hamiltonian is valid only for the level structure as in Fig. 7.1 a, where the cavity is at lower energy than the QD. For the situation in Fig. 7.1 b (where the cavity is of higher energy compared to the QD), the interaction Hamiltonian H_I is given by

$$H_I = g_v(a|3\rangle\langle 1| + a^\dagger|1\rangle\langle 3|) + \sum_j g_{23}^{j}(b_j|3\rangle\langle 2| + b_j^\dagger|2\rangle\langle 3|) \tag{7.7}$$

In the following derivation, we will use the situation shown in Fig. 7.1 a.

If we define the QD resonance frequency as ω_a, then $\omega_a = \omega_2 - \omega_1$; and the cavity frequency is given by $\omega_c = \omega_3 - \omega_1$. Then the QD-cavity detuning is given by $\Delta = \omega_2 - \omega_3$. Defining $\sigma_{ij} = |i\rangle\langle j|$, we can write

$$\begin{aligned} \dot{\sigma}_{13} &= -i[\sigma_{13}, H_0 + H_I] \qquad (7.8) \\ &= -i\omega_c\sigma_{13} - ig_v a(\sigma_{11} - \sigma_{33}) - i\sum_j g_{23}^{j} b_j^\dagger \sigma_{12} \end{aligned}$$

Similarly,

$$\begin{aligned} \dot{\sigma}_{23} &= -i[\sigma_{23}, H_0 + H_I] \qquad (7.9) \\ &= i\Delta\sigma_{23} - ig_v a\sigma_{21} - i\sum_j g_{23}^{j} b_j^\dagger(\sigma_{22} - \sigma_{33}) \end{aligned}$$

Separating the slow and the fast components of the operators, we can write

$$\sigma_{13} = \tilde{\sigma}_{13}e^{-i\omega_c t} \tag{7.10}$$

$$\sigma_{23} = \tilde{\sigma}_{23}e^{-i\omega_j t} \tag{7.11}$$

$$\sigma_{12} = \tilde{\sigma}_{12}e^{-i(\omega_c - \omega_j)t} \tag{7.12}$$

$$a = \tilde{a}e^{-i\omega_c t} \tag{7.13}$$

$$b_j^\dagger = \tilde{b}_j^\dagger e^{-i\omega_j t} \tag{7.14}$$

Hence the equations governing the dynamics of the system can be written as

$$\dot{\tilde{\sigma}}_{13} = -ig_v\tilde{a}(\tilde{\sigma}_{11} - \tilde{\sigma}_{33}) - i\sum_j g_{23}^{j}\tilde{b}_j^\dagger\tilde{\sigma}_{12} \tag{7.15}$$

and

$$\dot{\tilde{\sigma}}_{23} = i(\Delta - \omega_j)\tilde{\sigma}_{23} - ig_v\tilde{a}\tilde{\sigma}_{21} - i\sum_j g_{23}^j \tilde{b}_j^\dagger(\tilde{\sigma}_{22} - \tilde{\sigma}_{33}) \tag{7.16}$$

As level 3 is a virtual level, it is never populated. Hence by adiabatic elimination, using $\dot{\tilde{\sigma}}_{13} = \dot{\tilde{\sigma}}_{23} = 0$, we obtain

$$\tilde{\sigma}_{23} = \frac{g_v\tilde{a}\tilde{\sigma}_{21} + \sum_j g_{23}^j \tilde{b}_j^\dagger(\tilde{\sigma}_{22} - \tilde{\sigma}_{33})}{\Delta - \omega_j} \tag{7.17}$$

and

$$\tilde{\sigma}_{12} = \frac{-g_v\tilde{a}(\tilde{\sigma}_{11} - \tilde{\sigma}_{33})}{\sum_j g_{23}^j \tilde{b}_j^\dagger} \tag{7.18}$$

Using these values, we can find the interaction Hamiltonian. The first term $g_v(a\sigma_{31} + a^\dagger\sigma_{13})$ denotes the coherent dynamics. The second term, which signifies the effect of phonons, can be written as (using the Eqns. 7.17 and 7.18)

$$\begin{aligned}
H_{ph} &= \sum_j g_{23}^j(b_j^\dagger\sigma_{32} + b_j\sigma_{23}) && (7.19)\\
&= \sum_j g_{23}^j(\tilde{b}_j^\dagger\tilde{\sigma}_{32} + \tilde{b}_j\tilde{\sigma}_{23}) && (7.20)\\
&= \sum_j \frac{g_{23}^j g_v}{\Delta - \omega_j}(\tilde{b}_j^\dagger\tilde{a}^\dagger\tilde{\sigma}_{12} + \tilde{b}_j\tilde{a}\tilde{\sigma}_{21}) && (7.21)\\
&\quad + \sum_j \frac{(g_{23}^j)^2}{\Delta - \omega_j}(\tilde{\sigma}_{22} - \tilde{\sigma}_{33})(\tilde{b}_j^\dagger\tilde{b}_j^\dagger + \tilde{b}_j\tilde{b}_j) && (7.22)
\end{aligned}$$

The second term involves two-phonon processes which are less likely. If we neglect them, we can model the effect of phonons as follows:

$$H_{ph} = \sum_j \frac{g_{23}^j g_v}{\Delta - \omega_j}(\tilde{b}_j^\dagger\tilde{a}^\dagger\tilde{\sigma}_{12} + \tilde{b}_j\tilde{a}\tilde{\sigma}_{21}) \tag{7.23}$$

We can write this Hamiltonian as

$$H_{ph} = (\tilde{a}^\dagger\tilde{\sigma}_{12}\tilde{\Gamma}^\dagger + \tilde{a}\tilde{\sigma}_{21}\tilde{\Gamma}) \tag{7.24}$$

where, the operator $\tilde{\Gamma}$ can be written as

$$\tilde{\Gamma} = \sum_j \frac{g_{23}^j g_v}{\Delta - \omega_j}\tilde{b}_j \tag{7.25}$$

and

$$\Gamma = \sum_j \frac{g_{23}^j g_v}{\Delta - \omega_j} b_j e^{-i\omega_j t} \tag{7.26}$$

To obtain the familiar Lindblad term, we take the partial trace of the correlation between the reservoir operators over the reservoir variables. The correlation is given by

$$\langle \Gamma^\dagger(t')\Gamma(t)\rangle_R = \sum_j \left| \frac{g_{23}^j g_v}{\Delta - \omega_j} \right|^2 e^{-i\omega_j(t-t')} \langle b_j^\dagger b_j \rangle_R \tag{7.27}$$

As the operators b_j are bosonic and the system is in thermal equilibrium with a bath at temperature T, using the relation

$$\langle b_j^\dagger b_j \rangle_R = \bar{n}(\omega_j, T) = \frac{1}{e^{\frac{\hbar\omega_j}{k_B T}} - 1} \tag{7.28}$$

we find

$$\langle \Gamma^\dagger(t')\Gamma(t)\rangle_R = \sum_j \left| \frac{g_{23}^j g_v}{\Delta - \omega_j} \right|^2 e^{-i\omega_j(t-t')} \bar{n}(\omega_j, T) \tag{7.29}$$

and

$$\langle \Gamma(t')\Gamma^\dagger(t)\rangle_R = \sum_j \left| \frac{g_{23}^j g_v}{\Delta - \omega_j} \right|^2 e^{-i\omega_j(t-t')} (\bar{n}(\omega_j, T) + 1) \tag{7.30}$$

From the correlation, we find that the phonons with frequency Δ (corresponding to the difference between levels $|2\rangle$ and $|3\rangle$, i.e., QD-cavity mode detuning), have the maximum contribution in the interaction Hamiltonian. In the Born-Markov approximation, we can model the electron-phonon interaction (for Fig. 7.1 a) as an incoherent decay process by adding two extra terms to the master equation: $2\gamma_r \bar{n}\mathcal{L}(\sigma^\dagger a)$ and $2\gamma_r(\bar{n}+1)\mathcal{L}(\sigma a^\dagger)$, γ_r being the effective decay rate of the excited QD state and is given by

$$\gamma_r = \frac{1}{2}\sum_j \left| \frac{g_{23}^j g_v}{\Delta - \omega_j} \right|^2 \tag{7.31}$$

For the situation shown in Fig. 7.1 b, the decay terms are given by $2\gamma_r \bar{n}\mathcal{L}(\sigma a^\dagger)$ and $2\gamma_r(\bar{n}+1)\mathcal{L}(\sigma^\dagger a)$. We note that the different rates in both cases are due to an inherent asymmetry between the absorption and emission rates of the phonons.

The decay term $\sigma^\dagger a$ denotes the annihilation of a cavity photon and excitation of the QD, while the term $\sigma a^\dagger$ denotes the creation of a cavity photon and collapse of the QD to its ground state. Each process is then accompanied by the creation (or annihilation) of phonons to compensate for the QD-cavity frequency difference. Only the second process is important for observing cavity emission under resonant excitation of the dot. We also note that the observation of QD emission under resonant excitation of the cavity [2] can be modeled in the same way by changing the coherent driving term from $\Omega(\sigma + \sigma^\dagger)$ to $\Omega(a + a^\dagger)$. In this case, the collapse operator $\sigma^\dagger a$ is important. Similar decay channels have been proposed to model cavity assisted atomic decay [116]. We refer to this process as a cavity-enhanced phonon process.

As an example, consider the case where the QD is blue detuned from the cavity (Fig. 7.1 a). The qualitative nature of the dissipation of the QD polarization and population can be determined from the mean-field equations (in the limit $\bar{n} = 0$):

$$\frac{d\langle\sigma\rangle}{dt} = -\gamma\langle\sigma\rangle - \gamma_r(1 + \langle a^\dagger a\rangle)\langle\sigma\rangle \tag{7.32}$$

$$\frac{d\langle\sigma_z\rangle}{dt} = -2\gamma(1 + \langle\sigma_z\rangle) - 2\gamma_r(1 + \langle a^\dagger a\rangle)(1 + \langle\sigma_z\rangle) \tag{7.33}$$

We notice that unlike the pure dephasing case, both the QD population and polarization are affected by the cavity enhanced phonon process. The linewidth of the QD in the zero excitation power limit is given by $2[\gamma + \gamma_r(1 + \langle a^\dagger a\rangle)]$, which differs qualitatively from the pure QD dephasing model owing to the fact that the presence of cavity photons affects the QD linewidth.

7.1.3 Simulation results

The resonance fluorescence of the coupled system is given by the power spectral density (PSD). As we collect the fluorescence primarily from the cavity, the PSD is calculated as the Fourier transform of the cavity field auto-correlation $S(\omega) = \int_{-\infty}^{\infty}\langle a^\dagger(\tau)a(0)\rangle e^{-i\omega\tau}d\tau$. To determine the two time correlation functions $\langle a^\dagger(\tau)a(0)\rangle$ and, subsequently, the PSD, we use the quantum regression theorem [46].

We simulate the coupled system using numerical integration routines provided in the quantum optics toolbox [49] with realistic system parameters $\kappa/2\pi = g/2\pi = 20$ GHz and $\gamma/2\pi = 1$ GHz. Off-resonant coupling is observed for both strongly ($g > \kappa/2$) and weakly ($g < \kappa/2$) coupled QDs. Figure 7.1 c shows numerically calculated resonance fluorescence spectra obtained from the cavity under resonant excitation of a blue detuned QD for three different cases: no dephasing, pure QD dephasing and no dephasing with a cavity-enhanced phonon process at a bath temperature of 4 K. We first note that no emission is observed at the cavity frequency in the absence of either pure dephasing or a cavity enhanced phonon process (see inset of Fig. 7.1 c). Though the pure dephasing ($\gamma_d/2\pi = 0.5$ GHz) and the cavity-enhanced phonon process ($\gamma_r/2\pi = 0.5$ GHz) cases both show off-resonant cavity emission, the latter shows enhanced cavity emission. In all three cases, we also observe the Mollow triplet at the QD frequency, as expected from QD resonance fluorescence [117]. The Mollow side-band closer to the cavity is enhanced causing an asymmetric triplet. Fig. 7.1 d shows similar spectra for a red-detuned QD. Our model predicts that emission at the cavity frequency is considerably smaller for a red detuned QD than for a blue-detuned one at finite temperatures, as the process for a red-detuned dot relies on a less-likely phonon absorption and not on phonon emission.

We present more simulation results on the off-resonant cavity emission and QD linewidth by two different models: pure QD dephasing and cavity-enhanced phonon process. We observe that the cavity emission I increases almost linearly with the pure QD dephasing rate γ_d [Fig. 7.2 a], but exhibits a nonlinear dependence on the rate γ_r when the coupling is enhanced by the presence of the cavity. Fig. 7.2 b shows $log_e(I)$ as a function of the cavity decay rate κ, for a fixed detuning of $\Delta/2\pi = 200$ GHz. For both models, the emission falls off as $1/\kappa^2$, signifying that the off-resonant coupling does not depend on the overlap between the QD and the cavity spectra.

We now measure the QD line-width $\Delta\omega$ monitoring the cavity emission, while scanning the laser wavelength across the QD resonance, similar to the experiments in Ref. [4]. We observe that at very low excitation power $\Omega/2\pi = 1$ GHz and large QD-cavity detuning $\Delta/2\pi = 12\kappa$, the linewidths of the QD are very close to the theoretical linewidth in the absence of the cavity (shown by the solid black line in Fig. 7.2 c). At a constant QD-cavity detuning and laser excitation power, the QD line-width increases with increasing γ_d and γ_r (Fig. 7.2 c).

In experimental studies, QD saturation and power broadening have been observed with increasing resonant laser excitation power [4, 115]. These phenomena are also

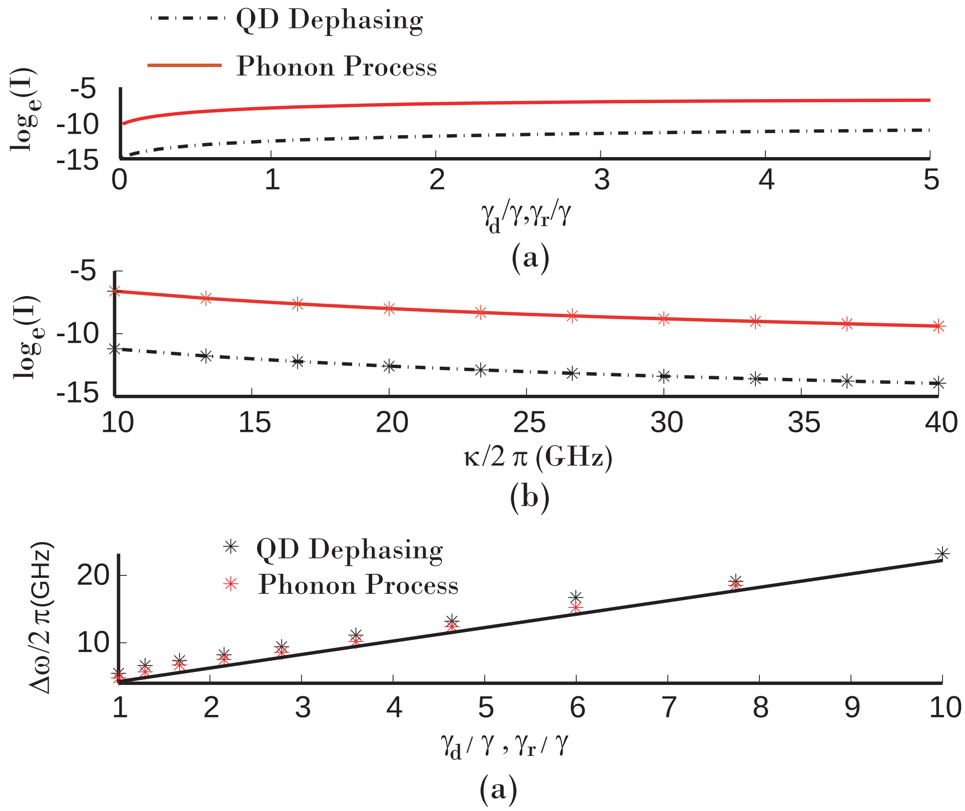

Figure 7.2: Resonance fluorescence I collected from the cavity for a blue-detuned QD ($\Delta > 0$). (a) $log_e(I)$ as a function of the rates γ_d and γ_r (for two models, respectively). $\Delta/\kappa = 10$. (b) $log_e(I)$ as a function of the cavity linewidth κ, when the dot-cavity detuning $\Delta = 10\kappa$. (c) QD linewidth as a function of the rates γ_d and γ_r for pure dephasing and the cavity enhanced phonon process, respectively. In both cases, $\Omega/2\pi = 1$ GHz and $\Delta = 12\kappa$. The solid black line shows the theoretical estimates of the QD linewidth when the laser excitation power is very low and the QD is not significantly perturbed by the cavity. (Parameters used for all the simulations are $g/2\pi = \kappa/2\pi = 20$ GHz; $\gamma/2\pi = 1$ GHz.)

observed in our theoretical simulations for both models of off-resonant coupling. We first treat the case of blue-detuned QD. Fig. 7.3 a plots the cavity fluorescence as a function of the laser Rabi frequency Ω. For both models, the cavity fluorescence I follows a saturation curve $I = I_{sat}\tilde{P}/(1+\tilde{P})$ where, $\tilde{P} \propto \Omega^2$ and I_{sat} is the saturated cavity emission intensity. Fig. 7.3 b shows the QD linewidth as a function of the laser Rabi frequency Ω. The power broadened QD linewidth $\Delta\omega$ is fit with the model $\Delta\omega = \Delta\omega_0\sqrt{1+\tilde{P}}$, where $\Delta\omega_0$ is the intrinsic line-width of the QD and $\tilde{P}$ is obtained from the fit to the saturation of the cavity emission. The theoretical model does not reproduce the additional power-independent broadening of the QD [4], which results from QD spectral diffusion [118].

However, the results are dramatically different for a red-detuned QD, as shown in Fig. 7.4. This is expected because at any temperature, the rates of absorption and emission of phonons are different. We observe that the difference in linewidths of the red and blue detuned QD (measured via the off-resonant cavity) is larger, when the QD is weakly driven and hence is not power broadened [4]. This difference reaches the maximum value of $2\gamma_r$ at high temperatures (Fig. 7.4 a). Fig. 7.4 b shows the ratio of the cavity emission as a function of the bath temperature for different driving laser Rabi frequencies Ω. The difference in cavity emission between a red and blue detuned QD is maximum at lower bath temperature and is almost zero at higher temperature.

In addition, we investigate the dependence of the saturation emission intensity I_{sat} on the QD-cavity detuning Δ for a blue detuned dot (Fig. 7.3 c). We note that we fit experimentally measurable quantities with an empirical exponential model $\Delta^{-\alpha}$ to estimate how rapidly the dot-cavity coupling decays as a function of the QD-cavity detuning Δ. This type of model is not valid when the QD is very close to the cavity. However, in experiments, this small detuning regime cannot be probed due to large laser background. Also, for very small detunings it cannot be assumed that the laser excites the dot without exciting the cavity, thus complicating the interpretation of experimental results. Simulation results show that I_{sat} falls off as $1/\Delta^2$ with the detuning Δ when the dot-cavity coupling is modeled as a pure dephasing process. However, when the coupling is modeled as a cavity enhanced phonon process,

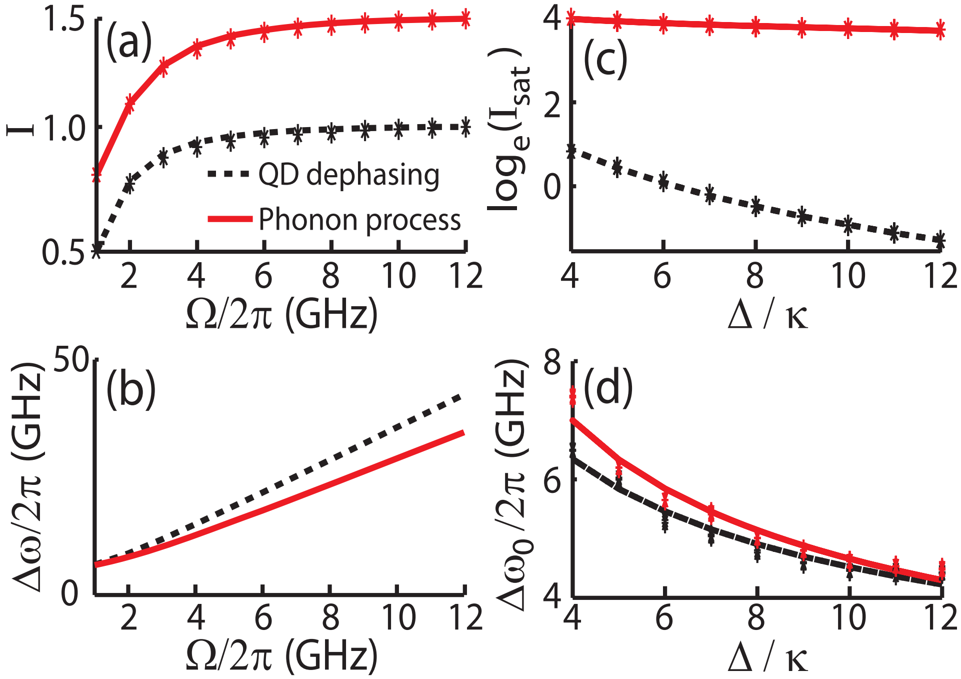

Figure 7.3: Theoretical resonance fluorescence I collected from the cavity and QD linewidth for a blue-detuned QD ($\Delta > 0$): (a) Normalized cavity fluorescence as a function of the Rabi frequency Ω of the laser for two models. Saturation of the cavity emission is observed. (b) Power broadened QD linewidth (read through the cavity, as in [4]) vs laser Rabi frequency Ω for QD-cavity detuning $\Delta/2\pi = 6$ GHz. (c) Dependence of the saturated cavity emission I_{sat} on the dot-cavity detuning Δ. (d) Dependence of the intrinsic QD linewidth $\Delta\omega_0$ on dot-cavity detuning Δ. $\Delta\omega_0/2\pi$ approaches $2(\gamma + \gamma_d)/2\pi$ or $2(\gamma + \gamma_r)/2\pi$ (both chosen to be 4 GHz) with large Δ. (Parameters used for all the simulations are: $\kappa/2\pi = g/2\pi = 20$ GHz; $\gamma/2\pi = 1$ GHz.)

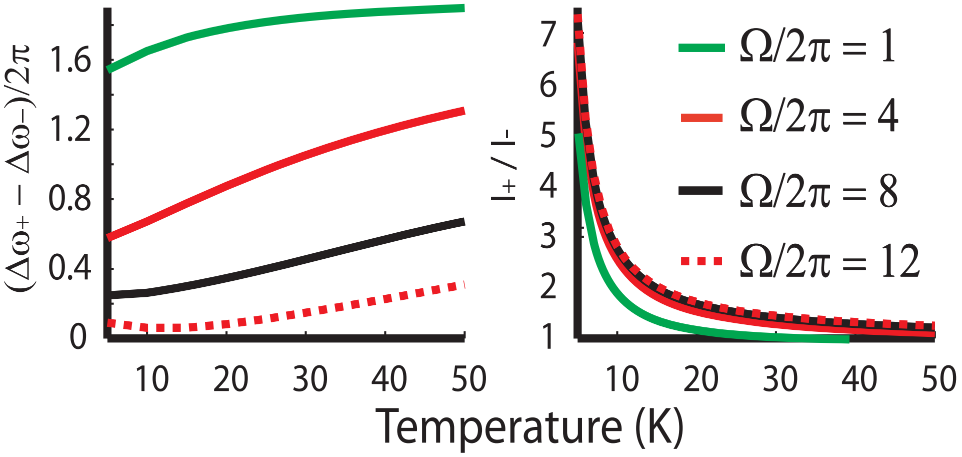

Figure 7.4: (a) The difference in QD linewidths measured via collected emission through the off-resonant cavity for a blue ($\Delta\omega_+$) and a red ($\Delta\omega_-$) detuned QD for different values of the excitation laser Rabi frequency Ω as a function of the bath temperature T. (b) Ratio of the cavity intensity for an off-resonant QD blue (I_+) and red (I_-) detuned from the cavity as a function of the bath temperature T. For all the simulations, the absolute value of the QD-cavity detuning is kept at 10κ.

the saturation intensity exhibits a much weaker dependence on detuning Δ (estimated to be $\sim 1/\Delta^{0.25}$ for the employed simulation parameters). This signifies an important difference between the two models: the cavity-enhanced phonon process permits observation of off-resonant coupling for a much larger detuning range than that associated with pure dephasing. We also analyze the intrinsic QD linewidth $\Delta\omega_0$ (obtained from Fig. 7.3 b at $\Omega = 0$ limit) as a function of the QD-cavity detuning Δ for two different models (Figure 7.3 d). We observe that at large detuning, $\Delta\omega_0$ approaches the unperturbed QD linewidth $2(\gamma + \gamma_d)$ and $2(\gamma + \gamma_r)$, respectively. The weak dependence of the intrinsic QD linewidths on the dot-cavity detuning shows that the off-resonant cavity does not perturb the QD significantly.

7.1.4 Experimental data

We now compare our theoretical model with experimental studies of the cavity emission as a function of QD-cavity detuning Δ for several QDs. Measurements are obtained using the same experimental setup and approach as in Ref. [4]. Here, the

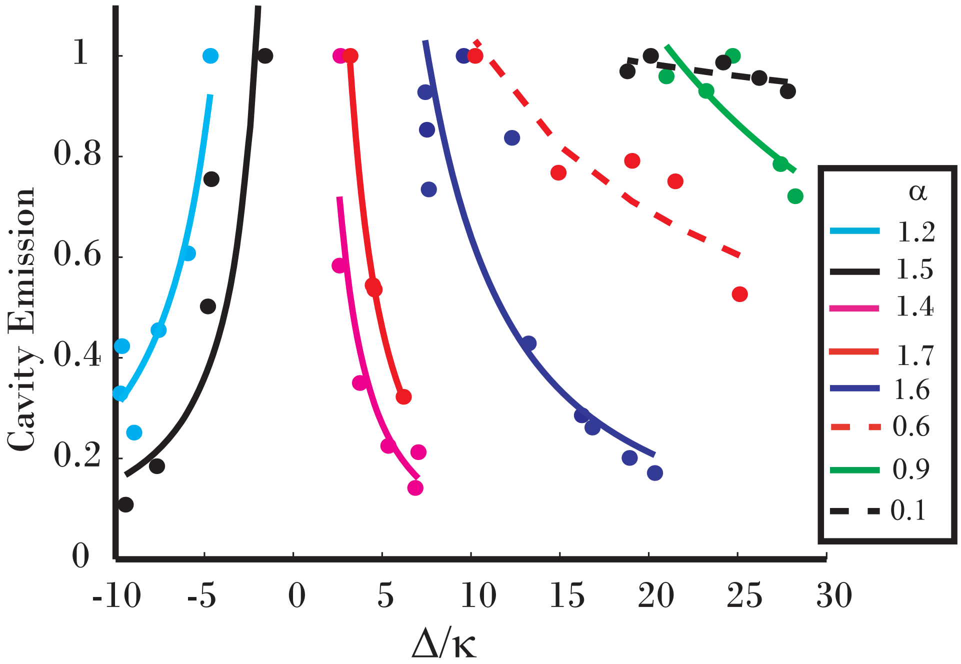

Figure 7.5: Experimentally observed off-resonant cavity emission as a function of the detuning Δ between the resonantly driven QD and the cavity. Data are fit with a model $\Delta^{-\alpha}$. Extracted values of α for the different curves are shown.

QD linewidth and off-resonant cavity emission are measured as a function of detuning Δ, where this detuning is varied by varying the sample temperature. Fig. 7.5 shows the saturated cavity intensity as a function of the detuning Δ for different QDs. The excitation laser power is same for all the detunings for a particular dot. For large detunings ($\Delta/\kappa > 10$), we do not expect significant cavity emission for the case of pure dephasing (which is described by Δ^{-2} dependence), but expect significant emission by the cavity-enhanced phonon model (see Fig.7.3 c). In our experiment, we observe significant cavity emission for such highly detuned QDs; the cavity emission is fit well with $\Delta^{-\alpha}$ with $\alpha < 2$. This weaker dependence on detuning is thus more consistent with the description of the off-resonant coupling as a cavity enhanced phonon process. On the other hand, for QDs with smaller detunings, α is very close to 2 and a role of pure dephasing is evident. We do not observe a significant change in the QD linewidth over the detuning range, due both to the weaker dependence of the linewidth on Δ as predicted by the theory (Fig. 7.3 d) and due to additional broadening caused by spectral diffusion.

Therefore, comparison with experimental results strongly suggests the role of the cavity enhanced phonon process in mediating the off-resonant coupling, particularly in the case of large QD-cavity detuning.

7.2 Single photon source

In this section, we will show how this off-resonance dot-cavity coupling can be used to make a single photon source. We measure antibunched population of the detuned cavity mode ($g^{(2)}(0) = 0.19$), under resonance excitation of the QD. Thus we demonstrate a single photon source, whose frequency is determined by the cavity resonance. In addition, because the QD is resonantly excited, the antibunched cavity emission has the potential for low timing jitter and high photon indistinguishability[119].

For this experiment, we employ a grating-integrated cavity (GIC) design[5], based on a linear three-hole defect cavity. The GIC design incorporates a second-order grating around the cavity, as seen in the perturbations in Fig. 7.6(b,c), which couples plane waves with low in-plane k-vectors with the cavity mode.

We first characterize the QD/cavity system by its photoluminescence (PL) under non-resonant excitation at a temperature between 10 K and 50 K. A continuous-wave (CW) laser at $\lambda_p = 860$ nm excites electron-hole pairs which can relax through a phonon-mediated process into radiative levels of the QD (Fig.7.6(d)). Fig.7.6(e) plots the anticrossing between the QD-like and cavity-like states. Fits to the anticrossing spectra yield the system parameters summarized in Fig.7.6(d).

We measure the reflection of the cavity by the cross-polarized reflectivity method illustrated in Fig.7.6(a). Fig.7.6(f) shows the vacuum Rabi splitting[1, 54]. We obtain good agreement with a theoretical model (solid line fit in Fig.7.6(f)) using the same parameters as derived from the photoluminescence.

We now describe autocorrelation measurements under resonant excitation. At low temperature, the detuning is large enough so that the single exciton can be resonantly excited while very little pump light overlaps with the cavity resonance. This is shown in Fig.7.7(a) for the narrow CW-wave pump laser. We spectrally filter the cavity

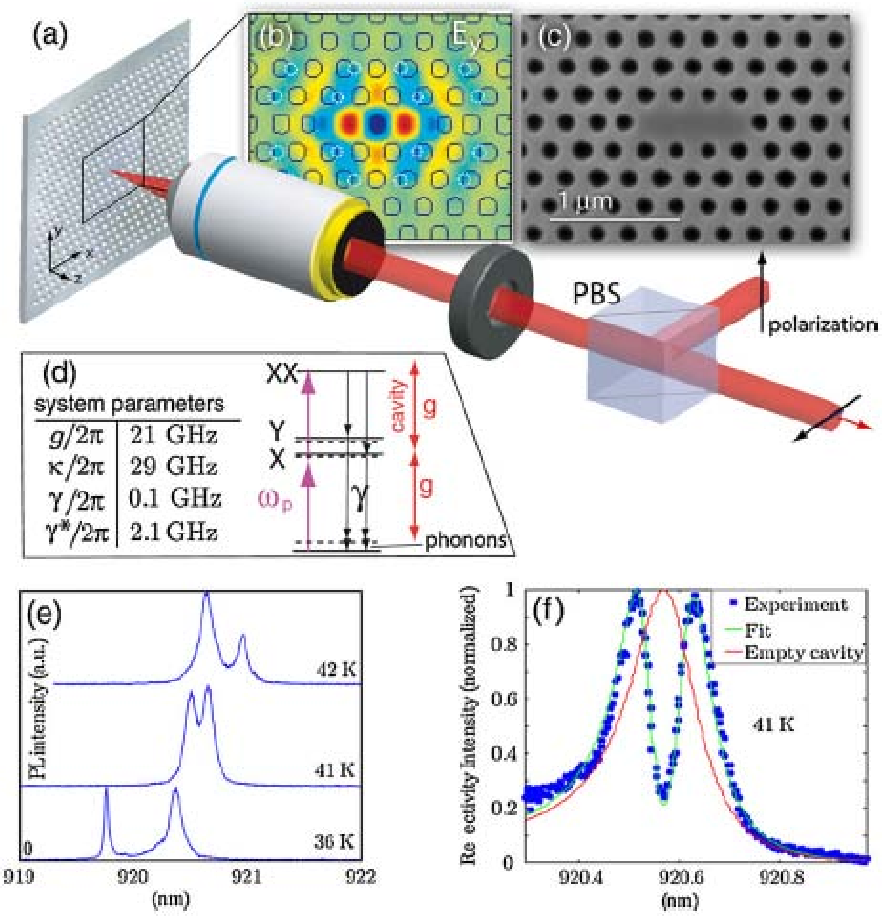
(a)
(b)
E_y
(c)
1 μm
PBS
polarization
(d)
system parameters
$g/2\pi$ 21 GHz
$\kappa/2\pi$ 29 GHz
$\gamma/2\pi$ 0.1 GHz
$\gamma^*/2\pi$ 2.1 GHz
XX
Y
X
ω_p
γ
cavity
g
g
phonons
(e)
PL intensity (a.u.)
42 K
41 K
36 K
0
919
920
921
922
(nm)
(f)
Experiment
Fit
Empty cavity
41 K
Re ectivity intensity (normalized)
1
0.8
0.6
0.4
0.2
0
920.4
920.6
920.8
(nm)

Figure 7.6: (a) Cross-polarized confocal microscope setup. (b) E_y field in the L3-cavity structure. The structure is perturbed at the sites indicated by dashed circles, as described in Ref.[5]. (c) Scanning electron micrograph of fabricated structure. (d) Energy levels of the coupled QD/cavity system showing the two polarization states of the single exciton (X,Y) and the biexciton state (XX). The table lists the system parameters derived from the measurements, where g, κ, γ^* are the vacuum Rabi frequency, cavity field decay rate, and dipole dephasing rate, respectively. The dipole decay rate γ is estimated from the lifetime of uncoupled QDs. (e) The photoluminescence (PL) shows the QD/cavity anticrossing as the QD is temperature-tuned through the cavity. (f) Vacuum Rabi splitting observed in the reflectivity from the strongly coupled QD/cavity system. For comparison, we show the reflectivity of an empty cavity.

emission using a dispersion grating-based filter (FWHM of 0.2 nm) before sending the signal to a Hnabury Brown Twiss (HBT) setup, described in chapter 5. Under the CW-excitation configuration, we observe only weak antibunching ($g^{(2)}(0) = 0.73(5)$) because the features are blurred by the 300 ps detector response time, which is slower than the $\sim$ 118 ps exciton lifetime. To overcome the detector timing resolution, we excite the single exciton line with 40 ps pulses at a repetition rate of 80 MHz. The center excitation wavelength is resonant with the QD at 919.5 nm. Fig.7.7(b) shows the autocorrelation histogram of the cavity emission, which indicates $g^{(2)}(0) = 0.19(1)$. The clear antibunching is markedly different from previous reports which observed weak or no antibunching of the detuned PC cavity mode[32, 104], and may be attributed to the expected absence of multi-exciton population of the QD under resonant excitation of the single exciton [59]. A significant contribution to the value of $g^{(2)}(0)$ is due to overlap of the 40-ps pulses with the filter at the cavity frequency, which could be improved by a narrower filter or larger QD-cavity detuning.

The autocorrelation measurements demonstrate the use of the resonantly driven QD as an on-demand single photon source. The resonant driving mechanism can reduce timing jitter due to the random relaxation time of electron-hole pairs under above-resonant excitation. The reduction in jitter would lead to an improvement in photon indistinguishability. Furthermore, the emission wavelength is given by the cavity frequency and would be less sensitive to spectral jumps in the QD emission wavelength. In this experiment, the cavity emission under resonant excitation of the QD was too low to measure the indistinguishability, in part because of low coupling efficiency ($\sim$ 0.1) into the single mode fiber in our Hong-Ou-Mandel setup.

We have also performed time resolved measurements of the emission of the resonantly excited QD into the cavity mode. Fig.7.7(c) shows the 40-ps pump pulse and cavity emission, measured simultaneously on a streak camera. The QD-driven cavity emission lifetime is $\tau \sim 118$ ps when the dot is detuned by $\delta = -1.2$ nm. We can use this lifetime measurement to infer the dephasing rate. We fit the decay time by a Monte Carlo simulation of the master equation, with the QD initialized in the ground state and resonantly excited by the 40-ps pump pulse. All parameters except for γ are fixed as before. The fit gives $\gamma^* = 0.10(1)g$.

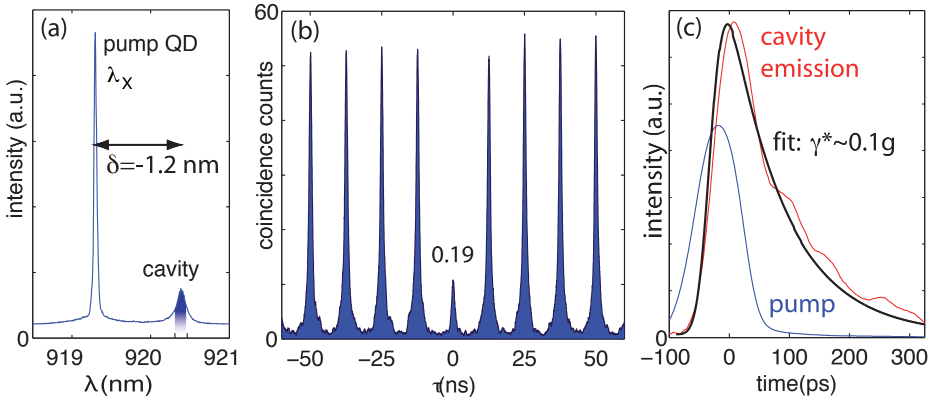

Figure 7.7: (a) Resonant QD excitation at 10K. For the autocorrelation measurements, the cavity emission is isolated from the pump using a grating filter providing 17 dB of isolation at $\delta = -1.2$ nm detuning. The laser is operated in continuous wave here so that is has low overlap with the cavity. (b) Autocorrelation histogram of cavity emission when the QD is pumped resonantly with 40-ps pulses (spectrum not shown). (c) Time-resolved resonant pumping of the quantum dot and emission into the cavity mode. A theoretical fit to the cavity emission yields an estimate of the pure dephasing rate.

7.3 Resonant QD spectroscopy

Another application of this off-resonant coupling is resonant QD spectroscopy. In conventional resonant spectroscopy, the probe light, and the light carrying information about the QD are at same wavelength. This makes the detection in presence of large laser background difficult. In general, people use polarization based background rejection technique [120] or complicated fabrication enabling orthogonal pumping and collection of light [121, 101]. However, we exploit off-resonant QD-cavity coupling to perform resonant QD spectroscopy, where the pump laser is resonant to the QD, but the signal is read-out at the cavity wavelength.

7.3.1 Probing exciton and biexciton

This experiment is performed on the same system, where we performed the auto-correlation measurements (as described in the last section). When the QD exciton line is blue-detuned from the cavity by $\delta = \lambda_d - \lambda_c = -1.17$ nm at a temperature of 10 K, the laser is scanned across the QD and cavity resonances, as shown in Fig.7.8. The excitation laser power is ~ 12 nW before the objective lens. Precisely when the laser becomes resonant with the QD, we observe a strong emission into the cavity mode; otherwise, the cavity is dark. We can view the cavity as an efficient read-out channel for resonant quantum dot spectroscopy: the QD emits into the cavity mode, which is far detuned and easy to separate spectrally. Alternatively, if the cavity mode is pumped, the QD single-exciton line radiates. Fig.7.8(b)[c] plots spectra when the QD[cavity] are pumped.

Fig.7.8(d) plots the integrated cavity emission as a function of the laser pump wavelength λ_p. We observe an absorption linewidth below 0.008 nm (2.7 GHz), which is better than 0.03 nm, the resolution of our spectrometer. The technique allows mapping of QD transitions with a resolution given by the excitation laser, which is in the MHz regime in our case. This cavity-enhanced spectroscopy technique adds an important tool to the repertoire for resonant single quantum dot spectroscopy.

Fig. 7.8(e) plots the integrated QD intensity as the laser is scanned over the cavity resonance. The transfer to the QD is strongly asymmetric towards higher

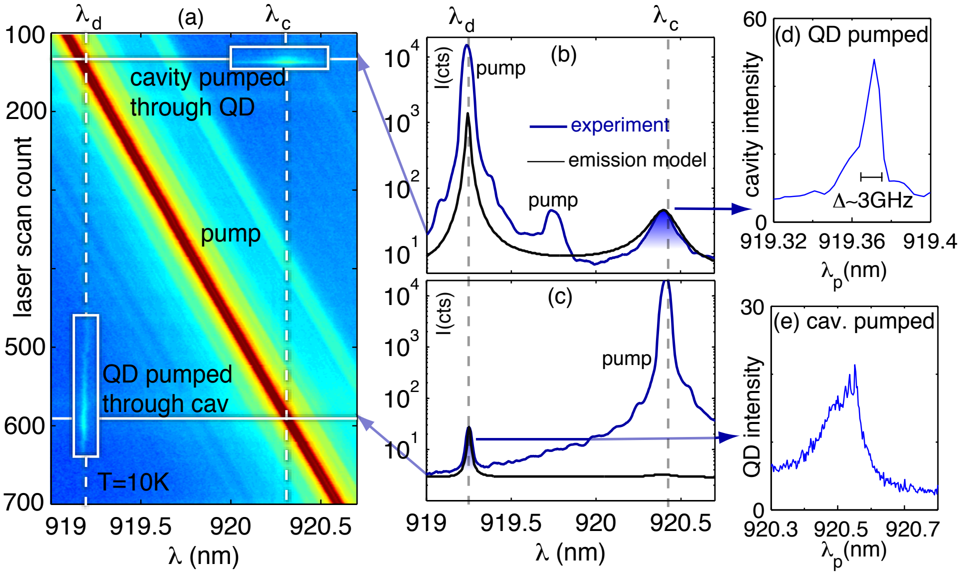

Figure 7.8: QD spectroscopy through cavity mode at 10K. (a) Intensity on spectrometer when the pump wavelength λ_p is scanned across the detuned QD/cavity system (the laser has a weak red-detuned side band; power is 12 nW before the objective lens). When λ_p is resonant with the dot (cavity), the cavity (QD) intensity rises. (b) Spectrum when QD is pumped (the middle peak corresponds to the laser side mode) (c) spectrum when cavity is pumped. In (b) and (c), we model the driving mechanism by a pure dephasing process with $\gamma^* = 0.1g$. The model agrees well with the emission through the cavity (QD) when the QD (cavity) is pumped. (d) The integrated cavity emission as a function of the pump wavelength λ_p shows the single exciton absorption resolved to 3 GHz. (e) The integrated QD emission.

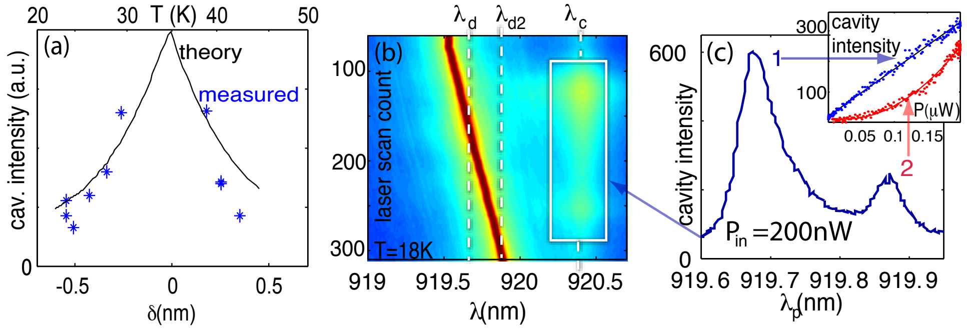

Figure 7.9: (a) Dependence of integrated cavity emission on QD detuning when the QD is resonantly pumped. (b) Pump power dependence: at a pump power of 200 nW, a second line becomes visible at a pump wavelength $\lambda_p = 919.87$ nm. (The lines are slightly shifted since the temperature was, for technical reasons, raised to 18 K). (c) Integrated cavity emission as λ_p is scanned. *Inset:* The power dependence of the two lines suggests exciton (X) and biexciton (XX) states; in this inset, a background of 40 was subtracted.

energy photons absorbed into the cavity, which are closer to the QD single exciton wavelength.

For this experiment, we describe our experimental data with a pure dephasing rate γ. The dephasing term allows driving of the cavity (QD) through the QD (cavity), as is shown in the fit in Figs.7.8(c,d), where we used $\gamma^* = 0.1\kappa$. This value of γ^* was fit to match the off-resonant excitation between QD and cavity in Fig.7.8(c,d) and was also estimated independently (see Fig.7.7(c)) and agrees with values cited in the literature for resonant excitation studies [122]. The dephasing rate $\gamma^* = 0.1\kappa$ also explains the 2.7 GHz linewidth of the exciton absorption (Fig.7.8(d)), which is broader by a factor of two than the radiative linewidth corresponding to the exciton lifetime of 118 ps at a similar QD-cavity detuning (Fig.7.7(c)).

In Fig.7.9(a), we explore the dependence of the cavity feeding mechanism on the QD single exciton-cavity detuning δ. We measured the cavity intensity through the resonantly driven QD for a temperature range of 28K-47K, corresponding to a QD-cavity detuning from -0.6 nm to 0.4 nm. At each temperature given in Fig.7.9(a), we tune the CW excitation laser to the QD, keeping the power constant at 50 ± 0.5 nW before the lens. In the dephasing model, shown in the black curve in Fig.7.9(a), we assume a temperature-dependent dephasing[123] rate $\gamma = \gamma_0 + \alpha_0 T$, with $\alpha_0 = 0.5\mu$ eV K^{-1} and $\gamma_0 = \kappa/100$. We use the dephasing model to model the experimental data at small detunings on the order of meV, where the dephasing processes are thought to be mediated by absorption or emission of acoustic phonons[123]. In the regime of larger detunings, up to tens of meV, the efficient cavity pumping persists through a process that has recently been attributed to transitions between excited multiexciton states[59].

Fig.7.9(b) shows the resonant excitation repeated at a higher power of $P_{in} = 200$ nW. One striking difference is that the features are far more blurred; we believe this results from power broadening and increased spectral diffusion at high intensity[123]. A scan across the QD, where the tail of the excitation laser is subtracted, gives the cavity emission spectrum shown in Fig.7.9(c). The data reveal a second peak when the pump is tuned to $\lambda_p = 919.85$ nm. In Fig.7.9(c, inset), we plot the cavity emission as a function of excitation power when λ_p is tuned to two resonant wavelengths. The single-exciton line shows a linear pump dependence, as expected. The second line shows a quadratic pump dependence. The power dependence suggests a biexciton state that is resonantly pumped by two-photon absorption; we note, however, that the X-XX energy splitting is rather low compared to values reported for resonant XX excitation in bulk semiconductor. Unfortunately, the signal-to-background was too low to confirm the biexciton nature of the second peak by cross-correlation measurements with the single exciton emission.

7.3.2 Emission saturation and linewidth broadening

This off-resonant interaction can also be employed to perform a power dependent resonant QD spectroscopy. Linewidths of the quantum dot and the cavity as a function of the excitation laser power are measured. We show that the linewidth of the quantum dot, measured by observing the cavity emission, is significantly broadened compared to the theoretical estimate. This additional broadening is due to spectral diffusion, as will be explained in the chapter 8.

When an off-resonant QD that is coupled to a cavity is coherently driven by a laser field, the QD is dressed by both the cavity and the laser field. When the coherent interaction strength g is greater than the decay rates κ and γ, the system is in strong coupling regime, and the eigen-states of the coupled system are polaritons possessing the characteristics of both the cavity and the QD. In this regime, when the QD-cavity detuning $\delta = 0$, the linewidth of the polaritons is $\kappa+\gamma$. However, when the QD-cavity detuning δ is much greater than g, the system is in the dispersive CQED regime. In this regime, one polariton develops a cavity-like character while the other becomes more QD-like. The linewidths Γ_c and Γ_{qd} of the cavity-like and QD-like polaritons, respectively, are given by (with a pure QD dephasing rate of γ_d) [45]

$$\Gamma_c \simeq 2\kappa + 2\left(\frac{g}{\delta}\right)^2 \gamma \tag{7.34}$$

$$\Gamma_{qd} \simeq 2(\gamma + \gamma_d) + 2\left(\frac{g}{\delta}\right)^2 \kappa \tag{7.35}$$

The linewidth Γ_{qd} can be interpreted as a combination of the QD spontaneous emission rate (2γ) and the QD emission rate into the cavity mode $2\left(g/\delta\right)^2 \kappa$.

On the other hand, when a QD is coherently driven by a laser field in the absence of any optical cavity, the system dynamics is described by the master equation

$$\frac{d\rho}{dt} = -\frac{i}{\hbar}[H,\rho] + 2\gamma\mathcal{L}[\sigma] + 2\gamma_d\mathcal{L}[\sigma^\dagger\sigma] \tag{7.36}$$

Here ρ is the density matrix of the QD optical transition and γ_d is the pure dephasing rate. $\mathcal{L}[D]$ is the Lindblad operator for an operator D. The Hamiltonian H describing the coherent dynamics of the driven QD is given by

$$H = \hbar\omega_d\sigma^\dagger\sigma + \hbar\frac{\Omega}{2}(\sigma e^{-i\omega_l t} + \sigma^\dagger e^{i\omega_l t}) \tag{7.37}$$

where, ω_d and ω_l are the QD resonance and the driving laser frequency, respectively, and Ω is the Rabi frequency of the driving laser field. In solving the master equation (Eq. 7.36), it is found that the intensity I of the QD resonance fluorescence for $\omega_d = \omega_l$ is given by

$$I = \frac{\frac{\Omega^2}{4\gamma(\gamma+\gamma_d)}}{1 + \frac{\Omega^2}{2\gamma(\gamma+\gamma_d)}} \propto \frac{\tilde{P}}{1+\tilde{P}} \tag{7.38}$$

where $\tilde{P} = \frac{\Omega^2}{2\gamma(\gamma+\gamma_d)}$. The QD linewidth $\Delta\omega$ is given by

$$\Delta\omega = 2(\gamma+\gamma_d)\sqrt{1+\frac{\Omega^2}{2\gamma(\gamma+\gamma_d)}} = 2(\gamma+\gamma_d)\sqrt{1+\tilde{P}} \tag{7.39}$$

The broadening of the QD linewidth with laser excitation power occurs due to increasing stimulated emission in the driving laser mode and is known as power broadening. Such power broadening of the QD linewidth has been reported by several other groups [121, 124].

Following the discussion above, the linewidth $\Delta\omega$ of a resonantly driven QD that is coupled to an off-resonant cavity has contributions from both the increased emission rate in the cavity mode and the increasing stimulated emission due to the driving laser. As the QD is detuned from the cavity (and hence the laser driving the QD resonantly is also detuned from the cavity), the QD emission into cavity mode and the stimulated emission into the driving laser mode are independent and $\Delta\omega$ is given by

$$\begin{aligned} \Delta\omega &= 2\left(\frac{g}{\delta}\right)^2\kappa + 2(\gamma+\gamma_d)\sqrt{1+\tilde{P}} \\ &= \Delta\omega_c + \Delta\omega_0\sqrt{1+\tilde{P}} \end{aligned} \tag{7.40}$$

Here, $\Delta\omega_c = 2\left(g/\delta\right)^2\kappa$ and $\Delta\omega_0 = 2(\gamma+\gamma_d)$. Similarly, as the cavity is coupled to the QD, the cavity-like polariton linewidth contains a contribution from the QD emission, as evident from Eq. 7.34. However as the cavity loss rate 2κ is much greater than the QD spontaneous emission rate 2γ, the modification of the cavity linewidth is negligible. From now on, we will refer to the cavity-like polariton as the "cavity" and QD-like polariton as the "QD".

We perform two different types of experiments to study the off-resonant QD-cavity coupling. For the first type, a narrow bandwidth ($\sim$ 300 kHz) laser is scanned across the QD optical transition while the emission at the cavity wavelength is observed. In the second type, the laser is scanned across the cavity linewidth and the QD emission is observed. Figs. 7.10 (a), (b) show the cavity and QD emission spectra for the first and second experiments, respectively. Figs. 7.10 (c), (d) show the integrated cavity and QD intensities as we scan the laser across the QD and the cavity, respectively. Lorentzian fits to the cavity and the QD intensities as a function of laser wavelength enable estimation of the QD and the cavity linewidths, respectively.

The first type of experiment is performed on three different QD-cavity systems for different detunings between the cavity and the QD transition. Details of three systems are given in the Table 7.1. The detuning between the cavity and a particular QD transition is controlled by varying the sample temperature. As the limited temperature tuning range limits the range of achievable QD-cavity detunings, multiple QDs must be chosen to cover an extended range of detunings. However, all three systems show similar qualitative behavior.

In the first experiment, we observe saturation of the cavity emission with increasing power of the laser used to excite the QD. We fit the cavity intensity with the model given by Eq. 7.38 [Figs. 7.11 (a),(c), and (e) (solid line)]. In actual experiments, $\Omega^2 \propto \eta P$, where P is the measured laser excitation power in front of the objective lens and η is a constant factor signifying the percentage of incident light coupled to the QD. Hence, assuming that both the QD spontaneous emission rate 2γ and the pure dephasing rate γ_d are independent of the laser excitation power, $\tilde{P} = \alpha P$, where α is a constant factor, independent of the laser power. α is determined from the fit to the cavity intensity with the excitation laser power. In addition to emission saturation, we see broadening of the QD linewidth with increasing excitation laser power, as measured from Lorentzian fits similar to the one shown in Fig. 7.10 (c). Measurements of the QD linewidth as a function of the laser power for the three different QDs studied are plotted in Figs. 7.11 (b), (d), and (f). Using the extracted values of $\tilde{P} = \alpha P$ (as previously explained), the linewidths are fit with the model given by Eq. 7.40 [Figs. 7.11 (b),(d), and (f) (solid line)]. The fitting parameters are shown in Table 7.1.

We note that for the QD $S1$, the value of $\Delta\omega_0$ obtained from the fit is of the same order of magnitude as the linewidth of a resonantly driven QD without a cavity ($\Delta\omega/2\pi \sim 2.5$ GHz) [121], although in this case we use an off-resonant cavity for read-out. Relatively higher values of $\Delta\omega_0$ for the second ($S2$) and the third ($S3$) QD can be attributed to the high dephasing rate at higher sample temperatures [125].

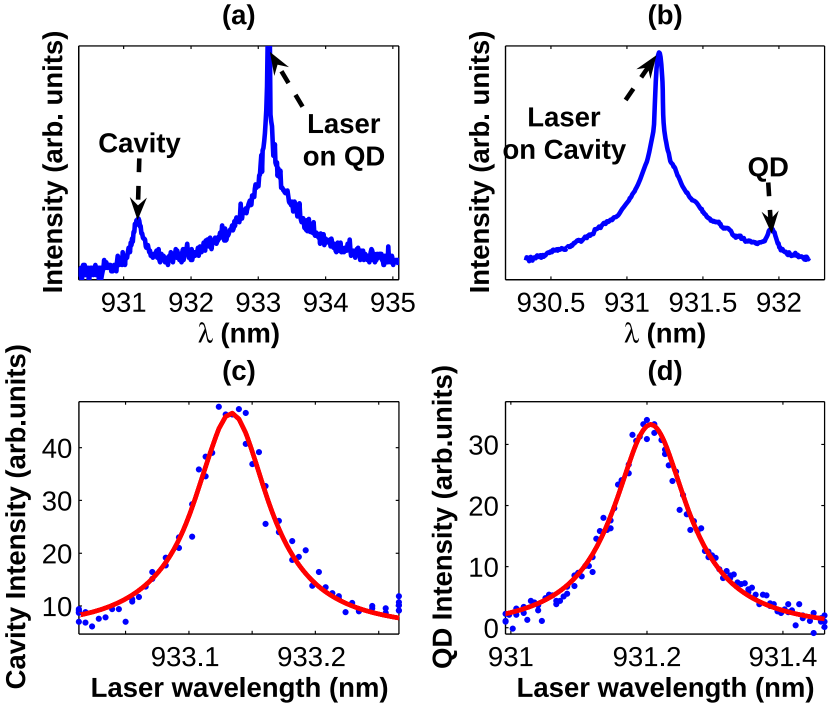

Figure 7.10: (a) Cavity emission when the QD is resonantly excited. (b) QD emission when the cavity is resonantly excited. Experiments to obtain (a) and (b) are performed at 55 K. The cavity wavelength is 931.2 nm. The QD resonances are at (a) 933.15 nm and (b) 931.9 nm. Emission from the QD at 933.15 nm is very weak under resonant excitation of the cavity. Hence, for (b) another QD at 931.9 nm is used. (c) Integrated cavity emission as a function of the pump laser wavelength when the QD is resonantly excited [as in (a)]. The solid line is a Lorentzian fit (with a linewidth of 0.075 nm, i.e., $\Delta\omega/2\pi \approx 25$ GHz). (d) Integrated QD emission as a function of laser wavelength for the case of resonant cavity excitation [as in (b)]. The solid line is a Lorentzian fit (with a linewidth of 0.1517 nm, i.e., $\Delta\omega/2\pi \approx 52$ GHz).

Table 7.1: Details of the QD-cavity systems employed in the first experiment, when the cavity emission is observed by resonantly exciting the QD. Also shown are the fits for two different contributions to the QD linewidth, $\Delta\omega_c$ and $\Delta\omega_0$, and the theoretical estimate for $\Delta\omega_c$ (see Eq. 7.40).

QD	Temperature (K)	QD Wavelength (nm)	Cavity Wavelength (nm)	$\Delta\omega_c/2\pi$ (Fit) (GHz)	$\Delta\omega_0/2\pi$ (Fit) (GHz)	$\Delta\omega_c/2\pi$ (Theory) GHz
$S1$	32	934.15	934.8	12.6	1.96	1.3
$S2$	44	932.3	931.9	9.9	9.8	2.34
$S3$	55	933.15	931.2	15	5.8	0.28

Table 7.2: Details of the QD-cavity systems employed in the second experiment, when the QD emission is observed by resonantly exciting the cavity. Also shown are the values of the $\Delta\omega_{c0}$.

QD	Temperature (K)	QD Resonance (nm)	Cavity Resonance (nm)	$\Delta\omega_{c0}/2\pi$ (GHz)
$S2$	44	932.3	931.9	35.6
$S4$	55	931.9	931.2	50.3

However, the linewidth of a QD also depends on its local environment, for example, presence of other nearby QDs or traps (which can be results of e.g., the proximity of the etched surfaces of the photonic crystal), which can explain the difference in $\Delta\omega_0$ for ($S2$) and ($S3$).

To theoretically estimate $\Delta\omega_c/2\pi$ (contribution from the increased emission into the cavity mode as given by Eq. 7.35) in Table 7.1 , we assume $g = \kappa$. This is an overestimated value of g as our system is not strongly coupled (which is confirmed by bringing the QD onto resonance with the cavity). The overestimated g leads to an overestimate of $\Delta\omega_c$. However, we find that even those theoretically overestimated $\Delta\omega_c$ values are still much lower than the experimental data shown in Table 7.1. Just pure QD dephasing cannot explain this finding as dephasing contributes only to the term $\Delta\omega_0$. The increased broadening indicates a higher coupling strength between the QD and the cavity exceeding what our theoretical model predicts.

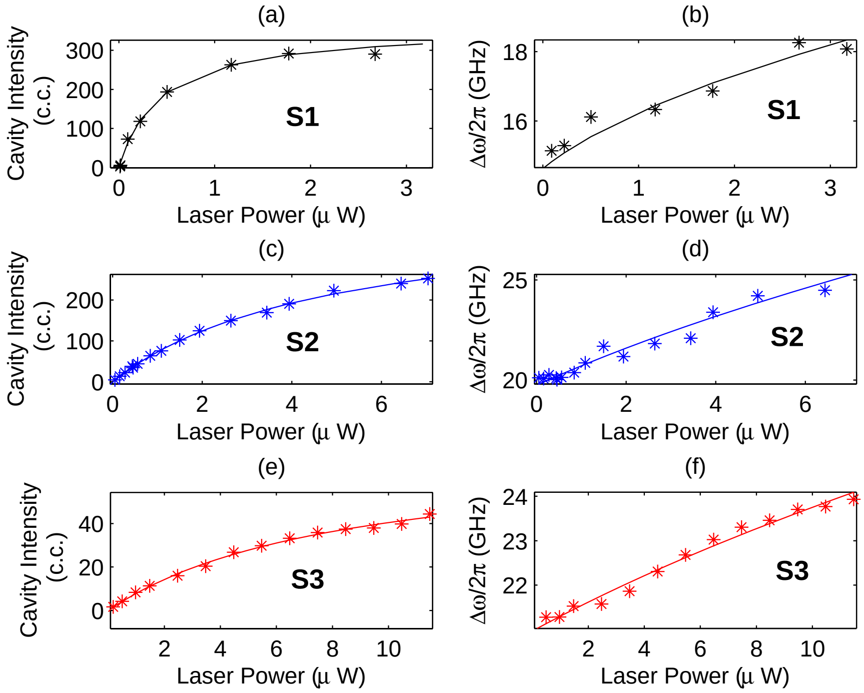

Figure 7.11: (a),(c),(e): Integrated cavity emission as a function of the excitation power of the laser resonantly pumping the QD, for the three QD-cavity systems studied. (c.c. stands for CCD count.) The solid lines are fits to the data using the model given by Eq. 7.38. (b),(d),(f): Corresponding measured linewidths [as in Fig. 7.10 (c)] as a function of the laser excitation power. The solid lines are fits to the data using the model given by Eq. 7.40. The excitation laser power is measured in front of the objective lens.

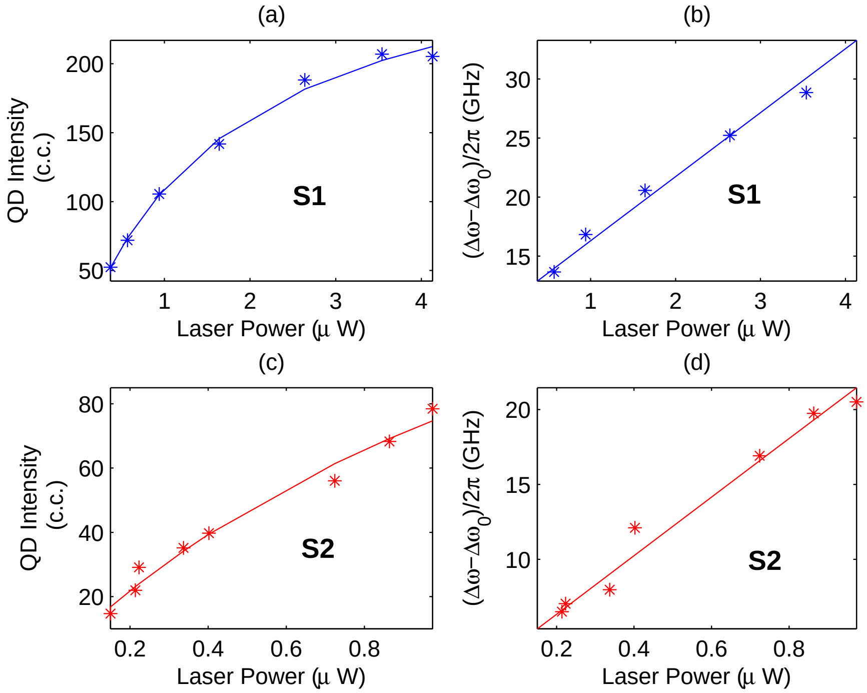

Figure 7.12: (a),(c): Integrated QD emission as a function of the excitation power of the laser resonantly pumping the cavity, for the two QD-cavity systems studied (see Table 7.2). (c.c. stands for CCD count.) The solid lines are fits to the data using model given by Eq. 7.38. (b),(d): The difference between the cavity linewidth $\Delta\omega_c$ measured by observing the QD emission and the cavity linewidth $\Delta\omega_{c0}$ obtained from the cavity reflectivity measurements, as a function of the laser power. The solid line is a linear fit to the difference. The excitation laser power is measured in front of the objective lens.

We now analyze the linewidth of the process [Fig. 7.10(d)] responsible for transferring photons from the resonantly excited cavity to the QD. We perform the second type of experiment (exciting the cavity and collecting emission from the QD) on two QD-cavity systems (Table 7.2). The QD described in the first row of Table 7.2 is the same as the QD used in the first experiment (second row of Table 7.1). The other two systems shown in Table 7.1 could not be employed in this experiment, as they either showed no emission or very weak emission from QD line under cavity excitation. Hence, we employed another QD system ($S4$) described in Table 7.2.

Figs. 7.12 (a),(c) show the QD intensity as a function of the power of the laser resonantly pumping the cavity. We observe saturation of the integrated QD emission and the data fit well with the model given by Eq. 7.38. In this experiment, we also measure the cavity linewidth $\Delta\omega_c$, but here we scan the laser wavelength across the cavity and collect the integrated emission from the QD. In addition, we also measure the intrinsic cavity linewidth $\Delta\omega_{c0}$ from cavity reflectivity measurements at low laser power. In reflectivity measurements, the laser is scanned across the cavity linewidth and the cavity reflected laser power is observed, as in our previous work [1]. For both cavities, the linewidths $\Delta\omega_c$, extracted from the second type of experiment (exciting cavity resonantly and imaging emission at QD wavelength) are larger than the linewidth $\Delta\omega_{c0}$ obtained in reflectivity measurements. Figs. 7.12 (b),(d) show the difference between two linewidths, i.e., $(\Delta\omega_c - \Delta\omega_{c0})$, which increases linearly with laser power. This additional broadening is attributed to the free carrier absorption losses. The carriers are generated in bulk GaAs by the laser excitation (via two-photon absorption).

7.3.3 QD dressing observed via off-resonant cavity

We showed previously (in our theoretical model) that the coupling between the QD and the off-resonant cavity is incoherent. Here we demonstrate that despite its incoherent nature, this process preserves the signatures of coherent interaction between a QD and a strong driving laser, which may be observed via the optical emission from the off-resonant cavity. Under bichromatic driving of the QD, the cavity emission exhibits spectral features consistent with optical dressing of the QD transition. These cavity emission measurements are more akin to absorption measurements of a strongly driven QD rather than resonance fluorescence measurements. In addition to revealing new aspects of the off-resonant QD-cavity interaction, this result provides a new, simpler means of coherently probing QDs and opens the possibility of employing off-resonant cavities to optically interface QD-nodes in quantum networks.

Here, a strong narrow-bandwidth CW pump laser serves to dress the QD, while a weaker continuous wave (CW) probe laser is scanned across the QD resonance; the output signal is always collected at the frequency of the spectrally detuned cavity (Fig. 7.13 a). We theoretically model the bichromatic driving of the QD coupled to an off-resonant cavity by adding an incoherent phonon-mediated coupling between the QD and the cavity and perform simulations with realistic system parameters. The bichromatic driving of a two-level system has been analyzed before [126]. We use similar techniques to analyze the driving of a two-level system such as a QD, incoherently coupled to an off-resonant cavity via phonons [41].

The dynamics of a driven QD-cavity system is given by the Jaynes-Cummings Hamiltonian:

$$H = \omega_{cav} a^\dagger a + \omega_{QD}\sigma^\dagger\sigma + g(\sigma^\dagger a + \sigma a^\dagger) + J\sigma + J^*\sigma^\dagger \tag{7.41}$$

J is the Rabi frequency of the driving laser. For bichromatic driving, the driving field J consists of a strong pump laser with Rabi frequency J_1 tuned to the QD resonance and a weak probe laser with Rabi frequency J_2, which can be tuned to arbitrary frequency, parameterized by the pump-probe detuning δ:

$$J = J_1 e^{i\omega_{QD}t} + J_2 e^{i(\omega_{QD}+\delta)t} \tag{7.42}$$

In a frame rotating with the pump laser frequency the Hamiltonian is

$$\begin{aligned} H &= H_0 + H(t) && (7.43)\\ &= \Delta a^\dagger a + g(\sigma^\dagger a + \sigma a^\dagger) + J_1\sigma_x + J_2\left(e^{i\delta t}\sigma + e^{-i\delta t}\sigma^\dagger\right) && (7.44) \end{aligned}$$

where $\Delta = \omega_{cav} - \omega_{QD}$ is the QD-cavity detuning. We note that for bichromatic driving, the Hamiltonian is always time-dependent. To treat incoherent processes we use the quantum optical master equation. We numerically calculate the emission spectrum of the cavity given by the Fourier transform of the two-time correlation function of the cavity field, proportional to $\langle a^\dagger(\tau)a(0)\rangle$. Under the quantum regression theorem the auto-correlation function is equal to $\text{tr}\{a^\dagger M(\tau)\}$ where $M(\tau)$ obeys the master equation with initial condition $a\rho(t \to \infty)$. The time dependence of the Hamiltonian is such that the master equation can be cast in terms of Liouvillian superoperators as

$$\dot{\rho} = \left(\mathcal{L}_0 + \mathcal{L}_+ e^{i\delta t} + \mathcal{L}_- e^{-i\delta t}\right)\rho \tag{7.45}$$

This equation is solved with Floquet theory, by assuming a solution of the form $\rho(t) = \sum\limits_{n=-\infty}^{\infty} \rho_n(t)e^{in\delta t}$. The number of terms in the expansion necessary to obtain any level of precision is determined by the relative strength of J_1 to J_2, and in this way the problem can be considered perturbative in the probe strength.

Introducing this trial solution to eq. 7.45, taking the Laplace transform, and equating terms proportional to $e^{in\delta t}$ yields the recurrence relation

$$z\rho_n(z) + \rho(0)\delta_{n0} + in\delta\rho_n(t) = \mathcal{L}_0\rho_n(z) + \mathcal{L}_+\rho_{n-1}(z) + \mathcal{L}_-\rho_{n+1}(z) \tag{7.46}$$

which can be solved numerically by the method of continued fractions. We seek the resonance fluorescence spectrum of the cavity which is found as the real part of the Fourier transform of the stationary two-time correlation function $\langle a^\dagger(t+\tau)a(t)\rangle$. Application of the quantum regression theorem allows this quantity to be calculated as $tra^\dagger M(\tau)$, where $M(\tau)$ solves the master equation with initial condition $M(0) = a\rho(t \to \infty)$. From the recurrence relation and the aforementioned initial condition the method of continued fractions allows us to obtain an expansion of the Laplace transform of $M(\tau)$ of the form $M(z) = \sum\limits_{n=-\infty}^{\infty} M_n(z + in\delta)$, from which the cavity resonance fluorescence spectrum is

$$S(\omega) = Re\left(tr\{a^\dagger M_0(i\omega)\}\right) \tag{7.47}$$

where ω is the angular frequency of the emitted light, centered at the frequency of the pump laser. In our calculation, ρ_0 is found to first order in J_2 by assuming all

ρ_n for $|n| > 1$ are 0, reflecting the relatively weak probe strength. In the regime under consideration much less than one photon is ever in the cavity at any time (i.e. $\langle a^\dagger a \rangle \ll 1$) and the photon basis is truncated to a small subspace of Fock states ($|0\rangle, |1\rangle, |2\rangle$). These approximations are validated by observing no change in the calculation with an expansion of either basis.

The height of the peak at the cavity resonance is calculated as a function of the probe detuning δ. The criterion for the appearance of dressed states is that the pump Rabi frequency J_1 should be higher than the QD linewidth 2γ. The inclusion of incoherent terms γ_r and γ_d effectively broadens the dot and alters this condition, but below a certain critical value of J_1 the change in the cavity height with probe detuning is a simple Lorentzian with a linewidth on the order of the natural QD linewidth. Above threshold, the dressed states are resolvable and the cavity height spectrum splits into two peaks in the experimental regime we considered. Broadening of the peaks in the experiment beyond the theoretical prediction is caused by spectral diffusion of the QD, which likely arises from the charge fluctuations on etched surfaces of the photonic crystal. The parameters used for the simulations are: $\kappa/2\pi = 17$ GHz, $\gamma/2\pi = 1$ GHz, $\gamma_r/2\pi = .5$ GHz, $\gamma_d/2\pi = 3$ GHz, $\Delta = 8\kappa$, $\bar{n} = 1$. In these simulations we neglect any coherent coupling between the QD and the cavity (i.e., the coherent dot-cavity coupling strength $g = 0$). Figure 7.13 c shows the theoretically calculated cavity output as a function of the probe laser wavelength λ_p for different powers P of the resonant pump laser. At low pump power, we observe a simple Lorentzian line-shape with QD linewidth [4]. However, as the pump power is increased, the Lorentzian peak splits into two peaks, the separation between the peaks increasing linearly with pump Rabi frequency. We find that these two peaks are separated by ~ 4 times the Rabi frequency J_2(Fig. 7.14 a). As the pump power is increased further, a third peak corresponding to the central Mollow peak appears at the QD resonance, leading to the emergence of two dips whose separation also increases linearly with pump Rabi frequency (Fig. 7.14 b).

We note that the lack of a prominent central Mollow peak as observed in resonance fluorescence studies of single QDs [121, 120] is a result of the saturation of the QD absorption and, hence, of the cavity emission. As such, these cavity emission measurements are more akin to absorption measurements of a strongly driven QD [127, 128] rather than the aforementioned resonance fluorescence measurements [121, 120]. Figure 7.13 d plots the cavity output for different detunings $\Delta\lambda_{pump} = \lambda_{pump} - \lambda_{QD}$ between the pump and the QD. We observe that the two peaks remain distinct but become asymmetric when the pump is detuned from the QD. This is consistent with the anti-crossing of the Rabi sidebands of the dressed QD that occurs as the pump is tuned through the QD resonance [129]. Inclusion of g makes the two peaks asymmetric. Fig. 7.14 c shows the cavity emission for a pump power of 25, with $g/2\pi$ ranging from 0 to 10. Here the cavity is at a shorter wavelength compared to the QD, and we observe that the peak closer to cavity is not enhanced. This observation is starkly different from the resonance fluorescence measurement, where the peak close to the cavity is enhanced, as observed in [41, 130]. This indicates again, that this way of measuring the coherent interaction between the QD and the laser is akin to an absorption measurement. These theoretical results demonstrate that measurements of cavity emission allow for the observation of phenomena associated with the coherent optical driving of the QD.

To demonstrate the use of such cavity emission to perform coherent optical spectroscopy of an off-resonantly coupled QD, we perform a series of experiments measuring the optical emission spectra of a system consisting of a single self-assembled InAs QD off-resonantly coupled to a linear three hole defect GaAs PC cavity kept at cryogenic temperatures ($\sim 30-35$ K) (Fig. 7.13 b) [1].

Experiments are performed by driving the QD-cavity system under different optical configurations and measuring optical emission. Optical emission is collected and dispersed by a single grating monochromator and then measured by a liquid nitrogen cooled charge coupled device (CCD). We first characterize the coupled QD-cavity system by measuring the photoluminescence (PL) spectrum obtained under above-band excitation by an 820 nm Ti:sapphire laser (Fig. 7.15 a). From the Lorentzian fit to the cavity resonance, we find that the cavity linewidth is $\Delta\lambda_{cav} = 0.1$ nm, corresponding to a cavity field decay rate of $\kappa/2\pi = 17$ GHz. We do not observe the anti-crossing of the cavity and QD peaks when the QD is tuned across the cavity resonance by

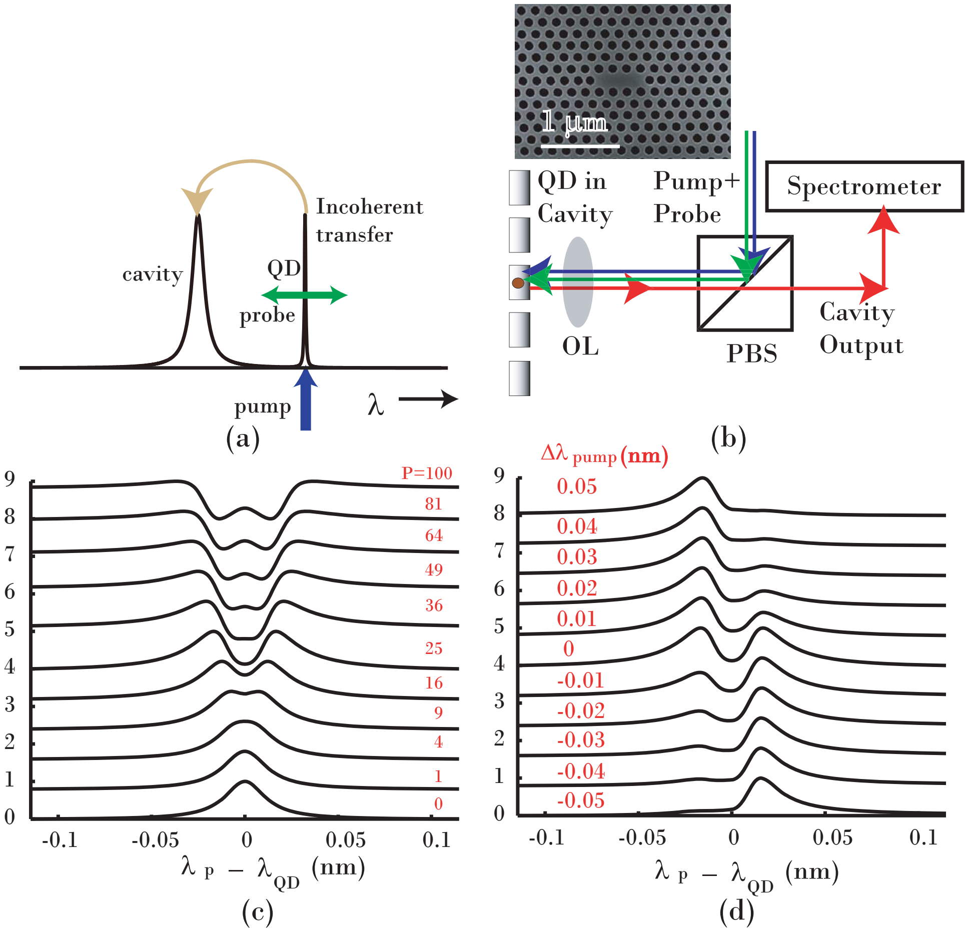

Figure 7.13: Experimental setup and numerical simulations. (a) The schematic shows the relative position of the QD and the cavity on a wavelength axis. For the particular QD-cavity system considered, the QD is red detuned from the cavity, though off-resonant coupling is observed for both red and blue detuned QDs. In experiments, a strong pump laser dresses the QD while a weak probe laser is scanned across the QD. QD emission is incoherently coupled to the cavity. The cavity emission is monitored as a function of probe laser wavelength λ_p. (b) The experimental setup is a confocal cross-polarization setup. The PBS (polarizing beam splitter) is used to perform cross-polarized reflectivity measurements, as in previous work [1]. The powers are measured in front of the objective lens (OL). The output is dispersed in a single-grating monochromator and measured by a nitrogen-cooled CCD. We employ a linear three hole defect PC cavity (a scanning electron micrograph is shown in the inset). (c) Normalized off-resonant cavity emission obtained by numerical simulation is plotted as a function of $\lambda_p - \lambda_{QD}$, λ_{QD} and λ_p being the QD resonance and probe laser wavelengths, respectively, for different pump powers P (normalized units) while the probe power is kept at 1. The pump laser is resonant with the QD. (d) For a pump power of $P = 25$, the cavity emission is plotted as a function of $\lambda_p - \lambda_{QD}$ for different pump-QD detunings $\Delta\lambda_{pump}$ (nm). In both (c) and (d), spectra are vertically offset for clarity.

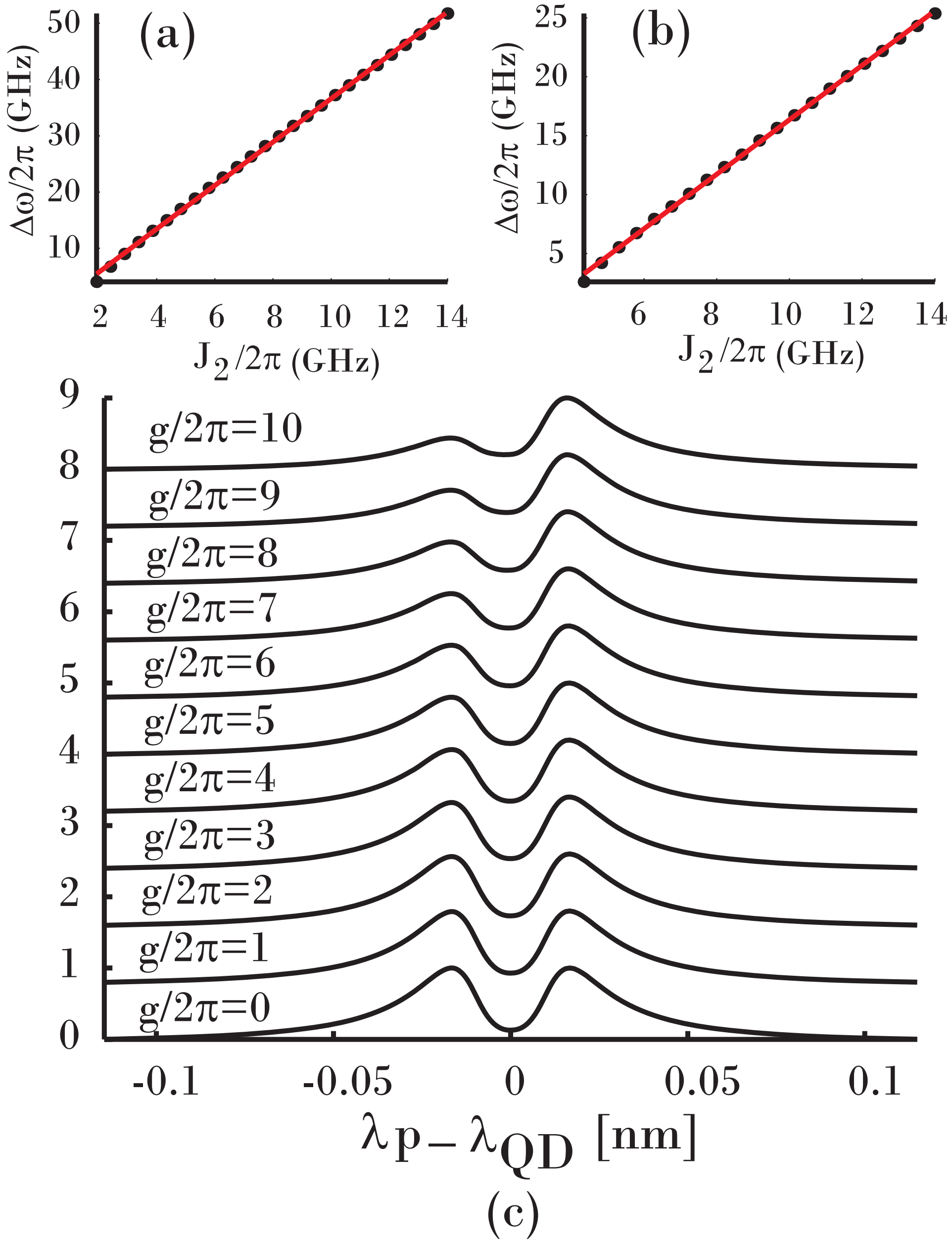

Figure 7.14: Power dependence of the peaks and dips in the cavity emission spectra and effect of coherent dot-cavity interaction strength g: (a) The separation between the two peaks (as shown in Fig. 7.13 c) as a function of the laser Rabi frequency. The slope of the linear fit is ~ 4. (b) The separation between the two dips (as shown in Fig. 7.13 c) as a function of the laser Rabi frequency. The slope of the linear fit is ~ 2(c) Cavity emission as a function of probe laser wavelength, for different dot-cavity coupling g.

changing temperature, indicating that the QD is not strongly coupled to the cavity. The QD resonance is at $\lambda_{QD} = 927.5$ nm and the cavity resonance is at $\lambda_{cav} = 927.1$ nm at 35 K temperature leading to a dot-cavity detuning $\Delta\lambda = \lambda_{QD} - \lambda_{cav} = 0.4$ nm. Once these system parameters are determined, we confirm the presence of off-resonant coupling effects by scanning a narrow-bandwidth CW field in wavelength across the QD-cavity system and measuring emission spectra, as shown in Fig. 7.15(b). In these spectra, off-resonant coupling leads to the observation of cavity emission under optical excitation of the QD and vice-versa. We note that these emission signatures depend on the polarization of the scanning laser and are maximum when the laser is co-polarized with the PC cavity mode. We can estimate the linewidth of the QD ($\Delta\lambda_{QD} = 0.06$ nm) and the cavity ($\Delta\lambda_{cav} = 0.11$ nm) by scanning the excitation laser across one resonance and observing emission at the other (Fig. 7.15 c and d). These measurements yield a broader cavity linewidth compared to that measured in standard PL measurements due to the heating of the structure caused by the resonant laser [4]. We now use this off-resonant cavity emission to probe the dressing of the QD by a strong resonant laser field.

To observe the QD dressed states, we scan the CW (probe) field across the QD resonance and measure the cavity emission signal [as in Fig. 7.15 c] in the presence of a strong CW pump field tuned resonantly to the QD transition. The pump laser, co-polarized with the probe laser, serves to dress the QD, thus qualitatively altering the observed cavity emission spectrum. To optimize the signal to noise ratio of cavity emission measurements, the polarization of the pump and probe fields is rotated 45 degrees with respect to the cavity mode polarization in front of the objective lens to minimize the amount of pump and probe light collected through the polarizing beam splitter (PBS) [Fig. 7.13 b]. High amounts of collected excitation light lead to higher noise in cavity emission as measured by the spectrometer CCD even when the cavity and the QD are detuned. Fig. 7.16 a shows the cavity emission intensity as a function of the probe laser wavelength λ_p. In the absence of the pump laser ($P = 0$), we observe that the cavity emission spectrum possesses a Lorentzian line-shape. However, when a strong pump drives the QD, the Lorentzian splits into two peaks, as observed in the simulations in Fig. 7.13 c. However experimentally

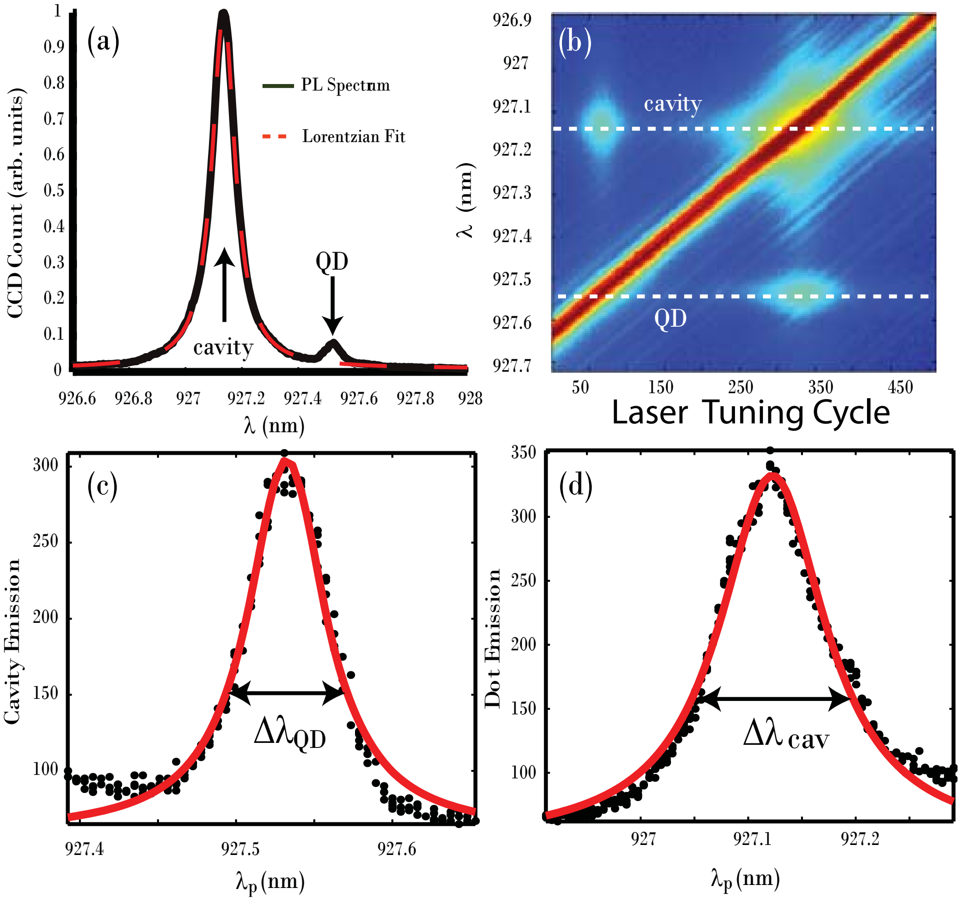

Figure 7.15: (Characterization of the QD-cavity system in photoluminescence (PL) and probing of the off-resonant dot-cavity coupling. (a) PL spectrum of the system. From the Lorentzian fit to the cavity we estimate a cavity linewidth $\Delta\lambda_{cav} = 0.1$ nm. (b) The laser is scanned across the QD-cavity system. Emission from the cavity is observed when the laser is resonant with the QD. Similarly, emission from the QD is observed when the laser is resonant with the cavity. (c),(d) The QD (cavity) linewidth is measured by monitoring the cavity (QD) emission as a function of the probe wavelength λ_p.

measured QD linewidths are broadened by spectral diffusion of the QD transition, which is not included in our theoretical model [118]. Hence, we fit a Lorentzian to each peak and study the splitting between two peaks as a function of the pump laser power. Fig. 7.16 b plots this splitting as a function of the square root of the laser power P measured in front of the objective lens (OL). We observe that the splitting increases linearly with $\sqrt{P} \propto E$, the laser field amplitude. The splitting is given by ~ 4 times the laser Rabi frequency $\Omega = \vec{\mu_d}.\vec{E}/\hbar$, where μ_d is the QD dipole moment. We note that in the results of Fig. 7.16 a, the peaks are not symmetric. This is mainly due to the fact that fixing the pump laser exactly to the QD resonance in experiments is made difficult by spectral drifts in both the QD resonance and the pump laser wavelength over time. However, this asymmetry can also be partially attributed to the coherent interaction g between the QD and the cavity (Fig. 7.14 b). For a detuned pump, the splitting is modified, and this causes a deviation of the Rabi frequencies from the linear relation as shown in Fig. 7.16 b. We also note that the high pump power regime of Fig. 7.13 c, which shows a central peak and two dips in the observed spectra, is difficult to observe in experiments due to the fact that there is still considerable pump leakage through the PBS. At higher powers, this transmitted pump light can saturate CCD pixels corresponding to wavelengths near the pump wavelength. This saturation can result in charge leakage across CCD pixels leading to a deterioration of the signal to noise ratio of cavity emission measurements. The use of improved spectral filtering techniques would reduce the amount of pump light collected, possibly enabling observation of this high power regime.

We estimate that the off-resonant cavity ($\Delta\lambda = 0.4nm$) enhances the laser electric field inside cavity by a factor of ~ 40, compared to the bare QD case, assuming a spot size of 3μm and QD at the field maximum. This agrees with the result shown in Fig. 7.16 c, where the cavity emission is plotted for two different QD-cavity detunings at the same pump power. We consider a Gaussian laser beam with power P and frequency ω incident on a photonic crystal cavity. The power is measured in front of the objective lens and the coupling efficiency of the laser to the cavity is η. If the cavity quality factor is $Q = \omega_0/\Delta\omega$, with cavity resonance frequency ω_0 and linewidth $\Delta\omega$, the energy inside the cavity (for a laser resonant to the cavity) is $W = P\eta/\Delta\omega$.

For an off-resonant cavity, where the laser is detuned from the cavity by Δ, the previous expression for energy is multiplied by a Lorentzian:

$$f = \frac{1}{1 + (2\Delta/\Delta\omega)^2} \tag{7.48}$$

where $\Delta = \omega - \omega_0$ with ω_0 being the resonance frequency of the cavity. The energy in the cavity can also be expressed as $\epsilon |E_{max}|^2 V_m$, where ϵ is the permittivity of the medium, and E_{max} is the electric field at the point of maximum electric energy density, and V_m is the cavity mode volume. Equating the two expressions of energy, we can write

$$\frac{P\eta}{\Delta\omega} \frac{1}{1 + (2\Delta/\Delta\omega)^2} = \epsilon |E_{max}|^2 V_m \tag{7.49}$$

Using

$$\Delta\omega = \frac{\omega_0}{Q} = \frac{2\pi c}{Q\lambda_0} \tag{7.50}$$

where c is the velocity of light and λ_0 is the resonance wavelength of the cavity, we can find that E_{max}:

$$|E_{max}| = \sqrt{\frac{\eta P Q \lambda_0}{2\pi c \epsilon V_m} \frac{1}{1 + (2\Delta/\Delta\omega)^2}} \tag{7.51}$$

If the quantum dot is not located at the point of the maximum electric field energy density, the electric field at its location will be smaller than E_{max} (and the spatial variation of the E-field is determined by the mode pattern $\psi(x, y)$). Therefore, the electric field at the location of the QD would be

$$|E_{cav}| = |E_{max}| \psi(x, y) \tag{7.52}$$

On the other hand, when there is no cavity present, the intensity I of the light (assuming a Gaussian beam) incident on the GaAs is given by

$$I = \frac{P}{2\pi\sigma_0^2} \tag{7.53}$$

where σ_0 is the Gaussian beam radius of the laser. Also the intensity of the laser is given by

$$I = \frac{1}{2} c\epsilon |E|^2 \tag{7.54}$$

Equating these two, the electric field is found to be

$$|E| = \sqrt{\frac{P}{c\epsilon\pi\sigma_0^2}} \tag{7.55}$$

Assuming normal incidence on the air-GaAs interface

$$|E_{GaAs}| = \frac{2}{1+n}|E| \tag{7.56}$$

where n is the refractive index of GaAs. We note that the effect of the reflection in the interface, is embedded in η for the analysis done for the cavity. From the above discussion, the electric field sensed by the QD in the absence of the cavity has the form

$$|E_{nocav}| = \frac{2}{1+n}\sqrt{\frac{P}{c\epsilon\pi\sigma_0^2}} \tag{7.57}$$

Comparing the cavity and no-cavity case, we can find that the electric field enhancement is given by

$$\frac{E_{cav}}{E_{nocav}} = \frac{1+n}{2}\sqrt{\frac{\eta Q\lambda_0\sigma_0^2}{2V_m}\frac{1}{1+(2\Delta/\Delta\omega)^2}}\psi(x,y) \tag{7.58}$$

When the laser is resonant with the cavity, the maximum field enhancement for a linear three hole defect (L_3) cavity is ~ 350, assuming $\eta = 1\%$, $Q = 10000$, $\lambda_0 = 927$ nm, $\sigma_0 = 3\mu$ m, $V_m = 0.8(\lambda_0/n)^3$, and the QD at the field maximum, i.e., $\psi = 1$. For a detuning of 4 linewidths (as is true for our experiment), the maximum enhancement is ~ 40. We note that this maximum enhancement can be increased by using a cavity with a higher quality factor or lower mode volume. Another way to increase the enhancement is by increasing the coupling efficiency η by using a waveguide or a fiber coupled to the cavity.

The Rabi frequencies of the laser at a QD-cavity detuning of $\Delta\lambda = 0.4$ nm are measured to be 8.15 and 8.9 GHz at input powers of 190 and 290 nW, respectively. The Rabi frequencies increase to 11.1 and 12.1 GHz when the pump is closer to the cavity resonance ($\Delta\lambda$ are 0.26 and 0.22 nm, respectively). We theoretically estimate these Rabi frequencies to be 11.6 and 13.8 GHz, which are close to the experimentally measured values. The data of Fig. 3 a, b allows for order of magnitude estimation of system parameters such as QD dipole moment and effective QD electric field. Assuming a coupling efficiency of the Gaussian laser beam to the PC cavity mode η, we can estimate the maximum laser field amplitude E at the position of the QD using the Eqn. 7.51. From the linear fit in Fig. 3 b, we estimate the dipole moment μ_d of the QD to be be on the order of 22 Debye, with $\eta = 1\%$ as obtained previously with the same grating coupled cavity design [5]. For this dipole moment, the maximum QD-cavity interaction strength $g/2\pi$ should be $\sim$ 29 GHz, assuming the QD is located at the electric field maximum, thereby leading to the strong coupling. As mentioned previously, we did not observe the anti-crossing of the QD and cavity peaks in PL and thus believe that the actual value of g is smaller than this calculated value most likely because the QD is not located at the cavity electric field maximum.

Finally, we study the effects of the detuning between the pump and the QD resonance on the off-resonant cavity emission. Fig. 7.17 shows the cavity emission as a function of probe laser wavelength λ_p for different pump laser-QD detunings $\Delta\lambda_{pump} = \lambda_{pump} - \lambda_{QD}$. The pump laser power is kept fixed at 290 nW. The detuning $\Delta\lambda_{pump}$ is changed from -0.04 nm (blue detuned) to 0.04 nm (red detuned). We observe that when the pump laser is far detuned from the QD resonance, the cavity emission shows a single peak with λ_p. As the pump is tuned closer to the cavity resonance, two peaks emerge in the spectrum, where the peaks are asymmetric when the pump is not exactly resonant with the QD. The fact that the peaks remain distinct as the pump is tuned through the QD resonance verifies experimental observation of the anti-crossing of the Rabi sidebands of the driven QD, consistent with the theory (Fig. 7.13 d).

Therefore, we demonstrate that signatures of the coherent driving of a QD by a strong pump laser are preserved after phonon assisted scattering to an off-resonant cavity despite the fact that this scattering process is incoherent. In addition to revealing new aspects of the off-resonant QD-cavity interaction, this result is also potentially useful for enabling simpler coherent optical spectroscopy of a QD, as the readout signal is offset in frequency and can be spectrally filtered using well-established techniques. Moreover, this approach may relax the requirement of working exclusively with strongly coupled QD-cavity systems in quantum networks.

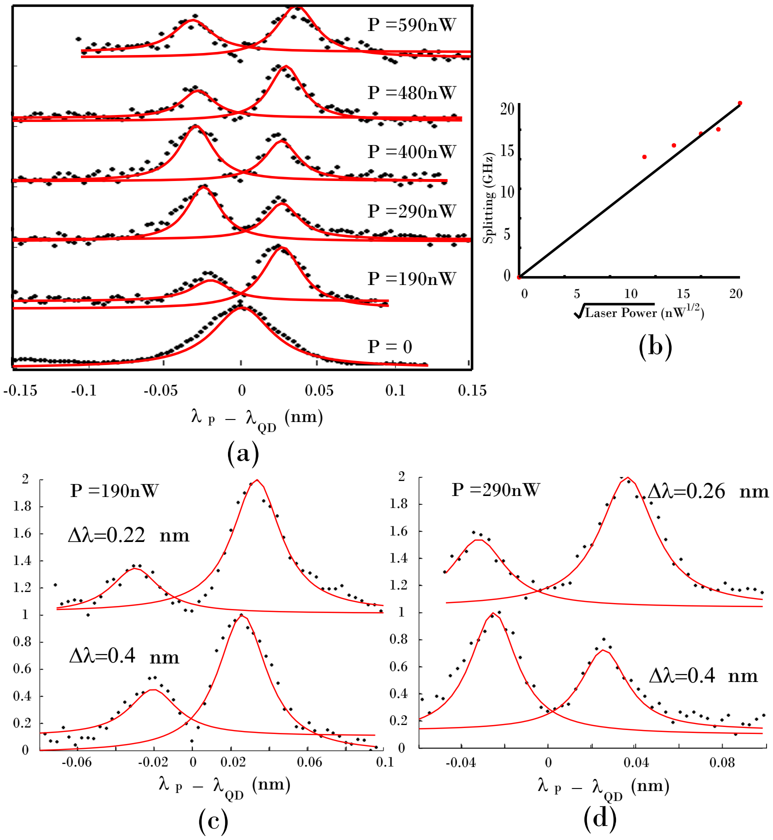

Figure 7.16: Coherent interaction between the QD and the laser observed through cavity emission. (a) Normalized cavity emission as a function of the probe laser wavelength for different pump powers (measured before the objective lens). We observe that a single QD resonance splits into two peaks. The splitting is linearly proportional to the Rabi frequency of the pump laser. Each peak is fit with a Lorentzian. (b) Rabi frequency Ω of the laser (estimated from the splitting) as a function of the square root of the pump power P. A linear relation exists between Ω and $\sqrt{P}$. (c) Normalized cavity emission for a pump power of 190 nW for two different QD-cavity detunings $\Delta\lambda = 0.22$ and 0.4 nm. (d) Cavity emission for a pump power of 290 nW at two different QD-cavity detunings $\Delta\lambda = 0.26$ and 0.4 nm. We observe that the splitting increases for smaller detuning (i.e., when the pump laser is closer to the cavity), which suggests that the input laser power is enhanced by the presence of the cavity. For all experiments the probe laser power is kept constant at 20 nW. The QD-cavity detuning is defined as $\Delta\lambda = \lambda_{QD} - \lambda_{cav}$. In (a), (c), (d) the spectra are vertically offset for clarity.

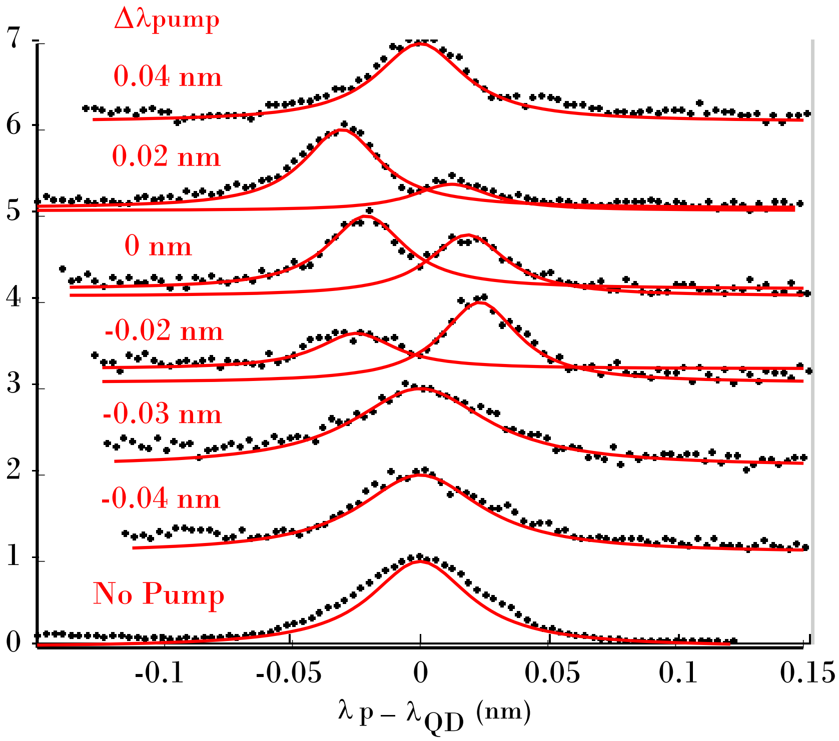

Figure 7.17: Dependence of the result on pump-QD detuning. Off-resonant cavity emission as a function of the probe laser wavelength for different pump-QD detunings $\Delta\lambda_{pump} = \lambda_{pump} - \lambda_{QD}$. We observe that the QD linewidth broadens when the pump is present and detuned from the QD resonance. As the pump is tuned through the QD resonance, we observe the emergence of two peaks in the cavity emission spectrum. This two-peak spectrum is consistent with the observation of the anti-crossing of Rabi sidebands. The pump and probe power are kept at 290 nW and 20 nW, respectively. The spectra are offset for clarity.

7.4 Time resolved study of the off-resonant cavity emission

Here we describe an experiment to estimate the time required to transfer the energy from a QD to the cavity, when the QD is resonantly excited. This measurement gives a way to estimate the incoherent coupling rate γ_r. The experiments are performed at cryogenic temperatures ($\sim 30-55$ K) on the same type of QDs embedded in a GaAs three-hole defect L_3 photonic crystal cavity.

We resonantly excite the QD with a laser pulse train consisting of $\sim$ 40 ps wide pulses with a repetition period of 13 ns. A grating filter is used to collect only the off-resonant cavity emission (at higher energy than the excited QD) and block all the background light from the excitation laser. The cavity emission signal is then sent to a single photon counter followed by a picosecond time analyzer (PTA), with a time resolution of $\sim$ 100 ps. The PTA is triggered by the excitation laser pulse, and the cavity emission is recorded. Fig. 7.19 shows the pulse shape (reflected from the semiconductor sample to show the delay and distortion of the pulse itself due to the setup and the PTA), as well as the rising and falling edges of the cavity emission for different temperatures. By fitting exponentials to the cavity signal, we estimate the fall times of the cavity emission. In practice, both the rise and fall times are complicated functions of the dipole decay rate γ, the phonon coupling rate γ_r and the cavity decay rate κ. From a simple rate equation calculation (where the population goes from the QD to the cavity with a rate γ_t), under the assumption that all the population is in the QD excited state at time zero, we can find that the cavity population is proportional to $e^{-(\gamma_t+\gamma)t} - e^{-\kappa t}$. The rate equations describing the dynamics of the coupled QD-cavity system are given by (Fig. 7.18)

$$\frac{da}{dt} = \gamma b + \kappa c - R \tag{7.59}$$

$$\frac{db}{dt} = R - (\gamma + \gamma_t) b \tag{7.60}$$

$$\frac{dc}{dt} = \gamma_t b - \kappa c \tag{7.61}$$

As in our experiment, we are mainly measuring the emission from the cavity (i.e.,

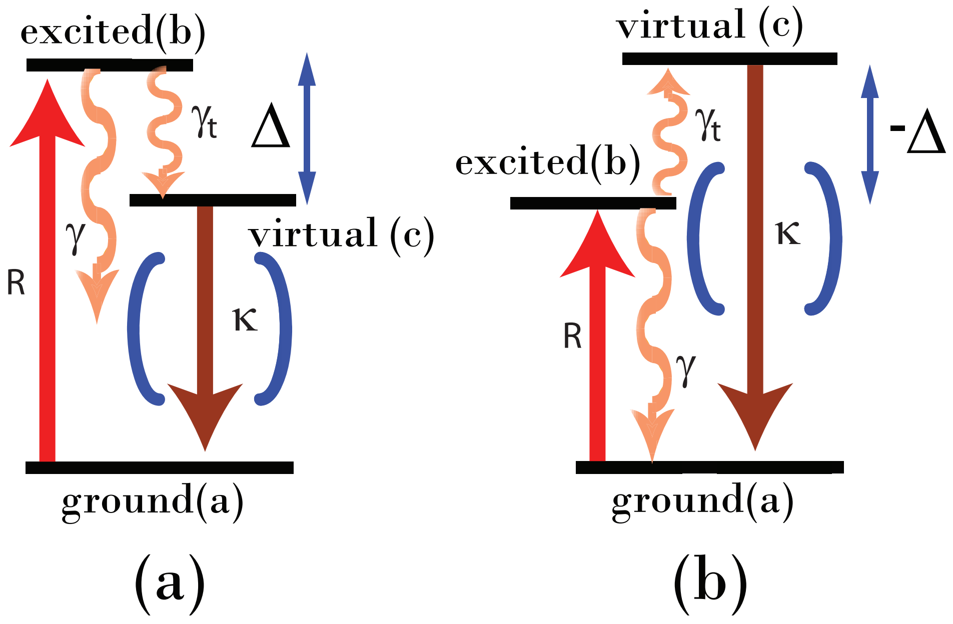

Figure 7.18: Simple level diagrams of the off-resonantly coupled QD-cavity system for a blue (a) and a red (b) detuned QD. The ground state a and excited state b of the QD are coupled via a laser. The excited state can decay to the ground state with a rate γ, and to the virtual state with a rate γ_t. The cavity couples the virtual state to the ground state, and the cavity decay rate is κ. In our experiment we measure the population in the virtual state, or, $c(t)$.

the $c(t)$) after the pump excites the QD, we can model the system as at time $t = 0$, $b(0) = 1$, $a(0) = 0$ and $c(0) = 0$, and there is no R. Hence the equations become

$$\frac{db}{dt} = -(\gamma + \gamma_t)b \tag{7.62}$$

$$\frac{dc}{dt} = \gamma_t b - \kappa c \tag{7.63}$$

This can be re-written as a second order differential equation for $c(t)$

$$\frac{d^2c}{dt^2} + (\gamma + \gamma_t + \kappa)\frac{dc}{dt} + \kappa(\gamma + \gamma_t)c = 0 \tag{7.64}$$

with the initial conditions $c(0) = 0$ and $\frac{dc}{dt}|_{t=0} > 0$. The solution is given by $c(t) = e^{-(\gamma_t+\gamma)t} - e^{-\kappa t}$ for $\kappa > (\gamma + \gamma_t)$.

We note that the newly introduced rate γ_t depends on γ_r, the phonon-QD incoherent coupling rate, but they are not same. In our system, the cavity decay rate κ

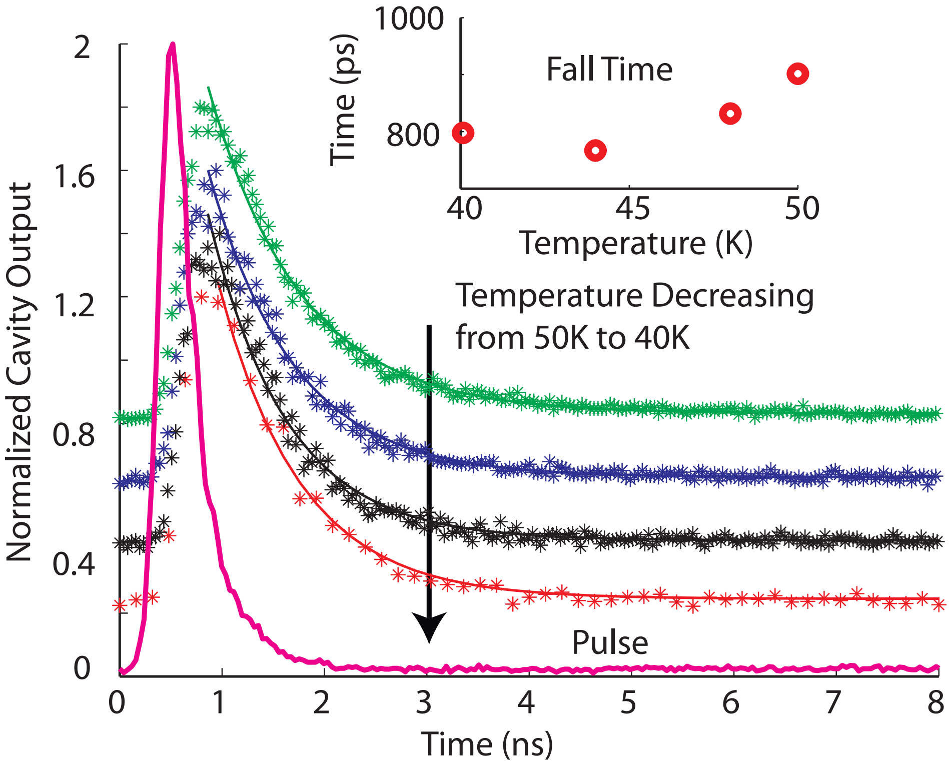

Figure 7.19: Time resolved measurement of the off-resonant cavity emission. The QD is resonantly excited with a 40 ps pulse, and the time-resolved measurement of the higher energy off-resonant cavity emission is performed. The inset plots the fall times of the cavity emission (extracted from the exponential fits) against the system's temperature.

is an order of magnitude larger than both γ and γ_t, and the fall time of the cavity emission mainly follows $e^{-(\gamma_t+\gamma)t}$. We fit the fall time of the cavity emission with an exponential and find a value of $\sim$ 850 ps. From independent measurements, we know that the radiative QD lifetime is $\sim$ 2 ns, when the QD is not Purcell enhanced. From this, we can estimate $\gamma_t/2\pi = 0.12$ GHz. The QD in this particular case is red detuned from the cavity, so to have off-resonant coupling, a phonon needs to be absorbed. The temperature is changed from 40 K to 50 K, corresponding to a change in dot-cavity detuning from 1.8 nm to 2.25 nm and a change in mean phonon number $\bar{n}$ only from 7.8 to 8 [41]. Hence, the slight difference between the fall-times cannot be attributed to the increase in phonon density.

7.5 Phonon assisted inter-dot coupling

All phonon-assisted off-resonant interaction experiments reported so far in the literature (and also in this thesis) are based on a single QD and a cavity. Recently, an experimental study of two spatially separated QDs interacting resonantly in a microcavity has been reported [131], as well as a theoretical analysis [132, 133, 134, 135, 136] of the possible energy transfer mechanisms between QDs in such a cavity. The interaction between two spectrally detuned QDs via a photonic crystal cavity has also been demonstrated recently under p-shell QD excitation [137]. However, the actual coupling mechanism between two QDs is not conclusively proven in that experiment, as the presence of a higher-energy pumping laser can create charges and multi-excitons, making the system more complex. In our work, we show that under resonant excitation (of one of the dots), two spectrally far-detuned QDs can interact with each other via an off-resonant cavity. More specifically, we observe emission from a spectrally detuned QD when another QD is resonantly excited. Both frequency down-conversion (energy transfer from a higher energy QD to a lower energy QD) and up-conversion (energy transfer from a lower energy QD to a higher energy QD) are observed for frequency separation of up to $\sim \pm 1.2$ THz. Such a large energy difference cannot be ascribed to an excited state of the same QD, as opposed to earlier work by *Flagg et. al.* [138] which was performed without a cavity and for frequency difference of $\sim \pm 0.2$ THz. Based on our observations, we believe this process occurs between two different QDs, and the coupling between the QDs is enhanced by the presence of the cavity.

7.5.1 Theory

The experimental system we want to model is shown in Fig. 7.20a. QD1, spectrally detuned from both the cavity and QD2, is resonantly excited with a pump laser. The excitation is transferred to the cavity and QD2 via an incoherent phonon-mediated coupling [41]. We note that, in theory, it is possible to transfer energy directly from QD1 to QD2 via phonons. However, we observe the QD2 emission to be strongly dependent on the QD2-cavity detuning, and hence the presence of a cavity is important for our experiment. In particular, for detunings greater than a few cavity linewidths, the QD2 emission becomes weak and eventually vanishes.

The master equation used to describe the lossy dynamics of the density matrix ρ of a coupled system consisting of two QDs and a cavity is given by

$$\frac{d\rho}{dt} = -i[\mathcal{H}, \rho] + 2\kappa\mathcal{L}[a] + 2\gamma_1\mathcal{L}[\sigma_1] + 2\gamma_2\mathcal{L}[\sigma_2]. \tag{7.65}$$

Assuming the rotating wave approximation, the Hamiltonian describing the coherent dynamics of the system $\mathcal{H}$ can be written in the interaction picture as

$$\begin{aligned} \mathcal{H} = \omega_c a^\dagger a &+ \omega_{d1}\sigma_1^\dagger\sigma_1 + g_1(a^\dagger\sigma_1 + a\sigma_1^\dagger) \\ &+ \omega_{d2}\sigma_2^\dagger\sigma_2 + g_2(a^\dagger\sigma_2 + a\sigma_2^\dagger), \end{aligned} \tag{7.66}$$

while the Lindblad operator modeling the incoherent decay via a collapse operator D is $\mathcal{L}[D] = D\rho D^\dagger - \frac{1}{2}D^\dagger D\rho - \frac{1}{2}\rho D^\dagger D$. Additionally, κ is the cavity field decay rate; γ_1 and γ_2 are the QD dipole decay rates; ω_c, ω_{d1} and ω_{d2} are the resonance frequencies of the cavity, QD1 and QD2; g_1 and g_2 are the coherent interaction strengths between the cavity and the two QDs. The resonant driving of QD1 or QD2 can be described, respectively, by adding the term $\Omega(\sigma_1 + \sigma_1^\dagger)$ or $\Omega(\sigma_2 + \sigma_2^\dagger)$ to the Hamiltonian $\mathcal{H}$. The driving laser frequency is denoted by ω_l. We model the incoherent phonon-mediated coupling by adding $2\gamma_{r1}\mathcal{L}[a^\dagger\sigma_1]$ and $2\gamma_{r2}\mathcal{L}[a\sigma_2^\dagger]$ to the Master equation [41]. We note that the phonon-QD interaction strength depends on the phonon frequency and is, in general, not a constant [107, 108]. However, as we are focusing only on a small range of detunings in our experiments, a constant rate of QD-phonon interaction can be assumed. The channel between QD1 and the cavity is then characterized by the rates γ_{r1} and g_1, while the channel between the cavity and QD2 is characterized by γ_{r2} and g_2. Fig. 7.20c shows the numerically simulated power spectral density (PSD) of the cavity output $S(\omega) = \int_{-\infty}^{\infty}\langle a^\dagger(\tau)a(0)\rangle e^{-i\omega\tau}d\tau$ when the lower energy QD1 is resonantly driven with a laser. We use only the cavity operator to calculate the PSD because experimentally most of the collected light (even off-resonant) is coupled to the cavity mode. For these simulations, we use $\gamma_1/2\pi = \gamma_2/2\pi = 1$ GHz, $\gamma_{r1}/2\pi = 0.5$ GHz, $g_1/2\pi = 20$ GHz, $\kappa/2\pi = 20$ GHz, QD1-cavity detuning $\Delta_1 = 6\kappa$ and QD2-cavity detuning $\Delta_2 = -6\kappa$ and the driving laser strength $\Omega_0/2\pi = 5$ GHz.

We first study the role of γ_{r2} and g_2 in the QD2 emission. Without g_2, no emission from QD2 is observed; in the presence of g_2, QD2 emission appears and γ_{r2} enhances it (Fig. 7.20 c). This shows that coherent coupling between the cavity and QD2 is required to observe this dot to dot coupling. Although QD2 emission is observed even in the absence of its coupling to phonons (for $\gamma_{r2} = 0$), such emission is much weaker than when phonon assisted process is present. The three peaks observed at the QD1 resonance are the usual Mollow triplet, modified due to the presence of the cavity and phonons [130, 139, 41]. We note that to observe the off-resonant emissions from the cavity and the QD2, we also need to have a phonon assisted interaction between the QD1 and the cavity, i.e., a nonzero γ_{r1}.

Next, we theoretically analyze the dependence of the inter-dot coupling on the spectral detuning between the undriven dot and the cavity. In an actual experiment it is very difficult to tune only one QD without affecting the other, as the two QDs are spatially very close to each other. Hence, in the simulation, we changed both QD resonances and kept the cavity resonance fixed. In Fig. 7.21a we excite lower energy QD1, which is spectrally far detuned from the cavity. QD2 is spectrally close to the cavity, and strongly coupled to it. The resonant excitation of QD1 causes light to be emitted both from the cavity and from QD2. Additionally, we observe anti-crossing between the cavity and QD2 as the frequency of QD2 is tuned. Following this, we excite higher energy QD2 resonantly, and observe emission from QD1 (Fig. 7.21b). We observe an increase in QD1 emission intensity when QD2 is resonant with the cavity. Finally, we calculate the linewidth of QD1 while measuring the emission from QD2 (inset of Fig. 7.21a), as well as the linewidth of QD2 while measuring the emission from QD1 (inset of Fig. 7.21b), for a weak excitation laser power ($\Omega_0/2\pi = 1$ GHz). The dotted black points are the simulation results, and we fit a Lorentzian to estimate the linewidth. We find that the linewidth of QD1 is 4 GHz and the linewidth of QD2 is 9 GHz. These simulated linewidths are larger than the linewidths one would expect based on just the decay rates, i.e. $2(\gamma + \gamma_r)/2\pi = 3$ GHz; this results from the presence of the cavity and from power broadening induced by the driving laser [41]. However, the linewidths are much smaller than that of the cavity (linewidth of 40 GHz) showing that the coupling is indeed between two QDs. We note that the slight

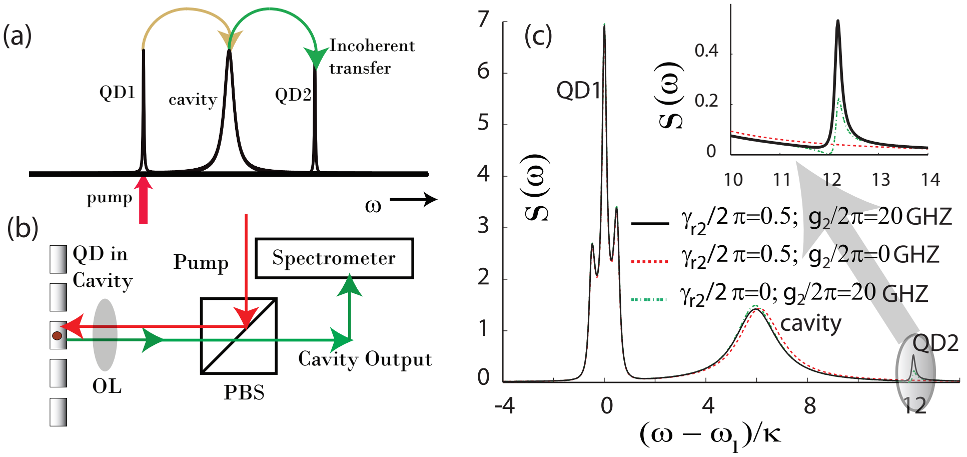

Figure 7.20: (a) Illustration of the phonon assisted inter-dot coupling. QD1 is resonantly driven with a pump laser. The excitation is transferred to QD2 via the cavity. (b) Experimental cross-polarized confocal microscopy setup. PBS: polarizing beam splitter, OL: objective lens. (c) Numerically calculated power spectral density $S(\omega)$ of the cavity output for different QD2-phonon coupling strengths γ_{r2} and QD2-cavity mode coupling g_2. QD1 is resonantly excited (i.e., $\omega_l = \omega_{d1}$) and QD1-cavity coupling is $g_1/2\pi = 20$ GHz, while QD1-phonon coupling rate is $\gamma_{r1}/2\pi = 0.5$ GHz. The cavity field decay rate is $\kappa/2\pi = 20$ GHz. Inset shows a zoom-in of the emission at the QD2 frequency.

shifts in the measured QD resonances from the bare QD resonances ω_{d1} and ω_{d2} arise from a dispersive shift caused by the cavity.

7.5.2 Coupling between two quantum dots

In this subsection, we present experimental data showing dot to dot coupling via an off-resonant cavity for two different systems: one with a strongly coupled QD, and the other with a weakly coupled QD. In the first system, we excite higher energy QD2 resonantly with a laser, and observe emission both from the lower energy off-resonant cavity and QD1 (Fig. 7.22). Note that QD1 is strongly coupled to the cavity and we observe anti-crossing between the cavity and QD1 in the off-resonant emission when the temperature of the system is changed (inset of Fig. 7.22). The experimental data match well qualitatively with the theoretical result shown in Fig. 7.21a. The emission from QD1 diminishes as QD1 is detuned from the cavity, which shows that

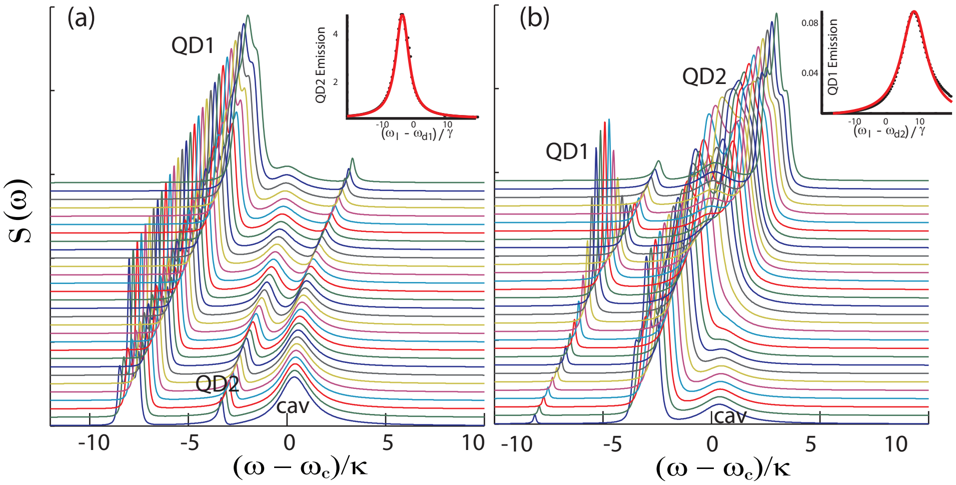

Figure 7.21: (a), (b) Calculated $S(\omega)$ when QD1(a) and QD2(b) are resonantly excited, and the dot-cavity detunings are changed. In other words, $\omega_l = \omega_{d1}$ for (a) and $\omega_l = \omega_{d2}$ for (b). QD1 and QD2 resonances are tuned together, as in the experiment. When QD1 is resonantly driven (a), we observe anti-crossing between QD2 and the cavity in the higher energy off-resonant emission. On the other hand, when QD2 is resonantly driven (b), we observe an increase in QD1 emission when QD2 is resonant with the cavity. For (a) and (b) parameters used for the simulations were: $\gamma_1/2\pi = \gamma_2/2\pi = 1$GHz, $\gamma_{r1}/2\pi = \gamma_{r2}/2\pi = 0.5$ GHz, $g_1/2\pi = g_2/2\pi = 20$ GHz, $\kappa/2\pi = 20$ GHz, detuning between two dots 5κ, driving laser strength $\Omega_0/2\pi = 5$ GHz. Inset of a(b), shows the QD1(2) linewidth measured via monitoring QD2(1) emission. The simulation result is fit with a Lorentzian to estimate the linewidths.

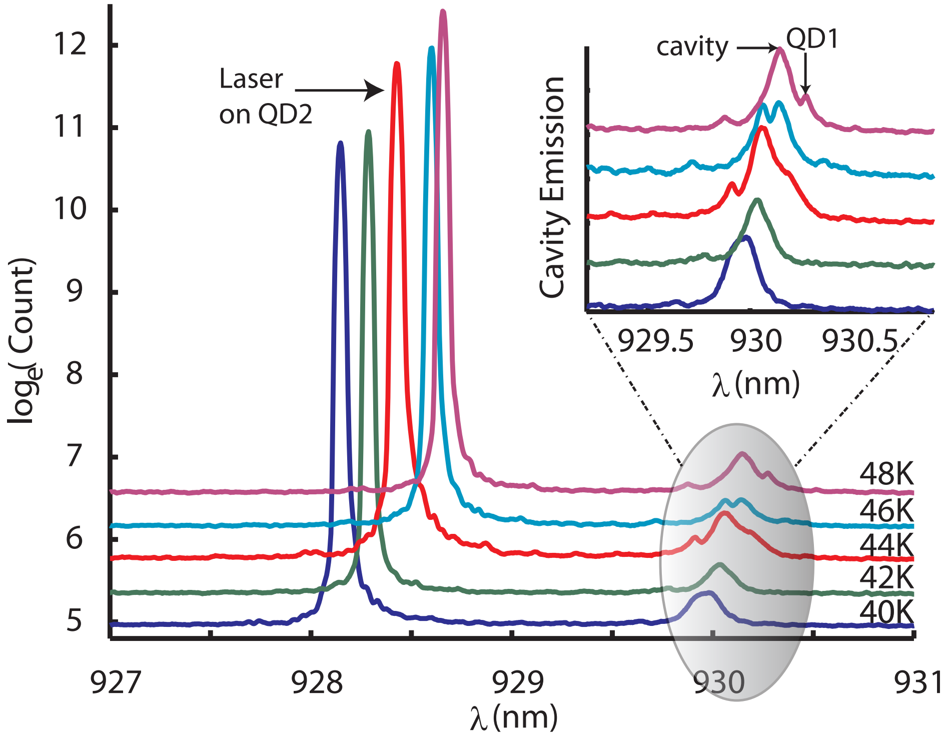

Figure 7.22: Measurement of the emission from the off-resonant cavity and QD1, under resonant excitation of QD2. We observe anti-crossing between QD1 and the cavity when the temperature of the system is changed. Natural log of the count from the spectrometer CCD is plotted. Inset zooms into the cavity emission showing the anti-crossing between the QD1 and the cavity. The plots are vertically offset for clarity.

the coupling between the two dots is enhanced by the presence of the cavity, and g_2 has an important contribution. However, when we scan the pump laser across lower energy QD1 and observe higher energy QD2 emission in this system, we obtain the cavity linewidth showing the usual cavity to QD2 coupling [4]. This might be due to the high temperature (40-48K) of the system, as will be explained later in this section.

In the second system, the higher energy QD2 that is spectrally close to the cavity is only weakly coupled to it. We observe emission from a lower energy QD1 when a laser resonantly excites a higher energy QD2 (Fig. 7.23 blue plot). We also observe up-conversion, i.e., emission from the higher energy QD2 under excitation of the lower energy QD1 (Fig. 7.23 red plot). The energy difference between the two QDs corresponds to a 1.2 THz acoustic phonon. The cavity is at ~ 935 nm, closer to the higher energy QD2, although its emission is not distinctly noticeable. The data is taken at 25K. In the inset (replicated in Fig. 7.24 a,b), we plot the collected emission from the QD which is not resonant with the laser and estimate the linewidth by a Lorentzian fit. The higher and lower energy QDs, respectively, have linewidths of $\sim$ 0.03 nm and $\sim$ 0.013 nm. These are comparable to the linewidths of the self-assembled QDs [4], and indicate that the coupling is indeed between two QDs. The broader linewidth of the higher energy QD is due to the presence of the cavity. Following this, we perform a more accurate measurement of the linewidths of each QD by observing the peak amplitude of the emission from the off-resonant dot as a function of the pump laser wavelength λ_p (Fig. 7.24 c,d), which gives us an estimate for the linewidth of the other (resonantly excited) QD, as the laser scans across it. [4]. From the Lorentzian fit, we estimate that linewidths of the higher and lower energy QDs are, respectively, $\sim$ 0.024 nm and $\sim$ 0.008 nm. The slightly smaller linewidths measured by the latter approach are due to the better spectral resolution offered by this method [4].

Finally, we performed a study of the effects of temperature on the inter-dot coupling. We note that while down-conversion of the pump light is observed at a temperature as low as 10 K, we did not observe any up-conversion at this temperature. This corroborates the fact that the observed dot to dot coupling is phonon-mediated, and at a low temperature up-conversion cannot happen due to the smaller number of phonons. We first scan the laser across the higher energy QD and observe the off-resonant emission from the lower energy QD; Fig. 7.25a shows the result of this measurement for a set of different temperatures. Similarly, Fig. 7.25b shows the data obtained by scanning the laser across the lower energy QD and observing the off-resonant emission from the higher energy QD for an assortment of temperatures. The cavity is spectrally closer to the higher energy QD. It can be seen from the down-conversion plots in Fig. 7.25a that at lower temperature we observe emission from the lower energy QD only when the pump is within the linewidth of the higher

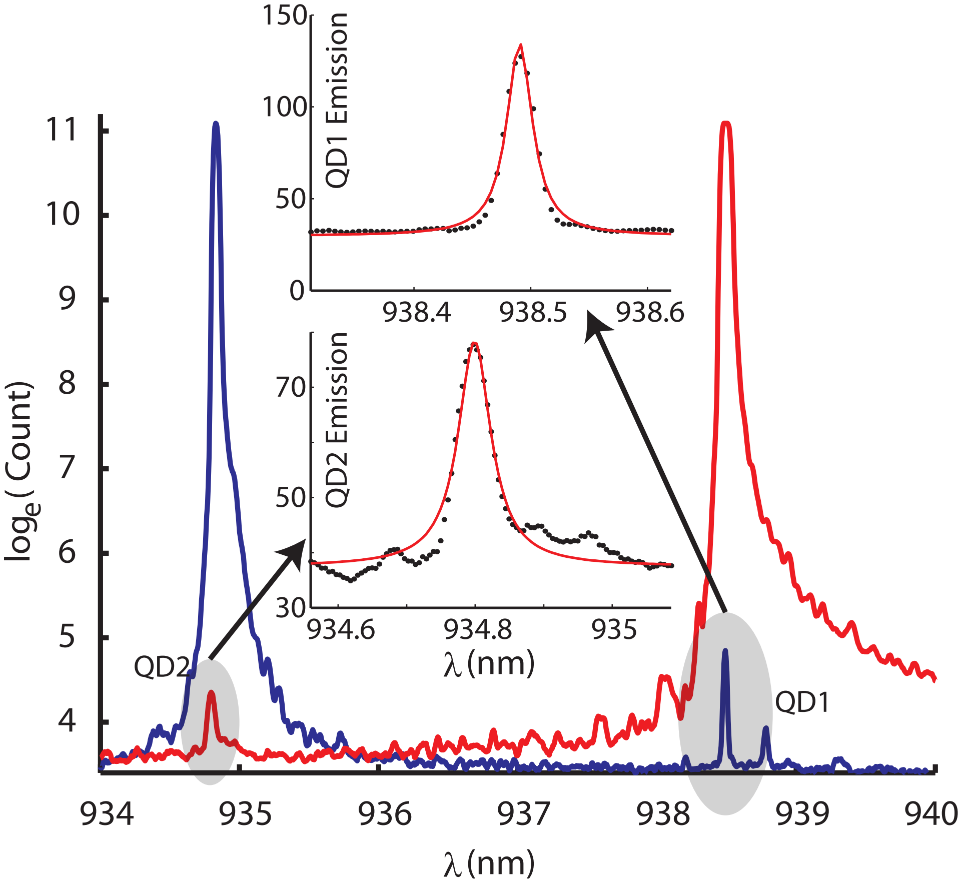

Figure 7.23: Experimental demonstration of the phonon mediated inter-dot coupling: we observe the emission from a lower energy QD1, when a higher energy quantum dot QD2 is resonantly excited (blue). Similarly, under resonant excitation of a lower energy QD1, emission from a higher energy QD2 is observed (red). Natural log of the count from the spectrometer CCD is plotted. Inset zooms into the QD emission (the actual spectrometer ccd counts are plotted). QD linewidths are estimated by fitting Lorentzians. Measured linewidths of the higher and lower energy QDs, respectively, are ~ 0.03 nm and ~ 0.013 nm. The cavity is at ~ 935 nm, close to the higher energy QD2.

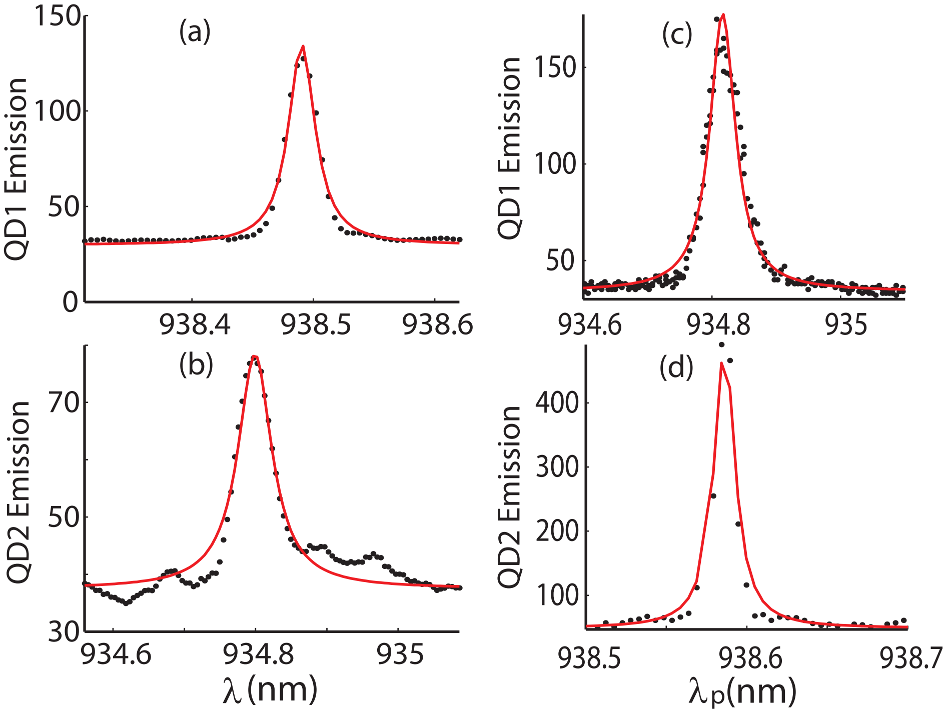

Figure 7.24: Comparison of the linewidths measured in direct off-resonant dot emission (Fig. 7.23) and from resonant spectroscopy of the QDs: (a),(b) the off-resonant QD emission (same as the inset of Fig. 7.23). QD linewidths are estimated by fitting Lorentzians. Linewidths of the higher and lower energy QDs, respectively, are ~ 0.03 nm and ~ 0.013 nm. The cavity is at ~ 935 nm, close to the higher energy QD. (c),(d) the off-resonant dot emission as a function of the pump laser wavelength λ_p. In this experiment, a laser is scanned across one QD and emission is collected from the other QD as a function of the laser wavelength, same as in Ref. [4]. By fitting Lorentzians, we estimate the linewidths of the higher and lower energy QDs to be ~ 0.024 nm and ~ 0.008 nm, respectively. The y-axis plots the photon counts obtained in the spectrometer CCD.

energy QD (the QD of interest and the cavity are shown by arrows). Upto 25 K, the coupling is mostly between two QDs: the emission from lower energy QD is collected only when the higher energy QD is excited, and the linewidth measured is closer to a QD linewidth. However, with increasing temperature (28 K and higher) we observe emission from the lower energy QD even when the cavity is pumped. When the temperature is raised to $\sim$ 40 K, we observe coupling only from cavity to the lower energy QD (i.e., emission from lower energy QD is collected only by exciting the cavity, and not anymore by exciting the higher energy QD); similar to the observations reported previously [2]. The disappearance of the dot to dot coupling (while preserving off-resonant cavity to dot coupling) is also noticed in Figure 7.22 (for the system with only a strongly coupled dot and at 45 K temperature). This effect might be caused by the increase in phonon density and the resulting broadening of the QD lines. In Fig. 7.25b, we monitor the effects of temperature on the up-conversion (the QD of interest is shown by an arrow). We cannot detect the up-conversion at 10 K, as it only becomes observable at higher temperatures. However, with increasing temperature, the QD lines disappear. This is most likely due to the fact that the QD starts losing confinement with higher temperature. The additional peaks in Fig. 7.25b show up-conversion of several other QDs.

In summary, we observed phonon mediated inter-dot coupling, both in systems with strongly and weakly coupled QDs. Both frequency up- and down-conversion were reported via a phonon of estimated frequency $\sim$ 1.2 THz. Our results indicate that this coupling is enhanced by the presence of the cavity, and that without a cavity spectrally close to one of the QDs this process does not occur.

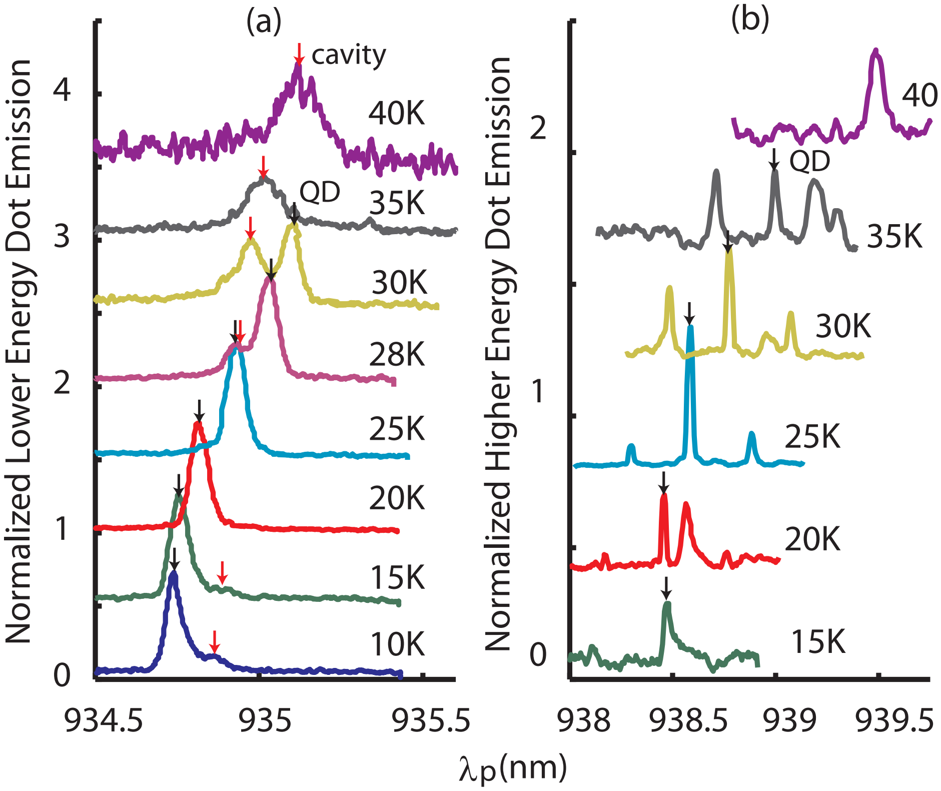

Figure 7.25: Effects of temperature on dot to dot coupling and the resulting frequency conversion of the pump. In the experiments, the wavelength of the pump, λ_p, is scanned through one QD and the peak intensity of the other QD is monitored. In (a), the pump is scanned through the higher energy QD and the down-converted light from the lower energy QD is collected and plotted. In (b), we plot the up-converted light emitted from the higher energy QD as the pump is scanned through the lower energy QD. All plots are separately normalized by the maximum QD emission intensity in each plot and are vertically offset for clarity.

Chapter 8

Spectral diffusion and its effect on CQED

In this chapter, we experimentally study the effect of photo-generated carriers on the spectral diffusion of a QD coupled to a PC cavity. In this system, spectral diffusion arises in part from charge fluctuations on the etched surfaces of the PC. We find that these fluctuations may be suppressed by photo-generated carriers, leading to a reduction of the measured QD linewidth by a factor of ~ 2 compared to the case where the photo-generated carriers are not present. This result demonstrates a possible means of countering the effects of spectral diffusion in QD-PC cavity systems and thus may be useful for quantum information applications where narrow QD linewidths are desired.

Although the solid-state cavity QED system consisting of a QD coupled to cavity behaves similarly to its atomic counterpart in a number of ways, the unavoidable interaction of the QD with its solid-state environment gives rise to phenomena specific to the solid-state system, for example, off resonant coupling as described in the chapter 7. Another important phenomenon arising from the solid state nature of the QD-cavity system is the random trapping and untrapping of charges in the vicinity of the QD due to defects, leading to spectral diffusion of the QD optical transition energy [140, 141, 142, 143]. Spectral diffusion (or jitter) is generally considered detrimental to the optical properties of QDs as it leads to the broadening of optical emission lines

[118, 144, 145]. Studies of spectral diffusion in bulk self-assembled QD systems have attributed its observation to defects provided by the highly disordered QD wetting layer [141, 146]. Additionally, it has been postulated that the proximity of etched surfaces near the QD can lead to spectral diffusion due to defects provided by the etched surface roughness [147]. Recent experimental studies of the linewidth of a QD off-resonantly coupled to a photonic crystal (PC) cavity mode have also observed broadening of QD linewidths that cannot simply be attributed to a pure dephasing process [4]. This is not surprising considering that in QD-PC cavity systems both the wetting layer and the presence of etched surfaces are expected to contribute to spectral diffusion, particularly for QDs close to the holes of the photonic lattice. Further, each contribution is expected to manifest under different system conditions. For instance, wetting layer defects predominantly trap charges through the ionization of excitons generated in the vicinity of the QD by above-band (AB) optical excitation. This contribution to spectral diffusion has been shown to depend on the strength of the AB laser and is absent at very low excitation powers [141]. For trap states provided by the rough etched surfaces of the photonic crystal, fluctuating surface charges are anticipated to contribute to spectral diffusion even in the absence of AB optical excitation. It is unclear, however, how this contribution to spectral diffusion may be affected by above-band excitation, if it can be affected at all.

Here, we experimentally analyze the dependence of spectral diffusion on the power of an AB laser for a QD off-resonantly coupled to a PC cavity. Specifically, we perform QD linewidth measurements by scanning a narrow-bandwidth continuous-wave (CW) laser across the QD resonance and observing optical emission from the detuned cavity. In the absence of AB pumping, we observe a broadened QD linewidth and attribute this broadening to fluctuating surface charges on the nearby etched surfaces. Surprisingly, we find that this contribution to spectral diffusion is suppressed in the presence of AB excitation. We attribute this suppression to the filling of trap states in nearby etched surfaces by photo-generated carriers leading to a drastic reduction of charge fluctuations. This in turn dramatically reduces the experimentally observed QD linewidth. For low AB laser powers, spectral diffusion becomes negligible and the QD linewidth exhibits the standard power broadening as the CW laser power is increased. These results demonstrate an optical excitation regime in which spectral diffusion may be overcome and provide a simple means of countering the degradation of the optical properties of QDs in PC structures. This approach could thus prove useful in QD-PC cavity based quantum technologies that benefit from narrower emitter linewidths.

8.1 Theory: QD linewidth broadening

The effect of the spectral diffusion is reflected in the measurement of the QD linewidth. In the linear response regime, the QD lineshape is characterized by the QD susceptibility [148]

$$\chi(t) \propto \mathcal{F}\left[e^{(i\omega_0-\frac{\gamma(\omega_0)}{2})t}\langle e^{-i\int_0^t d\tau\delta\omega(\tau)}\rangle\right] \tag{8.1}$$

where $\mathcal{F}$ denotes the Fourier transform, ω_0 is the QD resonance frequency, $\gamma(\omega_0)$ is the radiative QD linewidth and the statistical average is taken over all the possible frequencies at different times τ. The effect of spectral diffusion is reflected in this statistical average. This average depends on the underlying probability distribution of the random environment. Assuming a Gaussian fluctuation, by Cumulant expansion (and noting the odd moments are zero), we can write

$$\langle e^{-i\int_0^t d\tau\delta\omega(\tau)}\rangle = e^{-\frac{1}{2}\int_0^t d\tau_1\int_0^t d\tau_2\langle\delta\omega(\tau_1)\delta\omega(\tau_2)\rangle} \tag{8.2}$$

Assuming an exponential correlation function (with variance Γ and correlation time τ_c) of the form

$$\langle\delta\omega(\tau_1)\delta\omega\tau_2\rangle = \Gamma^2 e^{-\frac{|\tau_1-\tau_2|}{\tau_c}} \tag{8.3}$$

we find that

$$\langle e^{-i\int_0^t d\tau\delta\omega(\tau)}\rangle = e^{-\Phi(t)} \tag{8.4}$$

with

$$\Phi(t) = \Gamma^2\tau_c^2[e^{-t/\tau_c} + t/\tau_c - 1] \tag{8.5}$$

Hence, we can model the effect of the fluctuating environment by two quantities: the standard deviation Γ and the correlation time τ_c. In the limit of long measurement time ($t >> \tau_c$), the linewidth of the QD is given by $(\gamma + \Gamma^2\tau_c)$, where γ comes from the Lorentzian lineshape of the QD and $\Gamma^2\tau_c$ is the contribution of the fluctuating environment. In this article, we perform two separate sets of experiments to determine these characteristic quantities of the fluctuating environment. From the first set of experiments, we obtain a measure of the lifetime of the charges in the traps and estimate the correlation time τ_c to be approximately 22 ns. In the second set of experiments, we show how photo-generated carriers can mitigate the effect of the spectral diffusion that is present in the absence of any above-band excitation. From experimental results (see section IV) we determine the broadening due to the fluctuating environment and estimate the quantity $\Gamma^2\tau_c$ to be approximately 8.7 GHz, corresponding to $\Gamma \sim 600$ MHz. We note that as these values were obtained for two different QDs on the same wafer, they provide only order-of-magnitude estimates.

8.2 QD charging and modulation

In the first set of experiments, we investigate the time scale on which carriers generated by the above-band (AB) laser affect the QD environment. These experiments are used to provide a measure of correlation time τ_c associated with the fluctuating surface charges. To perform these measurements, we first identify a strongly coupled QD-cavity system in PL studies by observing the anti-crossing of the QD and cavity resonances that occurs as the temperature is varied. We then probe the system by measuring the transmission of a resonant continuous wave laser through the cavity. In the absence of the AB laser excitation, we observe a Lorentzian line shape for the cavity transmission, indicating that there is no QD coupled to the cavity despite the fact that coupling is observed in PL studies. When the weak AB laser is turned on, however, we observe a drastic change in the transmission spectrum as shown in Fig. 8.2a. The spectrum now appears to show two QDs strongly coupled to the cavity as indicated by the presence of two dips in the transmission spectrum. Inset of Fig. 8.2a shows the theoretically predicted spectrum of cavity transmission, in the absence and presence of two coupled QDs. The experimentally obtained spectra qualitatively match well with the numerical calculation. We note that, in presence of two strongly coupled QDs, the total loss of the system is distributed among the three peaks and

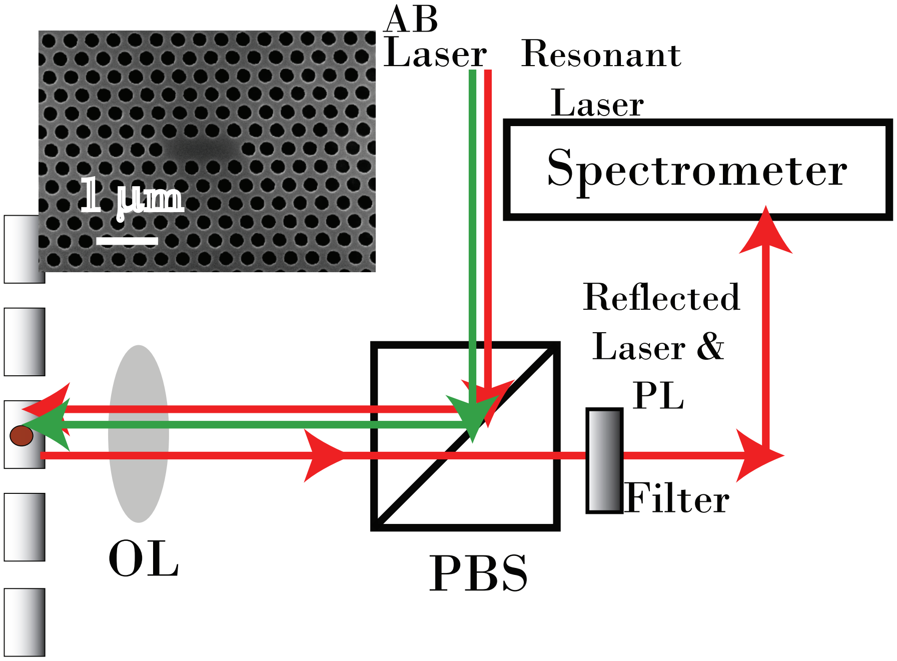
AB
Laser
Resonant
Laser
Spectrometer
1 µm
Reflected
Laser &
PL
Filter
OL
PBS

Figure 8.1: The cross-polarized confocal microscopy setup used to probe the coupled QD-cavity system. The inset shows a scanning electron micrograph of the fabricated PC cavity. OL and PBS stand for objective lens and polarizing beam splitter, respectively.

an apparent narrowing of the bare cavity linewidth is observed. Similar simultaneous strong coupling of two QDs with a semiconductor micro-cavity has previously been observed by other groups [149, 37, 131]. This dramatic change in the transmission spectrum could be caused by the capturing of optically generated carriers by the QD, which leads to the formation of charged excitons and a discrete shift in the QD resonance wavelength, which in this case aligns it with the cavity [150]. Another possibility is that both QDs are in the optically dark state, but are brought back to the optically active states (aligned with the cavity resonance) by the action of the AB laser. However, in the previous experiments on QD blinking it has been shown that QDs remain in such optically dark states typically for approximately several hundred nanoseconds [151] which is much smaller than our experimental integration time. Therefore, this would mean that splitting in the transmission spectrum in Fig. 8.2a should be observed even without the AB laser (although with smaller contrast). Another possible explanation is that the linewidth broadening caused by spectral diffusion suppresses the dips in the transmission spectrum. In the presence of the AB laser, the spectral diffusion is reduced (as will be discussed later in the chapter), leading to a reduction of QD linewidths and the appearance of the dips in the transmission spectrum. We note that in presence of the AB laser, the amount of light coming out of the cavity due to PL is negligible compared to the light transmitted through the cavity.

Next, we study the time dynamics of this resonance shift to obtain a measure of the time scale on which the charge environment surrounding the QD fluctuates. This is done by measuring the transient response of the transmitted resonant laser power to modulation of the AB laser. We note that this type of modulation is different from the all-optical modulation reported in [152], where the QD shifts continuously with increasing AB laser power and the modulation is caused by the screening of the built-in electric field by photo-generated carriers (in the present case, we use an undoped wafer, while Ref. [152] employed a wafer with a pin junction where such effect was significant). To obtain optimal modulation contrast we tune the CW laser to the dip in the cavity transmission spectrum (shown by the arrow in Figure 8.2 a). Figure 8.2 b shows the DC modulation behavior when the above-band laser is manually turned

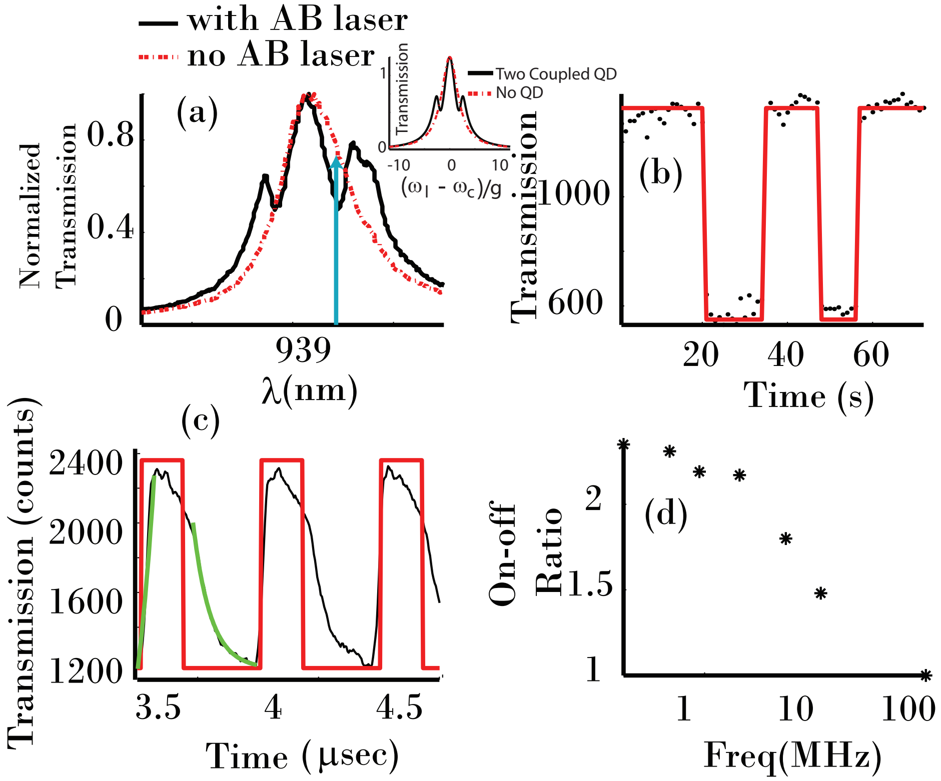

Figure 8.2: (a) Effect of the above-band (AB) laser on the transmission spectrum of a strongly coupled QD-cavity system. The arrow shows the wavelength of the other (resonant) CW laser, whose transmission is modulated by the AB laser in (b) and (c). Inset shows numerically simulated plots of a cavity with and without two strongly coupled QDs. The theoretical results qualitatively match the experimental data well. (b) The transmitted laser power in steady state when the AB laser is turned on and off manually, at intervals of several 10s. This shows the DC characteristics of the modulation. (c) The temporal dynamics of the QD-cavity system: the transmitted laser output as a function of time (black plot). The shown modulation signal (red) is used to modulate the above-band laser. From exponential fits (green) we estimate a time constant of $\sim$ 22 ns, which is obtained as the inverse of the total diffusion rate (equal to the sum of the rates for the rising edge, i.e., carrier capture, and the falling edge, i.e., carrier release). (d) The on-off ratio of the transmitted laser as a function of the modulation frequency.

on and off at varying time intervals and the resonant laser transmission is measured at steady-state. To measure temporal dynamics, we apply a square-wave modulation to the above-band laser and measure the CW laser transmission (at the wavelength indicated by an arrow in Fig. 8.2a) by a single photon counter and a pico-second time analyzer triggered by the modulated above-band laser [37]. We note that for this experiment, the powers of the above-band laser and the resonant CW laser are, respectively, 15 nW and 250 nW as measured in front of the objective lens of the confocal microscopy setup. Figure 8.2 c shows the modulated cavity transmission output with time, for a modulation frequency of 2 MHz. We observe an exponential rise (decay) of the resonant laser transmission when the AB laser is turned on (off). These two time-scales provide estimates of how much time it takes for the charges to get trapped or untrapped in the vicinity of the QD. We fit the exponentials and obtain a rising time constant of $\tau_r \sim 30$ ns and a decay time constant of $\tau_d \sim 80$ ns. From these two measurements we estimate the time-scale of the fluctuation of charges to be $\tau_c = \frac{\tau_r \tau_d}{\tau_r + \tau_d} \sim 22$ ns. This shows that the maximum modulation speed is $1/(2\pi\tau_c) \sim 7$ MHz. Finally, Fig. 8.2 d shows the on-off-ratio of the transmitted CW laser as a function of the modulation frequency of the above-band laser demonstrating that the maximum modulation speed is approximately on the order of ~ 7 MHz. We note that this measurement of correlation time only provides an order of magnitude estimation.

8.3 QD linewidth broadening

Having obtained a measure of the correlation time associated with local charge fluctuations, we now turn to experimental measurements of the broadening of QD linewidths by spectral diffusion. For this set of experiments, we consider a system where a QD is far off-resonantly coupled to a PC cavity mode. For this particular system the dot is 1.4 nm blue-detuned from the cavity (the dot and cavity are, respectively, at 934.9 and 936.3 nm; see Figure 8.3 a). QD linewidths are obtained by measuring the off-resonant cavity emission as the CW laser is scanned through the QD resonance, similar to experiments reported in Ref. [4]. We observe saturation of the cavity emission and power broadening of the QD with increasing excitation laser power. We emphasize that in the experimental data shown in Fig. 8.3, the additional AB laser is not used, and the QD is driven only by the resonant laser. By simultaneously fitting the cavity emission with the model $I_{sat}\tilde{P}/(1+\tilde{P})$ (Figure 8.3 b) and the QD linewidth with the model $\Delta\omega_0\sqrt{1+\tilde{P}}$ (Figure 8.3 c) [121], we find that the observed QD linewidth is significantly smaller than what is expected from ordinary power broadening of a two level system (the dashed line in Figure 8.3 c). Here, I_{sat} is the saturated cavity emission intensity, $\Delta\omega_0$ is the QD linewidth at the limit of zero excitation power and $\tilde{P}$ is proportional to the laser intensity at the position of the QD. Simple theoretical analysis shows that the QD linewidth exhibits power broadening similar to that of a two-level system [41], thus showing that the cavity read-out does not affect the QD linewidth significantly. This unusual broadening behavior cannot be explained by an increasing pure dephasing rate with increasing laser power or excitation induced dephasing [153], since those effects would lead to a broader linewidth than that predicted by standard power broadening. In fact, the nature of the broadening indicates a power-independent broadening mechanism.

We thus consider spectral diffusion as a means of modeling this additional power-independent broadening. We note that spectral diffusion is indeed power independent when the laser is resonant with the QD. The effect of spectral diffusion is modeled as a Voigt lineshape, which is a convolution of a Lorentzian lineshape (the actual QD linewidth $\Delta\omega_L$) and a Gaussian lineshape (the spectral fluctuations with a linewidth of $\Delta\omega_D$). The full width half maximum $\Delta\omega_V$ of a Voigt line-shape is given by [154]:

$$\Delta\omega_V \approx A\Delta\omega_L + \sqrt{(1-A)^2\Delta\omega_L^2 + \Delta\omega_D^2} \tag{8.6}$$

where the parameter $A = 0.5346$ is empirically determined. We use this model to fit the power broadened linewidth, where $\Delta\omega_L = \Delta\omega_0\sqrt{1+\tilde{P}}$. The model fits the experimental data very well, with parameters $\Delta\omega_0/2\pi = 4.7$ GHz and $\Delta\omega_D/2\pi = 8.7$ GHz. These results support the theory that spectral diffusion is caused by the trap states present on the etched surfaces of the photonic crystal. These traps can be randomly charged and discharged, resulting in a fluctuating charge environment that can modify the QD resonance frequency by random DC Stark shifts. As we perform time-averaged measurements on time scales much longer than the correlation time estimated in the preceding set of experiments, the measured QD linewidth is a statistical mixture of the QD resonances at different resonance frequencies.

We now repeat these experiments in the presence of an above-band laser. Although the QD transition energy is not shifted in the presence of the PL laser, we observe a significant reduction in the measured QD linewidth (by a factor of ~ 2) and an increase in the off-resonant cavity emission (Figure 8.4). The resonant laser power is kept at the same value ($\sim$ 100 nW) as used in the measurements of Fig. 8.3. The increased background in the cavity emission in the presence of the AB laser is caused by the small amount of PL generated by this laser. We find that the QD exhibits a Lorentzian line-shape in presence of the AB laser, but shows a nearly Gaussian lineshape in the absence of the AB laser. We attribute this difference to the fact that one of the effects of the AB laser is to create carriers that subsequently fill all the empty traps near the QD, thereby reducing spectral fluctuations. The dependence of the QD linewidth as a function of AB laser power is shown in the inset of Fig. 8.4. With increasing AB laser power, the PL adds noise to the off-resonant cavity emission, making linewidth measurements difficult. However, we do observe a slight increase in the QD linewidth with increasing AB laser power, consistent with previous studies [141]. We note that an AB laser can cause multiple effects such as an abrupt change in the QD resonance frequency [150], or saturation of the QD. Hence this type of linewidth narrowing in the presence of the AB laser is not observed for all the QDs. However, the additional power-independent broadening is present in the absence of AB pumping for all QDs studied.

For this particular QD, we also perform a power dependent study of the QD linewidth and cavity emission in the presence of the AB laser. The AB laser power is kept constant throughout experiments. The data in the absence of the AB laser is the same as shown in Figure 8.3. Figure 8.5a shows the off-resonant cavity emission intensity as a function of the excitation laser power both in the presence and absence of the AB laser. In the presence of the AB laser, we observe an increased cavity emission and also a saturation trend at lower laser power (shown by the fit). However, with increasing excitation laser power, the cavity emission decreases. This decrease

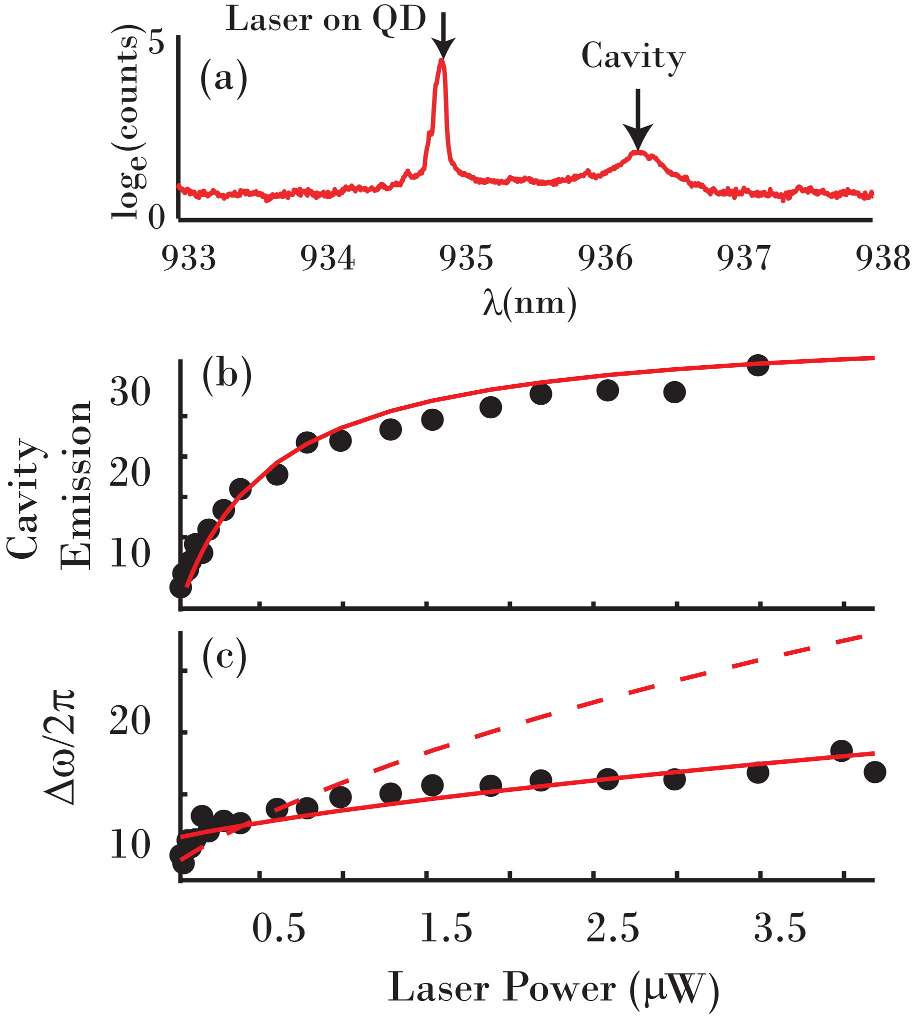

Figure 8.3: QD spectroscopy by off-resonant dot-cavity coupling: (a) The spectrum showing the laser resonantly driving the QD and the emission from an off-resonant cavity. A logarithmic scale is used to show both the strong laser and the weak cavity emission. (b) Cavity emission as a function of the power of the laser that is driving the QD resonantly. (c) QD linewidth $\Delta\omega$ measured by monitoring the cavity emission by scanning the laser across the QD. $\Delta\omega$ is plotted as a function of the excitation laser power. We find that the standard power broadening model over-estimates the measured QD linewidth (the dashed line). However, the model provides better agreement with experimental results when spectral diffusion is taken into account (solid line).

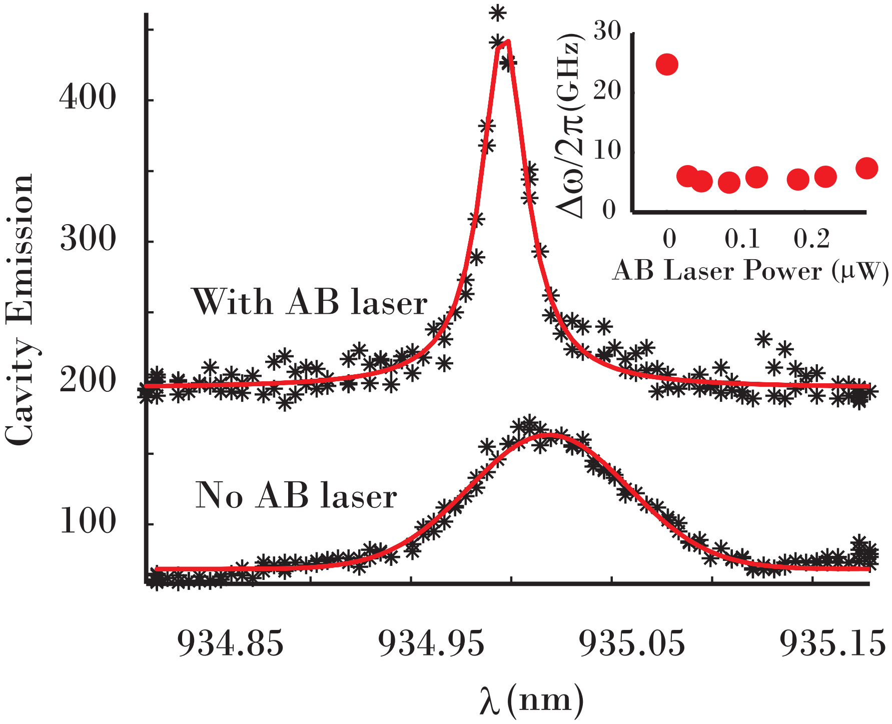

Figure 8.4: Effect of the AB laser on the QD spectrum as measured though off-resonant cavity emission. In the absence of the AB laser, we observe a broad QD linewidth. However, in the presence of this laser, a significant linewidth narrowing is observed. The increased background with the AB laser on is caused by the PL generated by the AB laser. The inset shows the QD linewidth measured as a function of the AB laser power.

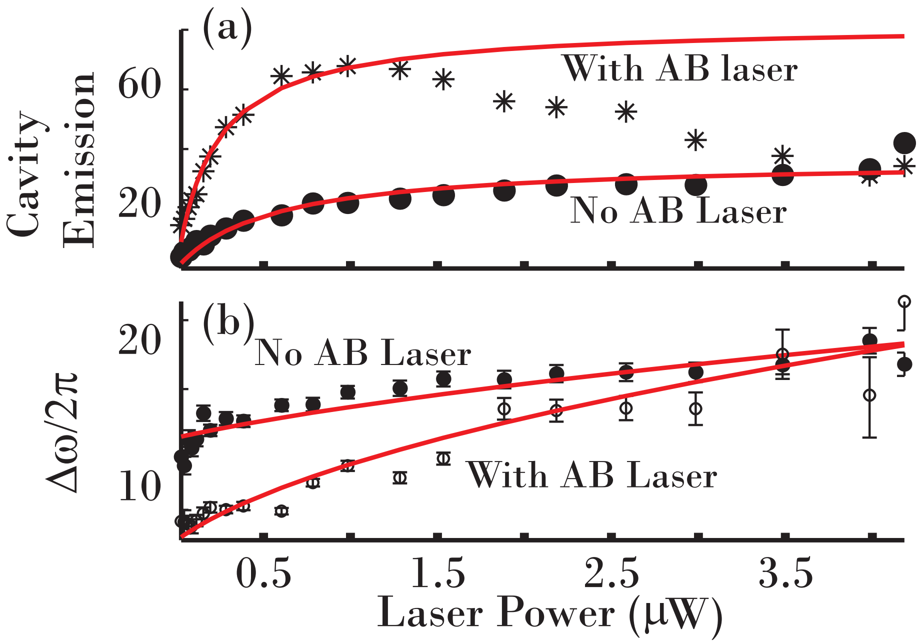

Figure 8.5: (a) Off-resonant cavity emission as a function of the laser power driving the QD resonantly for two cases: with and without the additional, weak above band laser. (b) Extracted QD linewidth as a function of the resonant driving laser power. A much narrower linewidth is observed in the presence of the AB laser at lower excitation powers. Also, the QD linewidth follows a simple power broadening with the excitation laser power when the AB laser is present. In the absence of the AB laser, we observe an additional power independent broadening, which can be explained by spectral diffusion of the QD.

in the cavity emission may be due to the presence of other QD excitonic states. The fact that those states are present only with the AB excitation may be an indication that these other excitonic states are multiply charged states arising from the capture of multiple photo-generated carriers [155]. Figure 8.5 b shows the measured QD linewidth as a function of the excitation laser power both in the presence and absence of the AB laser. We find that the QD linewidth is narrower with AB laser on at lower laser excitation power. In fact, the QD linewidth in that case follows ordinary power broadening (as shown by the solid line fit), with $\Delta\omega_0/2\pi = 4.7$ GHz, the same as the Lorentzian linewidth obtained from the fit to the linewidth data with spectral diffusion.

In summary, we have presented experimental studies showing the effect of the photo-generated carriers on spectral diffusion in the QD-PC cavity QED system. We first showed that the transmission spectrum of the strongly coupled QD-PC cavity system can be modified with a very low power of the additional above-band laser. We also show the significant effect of spectral diffusion in resonant QD spectroscopy, when the QD is embedded in a photonic crystal cavity. This spectral diffusion can be mitigated by photo-generated carriers that serve to fill the trap states occurring at the etched surfaces of the PC. This significant reduction of the QD linewidth by the additional weak, above-band excitation is an attractive prospect for potential quantum information applications employing QDs in PC structures. For those applications benefiting from narrow QD linewidths, the results presented here demonstrate a relatively simple means of improving the optical quality of QDs and thus system performance.

Chapter 9

Outlook

In this thesis, I have presented detailed experiments and theoretical studies of a cavity QED system consisting of a single QD and a PC cavity. We have shown that a very high optical nonlinearity can be achieved in this system, which is present almost at a single photon level. Such a strong light-matter interaction opens up several new directions to explore, which are both scientifically and technologically important. In this chapter, I briefly describe some of the future research directions, where such strong optical nonlinearity can be beneficial.

9.1 Coupled cavity array for quantum many body simulation

Solving strongly correlated quantum many body systems is a formidable task. One promising approach is to mimic such complicated systems using another simpler and easily controllable quantum system, as envisioned by Richard Feynman [156]. To that end, the first demonstration of quantum phase transitions with ultra-cold atoms in optical lattice [157] proliferated a significant amount of research on quantum simulation with atomic systems [158]. Another very promising direction of using photons themselves as the interacting particles has been conceived very recently, and generated considerable interest [159]. The main idea to obtain such a "Quantum fluids of

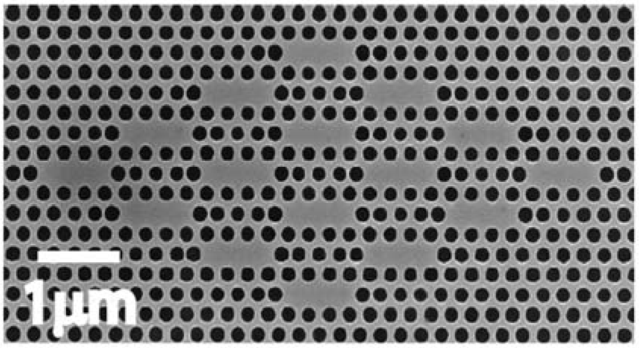

Figure 9.1: SEM of a coupled cavity array in photonic crystal. This particular structure contains 16 cavities.

light" [159] is to build a coupled network of non-linear electro-magnetic cavities. The photons can hop between cavities due to the electromagnetic coupling and can repel each other in the same cavity due to the nonlinearity present in the cavity. Obviously, the optical nonlinearity required for such strong repulsion at low photon number is very high, and in current technology, only quantum emitters strongly coupled to cavities (for example, atoms, dots or super-conducting transmon qubits) provide such strong nonlinearity in the photon blockade regime [3, 85]. As one needs to have many cavities for this operation, a solid-state system is obviously a better choice.

QDs coupled to photonic crystal cavities (as described in this thesis) can be used to build such a nanophotonic platform for quantum simulation. Photonic crystal cavities can be scaled very easily, the first step being the demonstration of the photonic molecule as described in the chapter 6. Figure 9.1 shows SEM image of a fabricated coupled cavity array in GaAs. In this particular structure we have 16 cavities with all the cavities having the same polarization. However, positioning one QD in each solid-state cavity is very difficult. Especially, it is very difficult to deterministically position the self-assembled QDs, which have the best performance in terms of cavity quantum electrodynamics (CQED). Recently several groups have demonstrated deterministic position of such QDs [113], and we hope that those QDs will also perform well in a cavity QED setting. Another approach will be to use a bulk nonlinearity or quantum well nonlinearity, but significantly enhanced by a high Q and low-mode-volume

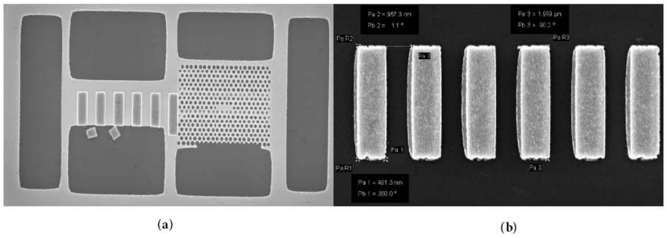

Figure 9.2: (a)SEM of a photonic crystal cavity with metallic grating on the side. (b) SEM of a metallic grating fabricated for generating surface acoustic wave.

nano-cavity [160, 95]. We also note that such a platform consisting of coupled non-linear cavities is useful not just for quantum simulation, but also for quantum error correction [161] as well as for classical optical signal processing [162].

9.2 Coherent control of phonons

In the chapter 7, we studied an incoherent phonon-mediated coupling between the QD and the cavity. This coupling results in a conversion of one frequency of light to a slightly detuned frequency. Such frequency conversion can be useful for quantum dot based implementation of a quantum repeater or a quantum computer, which is currently limited by the inhomogeneous broadening of the QDs. At present, the described phonon-mediated channel is incoherent, and it cannot be controlled deterministically. Although changing the temperature affects the phonon density of states, and thus affects such phonon-mediated process, the effect of temperature is not very large, and operating temperature range is limited by the QDs.

Hence, one can think of generating such phonons at nano-scale deterministically by optical means. More specifically, we have designed a metallic grating with spatial periodicity a (see Figure 9.2). Via a short laser pulse we can heat up the metal and the semiconductor (here GaAs) differently. Once the pulse is gone, the metal and the semiconductor start dissipating heat, but at different rates. With changing temperature, the size of the metal and the semiconductor also change due to thermal expansion and cause strain. Such strain generates surface acoustic waves (SAW), with wavelength $\lambda \sim a$. Thus one can deterministically generate phonons at the

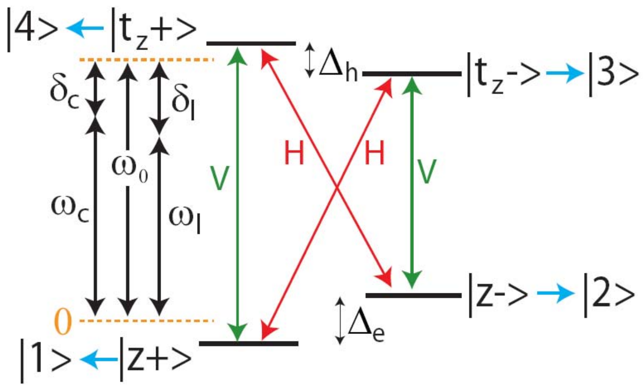

Figure 9.3: Energy-level diagrams of a single electron spin confined in QD under magnetic field (in the Voigt configuration). The two ground states are electron spin up and down. These two constitute the stable basis for the matter qubit. The two excited states are trion states.

nano-scale. We note that, in order to generate a 50 GHz signal (corresponding to QD-cavity detuning of ~ 0.02 nm), one needs the spatial periodicity of the metallic grating to be 100 nm (as the velocity of sound in GaAs is 5000 m/s), which is well within the reach of the current state-of-the-art fabrication techniques. However, to generate such high frequency SAW by electrical means, one needs to use a high frequency of electrical signal as well, which is difficult to generate.

9.3 Spin-photon interface

Another very important direction to exploit such low-power nonlinearity is to build a spin-photon interface for a quantum repeater. The necessity of quantum repeaters for long distance quantum communication is described in the introduction of the thesis. In fact, one of the main motivations for studying this cavity QED platform is to realize quantum information processing and communication methods.

The experiments described in the thesis mostly involve QD excitons. In this system, the basis for the qubits are the ground state and the single exciton state of the QD. However, the QD exciton state is short-lived, and coupling it to a cavity reduces the life-time further. Hence, even though the QD exciton qubit has two states, it is not a stable basis for a qubit. For that reason, we want to use the single electron spin confined in the QD as our qubit. In chapter 4 we showed that we can deterministically charge a single QD with an electron by applying a vertical electric field. A single electron confined in the QD has spin, and under the application of a magnetic field the energies of the spin-up state and the spin-down state differ, and a level splitting is observed. We note that the self-assembled QDs have significant strain and hence the only good quantization axis is along the growth axis, which is also the optical axis in our case. Hence all the spin states are specified along this direction, also called the z-direction. There are two different configurations for application of the magnetic field: Faraday configuration where the magnetic field is parallel to the quantization axis; and Voigt configuration, where the magnetic field is perpendicular to the quantization axis. In the Faraday configuration, although the spin up and spin down states acquire different energies, they do not mix. Hence we end up with two decoupled two level systems. On the other hand, in the Voigt geometry the spins mix, and thus we get a 4-level system, as shown in Fig. 9.3. This system is suitable for spin-manipulation. Significant progress has been made in the manipulation of QD spin without a cavity [163]. However, ultimately for practical application one needs to use a cavity to enhance the light-matter interaction. The cavity enhances the in-coupling of light, and thus ultimately enables single photon operation. The cavity also enhances the out-coupling, and thus makes the read-out efficient.

However, coupling the QD to the cavity perturbs the QD states strongly. This in turn affects the fidelity of the spin initialization and spin read-out. Hence, one can use the off-resonant QD-cavity coupling to ensure that the QD is not greatly perturbed by the cavity, but still maintaining good in-coupling (see chapter 7). Also, the off-resonant emission can be used for efficient readout.

Bibliography

[1] D. Englund, Andrei Faraon, Ilya Fushman, Nick Stoltz, Pierre Petroff, and Jelena Vučković. Controlling cavity reflectivity with a single quantum dot. *Nature*, 450:857, 2007.

[2] Dirk Englund, Arka Majumdar, Andrei Faraon, Mitsuru Toishi, Nick Stoltz, Pierre Petroff, and Jelena Vučković. Resonant excitation of a quantum dot strongly coupled to a photonic crystal nanocavity. *Phys. Rev. Lett.*, 104(7):073904, Feb 2010.

[3] Arka Majumdar, Michal Bajcsy, and Jelena Vučković. Probing the ladder of dressed states and nonclassical light generation in quantum-dot˘cavity qed. *Phys. Rev. A*, 85:041801, Apr 2012.

[4] A. Majumdar et al. Linewidth broadening of a quantum dot coupled to an off-resonant cavity. *Phys. Rev. B*, 82(4):045306, Jul 2010.

[5] Mitsuru Toishi, Dirk Englund, Andrei Faraon, and Jelena Vučković. High-brightness single photon source from a quantum dot in a directional-emission nanocavity. *Opt. Express*, 17(17):14618–14626, Aug 2009.

[6] Andrei Faraon, Arka Majumdar, Dirk Englund, Erik Kim, Michal Bajcsy, and Jelena Vučković. Integrated quantum optical networks based on quantum dots and photonic crystals. *New J. Physics*, 13:055025, 2011.

[7] Michael A. Nielsen and Isaac L. Chuang. *Quantum Computation and Quantum Information.* Cambridge University Press, 2001.

[8] L. Childress, J. M. Taylor, A. S. Sørensen, and M. D. Lukin. Fault-tolerant quantum repeaters with minimal physical resources and implementations based on single-photon emitters. *Phys. Rev. A*, 72(5):052330, Nov 2005.

[9] T D Ladd, P van Loock, K Nemoto, W J Munro, and Y Yamamoto. Hybrid quantum repeater based on dispersive cqed interactions between matter qubits and bright coherent light. *New Journal of Physics*, 8(9):184, 2006.

[10] L.-M. Duan andM. D. Lukin, J. I. Cirac, and P. Zoller. Long-distance quantum communication with atomic ensembles and linear optics. *Nature*, 414:413–418, 2001.

[11] M. Żukowski, A. Zeilinger, M. A. Horne, and A. K. Ekert. "event-ready-detectors" bell experiment via entanglement swapping. *Phys. Rev. Lett.*, 71:4287–4290, Dec 1993.

[12] Jian-Wei Pan, Christoph Simon, S caronaslav Brukner, and Anton Zeilinger. Entanglement purification for quantum communication. *Nature*, 410:1067–1070, 2001.

[13] J. I. Cirac, P. Zoller, H. J. Kimble, and H. Mabuchi. Quantum State Transfer and Entanglement Distribution among Distant Nodes in a Quantum Network. *Physical Review Letters*, 78(16):3221–24, April 1997.

[14] D. A. B. Miller. Device requirements for optical interconnects to silicon chips. *Proc. IEEE*, 97:1166, 2009.

[15] Ron Ho, Kenneth W. Mai, and Mark A. Horowitz. The Future of Wires. *Proceedings of the IEEE*, 89:490–504, 2001.

[16] Alexander A Sawchuk and Timothy C. Strand. Digital Optical Computing. *Proceedings of the IEEE*, 72:758–779, 1984.

[17] P. Michler. *Single Quantum Dots: Fundamentals, Applications and New Concepts*. Springer, 2003.

[18] R. Hanson, L. P. Kouwenhoven, J. R. Petta, S. Tarucha, and L. M. K. Vandersypen. Spins in few-electron quantum dots. *Rev. Mod. Phys.*, 79:1217–1265, Oct 2007.

[19] V. Klimov. *Nanocrystal Quantum Dots*. CRC Press, 2010.

[20] Sergio M. Dutra. *Cavity Quantum Electrodynamics: The Strange Theory of Light in a Box*. Wiley-Interscience, 2004.

[21] H. J. Kimble. *in Cavity Quantum Electrodynamics, edited by P. Berman*. Academic Press, San Diego, 1994.

[22] D. Felinto, C. W. Chou, J. Laurant, E. W. Schomburg, H. De Riedmatten, and H. J. Kimble. Conditional control of the quantum states of remote atomic memories for quantum networking. *Nature Physics*, 2:844–848, 2006.

[23] L.-M. Duan and H. J. Kimble. Scalable photonic quantum computation through cavity-assisted interactions. *Phys. Rev. Lett.*, 92(12):127902, Mar 2004.

[24] H. J. Kimble. The quantum internet. *Nature*, 453:1023–1030, 2008.

[25] T. Yoshie, A. Scherer, J. Hendrickson, G. Khitrova, H. M. Gibbs, G. Rupper, C. Ell, O. B. Shchekin, and D. G. Deppe. Vacuum rabi splitting with a single quantum dot in a photonic crystal nanocavity. *Nature*, 432:200, 2004.

[26] Sara Ferretti and Dario Gerace. Single-photon nonlinear optics with kerr-type nanostructured materials. *Phys. Rev. B*, 85:033303, Jan 2012.

[27] Yoshihisa Yamamoto, Francesco Tassone, and Hui Cao. *Semiconductor Cavity Quantum Electrodynamics*. Springer, 2000.

[28] Andrei Faraon, Paul E. Barclay, Charles Santori, Kai-Mei C. Fu, and Raymond G. Beausoleil. Resonant enhancement of the zero-phonon emission from a colour centre in a diamond cavity. *Nature Photonics*, 5:301–305, 2011.

[29] William F. Koehl, Bob B. Buckley, F. Joseph Heremans, Greg Calusine, and David D. Awschalom. Room temperature coherent control of defect spin qubits in silicon carbide. *Nature*, 479:84–87, 2011.

[30] J. Hwang, M. Pototschnig, R. Lettow, G. Zumofen, A. Renn, S. Gtzinger, and V. Sandoghdar. A single-molecule optical transistor. *Nature*, 460:76–80, 2009.

[31] KJ Vahala. Optical microcavities. *NATURE*, 424(6950):839–846, AUG 14 2003.

[32] K. Hennessy, A. Badolato, M. Winger, D. Gerace, M. Atature, S. Gulde, S. Falt, E. L. Hu, and A. Imamoglu. Quantum nature of a strongly-coupled single quantum dot-cavity system. *Nature*, 445:896, 2007.

[33] K. Srinivasan and Oskar Painter. Linear and nonlinear optical spectroscopy of a strongly-coupled microdisk-quantum dot system. *Nature*, 450:862, 2007.

[34] Arka Majumdar, Dirk Englund, Michal Bajcsy, and Jelena Vučković. Nonlinear temporal dynamics of a strongly coupled quantum-dot˘cavity system. *Phys. Rev. A*, 85:033802, Mar 2012.

[35] Dirk Englund, Arka Majumdar, Michal Bajcsy, Andrei Faraon, Pierre Petroff, and Jelena Vučković. Ultrafast photon-photon interaction in a strongly coupled quantum dot-cavity system. *Phys. Rev. Lett.*, 108:093604, Mar 2012.

[36] Arka Majumdar, Nicolas Manquest, Andrei Faraon, and Jelena Vučković. Theory of electro-optic modulation via a quantum dot coupled to a nano-resonator. *Optics Express*, 18(5):3974—3984, 2010.

[37] Andrei Faraon, Arka Majumdar, Hyochul Kim, Pierre Petroff, and Jelena Vučković. Fast electrical control of a quantum dot strongly coupled to a photonic-crystal cavity. *Phys. Rev. Lett.*, 104:047402, Jan 2010.

[38] Andrei Faraon, Arka Majumdar, and Jelena Vučković. Generation of nonclassical states of light via photon blockade in optical nanocavities. *Phys. Rev. A*, 81(3):033838, Mar 2010.

[39] Arka Majumdar, Michal Bajcsy, Armand Rundquist, and Jelena Vučković. Loss-enabled sub-poissonian light generation in a bimodal nanocavity. *Phys. Rev. Lett.*, 108:183601, May 2012.

[40] Arka Majumdar, Armand Rundquist, Michal Bajcsy, and Jelena Vuckovic. Cavity quantum electrodynamics with a single quantum dot coupled to a photonic molecule. *arXiv:1201.6244v1*, 2012.

[41] Arka Majumdar, Erik D. Kim, Yiyang Gong, Michal Bajcsy, and Jelena Vučković. Phonon mediated off-resonant quantum dot˘cavity coupling under resonant excitation of the quantum dot. *Phys. Rev. B*, 84:085309, Aug 2011.

[42] Arka Majumdar, Alexander Papageorge, Erik D. Kim, Michal Bajcsy, Hyochul Kim, Pierre Petroff, and Jelena Vučković. Probing of single quantum dot dressed states via an off-resonant cavity. *Phys. Rev. B*, 84:085310, Aug 2011.

[43] Arka Majumdar, Erik D. Kim, and Jelena Vučković. Effect of photogenerated carriers on the spectral diffusion of a quantum dot coupled to a photonic crystal cavity. *Phys. Rev. B*, 84:195304, Nov 2011.

[44] Q. A. Turchette, C. J. Hood, W. Lange, H. Mabuchi, and H. J. Kimble. Measurement of conditional phase shifts for quantum logic. *Phys. Rev. Lett.*, 75:4710–4713, Dec 1995.

[45] Alexandre Blais, Ren-Shou Huang, Andreas Wallraff, S. M. Girvin, and R. J. Schoelkopf. Cavity quantum electrodynamics for superconducting electrical circuits: An architecture for quantum computation. *Phys. Rev. A*, 69(6):062320, Jun 2004.

[46] C. W. Gardiner and P. Zoller. *Quantum Noise*. Springer-Verlag, 2005.

[47] Howard Carmichael. *An Open Systems Approach to Quantum Optics, Lecture Notes in Physics*. Springer, Berlin, 1993.

[48] Heinz-Peter Breuer and Francesco Petruccione. *The Theory of Open Quantum Systems*. Oxford University Press, 2002.

[49] Sze M Tan. A computational toolbox for quantum and atomic optics. *Journal of Optics B: Quantum and Semiclassical Optics*, 1(4):424, 1999.

[50] M. A. Armen and H. Mabuchi. Low-lying bifurcations in cavity quantum electrodynamics. *Phys. Rev. A*, 73:063801, Jun 2006.

[51] Deepak Sridharan, Ranojoy Bose, Hyochul Kim, Glenn S. Solomon, and Edo Waks. Attojoule all-optical switching with a single quantum dot. *arXiv:1107.3751v1*, 2011.

[52] David Miller. Are optical transistors the logical next step? *Nature Photonics*, 4:3–5, 2010.

[53] I. Fushman, D. Englund, A. Faraon, N. Stoltz, P. Petroff, and J. Vuckovic. Controlled phase shifts with a single quantum dot. *Science*, 320:769, 2008.

[54] Edo Waks and Jelena Vuckovic. Dipole induced transparency in drop-filter cavity-waveguide systems. *Phys. Rev. Lett.*, 96:153601, Apr 2006.

[55] J. Bochmann, M. Mücke, G. Langfahl-Klabes, C. Erbel, B. Weber, H. P. Specht, D. L. Moehring, and G. Rempe. Fast excitation and photon emission of a single-atom-cavity system. *Phys. Rev. Lett.*, 101:223601, Nov 2008.

[56] V. Savona and C. Weisbuch. Theory of time-resolved light emission from polaritons in a semiconductor microcavity under resonant excitation. *Phys. Rev. B*, 54:10835–10840, Oct 1996.

[57] T. B. Norris, J.-K. Rhee, C.-Y. Sung, Y. Arakawa, M. Nishioka, and C. Weisbuch. Time-resolved vacuum rabi oscillations in a semiconductor quantum microcavity. *Phys. Rev. B*, 50:14663–14666, Nov 1994.

[58] Hideo Mabuchi. Cavity-qed models of switches for attojoule-scale nanophotonic logic. *Phys. Rev. A*, 80:045802, 2009.

[59] Martin Winger, Thomas Volz, Guillaume Tarel, Stefano Portolan, Antonio Badolato, Kevin J. Hennessy, Evelyn L. Hu, Alexios Beveratos, Jonathan Finley, Vincenzo Savona, and Atac Imamoglu. Explanation of photon correlations

in the far-off-resonance optical emission from a quantum-dot–cavity system. *Phys. Rev. Lett.*, 103(20):207403, 2009.

[60] Isaac L. Chuang and Yoshihisa Yamamoto. Simple quantum computer. *Phys. Rev. A*, 52:3489–3496, Nov 1995.

[61] A. Högele, S. Seidl, M. Kroner, K.Karrai, R. J. Warburton, B. D. Gerardot, and P. M. Petroff. Voltage-Controlled Optics of a Quantum Dot. *Physical Review Letters*, 93(217401), nov 2004.

[62] A. Laucht, F. Hofbauer, N. Hauke, J. Angele, S. Stobbe, M. Kaniber, G. Bohm, P. Lodahl, M. C. Amann, and J. J. Finley. Electrical control of spontaneous emission and strong coupling for a single quantum dot. *arXiv:0810.3010v2*, 2008.

[63] B. D. Gerardot, S. Seidl, P. A. Dalgarno, R. J. Warburton, D. Granados, J. M. Garcia, K. Kowalik, O. Krebs, K. Karrai, A. Badolato, and P. M. Petroff. Manipulating exciton fine structure in quantum dots with a lateral electric field. *Applied Physics Letters*, 90(4):041101, 2007.

[64] A. Faraon, D. Englund, I. Fushman, J. Vuckovic, and Edo Waks. Efficient photonic crystal cavity-waveguide couplers. *Appl. Phys. Lett.*, 90(7):073102, 2007.

[65] T. Yoshie, A. Scherer, J. Hendrickson, G. Khitrova, H. M. Gibbs, G. Rupper, C. Ell, O. B. Shchekin, and D. G. Deppe. Vacuum Rabi splitting with a single quantum dot in a photonic crystal nanocavity. *Nature*, 432:200–203, November 2004.

[66] W. Heller, U. Bockelmann, and G. Abstreiter. Electric-field effects on excitons in quantum dots. *Phys. Rev. B*, 57(11):6270–6273, Mar 1998.

[67] Andrei Faraon, Ilya Fushman, Dirk Englund, Nick Stoltz, Pierre Petroff, and Jelena Vučković. Coherent generation of non-classical light on a chip via photon-induced tunnelling and blockade. *Nature Physics*, 4(11):859–863, NOV 2008.

[68] Qianfan Xu, David Fattal, and Raymond G. Beausoleil. Silicon microring resonators with 1.5-um radius. *Optics Express*, 16, 2008.

[69] Jifeng Liu, Mark Beals, Andrew Pomerene, Sarah Bernardis, Rong Sun, Jing Cheng, Lionel C. Kimerling, and Jurgen Michel. Waveguide-integrated, ultralow-energy gesi electro-absorption modulators. *Nature Photonics*, 2, 2008.

[70] Qianfan Xu, Sasikanth Manipatruni, Brad Schmidt, Jagat Shakya, and Michal Lipson. 12.5 gbit/s carrierinjection-based silicon micro-ring silicon modulators. *Optics Express*, 15, 2007.

[71] A. Liu, R. Jones, L. Liao, D. Samara-Rubio, D. Rubin, O. Cohen, R. Nicolaescu, and M. Paniccia. A high-speed silicon optical modulator based on a metal-oxide-semiconductor capacitor. *Nature*, 427, 2004.

[72] Andrei Faraon, Ilya Fushman, Dirk Englund, Nick Stoltz, Pierre Petroff, and Jelena Vuckovic. Dipole induced transparency in waveguide coupled photonic crystal cavities. *Optics Express*, 16:12154, 2008.

[73] C.H. Bennett and G. Brassard. . *Proceedings of IEEE International Conference on Computers, Systems, and Signal Processing, Bangalore, India IEEE, New York*, page 175, 1984.

[74] E. Knill, R. Laflamme, and G. J. Milburn. A scheme for efficient quantum computation with linear optics. *Nature*, 409:4652, 2001.

[75] B. Sanders, J. Vučković, and P. Grangier. Single photons on demand. *Europhysics News*, 36(2):56–58, March/April 2005.

[76] Markus Hijlkema, Bernhard Weber, Holger P. Specht, Simon C. Webster, Axel Kuhn, and Gerhard Rempe. A single-photon server with just one atom. *Nature Physics*, 3(4):253–255, APR 2007.

[77] A. Imamoglu, H. Schmidt, G. Woods, and M. Deutsch. Strongly Interacting Photons in a Nonlinear Cavity. *Physical Review Letters*, 79(8):1467–1470, August 1997.

[78] K. M. Birnbaum, A. Boca, R. Miller, A. D. Boozer, T. E. Northup, and H. J. Kimble. Photon blockade in an optical cavity with one trapped atom. *Nature*, 436:87–90, 2005.

[79] Jelena Vuckovic, Dirk Englund, David Fattal, Edo Waks, and Yoshihisa Yamamoto. Generation and manipulation of nonclassical light using photonic crystals. *Physica E,*, 31(2), 2006.

[80] M. Nomura, N. Kumagai, S. Iwamoto, Y. Ota, and Y. Arakawa. Transition from the strong-coupling to lasing regime in a single quantum dot-nanocavity. *arXiv:0906.4181v1*, 2009.

[81] J. McFarlane, P. A. Dalgarno, B. D. Gerardot, R. H. Hadfield, R. J. Warburton, K. Karrai, A. Badolato, and P. M. Petroff. Gigahertz bandwidth electrical control over a dark exciton-based memory bit in a single quantum dot. *Applied Physics Letters*, 94(9):093113, 2009.

[82] A. Kubanek, A. Ourjoumtsev, I. Schuster, M. Koch, P. W. H. Pinkse, K. Murr, and G. Rempe. Two-photon gateway in one-atom cavity quantum electrodynamics. *Physical Review Letters*, 101(20):203602, 2008.

[83] Hayato Goto et al. Quantum trajectory simulation of controlled phase-flip gates using the vacuum rabi splitting. *Phys. Rev. A*, 72(5):054301, 2005.

[84] A. Tandaechanurat, Satomi Ishida, Denis Guimard, Masahiro Nomura, Satoshi Iwamoto, and Yasuhiko Arakawa. Lasing oscillation in a three-dimensional photonic crystal nanocavity with a complete bandgap. *Nature Photonics*, 5:91–94, 2011.

[85] Andreas Reinhard, Thomas Volz, Martin Winger, Antonio Badolato, Kevin J. Hennessy, Evelyn L. Hu, and Atac Imamoğlu. Strongly correlated photons on a chip. *Nature Photonics*, 6, 2012.

[86] T. C. H. Liew and V. Savona. Single photons from coupled quantum modes. *Phys. Rev. Lett.*, 104:183601, May 2010.

[87] Motoaki Bamba, Atac Imamoğlu, Iacopo Carusotto, and Cristiano Ciuti. Origin of strong photon antibunching in weakly nonlinear photonic molecules. *Phys. Rev. A*, 83:021802, Feb 2011.

[88] Dario Gerace, Hakan E. Treciand Atac Imamoglu, Vittorio Giovannetti, and Rosario Fazio. The quantum-optical Josephson interferometer. *Nature Physics*, 281 - 284:5, 2009.

[89] Barak Dayan, A. S. Parkins, Takao Aoki, E. P. Ostby, K. J. Vahala, and H. J. Kimble. A photon turnstile dynamically regulated by one atom. *Science*, 319(5866):1062–1065, 2008.

[90] Kartik Srinivasan and Oskar Painter. Mode coupling and cavity˘quantum-dot interactions in a fiber-coupled microdisk cavity. *Phys. Rev. A*, 75:023814, Feb 2007.

[91] M. B. Plenio and S. F. Huelga. Entangled light from white noise. *Phys. Rev. Lett.*, 88:197901, Apr 2002.

[92] K. Hennessy, C. Hogerle, E. Hu, A. Badolato, and A. Imamoglu. Tuning photonic nanocavities by atomic force microscope nano-oxidation. *Appl. Phys. Lett.*, 89(4):041118, 2006.

[93] Michael J. Hartmann, Fernando G. S. L. Brandao, and Martin B. Plenio. Strongly interacting polaritons in coupled arrays of cavities. *Nature Physics*, 2:849–855, 2006.

[94] Andrew D. Greentree, Charles Tahan, Jared H. Cole, and Lloyd C. L. Hollenberg. Quantum phase transitions of light. *Nature Physics*, 2:856–861, 2006.

[95] I. Carusotto, D. Gerace, H. E. Tureci, S. De Liberato, Ciuti C. , and A. Imamoğlu. Fermionized photons in an array of driven dissipative nonlinear cavities. *Phys. Rev. Lett.*, 103:033601, Jul 2009.

[96] Kirill A. Atlasov, Karl F. Karlsson, Alok Rudra, Benjamin Dwir, and Eli Kapon. Wavelength and loss splitting in directly coupled photonic-crystal defect microcavities. *Optics Express*, 16:16255–16264, 2008.

[97] Kirill A. Atlasov, Alok Rudra, Benjamin Dwir, and Eli Kapon. Large mode splitting and lasing in optimally coupled photonic-crystal microcavities. *Optics Express*, 19:2619–2625, 2011.

[98] Adrien Dousse, Jan Suffczyski, Alexios Beveratos, Olivier Krebs, Aristide Lematre, Isabelle Sagnes, Jacqueline Bloch, Paul Voisin, and Pascale Senellart. Ultrabright source of entangled photon pairs. *Nature*, 466:217220, 2010.

[99] S. Mosor, J. Hendrickson, B. C. Richards, J. Sweet, G. Khitrova, H. M. Gibbs, T. Yoshie, A. Scherer, O. B. Shchekin, and D. G. Deppe. Scanning a photonic crystal slab nanocavity by condensation of xenon. *Applied Physics Letters*, 87(14):141105, 2005.

[100] Yoshiya Sato, Yoshinori Tanaka, Jeremy Upham, Yasushi Takahashi, Takashi Asano, and Susumu Noda. Strong coupling between distant photonic nanocavities and its dynamic control. *Nature Photonics*, 6:56–61, 2012.

[101] S. Ates et al. Non-resonant dot-cavity coupling and its potential for resonant single-quantum-dot spectroscopy. *Nature Photonics*, 3:724, 2009.

[102] Ulrich Hohenester. Cavity quantum electrodynamics with semiconductor quantum dots: Role of phonon-assisted cavity feeding. *Phys. Rev. B*, 81(15):155303, Apr 2010.

[103] David Press, Stephan Götzinger, Stephan Reitzenstein, Carolin Hofmann, Andreas Löffler, Martin Kamp, Alfred Forchel, and Yoshihisa Yamamoto. Photon antibunching from a single quantum-dot-microcavity system in the strong coupling regime. *Phys. Rev. Lett.*, 98(11):117402, 2007.

[104] M. Kaniber, A. Laucht, A. Neumann, J. M. Villas-Boas, M. Bichler, M.-C. Amann, and J. J. Finley. Investigation of the nonresonant dot-cavity coupling in

two-dimensional photonic crystal nanocavities. *Physical Review B (Condensed Matter and Materials Physics)*, 77(16):161303, 2008.

[105] Dan Dalacu, Khaled Mnaymneh, Vera Sazonova, Philip J. Poole, Geof C. Aers, Jean Lapointe, Ross Cheriton, Anthony J. SpringThorpe, and Robin Williams. Deterministic emitter-cavity coupling using a single-site controlled quantum dot. *Phys. Rev. B*, 82(3):033301, Jul 2010.

[106] A. Laucht, N. Hauke, A. Neumann, T. Gnthner, F. Hofbauer, A. Mohtashami, K. Mller, G. Bhm, M. Bichler, M.-C. Amann, M. Kaniber, and J. J. Finley. Nonresonant feeding of photonic crystal nanocavity modes by quantum dots. *Journal of Applied Physics*, 109(10):102404, 2011.

[107] Ulrich Hohenester, Arne Laucht, Michael Kaniber, Norman Hauke, Andre Neumann, Abbas Mohtashami, Marek Seliger, Max Bichler, and Jonathan J. Finley. Phonon-assisted transitions from quantum dot excitons to cavity photons. *Phys. Rev. B*, 80(20):201311, Nov 2009.

[108] S. Hughes, P. Yao, F. Milde, A. Knorr, D. Dalacu, K. Mnaymneh, V. Sazonova, P. J. Poole, G. C. Aers, J. Lapointe, R. Cheriton, and R. L. Williams. Influence of electron-acoustic phonon scattering on off-resonant cavity feeding within a strongly coupled quantum-dot cavity system. *Phys. Rev. B*, 83(16):165313, Apr 2011.

[109] J. Suffczyński, A. Dousse, K. Gauthron, A. Lemaitre, I. Sagnes, L. Lanco, J. Bloch, P. Voisin, and P. Senellart. Origin of the optical emission within the cavity mode of coupled quantum dot-cavity systems. *Phys. Rev. Lett.*, 103:027401, Jul 2009.

[110] I. Wilson-Rae and A. Imamoğlu. Quantum dot cavity-qed in the presence of strong electron-phonon interactions. *Phys. Rev. B*, 65(23):235311, May 2002.

[111] F. Milde, A. Knorr, and S. Hughes. Role of electron-phonon scattering on the vacuum rabi splitting of a single-quantum dot and a photonic crystal nanocavity. *Phys. Rev. B*, 78(3):035330, Jul 2008.

[112] N. Chauvin, C. Zinoni, M. Francardi, A. Gerardino, L. Balet, B. Alloing, L. H. Li, and A. Fiore. Controlling the charge environment of single quantum dots in a photonic-crystal cavity. *Physical Review B (Condensed Matter and Materials Physics)*, 80(24):241306, 2009.

[113] M. Calic, P. Gallo, M. Felici, K. A. Atlasov, B. Dwir, A. Rudra, G. Biasiol, L. Sorba, G. Tarel, V. Savona, and E. Kapon. Phonon-mediated coupling of *ingaas/gaas* quantum-dot excitons to photonic crystal cavities. *Phys. Rev. Lett.*, 106(22):227402, Jun 2011.

[114] R. Bose, D. Sridharan, G. S. Solomon, and E. Waks. Large optical stark shifts in semiconductor quantum dots coupled to photonic crystal cavities. *Appl. Phys. Lett.*, 98(12):121109, 2011.

[115] A. Ulhaq, S. Ates, S. Weiler, S. M. Ulrich, S. Reitzenstein, A. Löffler, S. Höfling, L. Worschech, A. Forchel, and P. Michler. Linewidth broadening and emission saturation of a resonantly excited quantum dot monitored via an off-resonant cavity mode. *Phys. Rev. B*, 82(4):045307, Jul 2010.

[116] G. Gangopadhyay, Samita Basu, and Deb Shankar Ray. Cavity-field-assisted atomic relaxation and suppression of resonance fluorescence at high intensities. *Phys. Rev. A*, 47(2):1314–1319, Feb 1993.

[117] Marlan O. Scully and M. Suhail Zubairy. *Quantum Optics*. Cambridge University Press, 2005.

[118] H. Kamada and T. Kutsuwa. Broadening of single quantum dot exciton luminescence spectra due to interaction with randomly fluctuating environmental charges. *Phys. Rev. B*, 78(15):155324, Oct 2008.

[119] Alexia Auffeves, Jean-Michel Gerard, and Jean-Philippe Poizat. Pure emitter dephasing: A resource for advanced solid-state single-photon sources. *Phys. Rev. A*, 79(5):053838, 2009.

[120] A. N. Vamivakas, Y. Xhao, C.Y. Lu, and M. Atature. Spin-resolved quantum-dot resonance fluorescence. *Nature Physics*, 5:198, 2009.

[121] E. B. Flagg, A. Muller, J. W. Robertson, S. Founta, D. G. Deppe, M. Xiao, W. Ma, G. J. Salamo, and C. K. Shih. Resonantly driven coherent oscillations in a solid-state quantum emitter. *Nature Physics*, 5:203, 2009.

[122] A. Vagov, V. M. Axt, T. Kuhn, W. Langbein, P. Borri, and U. Woggon. Non-monotonous temperature dependence of the initial decoherence in quantum dots. *Phys. Rev. B*, 70:201305, Nov 2004.

[123] I. Favero, A. Berthelot, G. Cassabois, C. Voisin, C. Delalande, Ph. Roussignol, R. Ferreira, and J. M. Gérard. Temperature dependence of the zero-phonon linewidth in quantum dots: An effect of the fluctuating environment. *Phys. Rev. B*, 75:073308, Feb 2007.

[124] Stefan Stufler, Patrick Ester, Artur Zrenner, and Max Bichler. Power broadening of the exciton linewidth in a single ingaas-gaas quantum dot. *Appl. Phys. Lett.*, 85(18):4202–4204, 2004.

[125] B. Urbaszek, E. J. McGhee, M. Krüger, R. J. Warburton, K. Karrai, T. Amand, B. D. Gerardot, P. M. Petroff, and J. M. Garcia. Temperature-dependent linewidth of charged excitons in semiconductor quantum dots: Strongly broadened ground state transitions due to acoustic phonon scattering. *Phys. Rev. B*, 69(3):035304, Jan 2004.

[126] H.S. Freedhoff Z. Ficek. Fluorescence and absorption by a two-level atom in a bichromatic field with one strong and one weak component. *Phys. Rev. A*, 53(6):4275–4287, 1995.

[127] Xiaodong Xu, Bo Sun, Paul R. Berman, Duncan G. Steel, Allan S. Bracker, Dan Gammon, and L. J. Sham. Coherent Optical Spectroscopy of a Strongly Driven Quantum Dot. *Science*, 317(5840):929–932, 2007.

[128] Gregor Jundt, Lucio Robledo, Alexander Högele, Stefan Fält, and Atac Imamoğlu. Observation of dressed excitonic states in a single quantum dot. *Phys. Rev. Lett.*, 100(17):177401, Apr 2008.

[129] Xiaodong Xu, Bo Sun, Erik D. Kim, Katherine Smirl, P. R. Berman, D. G. Steel, A. S. Bracker, D. Gammon, and L. J. Sham. Single charged quantum dot in a strong optical field: Absorption, gain, and the ac-stark effect. *Phys. Rev. Lett.*, 101(22):227401, Nov 2008.

[130] C. Roy and S. Hughes. Phonon-dressed mollow triplet in the regime of cavity quantum electrodynamics: Excitation-induced dephasing and nonperturbative cavity feeding effects. *Phys. Rev. Lett.*, 106(24):247403, Jun 2011.

[131] A. Laucht, J. M. Villas-Bôas, S. Stobbe, N. Hauke, F. Hofbauer, G. Böhm, P. Lodahl, M.-C. Amann, M. Kaniber, and J. J. Finley. Mutual coupling of two semiconductor quantum dots via an optical nanocavity. *Phys. Rev. B*, 82:075305, Aug 2010.

[132] Elena del Valle, F. P. Laussy, F. Troiani, and C. Tejedor. Entanglement and lasing with two quantum dots in a microcavity. *Phys. Rev. B*, 76:235317, Dec 2007.

[133] F. P. Laussy, A. Laucht, E. del Valle, J. J. Finley, and J. M. Villas-Bôas. Luminescence spectra of quantum dots in microcavities. iii. multiple quantum dots. *Phys. Rev. B*, 84:195313, Nov 2011.

[134] A. N. Poddubny, M. M. Glazov, and N. S. Averkiev. Nonlinear emission spectra of quantum dots strongly coupled to a photonic mode. *Phys. Rev. B*, 82:205330, Nov 2010.

[135] Paulo C Crdenas, Nicols Quesada, Herbert Vinck-Posada, and Boris A Rodrguez. Strong coupling of two interacting excitons confined in a nanocavityquantum dot system. *Journal of Physics: Condensed Matter*, 23(26):265304, 2011.

[136] K. J. Xu and C. Piermarocchi. Dynamics of elastic and inelastic energy transfer between quantum dots in a microcavity. *Phys. Rev. B*, 84:115316, Sep 2011.

[137] E. Gallardo, L. J. Martinez, A. K. Nowak, D. Sarkar, H. P. van der Meulen, J. M. Calleja, C. Tejedor, I. Prieto, D. Granados, A. G. Taboada, J. M. Garcia, and P. A. Postigo. Optical coupling of two distant inas/gaas quantum dots by a photonic-crystal microcavity. *Phys. Rev. B*, 81:193301, May 2010.

[138] Edward B. Flagg, John W. Robertson, Sébastien Founta, Wenquan Ma, Min Xiao, Gregory J. Salamo, and Chih-Kang Shih. Direct evidence of interlevel exciton transitions mediated by single phonons in a semiconductor quantum dot using resonance fluorescence spectroscopy. *Phys. Rev. Lett.*, 102:097402, Mar 2009.

[139] S. M. Ulrich, S. Ates, S. Reitzenstein, A. Loffler, A. Forchel, and P. Michler. Dephasing of triplet-sideband optical emission of a resonantly driven $inas/gaas$ quantum dot inside a microcavity. *Phys. Rev. Lett.*, 106(24):247402, Jun 2011.

[140] A. Berthelot, I. Favero, G. Cassabois, C. Voisin, C. Delalande, Ph. Roussignol, R. Ferreira, and J. M. Gerard. Unconventional motional narrowing in the optical spectrum of a semiconductor quantum dot. *Nature Physics*, 2:759, 2006.

[141] H. D. Robinson and B. B. Goldberg. Light-induced spectral diffusion in single self-assembled quantum dots. *Phys. Rev. B*, 61(8):R5086–R5089, Feb 2000.

[142] J. Seufert, R. Weigand, G. Bacher, T. Kummell, A. Forchel, K. Leonardi, and D. Hommel. Spectral diffusion of the exciton transition in a single self-organized quantum dot. *Applied Physics Letters*, 76(14):1872–1874, 2000.

[143] V. Türck, S. Rodt, O. Stier, R. Heitz, R. Engelhardt, U. W. Pohl, D. Bimberg, and R. Steingrüber. Effect of random field fluctuations on excitonic transitions of individual cdse quantum dots. *Phys. Rev. B*, 61(15):9944–9947, Apr 2000.

[144] G. Sallen, A. Tribu, T. Aichele, R. André, L. Besombes, C. Bougerol, M. Richard, S. Tatarenko, K. Kheng, and J.-Ph. Poizat. Subnanosecond spectral diffusion of a single quantum dot in a nanowire. *Phys. Rev. B*, 84(4):041405, Jul 2011.

[145] G. Sallen, A. Tribu, T. Aichele, R. Andr, L. Besombes, C. Bougerol, M. Richard, S. Tatarenko, K. Kheng, and J.-Ph. Poizat. Subnanosecond spectral diffusion measurement using photon correlation. *Nature Photonics*, 4:696, 2010.

[146] R. Heitz, T. R. Ramachandran, A. Kalburge, Q. Xie, I. Mukhametzhanov, P. Chen, and A. Madhukar. Observation of reentrant 2d to 3d morphology transition in highly strained epitaxy: Inas on gaas. *Phys. Rev. Lett.*, 78(21):4071–4074, May 1997.

[147] C. F. Wang, A. Badolato, I. Wilson-Rae, P. M. Petroff, E. Hu, J. Urayama, and A. Imamoglu. Optical properties of single inas quantum dots in close proximity to surfaces. *Applied Physics Letters*, 85(3423), 2004.

[148] Ryogo Kubo. *A Stochastic Theory of Line Shape*, pages 101–127. John Wiley and Sons, Inc., 2007.

[149] S. Reitzenstein, A. Lffler, C. Hofmann, A. Kubanek, M. Kamp, J. P. Reithmaier, A. Forchel, V. D. Kulakovskii, L. V. Keldyshand, I. V. Ponomarev, and T. L. Reinecke. Coherent photonic coupling of semiconductor quantum dots. *Opt. Lett.*, 31:1738–1740, 2006.

[150] Erik D. Kim, Arka Majumdar, Hyochul Kim, Pierre Petroff, and Jelena Vučković. Differential reflection spectroscopy of a single quantum dot strongly coupled to a photonic crystal cavity. *Applied Physics Letters*, 97(5):053111, 2010.

[151] Charles Santori, David Fattal, Jelena Vučković, Glenn S. Solomon, Edo Waks, and Yoshihisa Yamamoto. Submicrosecond correlations in photoluminescence from inas quantum dots. *Phys. Rev. B*, 69:205324, May 2004.

[152] Dirk Englund, Andrei Faraon, Arka Majumdar, Nick Stoltz, Pierre Petroff, and Jelena Vuckovic. An optical modulator based on a single strongly coupled quantum dot - cavity system in a p-i-n junction. *Optics Express*, 17:18651–18658, 2009.

[153] A. J. Ramsay, Achanta Venu Gopal, E. M. Gauger, A. Nazir, B. W. Lovett, A. M. Fox, and M. S. Skolnick. Damping of exciton rabi rotations by acoustic phonons in optically excited $ingaas/gaas$ quantum dots. *Phys. Rev. Lett.*, 104(1):017402, Jan 2010.

[154] J.J. Olivero and R.L. Longbothum. Empirical fits to the voigt line width: A brief review. *Journal of Quantitative Spectroscopy and Radiative Transfer*, 17(2):233 – 236, 1977.

[155] R. J. Warburton, C. Schflein, D. Haft, F. Bickel, A. Lorke, K. Karrai, J. M. Garcia, W. Schoenfeld, and P. M. Petroff. Optical emission from a charge-tunable quantum ring. *Nature*, 405:916, 2000.

[156] Richard P. Feynman. Simulating physics with computers. *International Journal of Theoretical Physics*, 21:467–488, 1982.

[157] Markus Greiner, Olaf Mandel, Tilman Esslinger, Theodor W. Hnsch, and Immanuel Bloch. Quantum phase transition from a superfluid to a mott insulator in a gas of ultracold atoms. *Nature*, 415:39–44, 2005.

[158] Immanuel Bloch, Jean Dalibard, and Sylvain Nascimbne. Quantum simulations with ultracold quantum gases. *Nature Physics*, 8:267–276, 2012.

[159] Iacopo Carusotto and Cristiano Ciuti. Quantum fluids of light. *arXiv:1205.6500v1*, 2012.

[160] Sara Ferretti and Dario Gerace. Single-photon nonlinear optics with kerr-type nanostructured materials. *Phys. Rev. B*, 85:033303, Jan 2012.

[161] Joseph Kerckhoff, Hendra I. Nurdin, Dmitri S. Pavlichin, and Hideo Mabuchi. Designing quantum memories with embedded control: Photonic circuits for autonomous quantum error correction. *Phys. Rev. Lett.*, 105:040502, Jul 2010.

[162] Hideo Mabuchi. Nonlinear interferometry approach to photonic sequential logic. *Applied Physics Letters*, 99(15):153103, 2011.

[163] D. Press, T. D. Ladd, B. Zhang, and Y. Yamamoto. Complete quantum control of a single quantum dot spin using ultrafast optical pulses. *Nature*, 456:218, 2008.